



HAL
open science

Frequency combs at the quantum limit

Roman Schmeissner

► **To cite this version:**

Roman Schmeissner. Frequency combs at the quantum limit. Physics [physics]. Université de Paris; Pierre et Marie Curie, Paris VI, 2014. English. NNT: . tel-01098503

HAL Id: tel-01098503

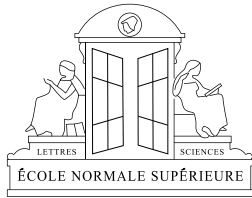
<https://theses.hal.science/tel-01098503>

Submitted on 25 Dec 2014

HAL is a multi-disciplinary open access archive for the deposit and dissemination of scientific research documents, whether they are published or not. The documents may come from teaching and research institutions in France or abroad, or from public or private research centers.

L'archive ouverte pluridisciplinaire **HAL**, est destinée au dépôt et à la diffusion de documents scientifiques de niveau recherche, publiés ou non, émanant des établissements d'enseignement et de recherche français ou étrangers, des laboratoires publics ou privés.

Thesis submitted to fulfill the requirements for the degree
Doctor of the University Pierre et Marie Curie, Paris VI



Frequency combs at the quantum limit

Roman Schmeissner



defended on 13th of June 2014

Jury members

Mme.	Marie-Christine Angonin	examinator
M.	François Bondu	examinator
M.	Fabien Bretenaker	examinator
M.	Yann Le Coq	examinator
M.	Claude Fabre	invited
M.	Franz Kärtner	rapporteur
M.	Daniele Romanini	rapporteur
M.	Nicolas Treps	director of thesis

Abstract

Precision metrology is one application of optical frequency combs. Classical noise in their properties typically limits achievable measurement sensitivity. Amplitude and phase noise in optical frequency combs have already been studied extensively. So far, noise sidebands close to the carrier of either individual optical frequencies or of the mean field have been considered. This thesis develops methods to precisely characterize amplitude and phase noise down to the quantum limit. To this aim a transmissive, broadband passive cavity is developed. It filters and inter-converts amplitude and phase noise. The analysis of its signal by the use of homodyne detection provides a quantum limited measurement of phase noise. The application of ultrafast pulse shaping enables the measurement of the spectral correlations of amplitude and phase noise. Being represented by the use of covariance matrices, the entire noise correlations over the optical spectrum are characterized on the example of a Ti:Sapph oscillator. The measured noise correlations exhibit spectral structures, so-called *modes*. Their shape matches with the theoretical prediction. This concept known from multi-partite optical quantum systems is consequently applicable to classical noise in frequency combs. The knowledge of the intrinsic noise modes is likely provide an improvement of precision metrology experiments with combs.

Résumé

La métrologie de haute précision est une application des peignes de fréquences optiques. Typiquement, la sensibilité de mesure est limitée par le bruit classique des propriétés des peignes. Leur bruit d'amplitude et de phase a été largement étudié et jusqu'à présent. Pourtant, uniquement des bandes latérales de bruit proche de la porteuse ont été caractérisées pour des fréquences individuelles et le champ moyen.

Cette thèse développe des méthodes de caractérisation de bruit d'amplitude et phase à la limite quantique. A cette fin, une cavité passive et large bande est développée. Elle filtre et inter-convertit les bruits d'amplitude et phase. L'analyse de son signal à l'aide d'une détection homodyne permet la mesure du bruit de phase d'un peigne avec une sensibilité à la limite quantique. L'application d'un façonnage des impulsions ultra brèves rend possible la mesure des corrélations spectrales du bruit. Tout en étant représentés par des matrices de covariance, l'ensemble des corrélations du bruit sur le spectre optique d'un oscillateur Ti:Sapph est caractérisé.

Les corrélations mesurées montrent des structures spectrales, dites *modes*, qui sont en accord avec la prédiction théorique. Ce concept apparait comme analogue au formalisme décrivant des systèmes multi-partites en optique quantique. Il est par conséquent aussi un moyen de description de bruit classique. La connaissance des modes intrinsèques du bruit est susceptible de mener à une amélioration de la précision de mesures avec des peignes de fréquences optiques.

Contents

1	Introduction	2
2	Theoretical considerations	7
2.1	Optical frequency combs	9
2.2	Principal concepts for noise analysis	17
2.3	Lower limits of amplitude and phase noise	22
2.4	Lower noise limits for laser radiation	25
2.5	Homodyne noise measurements with combs	36
2.6	Aspects of practical noise measurements	41
2.7	Passive cavities: filtering and analysis of noise	46
3	Experimental Framework	59
3.1	Properties of the Ti:Sapph oscillator	60
3.2	Design of a passive broadband cavity	80
4	A passive cavity for comb phase noise metrology	96
4.1	Analysis and filtering of phase noise in an optical comb	98
4.2	Broadband spectrally resolved phase noise analysis	107
4.3	The transfer function representation	122
4.4	Quantum-limited measurement of phase noise - ready to use	125
4.5	Spectral noise correlations in frequency combs.	134
5	Summary and Outlook	150
A	Appendix	155
A.1	Filtering the oscillator's pump laser	155

Chapter 1

Introduction

Femtosecond optical frequency combs have revolutionized optical metrology [1] given their intrinsic, relative and absolute phase lock of optical frequencies. Recent experiments have demonstrated that they can even be applied to massively parallel optical spectroscopy, within a dual comb configuration [2, 3].

In general, frequency combs permit numerous measurements. Therein, one domain is optical metrology and two main types of measurement can be distinguished: First, the link of optical frequency standards such as transitions of Sr-atoms to the radio-frequency domain [4]. The comb is used here as a *transfer-oscillator* and its linewidth limits the measurement precision. The second type exploits their dual time and frequency structure to perform *multi-spectral interferometry*. In such comb-comb interference measurements, e.g. periodic displacements are measurable with highest sensitivity [5]. Such measurements render them an ideal candidate for ranging or clock synchronization [6, 7]. For example, this approach has been proven to be optimal when used in a homodyne configuration with a pulse shaped reference beam [5]. The underlying concept of projection on a temporal mode carrying the information can even be extended to general parameter estimation [8].

In this context of very high sensitivity metrology, measurements are ultimately limited by the intrinsic noise of the laser source, whether it be of classical or quantum nature. The lowest level classically possible is set by the zero-point fluctuations of the electromagnetic field. The corresponding noise level is defined as the *standard quantum limit (SQL)*. Classical noise in frequency combs down to this limit is in the focus of this thesis.

Noise in femtosecond oscillators. The analysis of laser noise can be divided into three main time scales: First, the long-term stability of the absolute/relative comb frequencies on timescales of seconds. Drifts, jitter and $1/f$ noise are compensated here by active lock mechanisms and external radio-frequency references. Their properties typically determine the comb linewidth [9]. Second, the millisecond regime in a quiet environment: In this extensively studied regime [10, 11, 12, 7] the lowest noise levels of the comb generating ultrafast oscillator may be set by spontaneous emission (the Shawlow-Townes limit) and noise coupling processes related to the mode-locking principle. A third regime is expected for shorter timescales in the microsecond range: the standard quantum limit SQL of *white noise* properties. This regime is of particular interest as the low noise levels are promising for metrology experiments [5]. The main underlying idea is to detect signals at timescales where the laser is at the SQL. The decrease of signal associated with short integration times is compensated by the lowest possible level of noise.

The investigation of continuous wave Titanium-Sapphire (Ti:Sapph) lasers, indicated that the SQL could be reached at microsecond timescales [13]. For the repetition rate of a femtosecond oscillator, a very recent work [14, 15] studied the SQL, but only for exceptionally high photocurrents.

In summary, although the noise of Ti:Sapph and fiber oscillators has been characterized extensively relative to the carrier [16, 17, 18], no data are so far available relative and close to the quantum limit.

Spectral noise properties. The study of the noise in frequency combs at microsecond timescales was pioneered by Haus et al.[10]. Nevertheless, the results ignored any possible dependence of the noise on the optical frequency within the comb. It has been pointed out later by Paschotta et al. that this implicit assumption has to be questioned at RF-detection frequencies above 100 kHz [19]. A slight dependence of the linewidth on the optical frequency has been shown theoretically for a Ti:Sapph oscillator [20]. Another, indirect approach to spectral phase noise in frequency combs is the fix-point model [21]. It has recently been applied to a Ti:Sapph generated comb [16].

Spectral noise correlations. Furthermore, no experimental information has been previously available concerning the correlations of spectral noise properties for classical noise close to the SQL.

Noise correlations among various optical frequencies have been studied so far only for non-classical quantum states of light in frequency combs [22, 23, 24]. Such non-classical noise correlations introduced by nonlinear processes are most readily

detected under vanishing classical noise at the SQL. It turned out that spectral structures of noise are a suitable formalism to describe such correlations [25, 24]. They enable the use of frequency-combs as on-demand quantum-networks [22, 23, 24] and may even form so-called cluster-states [26].

It is nevertheless not clear how far this representation applies to classical noise in frequency combs close to the SQL. It turns out here that such *noise modes* are the underlying concept of a suggested, highly sensitive measurement scheme for femtosecond pulse timing jitter [5]. The direct measurement of the classical comb noise modes is the main purpose and result of this thesis. This concept is applied here for the first time to quantify the entirety of classical amplitude and phase noise correlations across a frequency comb. It is also important to note that the well known oscillator noise theory of H.A.Haus [10] relies implicitly on temporal modes of classical noise in frequency combs.

The typically characterized repetition rate and CEO-phase fluctuations [7, 27, 28] are both mean field properties of the entire frequency comb. They have been erstwhile measured ignoring spectral phase noise. Using the concepts of [5], it turns out here that both correspond to well-defined structures of noise correlations over the frequency comb.

Passive cavities and combs. Passive cavities are suitable filters of lowest levels of classical noise in continuous wave lasers [29]. It is shown here that the concept of a noise filtering resonator can be extended to optical frequency combs. In addition, their transmission and reflection turn out to be highly sensitive to phase noise of the resonant seed [30]. It is used in this thesis to precisely analyze low level noise properties and structures of spectral phase noise. The analysis has been accomplished for a approximately 60 nm broad optical frequency comb.

Furthermore, balanced homodyne detection is a well-known tool to characterize intensity and phase noise of lasers. It is used here together with the broadband passive cavity and femtosecond pulse shaping to measure the noise correlations in an optical frequency comb. Unprecedented, quantum-limited sensitivity is achieved. The eigendecomposition of the corresponding covariance matrices reveal correlated spectral structures of classical noise.

In summary, this thesis aims to characterize the entire structure of amplitude and phase noise in an optical frequency comb close to the standard quantum limit (SQL). Techniques aimed at improving these noise properties are developed.

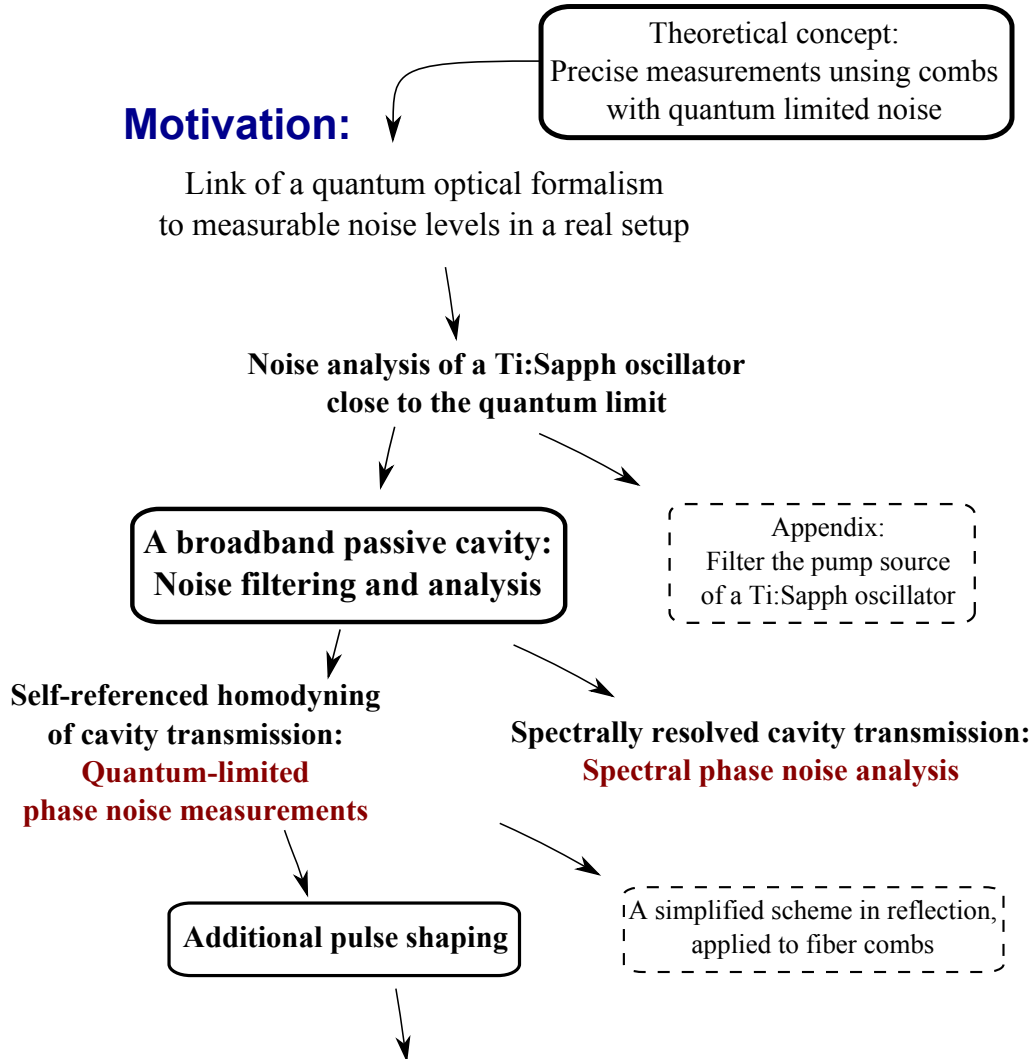
Structure of this document. The organization of this thesis is depicted by the chart on the following page. To start, the capacity of a frequency comb to be quantum-limited in amplitude and phase is put in the context of accessible measurements of noise. As such, the theoretical proposition for precision homodyne measurements [5] is placed in a realistic framework. A Ti:Sapph oscillator is subsequently analyzed using well-established measurement principles. Two possibilities for reducing its lowest levels of classical noise are studied. One is the further improvement of the pump laser properties by passive filtering and is discussed in the appendix. The second introduces a broadband passive cavity for filtering noise in a frequency comb. In addition to improving the noise properties of the comb, this new tool also turns out to be very versatile for characterizing the lowest levels of phase noise in frequency combs.

By interfering the cavity transmitted signal with a part of the seed, the phase noise of the frequency comb is measured with an unprecedented sensitivity down to the quantum limit. A simplified, but equivalent scheme using the reflection of a cavity is applied to study the phase noise of a fiber-based frequency comb.

Subsequently, it is shown that a spectrally resolved analysis of the cavity transmission signal reveals the spectral phase noise of a frequency comb close to the SQL. Without using this approach, similar results could only be obtained within a setup of highest complexity. Several single frequency lasers would have to be locked to a common reference to be beaten with the frequency comb [16].

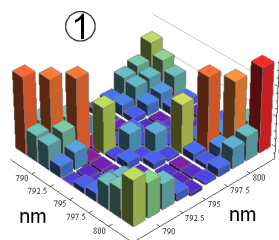
The principal result of this thesis stems from combining the cavity transmission with a homodyne detection, in which the local oscillator is subject to ultrafast pulse shaping [31]. This technique measures the correlations of spectral amplitude and phase noise in the frequency comb with quantum-limited sensitivity. With this information spectral correlations of classical noise are identified. A basis transformation is applied and reveals a set of independent, uncorrelated spectral structures. These structures are termed *noise modes*. They are a new representation for classical noise in frequency combs. The commonly used formalisms to describe phase noise in frequency combs (e.g. the repetition rate) turn out to be special cases of the noise mode representation.

Structure of this thesis:

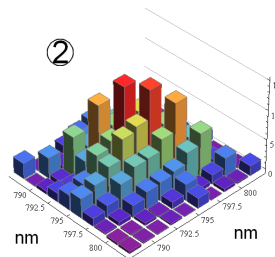


Modes of classical noise

Covariance matrices of
spectral amplitude and phase noise



Amplitude



Phase

Chapter 2

Theoretical considerations

Contents

2.1	Optical frequency combs	9
2.1.1	Time- and Frequency representation of optical combs	9
2.1.2	Temporal/Spectral-mode representation	11
2.1.3	Photodetection and shot noise	12
2.2	Principal concepts for noise analysis	17
2.2.1	The definition of the spectral variance	17
2.2.2	Other noise quantifiers and the Allan variance	20
2.3	Lower limits of amplitude and phase noise	22
2.3.1	The Standard Quantum Limit.	23
2.4	Lower noise limits for laser radiation	25
2.4.1	Shawlow-Townes-Limit	25
2.4.2	Noise in optical frequency combs	26
2.4.3	The oscillator noise model of H.A.Haus	29
2.4.4	The rubber band model of spectral phase noise	33
2.5	Homodyne noise measurements with combs	36
2.5.1	Realistic homodyne timing jitter measurement	37
2.6	Aspects of practical noise measurements	41
2.6.1	The measurement of phase noise	42
2.7	Passive cavities: filtering and analysis of noise	46
2.7.1	Cavity resonances	48
2.7.2	Transfer function of the noise field quadratures	52

2.1 Optical frequency combs

This chapter gives an overview on the key theoretical aspects used in this thesis. Starting with the principal methods describing laser radiation and optical frequency combs, concepts for noise analysis are discussed in the following. The focus is subsequently set on lower limits of noise in laser radiation and methods to analyze them.

2.1.1 Time- and Frequency representation of optical combs

The electric field at the output of a mode-locked laser is the coherent superposition of the individual longitudinal modes simultaneously resonant in the laser cavity and for which the gain is not vanishing [32]. In general, we write

$$E(z, t) = \text{Re} \left\{ \sum_{m=0}^{\infty} E_m e^{i(\omega_m t - k_m z + \phi_m)} \right\}, \quad \omega_m = \omega_{\text{CEO}} + m\Delta\omega, \quad k_m = \frac{\omega_m}{c} \quad (2.1)$$

The spacing of the underlying *frequency comb* ω_m is given by the laser cavity length L and the integer m multiples of the free spectral range $\Delta\omega = 2\pi c/L$. The field $E(z, t)$ of Eq.(2.1) is a periodic signal with the repetition time $T_{\text{rep}} = 2\pi/\Delta\omega$. This is the inverse of the *repetition rate* $f_{\text{rep}} = \omega_{\text{rep}}/2\pi = \Delta\omega/2\pi$ of the pulse train, and corresponds to the round-trip time of a pulse in the laser oscillator cavity. To describe the general case, an additional frequency shift ω_{CEO} is necessary. It is discussed below and corresponds to a slowly evolving phase property, the *carrier-envelope-phase (CEO)*. The possible representations of this quasi-periodic field have been studied in detail in [33].

A frequency comb can also be represented in the time domain. To this aim, one defines the *carrier frequency* ω_0 as the optical frequency of the spectral center of gain. In an ideal situation giving rise to shortest pulses, the spectral phase parameters ϕ_m are constant for all frequencies m . Using the definition of a light-cone variable $u = t - z/c$, Eq.(2.1) can be written using the complex temporal envelope $v(u)$:

$$E(u) = \text{Re} \left\{ e^{i\omega_0 u} \sum_{m=-\infty}^{\infty} E_m e^{im\Delta\omega u + \phi_m} \right\} = \text{Re} \{ v(u) e^{i\omega_0 u} \}. \quad (2.2)$$

This is the *temporal representation* of a coherent pulse train. Note that the envelope $v(u)$ is here a pulse train.

The CEO-phase. The temporal representation above distinguishes a carrier frequency ω_0 and an envelope $v(u)$. The phase of the carrier propagates with the phase velocity $v_\phi = c/n$ where n is the refractive index of the media at ω_0 . The envelope propagates with the group velocity $v_{gr} = [\partial k / \partial \omega]^{-1}$ at ω_0 . A difference of both velocities leads to a relative phase between envelope and carrier per pulse round-trip in the laser oscillator cavity. Being sampled periodically by the repetition rate T_{rep} , all comb frequencies ω_m are shifted by

$$\omega_{CEO} = \frac{\omega_{rep}}{2\pi} \Delta\phi_{CEO}, \quad \Delta\phi_{CEO} = \left(\frac{1}{v_g} - \frac{1}{v_\phi} \right). \quad (2.3)$$

The CEO-frequency is a property common to all longitudinal modes $\omega_m = \omega_{CEO} + m\Delta\omega$ in an optical frequency comb. It can be used to define a common phase for all comb lines.

The spectral phase. During propagation in a dispersive medium, a femtosecond pulse undergoes temporal broadening. The phase term for each tooth of the frequency comb in Eq.(2.1) contains the so-called *spectral phase* $\phi_m = \phi(\omega_m)$. The mode-locking in the optical oscillator sets these values to a constant for all m . A propagation in dispersive media with $n(\omega_m) \neq const.$ will modify this spectral phase. The consequences can be analyzed by using a Taylor-series approach. A constant offset ϕ_0 has no consequences, and a linear spectral phase $\phi' \neq 0$ will delay the pulse. In contrast, a quadratic phase $\phi'' \neq 0$ changes the temporal pulse length. It is called the *Group Velocity Dispersion (GVD)*. A Gaussian pulse of duration τ_0 propagating through a medium of dispersion $\phi'' \gg 0$ in fs^2 will spread to $\tau_{GVD} \simeq \phi'' / \tau_0$, see [34].

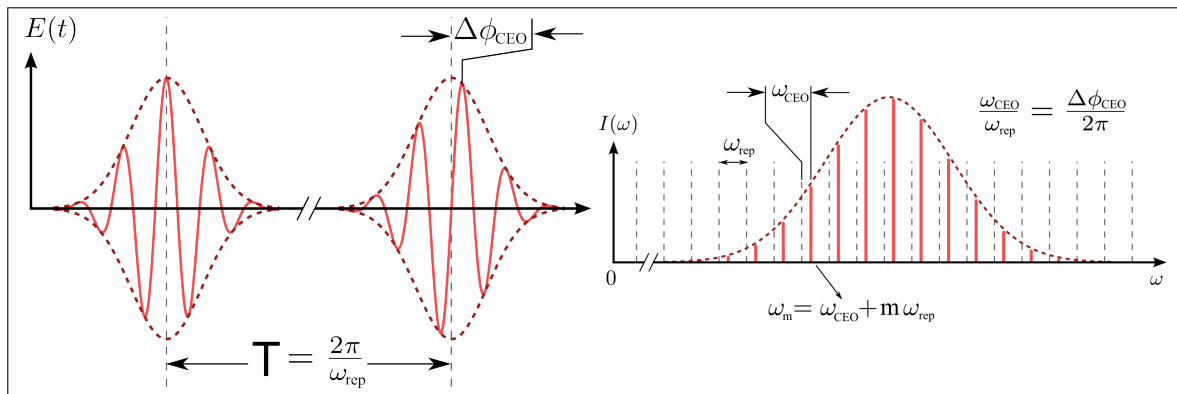


Figure 2.1: The two principal representations of coherent ultrashort optical pulse trains. *left:* the temporal representation, a fast oscillating carrier is modulated by an ultrafast envelope, their relative position defines the *carrier-envelope-phase*, shown are two subsequent pulse envelopes, the *single pulse mode* $\tilde{v}(u)$, *right:* the frequency comb representation, a superposition of longitudinal modes

2.1.2 Temporal/Spectral-mode representation

The representation of the pulse train Eq.(2.2) shows that a coherent train of pulse envelopes can be considered as a single envelope function $v(u)$: $E(u) = Re\{v(u)e^{i\omega_0 u}\}$. For this thesis, the individual pulse envelope \underline{v} with a factorization of the CEO-phase will play a significant role:

$$v(u) = \sum_{\tilde{m}} \underline{v}(u - \tilde{m}T_{rep})e^{i\tilde{m}\theta_{CEO}} \quad (2.4)$$

This single pulse envelope \underline{v} is well defined, square integrable and non zero in the interval $[0, T_{rep}]$, see [33]. It can consequently be written in a suitable basis \underline{v}_j :

$$\underline{v}(u) = \sum_i a_i \underline{v}_i(u), \quad \int_0^{T_{rep}} \underline{v}_i^*(u) \underline{v}_j(u) du = \delta_{ij} \quad (2.5)$$

The elements of this basis are called *temporal modes*. This representation can be entirely transposed into the frequency domain. The general expression for the electric field envelope is:

$$E(u) = Re \left\{ \sum_m \underline{v}(u - mT_{rep}) e^{i\omega_0 u} e^{im\theta_{CEO}} \right\} \quad (2.6)$$

Equation (2.6) together with (2.5) are the *modal representation* of a coherent train of ultrashort pulses, in terms of the single pulse *temporal modes* $\underline{v}(u)$. Eq.(2.6) can be simplified for a non-fluctuating field: There exists always a mode $v(u)$ proportional to the mean of the classical electric field [35]. This leads to a basis $\underline{v}(u)$ with only one element, the mean electric field of a single pulse. Note that the mode representation discussed here is analog to the decomposition of transverse beam intensity profiles into e.g. Hermite-Gauss modes of a light beam.

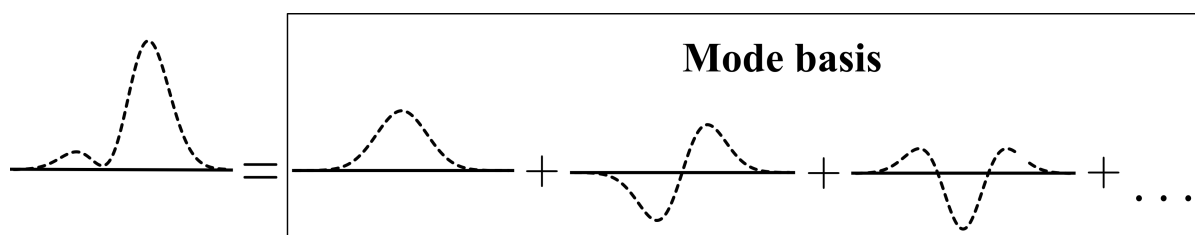


Figure 2.2: Mode representation of a coherent pulse train/a frequency comb. 1. *Time domain*: the horizontal axis is the time. Any pulse envelope $\underline{v}(u)$ can be represented as a superposition of orthogonal envelopes $\underline{v}_i(u)$. They are called *temporal modes*. 2. *Frequency domain*: This representation can be transposed to the spectral domain. The horizontal axis is then the optical frequency and the orthogonal envelopes are called *spectral modes*. Each spectral mode is a superposition of a large number of single frequency, longitudinal modes.

2.1.3 Photodetection and shot noise

Photodetection allows to link light properties to measurable, electrical quantities [36, 37]. The following discussions rely on [38].

Balanced homodyne detection. In order to detect the mode- and noise properties of the frequency combs described above, *balanced homodyne detection* plays an essential role in this thesis. It is depicted in Fig. 2.3. The principal application is here the mode selective detection of the relative phase noise of two beams. They are typically a bright *Local Oscillator* (LO) and an attenuated Signal (S). If both LO and S contain similar input powers, the scheme is subsequently called *balanced interference detection*. It is applied in the experimental section 4, page 96.

Considering the individual combs lines of the same optical frequency, the complex fields in both input ports can be written as $E_{LO,S}(t) = A_{LO,S}e^{i\omega t}$. After the beamsplitter, the fields E_1 and E_2 are incident to the photodetectors:

$$E_1 = \frac{1}{\sqrt{2}}(E_{LO} - E_S), \quad E_2 = \frac{1}{\sqrt{2}}(E_{LO} + E_S) \quad (2.7)$$

Assuming ideal quantum efficiency and time-response, noting q the elementary charge and assuming a suitable normalization, the difference of the two photocurrents becomes $i(t) = q(|E_2|^2 - |E_1|^2) = q(E_{LO}^*E_S + E_{LO}E_S^*)$. Using the notation $\phi = \arg(E_{LO}^*E_S)$, the mean squared signal is:

$$i_s^2 = q^2|E_{LO}^*E_S + E_{LO}E_S^*|^2 = 4q^2|A_{LO}|^2|A_S|^2 \cos^2 \phi \quad (2.8)$$

Using the setup Fig. 2.3, it is possible to lock the mean relative phase $\langle \phi \rangle$ of the two beams. Nevertheless, small fluctuations $\delta\phi = \langle \phi \rangle - \phi$ may still be present. Locking $\langle \phi \rangle = 0$ the output i_s^2 is sensitive to amplitude fluctuations but in the first order insensitive to phase noise $\delta\phi$. The opposite situation is of key importance for this thesis. Locking $\langle \phi \rangle = \pi/2$, the mean square output current is highly sensitive to the relative phase fluctuations between the two interferometer arms:

$$i_s^2 = 4q^2|A_{LO}|^2|A_S|^2 \sin^2 \delta\phi = 4q^2|A_{LO}|^2|A_S|^2(\delta\phi)^2 \quad (2.9)$$

In order to evaluate best possible signal to noise ratios for such a measurement, the impact of shot noise is considered in the next section. To reduce the sensitivity to amplitude noise, one of both beams can be of significantly higher amplitude. This configuration is called homodyne detection.

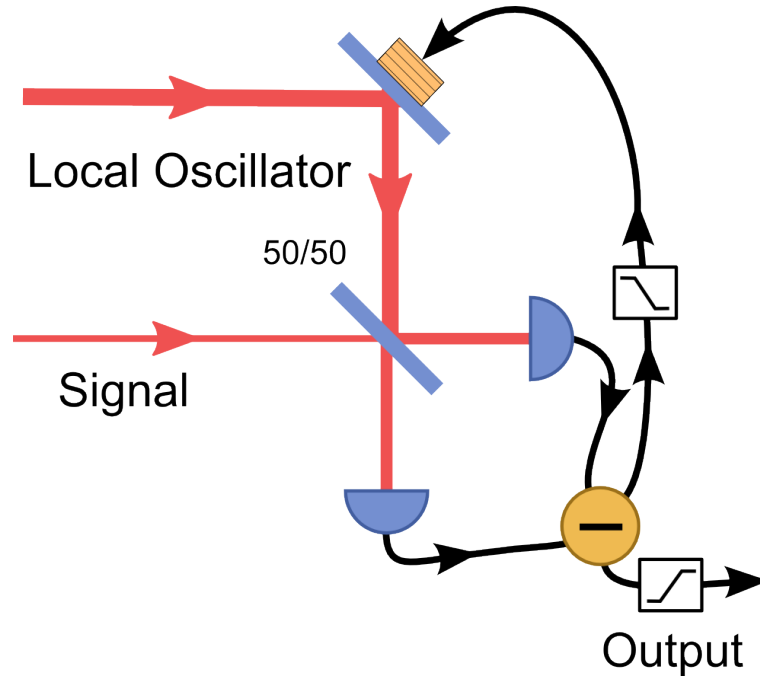


Figure 2.3: Balanced homodyne detection - the principal detection scheme used in this thesis. The principal elements are: a *local oscillator* beam much brighter than the *signal* beam, a 50/50 beam splitter, two identical photodetectors and an analog subtraction using electronic phase shifting and mixers. The resulting difference signal can be applied to the piezo-mounted mirror to lock the relative phase of the two input beams. To this aim it is low-pass filtered and proportional-integral amplified. The high-passed signal part is the output of the measurement scheme. A relative phase of the two beams of $\pi/2$ leads to a detection of the noise in their relative phase.

Discrimination of multimode structure. A balanced homodyne detection is sensitive to the mode-content of a beam and can be used to analyze it [24]. In a simplified classical representation, the field-strength products Eq.(2.8): $E_{\dots}E_{\dots}^*$ are measured with detectors significantly slower than the femtosecond timescales of the temporal pulse envelopes. Considering the example of one signal pulses the photocurrent difference is:

$$\langle i \rangle = \frac{1}{T_{\text{rep}}} q \int_0^{T_{\text{rep}}} E_{\text{LO}}^*(t') E_{\text{S}}(t') + E_{\text{LO}}(t') E_{\text{S}}^*(t') dt' \quad (2.10)$$

This structure is equivalent to a symmetrized temporal scalar product. By choosing the mode of the local oscillator, the balanced detection measures its scalar product Eq.(2.10) with the signal field. It consequently discriminates between the temporal modes described in Eq.(2.5).

It is remarkable that the same scalar-product appears in the theory of H.A.Haus concerning fluctuations of properties of coherent pulse trains [10]. The signal corresponds there to the investigated pulse train, the LO to a specific pulse property that can be represented in a corresponding temporal mode.

Field quantization. Fundamental noise properties of optical frequency combs are studied in this thesis. They are linked to the commutation relations of the operators that describe the measurement. A coherent train of light pulses can also be described using the formalism of quantum optics [36]. Using the second quantization formalism, the operator valued equivalent to Eq.(2.6), the field operator $\hat{E}(u)$, can be decomposed in pulse-train modes $v_i(u)$. It is then a superposition of modes associated with annihilation operators \hat{a}_i . Under the reasonable assumption of a finite measurement time T , this statement reads [36]:

$$\hat{E}(u) = \hat{E}^{(+)} + \hat{E}^{(+)\dagger}, \quad \hat{E}^{(+)}(u) = i\mathcal{E} \sum_i \hat{a}_i v_i(u), \quad \mathcal{E} = \sqrt{\frac{\hbar\omega_0}{2\epsilon_0 c T}} \quad (2.11)$$

In analogy to the harmonic oscillator, the photon number operator associated to a mode v_i can be defined as $\hat{N}_i = \hat{a}_i^\dagger \hat{a}_i$, where \hat{a} and \hat{a}^\dagger follow $[\hat{a}_i, \hat{a}_j^\dagger] = \delta_{ij}$. This is a consequence of the orthogonality of the modes v_i .

Field quadratures and quantum noise. Observables are obtained from linear combinations of \hat{a}_i and define the quadrature operators P_i and Q_i :

$$\hat{Q}_i = \hat{a}_i^\dagger + \hat{a}_i, \quad \hat{P}_i = i(\hat{a}_i^\dagger - \hat{a}_i), \quad [\hat{Q}_i, \hat{P}_j] = 2i\delta_{ij} \quad (2.12)$$

For any mode i , the commutation relation Eq.(2.12) leads directly to a Heisenberg inequality for the two operators and thus sets minimal variances for an ideal coherent state of light:

$$\sigma_{P,\min}^2 = \sigma_{Q,\min}^2 = 1. \quad (2.13)$$

These are the variances of the outcomes of a large number of measurements. They can be associated with noise in the measurement that is in consequence equally distributed on both quadratures.

The classical analog to the observables \hat{P} and \hat{Q} are under a suitable transformation the amplitude and phase of the electric field. They will be used in section 2.7.2 to describe the noise properties of the transmission and reflection of a passive cavity.

Shot noise in photodetection. A large part of the experimental results of this thesis calibrate recorded intensity noise levels to the shot noise level. Its emergence can be shown as follows [38]: For a given time interval, propagation constant and ideal photodetection, assume the charge registered by the detector to be the Hermitian operator $\hat{Q} = q\hat{a}^\dagger\hat{a}$. For a coherent state $|\alpha\rangle$, the expectation value of the charge is proportional to the expected photon number $\langle n \rangle$:

$$\langle \alpha | \hat{Q} | \alpha \rangle = q \langle \alpha | \hat{a}^\dagger \hat{a} | \alpha \rangle = q |\alpha|^2 = q \langle n \rangle \quad (2.14)$$

In order to calculate the photon number variance, $\sigma_{\hat{Q}}^2 = \langle \alpha | \hat{Q}^2 | \alpha \rangle - \langle \alpha | \hat{Q} | \alpha \rangle^2$:

$$\langle \alpha | \hat{Q}^2 | \alpha \rangle = q^2 \langle \alpha | \hat{a}^\dagger \hat{a} \hat{a}^\dagger \hat{a} | \alpha \rangle = q^2 \langle \alpha | \hat{a}^\dagger \hat{a}^\dagger \hat{a} \hat{a} + \hat{a}^\dagger \hat{a} | \alpha \rangle \quad (2.15)$$

$$= q^2 |\alpha|^4 + q^2 |\alpha|^2 = q^2 \langle n \rangle^2 + q^2 \langle n \rangle \quad (2.16)$$

The variance of the photon number is consequently equal to the average photon number:

$$\sigma_{\hat{Q}}^2 = q^2 \langle n \rangle \quad (2.17)$$

This is the property of a Poisson process, a completely random flow of charges. It arises from the bosonic commutation relation of \hat{a} and \hat{a}^\dagger that enters Eq.(2.15). The zero-point fluctuations of the vacuum are its cause. Applied here to a coherent state, these fluctuations are the fundamental origin of shot noise.

Signal-to-noise ratio. Assume the detection of an optical signal at a single carrier frequency. The detected, squared d.c. photocurrent signal is $\langle i_S^2 \rangle = \langle i_S \rangle^2 = q^2 \gamma^2 \langle n \rangle^2$. Here γ is a proportionality constant. The mean square current fluctuations are obtained using Eq.(2.17). Being originated by white shot noise, the detected noise level is addition a function of the measurement bandwidth B : $\langle i_N^2 \rangle = q^2 \gamma \langle n \rangle \cdot 2B$. A detailed derivation is given in [38]. The signal-to-noise ratio S/N is consequently:

$$\frac{S}{N} = \frac{\langle i_S^2 \rangle}{\langle i_N^2 \rangle} = \frac{\gamma \langle n \rangle}{2B} \quad (2.18)$$

It is proportional to the photon number current and to the inverse measurement bandwidth.

The sensitivity of any measurement is proportional to the signal to noise ratio S/N and Eq.(2.18) provides the following insight: For shot noise limited classical noise, the S/N can always be improved by either by increasing the detected photon number or by decreasing the measurement bandwidth.

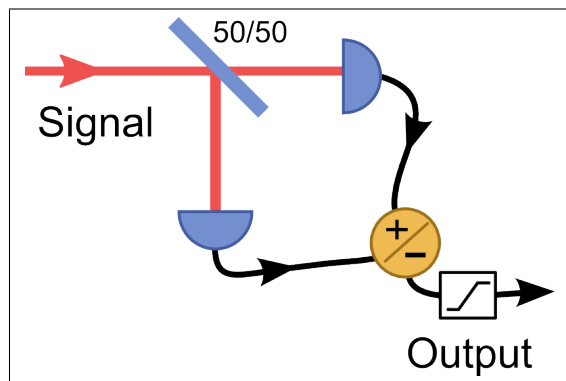


Figure 2.4: The balanced detection. This type of photodetection directly measures the shot noise level of a beam. It consists of two identical, broadband photodetectors, a 50/50 beamsplitter and an analog signal sum/difference. The difference photocurrent suppresses all classical modulations. Its noise level is the shot noise of the signal beam.

Balanced detection. One main focus of this thesis is the characterization of noise relative to the shot noise level. In order to calibrate such measurements for intensity-noise, a balanced detection as shown in Fig. 2.4 can be used. It distinguishes between classical optical noise (intensity modulations) and noise on the photon level [39]:

If the sum of the photocurrents is analyzed, the two detectors appear as a single one and the classical noise is detected. The photocurrent difference ideally suppresses all classical intensity noise. Any classical noise or signal modulation is detected identically by both photodetectors. The attenuation of this common signal reaches in practice 20 to 30 dB. Nevertheless and in a simplified representation, single photons are not split by the beamsplitter. Photocurrent noise arising from their uncorrelated detection in time domain is summed up although the current difference is measured. Recorded with a spectrum analyzer, the resulting level of white noise is the shot noise level of the signal beam. A comparison of the sum signal to this level permits to calibrate classical noise relative to the shot noise level.

2.2 Principal concepts for noise analysis

This thesis analyzes noise properties of frequency combs: relative to the lower limits set by quantum mechanics and based on measurements. The measured noise data will be interpreted in a unified form, using the *spectral variance* defined in this section. It is obtained as a time-independent property of a stationary noise process either by the use of the Parseval-Theorem or the Wiener-Khintchine-Theorem. The *spectral variance* is subsequently compared to another common choice of phase/frequency noise quantification, the *Allan variance*.

2.2.1 The definition of the spectral variance

Spectral density of a noise-process - Parseval Theorem. In order to analyze the noise of any physical quantity X_0 characterizing an optical frequency comb, its fluctuations $X(t) = X_0 - \bar{X}_0$ can be assumed to be given as a real continuous time series $X(t)$. This is called a *stochastic process* with zero mean, and stationarity is assumed for large measurement times T . The process $X(t)$ can be developed in a Fourier series and the coefficients follow:

$$A(f) = \int_{-\infty}^{+\infty} dt X(t) e^{-2\pi i f t}, \quad \int_{-\infty}^{+\infty} |X(t)|^2 dt = \int_{-\infty}^{+\infty} |A(f)|^2 df \quad (2.19)$$

The variance σ^2 of the process $X(t)$ can be expressed starting from this Parseval Theorem [40]. Nevertheless, the Fourier Transform (FT) may not always exist. In order to insure integrability for large measurement times T , it is suitable to introduce a truncated FT:

$$A_T(f) = \int_{-T/2}^{+T/2} dt X(t) e^{-2\pi i f t} \quad (2.20)$$

The variance σ^2 of the process $X(t)$ can now be expressed in terms of the spectrum using Eq.2.20 and division by the interval size:

$$\sigma^2 = \lim_{T \rightarrow \infty} \frac{1}{T} \int_{-T/2}^{+T/2} |X(t)|^2 dt \quad (2.21)$$

$$= \lim_{T \rightarrow \infty} \frac{1}{T} \int_{-\infty}^{+\infty} |A_T(f)|^2 df. \quad (2.22)$$

Since $X(t)$ is real, one has $A(f) = A^*(-f)$ and $|A(f)|$ is an even function. The variance σ^2 can consequently be written in terms of a density $S(f)$ that is only defined for positive frequencies:

$$\sigma^2 = \int_0^{\infty} S(f)df \quad \text{with} \quad S(f) = \lim_{T \rightarrow \infty} \frac{2}{T} |A_T(f)|^2 \quad (2.23)$$

The distribution $S(f)$ is called *the single side-band (SSB), power spectral density* of the process $X(t)$.

Spectral density of a noise-process - Wiener-Khintchine-Theorem. The variance σ^2 above is defined based on the limit of a truncated Fourier Transform. An other approach uses the autocorrelation function $\Gamma_{xx}(\tau)$, that is always well defined:

$$\Gamma_{xx}(\tau) = \langle X(t)X(t + \tau) \rangle = \lim_{T \rightarrow \infty} \frac{1}{T} \int_{-T/2}^{+T/2} X(t)X(t + \tau)dt \quad (2.24)$$

The *Wiener-Khintchine theorem* [41] states that Γ_{xx} is a Fourier transform pair with a spectral density. Using the Fourier integral theorem it can be shown that the single side-band, power spectral density of $X(t)$ is obtained using a cosine transform [40]:

$$S(f) = 4 \int_0^{\infty} \Gamma_{xx}(\tau) \cos(2\pi f\tau) d\tau \quad (2.25)$$

Both definitions of the power spectral density, using the autocorrelation function or the Parseval Theorem are equivalent.

The spectral variance. Experimentally, the measurement of the variance σ^2 corresponds to an r.m.s. noise measurement with an oscilloscope of large bandwidth. In order to obtain more detailed information on the noise process, a spectral resolved link between the density $S(f)$ and the variance is necessary. This corresponds to a spectrum analyzer measurement resolving the variance for each detection frequency:

Assuming a known spectral density $S(f)$, the variance σ^2 of the process $X(t)$ can also be defined for frequency intervals. They can be infinitely small:

$$\sigma^2(f_1, f_2) = \int_{f_1}^{f_2} S(f)df, \text{ so for } f_2 \rightarrow f_1 = \tilde{f} : S(\tilde{f}) = \frac{\partial \sigma^2(f)}{\partial f} \Big|_{\tilde{f}} \quad (2.26)$$

For the considerations of this thesis, the function $S(f)$ can be assumed to be slowly varying on a frequency interval of 1 Hz and consequently $\sigma^2(f_1, f_1 + 1 \text{ Hz}) \approx S(f) \cdot 1 \text{ Hz}$. This gives the possibility to a normalization and the important definition:

$$\boxed{\sigma_X^2(f) = S(f) \cdot 1 \text{ Hz}} \quad (2.27)$$

The quantity $\sigma_X^2(f)$ is called the *spectral variance of $X(t)$* . It is defined from the power spectral density $S(f)$. It is of fundamental importance for this thesis in following context:

Quantum optical noise calculus normalizes e.g. shot noise to $\sigma_{\text{shot}}^2 = 1$ without specifying detection conditions [5]. In an experiment, the spectral density of shot- and classical noise $S(f)$ is measurable with a spectrum analyzer and can be normalized to 1 Hz measurement bandwidth. It is Eq.(2.27) that links the two. The variance of e.g. intensity noise can be written in terms of simplified units and for any detection frequency f :

$$\sigma_X^2(f) = \frac{S(f)}{S_{\text{shot}}} \sigma_{\text{shot}}^2 = \frac{S(f)}{S_{\text{shot}}} \quad (2.28)$$

This relation is of principal importance for the interpretation of the experimental results in sections 4.1 and 4.2. The established relation between variance and spectral density occurs in the literature [42, 43, 44, 45] but without detailing the background.

2.2.2 Other noise quantifiers and the Allan variance

The characterization of the stability of oscillators has been a subject of research for many years. Excellent reviews are given by [46, 47, 48]. There exists a large zoology of stability measures and criteria. Distinguishing them requires significant expertise. In this thesis, only the power spectral density $S_X(f)$ and the spectral variance $\sigma_X^2(f) = S_X(f) \cdot 1 \text{ Hz}$ are used to characterize phase noise. This section puts them in the context of other commonly used measures.

Frequency fluctuations. To characterize the stability of oscillators, an often used measure is the *Allan Variance* $\sigma_y^2(\tau)$, see e.g. [49]. A comparison to the *spectral variance* $\sigma_X^2(f)$ from above can be established as follows: In the metrology domain, the noise process $X(t)$ from Eq.(2.19) typically affects the phase of a classical oscillator $E(t) = E_0 \sin(\omega_0 t + X(t))$. The main interest lies on the fluctuations of the instantaneous frequency $y(t)$:

$$y(t) = \frac{1}{\omega_0} \frac{dX}{dt}(t) \quad (2.29)$$

For a noise frequency f , the spectral densities of phase and frequency fluctuations are related by

$$S_y(f) = \frac{4\pi^2 f^2}{\omega_0^2} S_X(f). \quad (2.30)$$

On the definition of a variance for frequency fluctuations. Using the Wiener-Khintchine theorem, the variance of the instantaneous frequency $\tilde{\sigma}_y^2$ has been expressed in terms of $S_y(f)$ by Cutler and Searle [50]:

$$\tilde{\sigma}_y^2(\tau) = 2 \int_0^\infty S_y(f) \left[\frac{\sin(\pi f \tau)}{\pi f \tau} \right]^2 df = 2 \int_0^\infty S_y(f) \alpha(f) df \quad (2.31)$$

A typical metrology purpose is the characterization of drifts of frequency sources on time-scales τ larger than seconds. In practice, measured frequency noise distributions typically follow $S_y(f) \sim 1/f$ or $1/f^2$ laws. The integral Eq.(2.31) diverges here due to the factor $\alpha(f)$ in the limit of a small detection frequencies/long time-scales. The variance $\tilde{\sigma}_y^2(\tau)$ is consequently not of practical use. The highest integrable order is white Shawlow-Townes frequency noise with a constant $S_y(f)$, see Tab. 2.1, page 26.

A commonly used solution. The *Allan variance* $\sigma_y^2(\tau)$ solves this problem. It is a well-defined estimator of the variance $\tilde{\sigma}_y^2(\tau)$ of a frequency signal. It can be defined either from a given frequency noise density $S_y(f)$, or from the *two-sample fractional frequency variance*:

$$\sigma_y^2(\tau) = 2 \int_0^{\infty} S_y(f) \frac{\sin^4(\pi f \tau)}{(\pi f \tau)^2} df = \frac{1}{2} \langle (\bar{y}_1 - \bar{y}_2)^2 \rangle, \quad \bar{y}_n = \frac{\bar{f}_n - \bar{f}_0}{\bar{f}_0} \quad (2.32)$$

The underlying approach is to apply an additional filter $H(f) = \sin(\pi f \tau)^2$ to the signal. In a typical measurement one continuously counts a frequency signal, records the data and calculates this *two sample variance*. The Allan variance is the most common example of a larger class of variance estimators, see [46] for details.

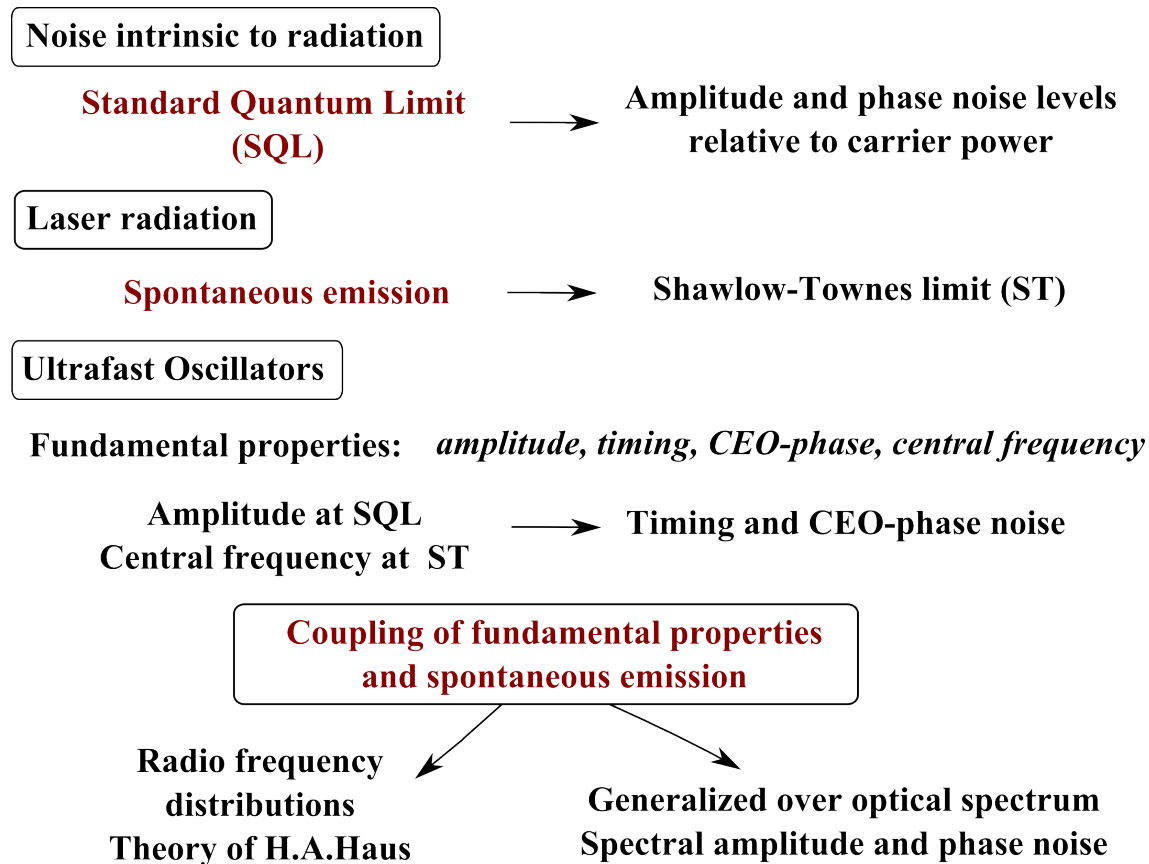
As an example, the quantum-limited, white phase noise discussed in section 2.3 corresponds in an Allan variance plot to a distribution of $\sigma_y^2(\tau) \sim \tau^{-2}$.

Allan Variance versus spectral phase noise. The Allan variance is typically used to characterize frequency sources at detection frequencies below kHz frequencies, i.e. timescales significantly larger than seconds. Therein, frequency counting plays an essential role. The main focus of this work is phase noise at detection frequencies above 100 kHz, at lowest levels close to the quantum-limit. Typical measurement schemes of the Allan variance are difficult to apply to such side-band frequencies while keeping high measurement precision. In addition, this work focuses on the characterization of broadband noise distributions. The Allan variance and its modifications are in conclusion not useful here.

2.3 Lower limits of amplitude and phase noise

This thesis aims to provide a better understanding of noise of optical frequency combs close to the lower limits set by quantum mechanics. As an example, the results are applied to determine the ultimate sensitivities of a pulse-timing measurement proposed in [5].

Related to lowest noise properties of light, different terms exist in the literature and have to be distinguished by their physical origin. As sketched below, this section is consequently organized as follows: The lowest noise levels in any radiation, originated by the vacuum-fluctuations, are described first. Second, spontaneous emission in lasers is considered. After applying these concepts to an ultrafast oscillator, the complex noise coupling processes in such lasers are studied.



2.3.1 The Standard Quantum Limit.

The noise level of a perfectly coherent light beam with an average power \bar{P} is called *standard quantum limit*, *SQL*. This lowest level of classical noise arises from the quantization of the electromagnetic field, the so-called vacuum fluctuations. It has been shown in Eq.(2.17), that the variance of the photon number N follows $(\Delta N)^2 = N$ and that their arrival time is a δ -correlated Poisson process. The aim is here to quantify the corresponding measurable noise density S . First for shot noise, but in general for both amplitude and phase fluctuations.

Considering a beam of power $P(t) = \bar{P} + \delta P(t)$, the autocorrelation function of its fluctuations δP is

$$\Gamma_{\delta P}(\tau) = \langle \delta P(t) \delta P(t + \tau) \rangle = \bar{P} h \nu \delta(\tau). \quad (2.33)$$

Using the Wiener-Khintchine theorem, the single-sided power spectral density of shot noise is obtained to be

$$S_{\text{shot}}(f) = \frac{2}{\bar{P}^2} \int_{-\infty}^{+\infty} \Gamma_{\delta P}(\tau) e^{2\pi i f \tau} d\tau = \frac{2h\nu}{\bar{P}} \quad (2.34)$$

It describes the shot noise in units relative to the carrier power, commonly known as a *relative intensity noise RIN* - density [51]. To unify the representation of noise in this thesis, spectral densities will always be given in the single side-band (SSB) representation, relative to the carrier power. In addition, the noise level of vacuum fluctuations are called the *standard quantum limit*, *SQL*. This leads to the following definition of the symbol S_{SQL} :

$$\boxed{S_{\text{SQL}} = \frac{2h\nu}{\bar{P}} = \text{const.} \quad [S_{\text{SQL}}] = \text{dBc/Hz}} \quad (2.35)$$

It is here the spectral density of shot noise. Due to the isotropy of vacuum, it will turn out that the same symbol and formula applies to phase noise at the SQL.

Optical frequency combs have a high coherence length and can be considered as an individual coherent state. Eq.(2.35) can consequently be applied to them. The optical frequency $\nu = \omega_0/2\pi$ is then the center of gravity of the spectrum, see Eq.(2.2).

Quantum-limited phase noise: Two approaches

The isotropy of vacuum. At the quantum limit, the variances of both field quadratures Q and P of a quasi-classical coherent light state, σ_P^2, σ_Q^2 , are both equal to one for any timescale [36]. The spectral noise distributions $S_{Q,P}(f)$ are stationary and independent of the chosen quadrature. The field quadratures can be defined such that one, Q , represents the amplitude- and the other, Q the phase quadrature. At the quantum limit, the power in the side-bands originating from amplitude and phase noise $S(f)$ has to be the same. The SQL is consequently the same:

$$S_{\text{SQL,phase}} = S_{\text{SQL,amplitude}} = S_{\text{SQL}} = \frac{2h\nu}{\bar{P}} \quad (2.36)$$

This fact is of fundamental importance: it permits to calculate the SQL for phase noise in units that are experimentally simple to access. It simplifies the formula that calculates the sensitivity of a realistic homodyne timing measurement [5]. This leads to the simple and easy to interpret result Eq.(2.72), page 39.

Uncertainty relation between photon flux and phase. The equivalence of the amplitude and phase SQL becomes also evident within another perspective: An uncertainty relation for the photon flux Φ^{Phot} and the phase ϕ of a given optical carrier can be obtained starting from first principles of quantum optics. The quantization of radiation in free space, the commutation relations for the quadrature operators and a large photon number have to be considered. Defining the acquisition bandwidth from the measurement time T as $B = 1/T$, this uncertainty relation yields [36]:

$$\sigma_{\Phi}\sigma_{\phi} \geq B. \quad (2.37)$$

It is minimized by a coherent state. The variance of the photon flux is given by $\sigma_{\Phi}^2(B) = B\bar{P}/h\nu$ [36]. For a frequency interval $B = [f_2 - f_1] \rightarrow [1/T - 0]$ the spectral density of the SQL of phase fluctuations is:

$$\sigma_{\phi}^2(B) = B \cdot \frac{h\nu}{\bar{P}} = \int_0^{1/T} \frac{h\nu}{\bar{P}} df \implies S_{\phi} = \frac{h\nu}{\bar{P}} \quad (2.38)$$

Extending the analysis to the negative frequencies, the single side-band phase noise density is again $S_{\text{SQL,phase}} = 2S_{\phi} = 2h\nu/\bar{P}$ as in Eq.(2.36), above.

2.4 Lower noise limits for laser radiation

Noise quantification by the linewidth. Although one can calculate the quantum-limited noise levels using Eq.(2.36) for an ideal coherent state of light, it is not clear if a realistic light-source can attain these noise levels. Lasers are a source of light with highest coherence length and consequently best quasi-classical properties. The coherence length ΔL of a laser beam is a stability criterion for phase properties. Phase stability is typically limited by fluctuations of the laser cavity length, by spontaneous emission in the active medium or by gain fluctuations. Cavity length fluctuations are typically of below 10 kHz bandwidth and can be eliminated by careful engineering and vibration isolation. In the domain of frequency metrology, laser noise properties are typically characterized by the 3 dB linewidth $\Delta\nu = c/\Delta L$. The linewidth $\Delta\nu$ is defined from the phase noise single side-band power spectral density $S_\phi(f)$:

$$\frac{1}{\pi} = \int_{\Delta\nu/2}^{\infty} S_\phi(f) df \quad (2.39)$$

In the case of amplitude noise, the factor π has to be replaced by 2. The average linewidth of two different frequency combs is experimentally determined in section 3.1.4, page 74.

2.4.1 Shawlow-Townes-Limit

Spontaneous emission in the laser active medium and the coupling of the cavity field to the outside vacuum are the principal drivers of phase noise and set a lower limit to the laser linewidth $\Delta\nu$. First studied by [52], the resulting linewidth is called the *Shawlow-Townes* linewidth $\Delta\nu_{ST}$. In the case of a free-running laser, there is no force to these phase fluctuations fixing its mean. In this framework, spontaneous emission leads to white frequency noise $S_\nu(f) = \text{const}$. The corresponding phase noise density is:

$$S_\phi(f) = \frac{S_\nu}{f^2} \quad (2.40)$$

The resulting laser line $I(\omega)$ is of Lorentzian shape. Typical Shawlow-Townes limited linewidths $\Delta\omega_{ST}$ are 10^{-3} Hz for a 1 mW He-Ne and 10^6 Hz for a 1 mW diode laser. The value of $\Delta\omega_{ST}$ is proportional to the cavity linewidth $\Delta\omega_{cav}$ and the inverse number of photons in the cavity N : $\Delta\omega_{ST} \sim \Delta\omega_{cav}/N$.

Broadband noise drivers besides spontaneous emission and shot noise. In practice, lasers are typically pumped by a diodes which are subject to a number of instabilities. To classify different types of phase noise drivers as shown in Tab. 2.1, one typically fits several known power laws f^β to the experimentally obtained distribution $S_\phi(f)$.

$$S_\phi(f) = \sum_{\beta} b_{\beta} f^{\beta} \quad (2.41)$$

A $1/f$ distribution is commonly interpreted as to be of electronic origin. This method of phase noise characterization will not be extensively exploited in this thesis, but is part of the typical methods used in the frequency- and phase-noise literature.

β	denomination	electronic oscillator	optical oscillator
0	white PM		shot noise
-1	Flicker PM	recombination noise, resistance fluctuations	
-2	white FM		Shawlow-Townes phase random walk

Table 2.1: Phase noise distributions and their origins. For an exhaustive list and further interpretation see e.g. [53] or [48]. PM: phase modulation, FM: frequency modulation

2.4.2 Noise in optical frequency combs

One of the aims of this thesis is the estimation of realistic sensitivities of a highly sensitive pulse timing measurement [5]. It turns out in section 2.5, page 36, that the fluctuations of the CEO-phase and the repetition rate of an optical frequency comb limit any achievable sensitivity. Both contribute to the phase noise in any individual line of a frequency comb, but it is so far not clear which of the two is the principal limitation.

As a first step, their orders of magnitude are estimated here from a priori considerations. To this aim, an approach used from the literature [54, 19] is summarized here. Starting from the results above on the Shawlow-Townes limited laser linewidth, expected orders of magnitude and power laws for the phase noise of the repetition rate ω_{rep} and the CEO frequency ω_{CEO} can be calculated. In addition, the phase noise of individual lines m of the comb $\omega_{\text{opt}} = \omega_{\text{CEO}} + m \cdot \omega_{\text{rep}}$ is studied.

Shot noise and timing jitter of a coherent pulse train. In addition to amplitude and the CEO-phase property common to an entire frequency comb, a coherent train of ultrashort pulses carries two other fundamental properties [10]: the pulse timing and the central frequency, see section 2.4.3. The fluctuations of the pulse timing, or the repetition rate, are of principal importance for this thesis. It is consequently interesting to consider the impact of shot noise on the pulse timing within a coherent train - without considering the generating oscillator. An excellent overview of the relevant arguments is given by [54]. The principal results therein are:

For a pulse of an optical power $P(t) = \bar{P}(t) + \delta P(t)$ within a reference frame moving with the pulse, the noiseless part $\bar{P}(t)$ is centered at time $t = 0$. Here t is a fast timescale and the average \bar{P} is calculated over a large number of pulses. The variance of the pulse position turns out to be a function of the pulse energy E_p and its duration τ_p . In a very shortened form, the calculus of [54] is:

$$\sigma_{\text{tm}}^2 = \frac{1}{E_p^2} \left\langle \left(\int t \delta P(t) dt \right)^2 \right\rangle = \frac{h\nu}{E_p^2} \int t^2 \bar{P}(t) dt \approx \frac{h\nu}{E_p} \tau_p^2 \quad (2.42)$$

The underlying method is the definition of the pulse within a center of gravity approach. It is shown in [55] that this approach is equivalent to the one using temporal modes [5], to which this thesis refers most often. From Eq.(2.42), the power spectral density of the phase noise of a repetition rate signal recorded with a photodiode is obtained to:

$$S_{\phi, \text{tm}} = S_{\text{SQL, TOF}} \approx (2\pi f_{\text{rep}} \tau_p)^2 S_{\text{SQL}} \quad (2.43)$$

This noise level will subsequently be called the *SQL of the Time of Flight: SQL-TOF*. It is important to note that this result is equivalent to the one recently obtained by [14, 15]. This literature considers a non-stationary distribution of photons and calculates the SQL-TOF from this assumption. For typical fs-oscillators with MHz repetition rates and fs-pulse durations one obtains different quantum limits for amplitude/phase and the phase of the repetition rate:

$$S_{\text{SQL, TOF}} \ll S_{\text{SQL}} \quad (2.44)$$

This result shows that a detection scheme sensitive to timing jitter but being also sensitive to the shot noise carried by the signal(s) - e.g. simple detection with a photodiode or homodyne detection - will not be able to resolve the shot-noise induced timing jitter in a coherent pulse train.

CEO-phase noise from repetition rate noise. The aim is here to express the noise of the CEO-phase S_{CEO} in terms of those of the repetition rate S_{rep} and of an individual line S_{opt} . This could permit to estimate lowest levels for CEO-phase noise. The SQL for a single comb line can be calculated easily and an approach to the SQL of repetition rate phase noise was given by Eq.(2.43).

The repetition rate induced CEO phase noise can be calculated as follows [19]: For a timing fluctuation Δt , the repetition rate phase undergoes a shift $\phi_t = \omega_{\text{rep}}\Delta t$. The noise spectral densities are linked by $S_{\phi,t}(f) = \omega_{\text{rep}}^2 S_{\Delta t}(f)$. The timing phase of an arbitrary comb frequency $\omega = \omega_0 + \Delta\omega = \omega_{\text{CEO}} + n\omega_{\text{rep}}$ can be written as:

$$\phi_t(\omega_0 + \Delta\omega) = \phi_t(\omega_0) + \frac{\partial\phi_t}{\partial\omega}\Delta\omega = \phi_t(\omega_0) + \Delta\omega\Delta t. \quad (2.45)$$

This approach can be extended to the lowest possible comb frequency ω_{CEO} , by setting $\Delta\omega = -\omega_0$. This leads to the spectral density of CEO phase noise:

$$S_{\phi,\omega_{\text{CEO}}}(f) = S_{\phi,\omega_0}(f) + \omega_0^2 S_{\Delta t}(f) \quad (2.46)$$

$$= \dots + \frac{\omega_0^2}{\omega_{\text{rep}}^2} S_{\phi,\Delta t}(f) \quad (2.47)$$

The same statement written in the usual notation of this thesis is:

$$S_{\text{CEO}}(f) = S_{\omega_0}(f) + \frac{\omega_0^2}{\omega_{\text{rep}}^2} S_{\text{rep}}(f) \quad (2.48)$$

The minimal CEO-phase noise, driven only by repetition rate noise is consequently expected to be several orders higher than this repetition rate noise.

CEO-phase noise from shot noise. Assuming only shot noise in the frequency comb, S_{ω_0} is at the SQL. S_{rep} has been determined in Eq.(2.43) and can be expressed in terms of the SQL. The CEO-phase noise is consequently:

$$S_{\text{CEO}}(f) \simeq S_{\omega_0}(f) + \omega_0^2 \tau_p^2 S_{\text{SQL}} \sim S_{\text{SQL}} \quad (2.49)$$

In a first approximation, the expected lowest level of the CEO-phase noise is consequently equivalent to the SQL. This is an important statement: In later considerations, the phase quadrature of an entire frequency comb will be assumed to be equivalent to the CEO-phase of the frequency comb. Measured noise levels will be compared to the SQL for the CEO-phase noise, given here by Eq.(2.49).

A laser source: Shawlow-Townes limits to frequency-comb noise. In addition to the intrinsic properties of the radiation, spontaneous emission in the laser source drives the noise in the emitted frequency comb. The simplest approach to consider such effects is to assume Shawlow-Townes phase noise [52]: $S_{\omega_0}(f) \propto 1/f^2$. From this, it is possible to estimate and compare $S_{\omega_0}(f)$, $S_{\phi_{\text{rep}}}(f)$ and $S_{\text{CEO}}(f)$ for a typical oscillator¹:

$$S_{\text{rep,ST}}(f) = k \cdot \tau_p^2 \omega_{\text{rep}}^2 \cdot f^{-2}, \quad \tau_p^2 \omega_{\text{rep}}^2 \approx 10^{-9} \quad (2.50)$$

$$S_{\omega_0, \text{ST}}(f) = k \cdot f^{-2}, \quad (2.51)$$

$$S_{\text{CEO,ST}}(f) = k \cdot \tau_p^2 \omega_0^2 \cdot f^{-2}, \quad \tau_p^2 \omega_0^2 \approx 10 \quad (2.52)$$

All phase noise properties follow the the Shawlow-Townes f^{-2} -slope. Compared to the CEO frequency and the optical carrier, the repetition rate phase noise is significantly smaller:

$$S_{\text{CEO,ST}} \sim S_{\omega_0, \text{ST}} \gg S_{\text{rep,ST}} \quad (2.53)$$

The phase noise on the RF-signals of repetition rate and CEO-frequency have to be well distinguished from their contribution to the phase noise in any line of the optical frequency comb. The relative impact can be compared by taking into account the mode number n of $10^5 \dots 10^6$ under the gain profile. Nevertheless, although if this aspect is integrated into the comparison of Eq.(2.50) and Eq.(2.52), repetition rate phase noise is expected to be negligible.

2.4.3 The oscillator noise model of H.A.Haus

The estimations above consider either an ideal optical frequency comb or a CW-laser like source that is only subject to spontaneous emission as additional noise driver. Nevertheless, compared to a CW-operation, the generation of coherent femtosecond light pulses is linked to additional physical conditions [10, 56, 57] that provide stable mode-lock. The essential contributions are an intracavity non-linearity and dispersion. They can be summarized in a non-linear Schrödinger equation (NLSE). Their stable soliton-solutions describe the behavior and time dependent dynamics of such optical oscillators well [58]. Based on partial derivatives of these solutions, the noise properties of such oscillators can be described as follows [10, 59].

¹ for the here considered Ti:Sapph: average power $\bar{P} = 1 \text{ W}$, $k = \theta^3 h \nu_{\text{opt}} / 4\pi^2 \bar{P}$, $\theta \dots$ total cavity losses

A model for noise of ultrafast oscillators. Starting from the NLSE, using a linearization and projecting the solutions on a set of four envelope functions, the noise of a fs-soliton laser can be described [10, 59]. A Langevin-Type system of coupled differential equations is obtained for timescales $T \geq 2\pi/\omega_{\text{rep}}$. For a vector \mathbf{v} containing the fluctuating properties of a soliton pulse, the following, simple form is obtained:

$$\frac{d\mathbf{v}}{dT} = -\mathbf{A} \cdot \mathbf{v}(T) + S(T), \quad (2.54)$$

The vector $\mathbf{v} = (\delta\theta, \delta w, \delta t, \delta\bar{\omega})^T$ contains θ the CEO phase, w the instantaneous power, t the temporal center of gravity of the pulse (timing jitter) and $\bar{\omega}$ the central frequency. For each of these properties x , an operating laser will work at an equilibrium x_{eq} and undergo fluctuations δx : $x = x_{eq} + \delta x$. The fluctuations are coupled by the coupling matrix \mathbf{A} and driven by the noise driver S . The latter represents the spontaneous emission in the gain medium and classical noise sources.

The off-diagonal elements of the coupling matrix \mathbf{A} are of principal importance, they describe the coupling of fluctuating pulse-properties. Using only the most important couplings $a_{\theta w}$ and $a_{t\bar{\omega}}$, the matrix \mathbf{A} is obtained to

$$\mathbf{A} = \begin{vmatrix} 1 & a_{\theta w} & 0 & 0 \\ 0 & 1 & 0 & 0 \\ 0 & 0 & 1 & a_{t\bar{\omega}} \\ 0 & 0 & 0 & 1 \end{vmatrix} \quad \mathbf{v} = \begin{vmatrix} \delta\theta \\ \delta w \\ \delta t \\ \delta\bar{\omega} \end{vmatrix} \quad (2.55)$$

Most important for this thesis, the fluctuations of the intracavity power δw (arising from pump and gain fluctuations) drive the CEO-phase noise $\delta\theta$ through the coefficient $a_{\theta w}$. See [60] for a nice summary. Fluctuations of the central frequency $\delta\bar{\omega}$ drive the timing jitter δt through $a_{t\bar{\omega}}$. It is essentially a function of the oscillator dispersion. All noise parameters are driven by spontaneous emission. The matrix \mathbf{A} has been extensively characterized for a Ti:Sapph oscillator [61, 62]. Nevertheless, only the principal results concerning expected noise levels and distributions are important for this thesis.

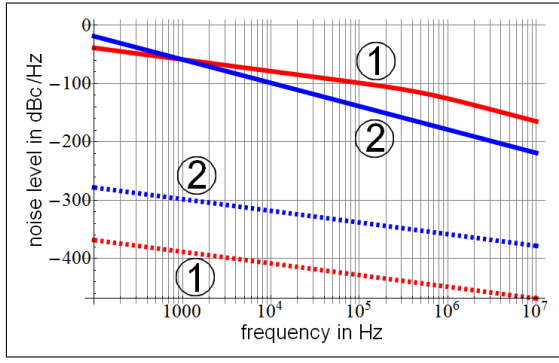


Figure 2.5: Calculated qualitative behaviour of CEO ① and repetition rate ② phase noise spectral densities for the Ti:Sapph oscillator. To distinguish their origin according to Eq.(2.56): *dashed line* direct impact of spontaneous emission, *continuous line* coupling from another, spontaneous emission driven property. These are for CEO: the gain fluctuations, for the repetition rate: the central frequency fluctuations. The transition frequency for the CEO phase noise $1/f^2 \rightarrow 1/f^4$ depends on gain parameters.

Spectral densities of noise from the model of H.A.Haus. The focus of this thesis lies on the analysis of CEO and repetition-rate phase noise: S_{CEO} and S_t . The theory above has been verified experimentally for both [63, 42]. For detection frequencies up to several MHz, their power spectral densities are given by [10]:

$$S_t(f) = \frac{D_{\bar{\omega}}}{(2\pi f)^2[(2\pi f)^2 + \tau_{\bar{\omega}}^{-2}]} + \frac{D_t}{(2\pi f)^2}$$

$$S_{CEO}(f) = \frac{D_w}{(2\pi f)^2[(2\pi f)^2 + \tau_w^{-2}]} + \frac{D_\theta}{(2\pi f)^2} \quad (2.56)$$

The constants D and τ are obtained from the properties of the oscillator and depend essentially on the intracavity dispersion D and the oscillator gain properties².

$$D_{\bar{\omega}} = \frac{16D^2 f_r^2}{3w_0 \tau^2} \cdot \kappa, \quad D_t = \frac{\pi^2 \tau^2}{3w_0} \cdot \kappa, \quad D_w = \frac{4D^2 f_r^2 w_0}{\tau^4} \cdot \kappa, \quad D_\theta = \frac{5}{w_0} \cdot \kappa, \quad \kappa = gh\nu f_r$$

$$\tau_{\bar{\omega}} = \frac{3\Omega_G^2 \tau^2}{4gf_r}, \quad \tau_w = \frac{g-\alpha}{f_r} \quad (2.57)$$

The time constants τ are decay constants for fluctuations of the center frequency $\tau_{\bar{\omega}}$ and the pulse energy τ_w . The second term in the sums Eq.(2.56) arises directly from spontaneous emission. It is typically neglectable compared to the first term that describes the influence of the spontaneous emission driven gain fluctuations/central frequency on the CEO/repetition rate through coupling. The time constants in these first terms can be estimated to $\tau_{\bar{\omega}} \ll 1$ and $\tau_w < 1/f_{rep}$.

Conclusion: As shown in Fig. 2.5, and in contrast to an $1/f^2$ Shawlow-Townes behavior, the CEO and repetition rate phase noise are expected to follow

$$S_{CEO}(f) \sim 1/f^4 \quad S_{rep}(f) \sim 1/f^4 \quad (2.58)$$

Depending on the gain properties, the CEO-phase noise follows a $1/f^2$ up to $1/\tau_{\bar{\omega}}$.

² For the oscillator used in this thesis: the repetition rate $f_r = 156$ MHz, the $1/e$ pulse duration $\tau \approx 25$ fs. It is possible to approximate the saturated gain $g \approx 0.05$, the intracavity pulse energy at 1 W output power $w_0 \approx 60$ nJ, the central frequency $\nu = 3.75 \cdot 10^{14}$ Hz, the gain bandwidth $\Omega_G = 5 \cdot 10^{13}$ Hz and the effective saturable absorber action α .

A global minimum for spectral phase noise. The formalism of Haus et al. can be extended to obtain information about the phase noise distribution over the optical spectrum [20]. The vector $\mathbf{v} = (\delta\theta, \delta\omega, \delta t, \delta\bar{\omega})^T$ of laser fluctuations, the coupling matrix \mathbf{A} and the noise driver \mathbf{S} are used again. In addition, the second-order moments of \mathbf{v} : $\langle \delta v_i \delta v_j \rangle$ are considered. After the experimental measurement of the entire noise coupling matrix \mathbf{A} [61, 62], the underlying equations can be solved according to Wai et al.[64].

It is useful to note $\Omega = \omega - \omega_0$ the distance of a comb line ω to the central frequency ω_0 . The PSD of the fluctuations of the line $S_\Omega(f)$ turns out to be a quadratic function in Ω [20]. The spectral position of the minimum is set by the PSDs of timing S_t and CEO-phase S_θ and the correlation term $\langle \delta t \delta \theta \rangle$:

$$S_\Omega \simeq \Omega^2 S_t - 2\Omega \langle \delta t \delta \theta \rangle + S_\theta \quad (2.59)$$

The position of this frequency is shifted from the spectral center by the correlation term $\langle \delta t \delta \theta \rangle$. It arises from the Kerr-effect that affects both phase and timing.

Simulation of a realistic oscillator. Wahlstand et al. [20] characterized a 15 fs, 100 MHz, 5 W, Ti:Sapph oscillator. It is similar to the commercial SYNERGY, 25 fs, 156 MHz, 1 W, investigated here. The shift of the frequency of minimal noise from spectral center is given there as follows: It is of positive sign for timing and phase jitter driven by intensity fluctuations. It is of negative sign for timing jitter caused by oscillator dispersion.

A principal result of this thesis is the measurement of the distribution of phase noise over the comb's spectrum. Therein, the phase noise distribution is revealed to be asymmetric relative to the central frequency. It decreases to the lower frequency part of the comb. This is equivalent to a negative sign of the term $\langle \delta t \delta \theta \rangle$. With the above, it can be supposed that it is the non-zero, residual dispersion of the oscillator - required for stable soliton generation - that governs this behavior.

2.4.4 The rubber band model of spectral phase noise

The model of comb noise Eq.(2.45) above is bottom-up: the equations describing the oscillator are used to determine noise couplings and the distribution for each comb parameter. Another, more phenomenological model is the so-called *rubber-band-model* [21]. It describes how different noise drivers as pump power, spontaneous emission or mechanical fluctuations influence the noise properties of each individual line of a frequency comb. This model will be useful within the analysis of spectral phase noise of a frequency comb using the experimental results of section 4.2, page 107.

It consists of the following [66]: Any mode frequency of the comb can be represented as a sum of the CEO-frequency ω_{CEO} and the repetition rate ω_{rep} . The same is valid for the phase/frequency fluctuations of this line.

$$\omega_n = n \cdot \omega_{\text{rep}} + \omega_{\text{CEO}}, \quad \delta\omega_n = n \cdot \delta\omega_{\text{rep}} + \delta\omega_{\text{CEO}} \quad (2.60)$$

The fluctuations of the constituents can now be represented in terms of their origin, the noise driver X :

$$\delta\omega_{\text{CEO}} = \frac{d\omega_{\text{CEO}}}{dX} \cdot \delta X, \quad \delta\omega_{\text{rep}} = \frac{d\omega_{\text{rep}}}{dX} \cdot \delta X \quad (2.61)$$

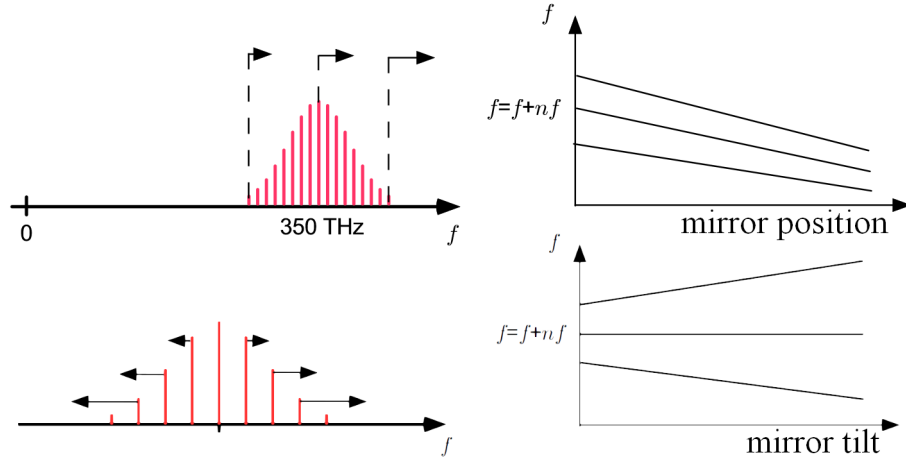


Figure 2.6: A visualization of the rubber-band model as shown in [65]. An oscillator cavity with a mirror of variable position and tilt is assumed. The horizontal axis of the right plots are indicate the magnitude of perturbation. *above* Pure repetition-rate fluctuations lead to a fix-point close to zero frequency. *below* Fluctuations of the geometry (mirror tilt) in a prism-based dispersion compensating oscillator cavity lead to a non-zero fix-point frequency. Both rep-rate and CEO-frequency are concerned. The fix-points are abstract values, for a realistic comb they may be situated even outside the laser gain profile.

	from the literature			this work	
	δL	δP_{pump}	SE	δL	δP_{pump}
fix-point in THz	~ 2.5	~ 150	~ 375	~ 1.7	~ 233
driving strength	$\sim 10^{-18}$	$\sim 10^{-17}$	$\sim 10^{-28}$	-	-

Table 2.2: Lines of minimal phase noise (fix-points) and driving strength to the repetition rate fluctuations. Here for fluctuations of a Ti:Sapph oscillator length, the pump intensity and spontaneous emission (SE). *Left:* from the literature [16], *right:* for the Ti:Sapph oscillator characterized in this thesis, section 3.1, *Note:* 800 nm \simeq 375 THz.

These equations define a *fix-point frequency for the driver X*, at which the frequency noise of line n vanishes $\delta\omega_n = 0$:

$$\omega_{\text{fix}}^X = n_{\text{fix}}^X \omega_{\text{rep}} + \omega_{\text{CEO}}, \quad n_{\text{fix}}^X = -\frac{\frac{d\omega_{\text{CEO}}}{dX}}{\frac{d\omega_{\text{rep}}}{dX}} \quad (2.62)$$

This fix-point is consequently readily measurable from the ratio of repetition rate and CEO-frequency change under the perturbation X . The comb will breathe around the fix-point of minimal phase noise and linewidth. Nevertheless, the frequency ω_{fix} does not necessary lie in the gain profile of the spectrum. As an example, a length perturbation changes the round-trip time of a pulse-train but that is negligible to the carrier-frequency of a pulse. It will have a fix-point frequency near the zero frequency. Such fix-point frequencies have been extensively studied for an Er-fiber based comb [66] and recently for a 17 nm FWHM Ti:Sapph based frequency comb [16]. The obtained fix-points for length-fluctuations δL , pump-noise δP and spontaneous emission are shown in Table 2.62.

Noise distribution from the fix-point model. In chapter 4.2, page 107, the spectral phase noise distribution of a Ti:Sapph oscillator will be analyzed experimentally. The fix-point model may predict the general shape of the expected noise distribution along the frequency comb. A pre-requisite is the knowledge of how the different noise drivers X contribute to the phase noise distribution of individual comb-lines.

Once the fix-point ω_{fix}^X of a frequency comb is known, the fluctuations of each line ω are given by [16]:

$$S_{\omega}^X(f) \simeq (\omega - \omega_{\text{fix}}^X)^2 S_{\text{rep}}^X(f) \quad (2.63)$$

The symbol $S_{\text{rep}}^X(f)$ is the so-called driving-strength to the repetition rate originated by the noise driver X : $S_X(f)$. Example values are given in Tab. 2.2.

The most important noise drivers X are fluctuations of the cavity-length and the pump-power, amplified spontaneous emission (ASE) and Shawlow-Townes noise. A simple approach to quantify their weighting experimentally is to determine S_{rep}^X at a low modulation frequency providing thermal equilibrium, e.g. 1 Hz. Such a characterization has been done by [16] and the results are depicted in Tab. 2.2: pump-power fluctuations are, together with mechanical issues by far the most important noise driver. From this low frequency property, pump power noise decays with $1/f$ where mechanical noise decays by $1/f^2$ and is typically strongly attenuated above 10 kHz. It is consequently possible to simplify the analysis of the entire comb noise within the rubber-band model to the analysis of the impact of pump power fluctuations. This leads for a comb frequency ω to:

$$S_{\omega}(f) \simeq (\omega - \omega_{\text{fix}})^2 S_{\text{rep}}^{\text{pump}}(f) \quad (2.64)$$

The fix-point frequency ω_{fix} Eq.(2.62) is simple to measure by a modulation experiment and found at approximately 233 THz on the IR-side of the frequency comb spectrum. With Eq.(2.64) the phase noise of the frequency comb is consequently expected to decrease towards this IR-side of the spectrum. This confirms the general slope of the measured spectral phase noise distribution in chapter 4.2, page 107.

2.5 Homodyne noise measurements with combs

It has been shown in the literature that any pointing deviation of a CW beam can be interpreted as a superposition of *spatial modes* [67]. Balanced homodyne detection can precisely discriminate any such mode structure of a beam, and has been used to measure pointing fluctuations with ultimate precision [68]. As shown in Eq.(2.11), a coherent pulse train can be represented as a superposition of orthogonal *temporal pulse-envelopes*. These spectral/temporal envelopes will subsequently be called *modes*.

It has been demonstrated theoretically that an envelope- or mode-selective measurement can resolve *timing fluctuations* of coherent fs-pulse trains [5]. The principal measurement scheme of this reference is shown in Fig.2.7. Homodyne detection of temporal modes is used to obtain relative space-time information between two signal sources which are femtosecond oscillators. In order to generalize the concept towards applicability, in this section realistic noise conditions are added to the considerations of [5].

This section is organized as follows: first, the theoretical concept of a timing measurement by homodyne detection is revisited. Realistic measurement conditions with classical noise are then associated to the theory of its sensitivity. Subsequently, it is shown how the CEO-phase noise of the involved frequency combs sets the lower limit of sensitivity.

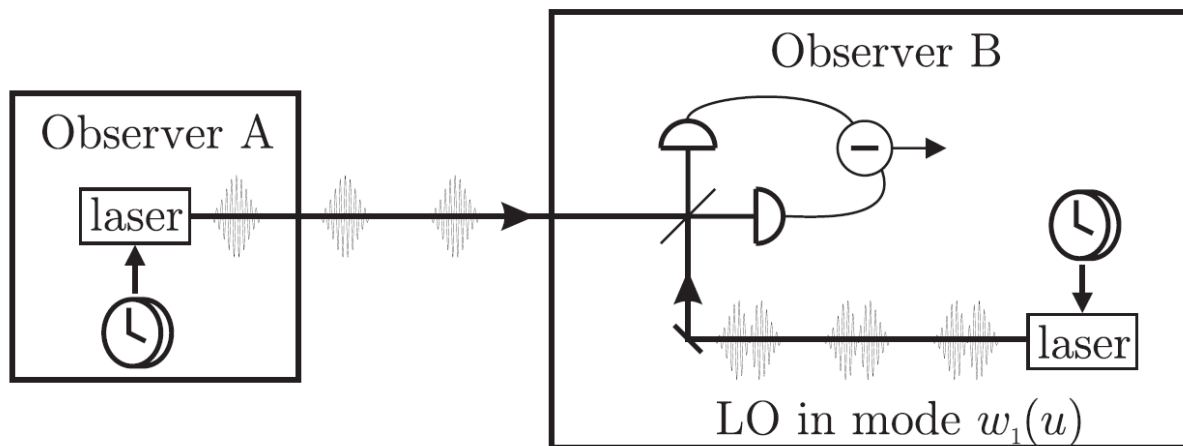


Figure 2.7: The suggested experiment that was the principal motivation for this thesis. Picture from [5]. Both signals of femtosecond oscillators interfere in a homodyne configuration. The bright local oscillator is in a special temporal mode. Precise information about the relative space-time position $u = r - ct$ of the two oscillators can be obtained from the signal. If the relative space-time position of both signals is constant, the phase noise of source Observer A can be precisely characterized.

2.5.1 Realistic homodyne timing jitter measurement

A pulse delay can be measured by the arrival time of the maximum of the pulse envelope, called the *time-of-flight (TOF) measurement*. This corresponds to a simple time-dependent intensity measure with a photodiode. Another method consists in using the phase of the electric field oscillation. It corresponds to an interference between the signal pulses and a reference pulse train. We denote this reference the *Local Oscillator (LO)* and the method is called a *phase measurement*. Both techniques can be combined as follows:

Timing shift as a superposition of modes. The electric field operator of a pulse train can be written as a superposition of an arbitrary number of temporal modes $\underline{v}_n(u)$, see Eq.(2.5). They are a function of the general space-time light-cone variable $u = z - ct$. In addition, there exists always one mode v_0 to which the mean field is proportional [35]:

$$E_0^+(u) = \mathcal{E}\sqrt{N}v_0(u), \quad v_0(u) = g_0(u)e^{-i\omega_0 u} \quad (2.65)$$

Here \mathcal{E} is a normalization constant and N the photon number. Assuming a space-time shift $u' = u - \Delta u$, this single mode $v_0(u - \Delta u)$ field can be written in a Taylor series [5]:

$$v_0(u - \Delta u) \simeq v_0(u) - \Delta u \cdot \frac{dv_0(u)}{du} \quad (2.66)$$

$$= v_0(u) + \Delta u \cdot \left[i\omega_0 \cdot g_0(u) - \frac{dg_0(u)}{du} \right] e^{-i\omega_0 u} \quad (2.67)$$

The temporal mode that contains the information on Δu is a superposition of two modes that are proportional to g_0 (I) and dg_0/du (II), see Fig. 2.8. They represent two types of measurements: a CW like phase measurement (I) and a detection of the time-of flight (group delay) of the light-pulses (II), see Fig. 2.8.

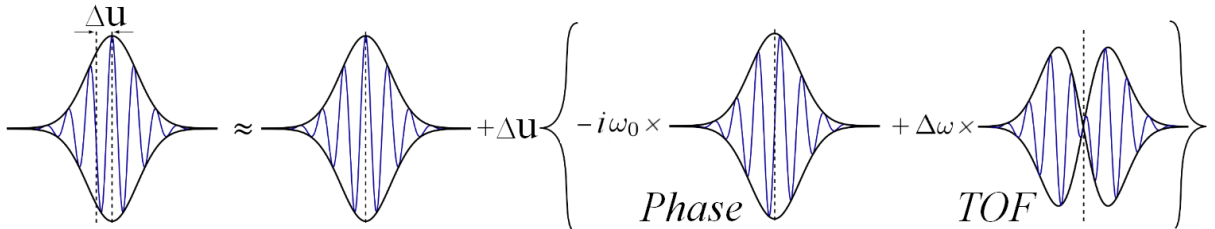


Figure 2.8: Illustration of the representation of a timing-shift using temporal modes.

According to Lamine et al. [5], a pulse undergoing a timing shift can be represented as a superposition of two different temporal modes. One is the initial envelope. The second is a superposition of two modes itself: they are equivalent to a separate phase- and group delay/time-of-flight measurement. The coefficients of the carrier ω_0 and the pulse bandwidth $\Delta\omega$ ensure same normalization for both modes. The timing shift Δu appears as a linear coefficient measurable by homodyne detection.

The value of Δu can be extracted from a pulse by measuring the signal via balanced homodyne detection. As shown in Fig.2.7, the equivalent experiment detects the signal comb with a local oscillator (LO) in the superposition of the modes I and II. Unprecedented sensitivities for pulse delays down to 10^{-24} s (yoctoseconds) have been predicted theoretically for this scheme.

Quantum limited sensitivities. For a pulse train of an optical bandwidth $\Delta\omega$, a carrier frequency ω_0 and N detected signal-photons one can compare the sensitivity of the *time-of-flight/group delay* (I), the *phase-based* (II) and the *combined homodyne* (I+II) measurement scheme [5]:

$$(\Delta u)_{\text{SQL}}^{\text{I}} = \frac{1}{2\omega_0\sqrt{N}}, \quad (\Delta u)_{\text{SQL}}^{\text{II}} = \frac{1}{2\Delta\omega\sqrt{N}}, \quad (\Delta u)_{\text{SQL}}^{\text{I+II}} = \frac{1}{2\sqrt{N}\sqrt{\omega_0^2 + (\Delta\omega)^2}} \quad (2.68)$$

The minimum is given if the detecting (LO) is in the superposition of modes I+II. Nevertheless, the underlying key assumption is, if the classical noise in the LO does not contribute to the output, a signal in a perfect coherent state. This is equal to a noise level in both field quadratures at the standard quantum limit SQL [5].

Realistic sensitivities. Within the definitions of Eq.(2.11), the noise of a perfect coherent state is at the SQL. The variances of the amplitude and phase quadrature operators \hat{Q} and \hat{P} of the modes I and II are:

$$\text{SQL: } \sigma_P^2 = \sigma_Q^2 = 1 \quad (2.69)$$

Regarding Eq.(2.67), a homodyne measurement of Δu corresponds to the detection of the phase quadrature of the normalized modes: I proportional to g_0 and the amplitude quadrature of mode II proportional to dg_0/du . For a signal to noise ratio of one, SNR=1, the sensitivity of the homodyne measurement of Δu is given by

$$\Delta u_{\min} = \frac{\alpha}{\sqrt{\tau}} \cdot \frac{[\omega_0^2\sigma_{P\text{I}}^2 + (\Delta\omega)^2\sigma_{Q\text{II}}^2]^{1/2}}{(\Delta\omega)^2 + \omega_0^2}, \quad \alpha = \sqrt{\frac{\hbar\omega_0}{P_0}} \quad (2.70)$$

Here τ is the measurement time, P_0 the average signal power and σ^2 the variance of the quadratures P and Q of the modes I and II respectively. It is a choice of normalization to set the quantum-limited variance to one: $\sigma_{P,Q}^2 = 1$.

Realistic sensitivities from measured noise spectral densities. It has been shown in Eq.(2.27) that the variance of a noise process $X(t)$ can be expressed in terms of a spectral density S_X : $\sigma_X^2(f) = S(f) \cdot 1 \text{ Hz}$. The spectral density of amplitude and phase noise of a frequency comb at the quantum limit can be calculated in units relative to the carrier power, dBc/Hz. Classical amplitude and phase noise is typically measured - even down to the SQL - in densities dBc/Hz.

In order to allow an interpretation of Eq.(2.70) under not quantum-limited noise conditions, the quadrature variances σ_X^2 , $X = P, Q$ can be expressed in terms measured noise levels $S(f)$ relative to the expected or measured quantum limit:

$$\sigma_X^2(f) = \frac{S_X(f)}{S_{\text{SQL}}} \quad (2.71)$$

Inserted into Eq.(2.70), it permits to link and apply the results of a quantum optical calculus to classical noise³.

The fluctuations of the phase of the repetition rate of a frequency comb have been shown to be negligible compared to the CEO-phase noise. In order to study the impact of noise in a frequency comb to the sensitivity in Eq.(2.70), the CEO-phase noise can be identified with the measurement of mode I of the comb, as it contains all the phase noise common to the comb. The repetition rate noise can be identified with the time-of-flight or group-delay measurement.

The experimental part of this thesis considers in addition a frequency comb centered at 800 nm with a bandwidth of 40 nm FWHM. By the scaling factors arising from normalization, the resulting $\Delta\omega \ll \omega_0$ in Eq.(2.70) transforms the homodyning of both modes I and II essentially into a phase measurement.

Applying Eq.(2.71) to Eq.(2.70) and as shown in [69], one obtains the following realistic sensitivity for a homodyne measurement of Δu :

$$\Delta u_{\min}(f) \approx \frac{1}{2\sqrt{\tau}} \frac{\sqrt{S_{\text{CEO}}(f)}}{\omega_0} \quad (2.72)$$

The sensitivity Δu_{\min} for a timing modulation at the homodyning frequency f scales with the integration time of detection τ . It is principally limited by the single side-band power spectral density of the carrier-envelope-phase fluctuations $S_{\text{CEO}}(f)$.

³ For a frequency comb of central frequency ν and average power \bar{P} , the single side-band power spectral density of quantum limited amplitude and phase noise was found in Eq.(2.36) to $S_{\text{SQL}} = 2h\nu/\bar{P}$.

Spectral interpretation of the mode-based timing-jitter measurement. In the considerations above, a deviation of the space-time position of a pulse train, Δu is measured and interpreted in terms of temporal modes. It is instructive and necessary for the experimental considerations of section 4.5, to transpose these considerations in the spectral domain. From an experimental point of view it is in addition always simpler to characterize and manipulate the spectral properties of a pulse train. Using Eq.(2.65), the mean field $E_0^+(u) = \mathcal{E}\sqrt{N}v_0(u)$ of a frequency comb can be written as

$$v_0(u) = g_0(u)e^{i\omega_0 u} = \int \tilde{g}_0(\Omega)e^{-i\omega u} d\omega, \quad \Omega = \omega - \omega_0 \quad (2.73)$$

in the spectral domain. Using $\Omega = \omega - \omega_0$, a small space-time deviation Δu can then be written as:

$$v_0(u + \Delta u) = \int \tilde{g}_0(\Omega)e^{-i\omega(u+\Delta u)} d\omega \quad (2.74)$$

$$= \int \tilde{g}_0(\Omega)e^{-i\omega u}(1 - i\omega\Delta u)d\omega, \quad \omega = \Omega + \omega_0 \quad (2.75)$$

$$\simeq v_0(u) + \Delta u \int -i\omega_0\tilde{g}_0(\Omega) - i\Omega\tilde{g}_0(\Omega)d\omega \quad (2.76)$$

The deviation Δu is consequently represented by the phase quadrature of two spectral modes:

$$\text{I: } \omega_0\tilde{g}_0(\Omega), \quad \text{II: } \Omega\tilde{g}_0(\Omega) \quad (2.77)$$

In analogy to Eq.(2.67), the mode I corresponds to a phase measurement of a CW-signal and the mode II to a measurement of the deviation time-of-flight or the group-delay of the light pulses. The comparison of the modes I and II shows here directly that a homodyne measurement in a superposition mode I+II corresponds essentially to a measurement of I, unless the frequency spread $\Delta\Omega$ of \tilde{g}_0 is similar to ω_0 . This means that homodyne measurements with frequency combs are only advantageous to CW measurements if their bandwidth covers at least one octave.

It is remarkable from Eq.(2.76) that both modes I and II appear in the phase quadrature. This shows that any modulation of the spectral amplitude of the frequency comb will never change either CEO-frequency (I) or repetition rate (II).

2.6 Aspects of practical noise measurements

According to Eq.(2.72), the sensitivity of a homodyne timing measurement with a 25-fs Ti:Sapph oscillator is essentially limited by the CEO-phase noise. The quantification of phase noise can be done with different techniques and within different units. The possible choices are depicted in this section in order to provide all necessary tools for the experimental part of this thesis. An additional method to measure timing-jitter is cited from the literature.

A coherent pulse train contains a number of possible noise terms. The most prominent are fluctuations of the repetition rate δf_{rep} and of the carrier-envelope offset frequency, δf_{CEO} . The first can be detected by an intensity measurement using a photodiode. The latter requires a more involved scheme:

CEO phase noise, the f-2f method. The most common technique to detect the CEO-frequency and its phase noise is to beat the second harmonic of the lower frequency part of an optical frequency (I) comb with the comb itself at the doubled frequency (II). This is the so-called f-2f beating technique [1]:

$$f_{\text{ceo}} = 2(\underbrace{n \cdot f_{\text{rep}} + f_{\text{ceo}}}_{\text{I}}) - (\underbrace{2n \cdot f_{\text{rep}} + f_{\text{ceo}}}_{\text{II}}) \quad (2.78)$$

If the spectrum of the laser does not cover one octave it can be broadened coherently in a photonic crystal fiber (PCF). The beating-signal is typically detected with an avalanche photodiode (APD) and gives rise to a classical periodic electronic signal:

$$V(t) = A(t) \cdot \cos [2\pi f_{\text{ceo}}t + \phi(t)] \quad (2.79)$$

A signal of the same structure is obtained when detecting the repetition rate. Here, amplitude $A(t)$ and phase $\phi(t)$ vary slowly compared to the optical carrier frequency. The following subsection discusses theoretical aspects of the measurement of $\phi(t)$. Details of the measurement apparatus and data are presented in section 3.1.

2.6.1 The measurement of phase noise

When the total *modulation power noise* of the signal $V(t)$ is considered, a simple RF power spectrum measurement with a spectrum analyzer cannot distinguish PM from AM noise. Nevertheless, this disadvantage indicates the natural, common units of amplitude and phase noise on a given carrier: **dBc/Hz, side-band power relative to the carrier power**. A discussion of the origin of these units provides a link between measured noise levels and calculated standard quantum limits Eq.(2.36) for both amplitude and phase noise.

A short modulation theory. It is instructive to review the effect of a modulation on a periodic electric signal $i(t)$ with a carrier power P_c (on 1Ω). It is obtained by ideal photodetection from $V(t)$, Eq.(2.79). As done in [12], for an amplitude modulation depth/index α and a modulation frequency ω_α , an AM signal is equivalent to:

$$i_{AM}(t) = \sqrt{2P_C} [1 + \alpha \cos(\omega_\alpha t)] \cos(\omega_0 t) \quad (2.80)$$

$$= \sqrt{2P_C} \operatorname{Re} \left\{ e^{i\omega_0 t} \left[1 + \frac{\alpha}{2} (e^{i\omega_\alpha t} + e^{-i\omega_\alpha t}) \right] \right\} \quad (2.81)$$

The same decomposition can be done for a phase modulation PM using Bessel functions and for β being the phase modulation index:

$$i_{PM}(t) = \sqrt{2P_C} \cos(\omega_0 t + \beta \sin(\omega_\beta t)) \quad (2.82)$$

$$\approx \sqrt{2P_C} \operatorname{Re} \left\{ e^{i\omega_0 t} \left[1 + \frac{\beta}{2} (e^{i\omega_\beta t} - e^{-i\omega_\beta t}) \right] \right\} \quad (2.83)$$

The structure of Eq.(2.81) and Eq.(2.83) can be compared for the resulting single side-band modulation-to-carrier power ratio (dBc). Side-band to carrier power ratio densities are denominated by $L(f)$ in the literature:

$$L_{AM} = \frac{P_{SSB-AM}}{P_C} = \frac{\alpha^2}{4}, \quad L_{PM} = \frac{P_{SSB-PM}}{P_C} \approx \frac{\beta^2}{4} \quad (2.84)$$

For any modulation frequency, both equations relate modulation depth, side-band power and carrier power in the same way. Any measured $L_{AM/PM}(f)$ in units dBc/Hz is consequently in the same way proportional to the modulation depth of amplitude and phase. As depicted in the next section, single side-band noise to carrier ratios $L(f)$ are very simple to measure. Their link to the r.m.s. deviation spectral densities $S(f)$ provides a comparison to then calculated noise levels of the standard quantum limit S_{SQL} , see also Eq.(2.36).

Noise levels relative to carrier $L(f)$ versus r.m.s. $S(f)$. The link is obtained by extending the considerations of [70] to amplitude noise: The mean squared deviation of a stochastic process $X(t)$ is $\langle X^2 \rangle = \int S_X(f)df$, see Eq.(2.23). If an amplitude modulation $a(t)$ and a phase modulation $\phi(t)$ are given at frequency f , the mean squared deviations $S(f)$ are easily obtained:

$$a(t) = \alpha \cdot \sin(\omega_\alpha t), \quad \phi(t) = \beta \cdot \sin(\omega_\beta t), \quad (2.85)$$

$$S_a(\omega_\beta) = \alpha^2/2, \quad S_\phi(\omega_\beta) = \beta^2/2. \quad (2.86)$$

Using Eq.(2.84) for both quadratures, the SSB noise/carrier-ratio $L(f)$ is therefore linked to the mean squared fluctuations $S(f)$ by:

$$L(f) = \frac{P_{\text{SSB}}(f)}{P_C} = \frac{S(f)}{2} \quad (2.87)$$

This conclusion is also important as it links the units: $\text{dBc/Hz} = (1/2) \cdot \text{rad}^2/\text{Hz}$ for phase modulations. Another measure for phase noise is the spectral density of frequency fluctuations $S_{f_0}(f) = f_0^2 S_\phi(f)$ in Hz^2/Hz . To avoid ambiguities in the case of strong phase modulations $L(f)$ is defined by $S(f)$, see [70].

The measurement of phase noise: principal techniques. Figure 2.9 shows the two main techniques used in this thesis. If amplitude noise is negligible, the direct measurement technique can be applied. It is the simplest method to quantify phase noise and uses directly a spectrum analyzer. Any measured side-band corresponds to a phase modulation. Taking into account the measurement resolution bandwidth and the carrier linewidth, one can easily obtain the ratio of the side-band power to the carrier power at 1 Hz resolution bandwidth. This distribution is $L(f)$, in dBc/Hz . It is linked to $S_\phi(f)$ by Eq.(2.87) above. The carrier power P_C be determined defined by a simple band-power measurement over the -3dB bandwidth of the signal.

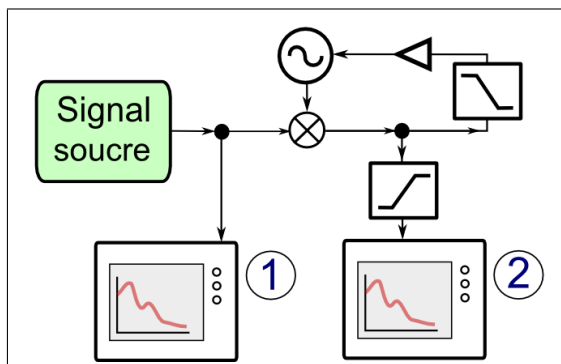


Figure 2.9: The two most important techniques to measure phase noise of an electronic signal: ① *direct measurement* of the noise side-bands with a spectrum analyzer, ② the *phase-lock-loop* (PLL) technique: the signal is demodulated by a voltage controlled oscillator (VCO) locked to the signal carrier frequency and its phase quadrature, within a feedback loop of low bandwidth. The phase noise is analyzed outside this bandwidth.

The phase-lock loop technique is insensitive to amplitude noise but more complex: It is depicted in Fig. 2.9 and consists of passing a given signal through a phase comparator and measuring the detector's output spectrum. The phase of the reference RF-source is locked in a low bandwidth phase-lock-loop (PLL) [71]. The mean squared signal of the phase comparator $\langle V^2(f) \rangle$ is measured with a spectrum analyzer in V^2/Hz and normalized by the resolution bandwidth (RBW) of the measurement. Together with the phase-to-voltage conversion factor K_d of the mixer/comparator, the distribution of $S_\phi(f)$ is directly obtained:

$$S_\phi(f) = \frac{1}{\text{RBW}} \frac{\langle V^2(f) \rangle}{K_d^2} \quad (2.88)$$

The sensitivity K_d in V/rad is measured with an oscilloscope at the output of the comparator: The beating of the signal with a reference slightly shifted in frequency is recorded with an oscilloscope. The slope of a linear fit at the zero-crossing of the output is K_d . If the phase fluctuations σ_ϕ are large and exceed 1 rad, the error signal of the mixer PLL has to be exploited for phase noise analysis.

The measurement of phase noise is a science and an art by itself. Further techniques are depicted in [72] and [12].

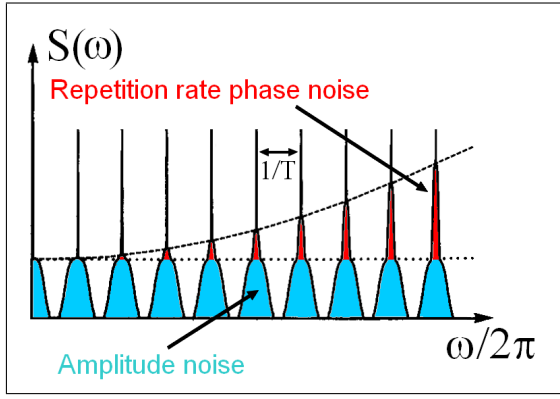


Figure 2.10: Amplitude and timing-phase noise side-bands as a function of the harmonic of the repetition rate. In the case of perfect photodetection, the measured amplitude noise side-bands are invariant against the considered harmonic of the repetition rate. In contrast, the detected side-bands arising from the timing-phase noise increase with the squared order of the repetition rate harmonic. Picture similar to [73].

Timing phase noise of a periodic pulse train. The measurement concept above can be applied to electronically available repetition rate and CEO-frequency of an optical frequency comb. Nevertheless, phase noise in a periodic pulsed signal, so the repetition rate, has an additional property: Being of a temporal periodicity of $T = 1/f_{\text{rep}}$, the ideal case of Dirac like pulses corresponds to a Dirac comb in frequency space: each line is a harmonic of f_{rep} . For an average power \bar{P} the pulsed temporal signal $P(t)$ gives rise to the spectral density $S(\omega)$:

$$P(t) = \bar{P}T \sum_{n=-\infty}^{n=+\infty} \delta(t - nT), \quad S(\omega) = \bar{P}^2 \sum_{n=-\infty}^{n=+\infty} \delta(\omega - n\omega_{\text{rep}}) \quad (2.89)$$

Introducing zero mean power fluctuations $N(t)$, $P(t) = \bar{P}(1 + N(t))$, one obtains:

$$P(t) = (1 + N(t))\bar{P}T \sum_{n=-\infty}^{n=+\infty} \delta(t - nT), \quad S(\omega) = \bar{P}^2 \sum_{n=-\infty}^{n=+\infty} [\delta(\omega - n\omega_{\text{rep}}) + S_N(\omega - n\omega_{\text{rep}})]$$

Repetition rate fluctuations δT imply the spectral density [73]:

$$P(t) = \bar{P}T \sum_{n=-\infty}^{n=+\infty} \delta(t - nT - \delta T(t)) \quad (2.90)$$

$$S(\omega) = \bar{P}^2 \sum_{n=-\infty}^{n=+\infty} [\delta(\omega - n\omega_{\text{rep}}) + n^2\omega_{\text{rep}}^2 S_{\delta T}(\omega - n\omega_{\text{rep}})] \quad (2.91)$$

It grows with the square of the order of the repetition rate harmonic n . This is in contrast to the amplitude noise, which appears for each harmonic with the same coefficient. This behavior is schematically shown in Fig.2.10. It can be used to quantify and to distinguish repetition-rate phase noise.

2.7 Passive cavities: filtering and analysis of noise

The main experimental results of this thesis, chapter 4, are obtained from the interaction of a broadband passive cavity with the noise of an optical frequency comb. The generic underlying measurement concept is depicted in Fig. 2.11. The frequency comb to analyze seeds a passive cavity and is transmitted at resonance. Subsequent homodyne or direct photodetection provide a sensitive detection of phase noise in the frequency comb.

A pre-requisite to this scheme is a broadband resonant passive cavity. Its theoretical and necessary properties are studied in this section. A special focus is set on the interaction of the noise in resonant optical frequency comb with the cavity: Its filtering could provide for an increased sensitivity of a possible homodyne timing measurement see section 2.5.1, page 37. Homodyne detection with the seed itself can be used to detect phase noise with highest sensitivity. The conversion of phase-to amplitude noise permits a simple, direct detection of spectral phase noise. In the beginning, the context of the literature is summarized.

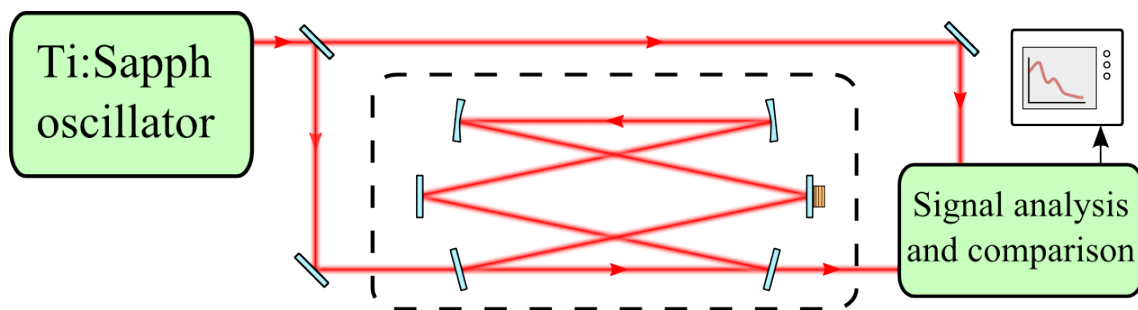


Figure 2.11: Main experimental scheme of this thesis. The signal of a Ti:Sapph oscillator is transmitted by a cavity. The resulting signal is either directly analyzed or compared to the initial seed within a homodyne detection.

Context of the literature. A transmissive passive cavity can act as a spatial and temporal filter on an optical signal. It has been shown in the literature that even the intensity noise of an 10 W Nd:YAG laser beam can be filtered down to the shot noise level at detection frequencies in the MHz region [74]. On the example of noisy diode-lasers, a passive optical cavity has also been proven to filter phase noise efficiently [29]. An optical cavity converts in addition phase noise into amplitude noise. This can be understood as a rotation of the noise ellipse in the Fresnel plane [75] or within the transfer functions of the noise quadrature operators [29].

Several techniques are available to lock a passive cavity on the mean incident field. Their frequency response and bandwidth have to be considered, when the noise properties of cavity-transmitted or -reflected beams are studied. A sufficiently high locking bandwidth (kHz) prevents also the cavity length fluctuations to couple on the transmitted field [76]. Three principal locking methods are suitable for consideration in this thesis: first, using the transmitted intensity; second, using the dichroic properties of a cavity [77] and third, based on the interference of phase modulation side-bands. The latter is known as the Pound-Drever-Hall (PDH) scheme, [78, 79]. The two first do not require modulation and are consequently more sensitive to environmental noise. The PDH-scheme uses a MHz phase modulation and is simple to implement. A demodulation of the transmitted or reflected beam provides the error signal. Typically, the cavity reflection is used: the cavity bandwidth may limit the error signal in transmission [80].

Broadband cavities have been developed for molecular spectroscopy [81] and field enhancement [82, 83]. A transmissive passive broadband cavity has been reported for repetition-rate filtering [84].

The focus of this thesis is filtering of amplitude and phase noise in a 45 nm FWHM broad frequency comb [69], the detection of its spectral phase noise [85] and the complete analysis of phase noise correlations [86]. The underlying studies rely on a broadband resonant passive cavity. Its theory is developed in this chapter.

2.7.1 Cavity resonances

The optical resonance frequencies of a passive cavity are determined by its round-trip length L . The minimal difference between resonant frequencies ω_n is the free spectral range $\Delta\Omega_{\text{FSR}}$. Another principal parameter is the cavity finesse \mathcal{F} . It is a function of the transmission coefficient of all mirrors: $T = \sum_i T_i$, of all other losses l and corresponds to the quality factor of a resonator. The finesse determines the FWHM of the cavity resonances Ω_{BP} . For small $T \ll 1$:

$$\mathcal{F} = \frac{2\pi}{T+l} = \frac{\Delta\Omega_{\text{FSR}}}{\Omega_{\text{BP}}}, \quad \Omega_{\text{FSR}} = \frac{2\pi c}{L} = \omega_n - \omega_{n+1} \quad (2.92)$$

An important case is an empty cavity consisting of an arbitrary number of high-reflective mirrors $R_{\text{HR}} = 1 - T_{\text{HR}} \approx 1$ and two coupling mirrors with $T_{\text{OC}} > T_{\text{HR}}$. This type of cavity is called *impedance matched*. If dispersion and intracavity losses can be neglected, it has a transmission of one at resonance.

Geometrical stability condition. A typical laser beam fulfills the *paraxial approximation* and the propagating field amplitude is described by the *paraxial Helmholtz equation*. An orthogonal basis solving this equation is the one of *transverse Hermite Gauss modes* u_n . They correspond to the property of many lasers to have transverse reflection symmetry. Along the two transverse coordinates, the electric field propagating along z , $E(x, y, z)$, can be factorized into the transverse modes u_n :

$$E(x, y, z) \propto u_{mn}(x, y, z) = u_n(x, z)u_m(y, z). \quad (2.93)$$

It is called a *transverse electric mode* $\text{TEM}_{m,n}$. For such a Gaussian beam, the propagation along the longitudinal coordinate z can be described by the *beam parameter* q that takes into account the beam radius w , the radius of curvature R of the wave-fronts and the central wavelength $\lambda_0 = 2\pi c/\omega_0$:

$$\frac{1}{q} = \frac{1}{R} - \frac{i\lambda_0}{\pi n w^2} \quad (2.94)$$

The condition of identical spatial field properties after each cavity round-trip can be written using the Gaussian beam parameter q and the transfer matrix formalism: Every mirror and free-space propagation step corresponds to a matrix M . It is given for the principal interactions of the cavity with the light beam: propagation over a distance d and the reflection by a spherical mirror of radius of curvature R .

Any sequence of linear optical elements, e.g. one round-trip in a even more involved cavity, results in a transfer-matrix M :

$$M = \begin{pmatrix} A & B \\ C & D \end{pmatrix}, \quad M_{propag} = \begin{pmatrix} 1 & d \\ 0 & 1 \end{pmatrix}, \quad M_{spherical\ mirror} = \begin{pmatrix} 1 & 0 \\ -2/R & 1 \end{pmatrix} \quad (2.95)$$

The transverse round-trip condition, i.e. unchanged q per round-trip, becomes [87]:

$$q_2 = \frac{Aq_1 + B}{Cq_1 + D} \quad \text{and} \quad q_2 = q_1 \quad (2.96)$$

Here q_1 and q_2 are the beam parameters at the beginning and the end of a resonator round-trip. For the setup of a cavity of a priori undefined mirror distances d_i , radii R_i and a beam radius w , suitable combinations of values are found numerically. The stability criterion above can be written as: [88]:

$$Tr|M| = |AD - BC| < 2 \quad (2.97)$$

As a consequence of this criterion and the properties of Gaussian beam propagation, any stable cavity contains at least one beam waist w_0 . It turns out that any beam acquires the so-called *Gouy phase* ϕ_{Gouy} when passing through a waist. This behavior is sketched in Fig. 2.12, right. The acquired phase depends on the indices m, n of the transverse mode $TEM_{m,n}$ and can be written with a constant α as $\phi_{Gouy,n,m} = (n + m + 1) \cdot \alpha$. See [89] for details. It impacts the resonance condition of a passive cavity as follows:

Transmission of a resonant cavity. A cavity transmits most intensity at resonance. With Eq.(2.92), this transmission $I(\omega)$ is a function of the optical frequency ω . It can also be written as a function of the spectral phase $\phi(\omega) \bmod 2\pi$, acquired by propagation over one cavity length. From the energy conservation for the fields that are incident to, transmitted by and stored in the cavity [90] one obtains:

$$I(\omega) \simeq \frac{I_0(\omega)}{1 + \left(\frac{2\mathcal{F}}{\pi}\right)^2 \sin^2\left(\frac{\phi(\omega)}{2}\right)} \quad (2.98)$$

The typical shape of $I(\omega)$ is sketched in Fig. 2.12, left. The resonances are consequently located at $\phi(\omega) = p \cdot \pi$.

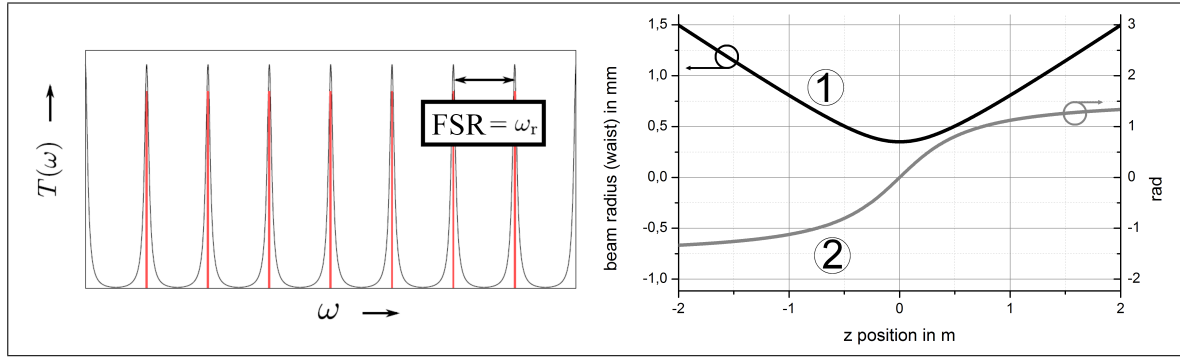


Figure 2.12: Left: The transmission of a passive cavity. The spacing of the individual resonances by the free spectral range $\Delta\Omega_{\text{FSR}}$ corresponds to the repetition frequency ω_r of a frequency comb.

Right: Example of a Gouy phase shift ϕ_{Gouy} . Beam parameters as used in the following section: wavelength 800 nm, beam waist 350 μm . The beam undergoes the Gouy phase periodically at each round-trip. This causes a collective shift of the cavity resonance frequencies by $\Omega_{\text{Gouy}} = \phi_{\text{Gouy}}/2\pi \cdot \Delta\Omega_{\text{FSR}}$. It corresponds to an eigen-CEO frequency of a broadband resonant cavity $\omega_n = n \cdot \omega_r + \omega_{\text{CEO}}$. In order to transmit a frequency comb through a passive cavity with best efficiency, its CEO-frequency has to be set with respect to the cavity's Ω_{Gouy} .

In a realistic cavity, $\phi(\omega)$ depends also on the refractive index $n(\omega)$ of the gas inside the cavity. Chirped mirrors may lead to a non constant round-trip cavity length $L(\omega)$. The complete resonance condition is consequently:

$$\phi(\omega) = \omega_{nmp} \frac{n(\omega)L(\omega)}{c} - (n + m + 1)\alpha = p \cdot \pi, \quad p, n, m \in \mathbb{N} \quad (2.99)$$

This definition of the resonant frequencies ω_{nmp} has two important consequences:

Spatial mode discrimination. Eq.(2.99) can be considered for a given seed optical carrier ω_0 in the mode $\text{TEM}_{m,n}$. It defines different lengths $L_{m,n}$ at which the mode $\text{TEM}_{m,n}$ is resonant in the cavity. As these lengths are well distinguished, a transmissive cavity is a spatial mode filter at a the resonant length L .

A resonant frequency comb and the eigen-CEO. For a given cavity length L and an arbitrary selected mode $\text{TEM}_{0,0}$, Eq.(2.99) sets the resonant frequencies.

$$\omega_p = (p\pi + \alpha) \frac{c}{nL}, \quad \omega_{\text{CEO}} = \alpha \frac{c}{nL}, \quad p \in \mathbb{N} \quad (2.100)$$

This is a filter with equally spaced frequency resonances and an offset ω_{CEO} to the zero frequency. An optical frequency comb can be matched to it, if both have the same frequency spacing and offset ω_{CEO} . This offset will be called *eigen-CEO* of a broadband resonant cavity. In a realistic situation the cavity resonances are not equally spaced due to intracavity dispersion. The possible transmission of a seeding, equally spaced frequency comb will therefore depend also on the linewidth of each resonance and the spacing between neighboring resonances.

Secondary resonances. The free spectral range of the cavity Ω_{FSR} might be slightly different from the spacing of the seeding comb $\omega_{\text{rep}} = \Omega_{\text{FSR}} + \epsilon$. If the round-trip cavity length is in addition a multiple m of the central wavelength λ of the comb $L' = c/\Omega_{\text{FSR}} + m \cdot \lambda$ the resonance is called the *secondary resonance* of order m . If the cavity is resonant at $\omega_{p, \text{res}}$, any comb frequency acquires a frequency dependent phase $\Phi_m(\omega)$ per round-trip. This leads to resonance properties depending on the comb line frequency ω_n :

$$\Phi_m(\omega_n) = 2\pi m \frac{\omega_n}{\omega_{p, \text{res}}} \Rightarrow I_{\omega_n}(\omega) \simeq \frac{I_0(\omega_n)}{1 + \left(\frac{2m\mathcal{F}}{\omega_{p, \text{res}}}\right)^2 \omega_n^2} \quad (2.101)$$

Secondary resonances can be distinguished from primary resonances by their smaller bandwidth. Figure 2.13 shows the typical effect of secondary resonances on a recorded transmission signal when sweeping the cavity length. With increasing order of the secondary resonance, simultaneous resonance is provided for a less broad spectrum: When sweeping the cavity-length, the apparent peak power decreases and the apparent width of the resonance peak increases. See also [91] for further discussion.

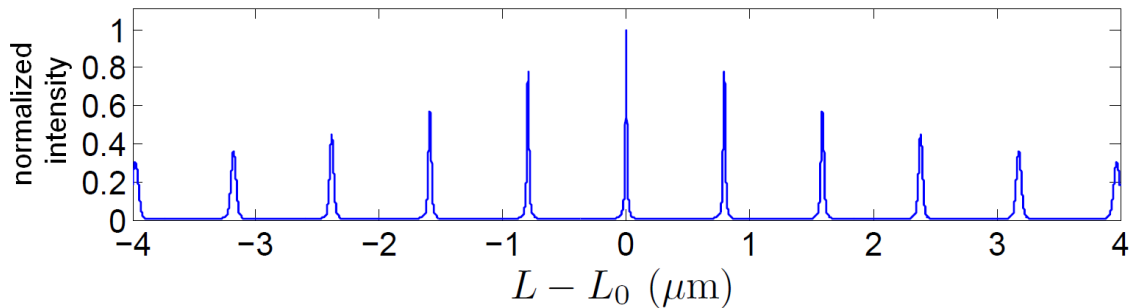


Figure 2.13: The secondary resonances of a swept, broadband cavity. Picture from [34]. A frequency comb of 800 nm central wavelength, 6 nm FWHM is assumed to seed a cavity of finesse 125.

2.7.2 Transfer function of the noise field quadratures

The aim of this section is to show that a passive cavity is an intrinsic filter of amplitude and phase fluctuations of seeding fields [29]. It inter-converts in addition amplitude and phase fluctuations [75]. The necessary theory can be developed by considering an individual noisy line ω_0 of a frequency comb seeding a cavity at or close to resonance. In the carrier-envelope representation, the real electric field of the frequency comb can be written using the complex field envelope $\alpha(t)$:

$$E_{\text{in}}(t) = E_0 \alpha(t) e^{-i\omega_0 t} + c.c. \quad (2.102)$$

A Fourier transform gives the field in the spectral domain:

$$E_{\text{in}}(\omega) = E_0 \frac{1}{\sqrt{2\pi}} \int dt \alpha(t) e^{-i(\omega - \omega_0)t} + c.c. \quad (2.103)$$

$$= E_0 [\alpha(\omega - \omega_0) + \bar{\alpha}(\omega_0 - \omega)] \quad (2.104)$$

$$\text{with } \bar{\alpha}(\omega) = \frac{1}{\sqrt{2\pi}} \int dt \bar{\alpha}(t) e^{-i\omega t} \rightarrow \overline{\alpha(\omega)} = \bar{\alpha}(-\omega) \quad (2.105)$$

Using $\Omega = \omega - \omega_0$ the *noise field-* or *side-band quadratures* or $P(\Omega)$ and $Q(\Omega)$ are defined as:

$$P_{\text{in}}(\Omega) = i [\bar{\alpha}(-\Omega) - \alpha(\Omega)], \quad Q_{\text{in}}(\Omega) = \alpha(\Omega) + \bar{\alpha}(-\Omega) \quad (2.106)$$

The next paragraph studies the formal description of the transmission of noise through a passive cavity. It turns out that a description in terms of $Q(\Omega)$ and $P(\Omega)$ is of a particular simple form. They correspond to a modulation of the amplitude (Q) and phase (P) of a carrier ω_0 at the side-band frequency Ω . See also section 2.6.1.

Transmission and reflection of a passive cavity. The transmission and reflection of a passive linear cavity can be modeled using the complex amplitudes of the respective fields and the assumption of energy conservation [87]. It is sufficient to study a cavity of two identical mirrors to obtain the relations necessary for this thesis. This model is depicted in Fig. 2.14, *left*. With R and T being the coefficients of intensity reflection and transmission of the mirrors, the respective coefficients for the field and mirror i are $r_i = \sqrt{R_i}$, $t_i = \sqrt{T_i}$. Loss-less reflection $R_i + T_i = 1$ can be assumed, so $T = t_1 t_2$ and $R = r_1 r_2$ for identical mirrors. The ratio of the complex incident, reflected and transmitted fields E_{in} , E_{refl} , E_{tr} give rise to the complex transmission and reflection coefficients t_c and r_c .

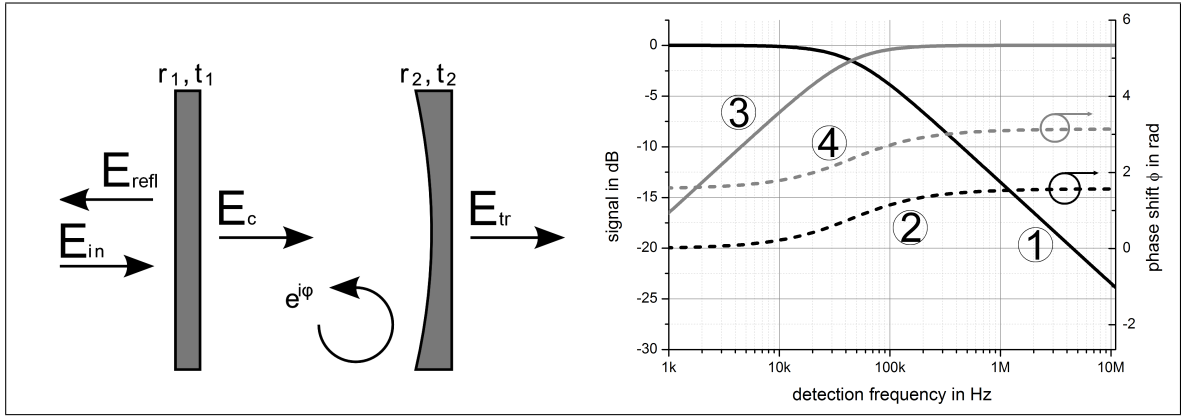


Figure 2.14: *Left: Model of a transmissive cavity.* The incident field is E_{in} , the reflected E_{refl} , the intracavity E_c and the transmitted E_{tr} . The field-reflectivity and transmission of the mirrors is given by r and t . The model defines the complex transmission and reflection coefficients t_c and r_c . *right: Modulus and phase of the cavity transmission and reflection coefficients.* Calculated for a cavity length 1.92 m, finesse 1500. Transmission τ ① and Φ_t ②, reflection ρ ③ and Φ_r ④.

Assuming the cavity to be resonant at a frequency ω , one obtains for a noise side-band frequency Ω :

$$t_c(\Omega) = \frac{E_{tr}}{E_{in}} = \frac{T e^{i\phi(\Omega)/2}}{1 - R e^{i\phi(\Omega)}} = \tau(\Omega) e^{i\Phi_t(\Omega)}, \quad \phi(\Omega) = \frac{\Omega L}{c} \quad (2.107)$$

$$r_c(\Omega) = \frac{E_{refl}}{E_{in}} = \frac{T(e^{i\phi(\Omega)} - 1)}{1 - R e^{i\phi(\Omega)}} = \rho(\Omega) e^{i\Phi_r(\Omega)} \quad (2.108)$$

This is a decomposition into absolute value and phase: $\tau(\Omega) = |t_c(\Omega)|$, $\rho(\Omega) = |r_c(\Omega)|$. Their RF-spectral dependence on Ω is shown in Fig.2.14, *right*. Nevertheless, a simpler representation is obtained using $t_c(-\Omega) = t_c^*(\Omega)$, $r_c(-\Omega) = r_c^*(\Omega)$. The noise field quadratures can be written in terms of the transmission (tr) and reflection (refl) coefficients as well as the incident field amplitudes α . For example:

$$Q_{tr}(\Omega) = -i[t_c(-\Omega)\alpha(-\Omega) - t_c(\Omega)\alpha(\Omega)] \quad (2.109)$$

$$= \tau(\Omega) \left[i \frac{e^{i\Phi_t(\Omega)} - e^{-i\Phi_t(\Omega)}}{2} P_{in}(\Omega) + \frac{e^{i\Phi_t(\Omega)} + e^{-i\Phi_t(\Omega)}}{2} Q_{in}(\Omega) \right] \quad (2.110)$$

Similar equations are obtained for P_{tr} , P_{refl} and Q_{refl} .

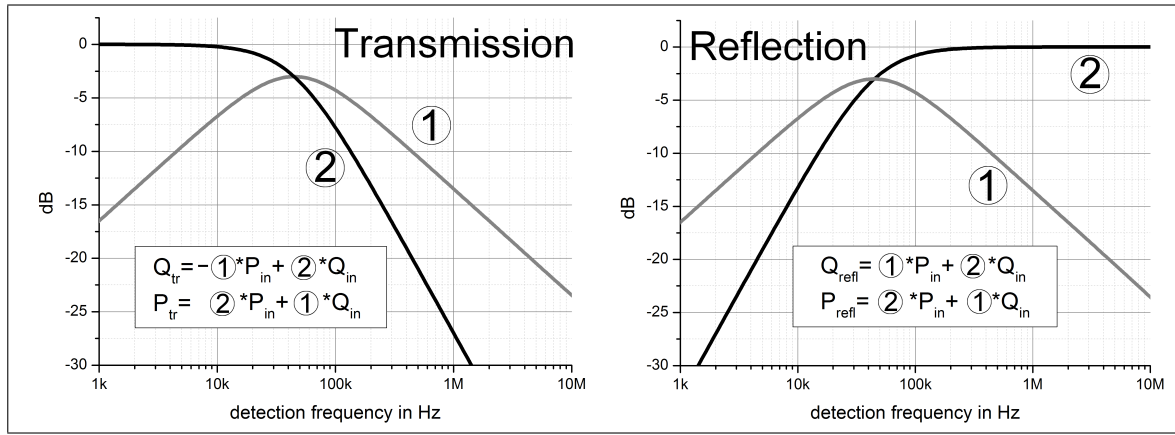


Figure 2.15: Noise quadrature conversion by an optical cavity. Parameters as in the experimental section 4: cavity length 1.92 m, finesse 1500. Shown is the contribution of the seeding field to the *left* transmitted and the *right* reflected field quadratures. Q and P are the amplitude and phase quadrature.

They can be summarized in matrix form for transmission (out) or reflection properties τ , ρ and Φ :

$$\boxed{\mathbf{v}_{out}(\Omega) = \tau(\Omega)\mathbf{A}_{tr}(\Omega)\mathbf{v}_{in}(\Omega)} \quad (2.111)$$

$$\mathbf{A}_{tr}(\Omega) = \begin{bmatrix} \cos \Phi_t(\Omega) & \sin \Phi_t(\Omega) \\ -\sin \Phi_t(\Omega) & \cos \Phi_t(\Omega) \end{bmatrix}, \quad \mathbf{v}_{in}(\Omega) = \begin{bmatrix} P_{in}(\Omega) \\ Q_{in}(\Omega) \end{bmatrix} \quad (2.112)$$

The same structure is obtained in the case of reflection. It is clear from the above equations that a resonant cavity rotates the (noise) field quadratures \mathbf{v} by the unitary matrix \mathbf{A} - as a function of the side-band frequency Ω . The additional attenuation of noise is described by the factors τ or ρ , depending if either transmission or reflection is considered. Figure 2.15 shows the conversion on the example of the Q quadrature, in reflection and transmission. Used in reflection, the cavity acts as a *notch filter* for the resonance frequency. In transmission, phase and amplitude noise are attenuated with increasing side-band frequency. The effect of quadrature interconversion is significant above the 3 dB cutoff-frequency of the cavity. This fact will be exploited in the experimental section to detect phase noise of an optical frequency comb.

Quadrature conversion and dispersion. A passive cavity can be simultaneously resonant for an entire frequency comb. To provide this, its free spectral range (FSR) must be equal to the signal repetition rate and the accumulated phase per round-trip equivalent to the CEO-phase of the frequency comb.

The round-trip phase and thus the eigen-CEO of the cavity can be fine-tuned using the air-pressure inside the cavity-container. This pressure also tunes the linear change of the round-trip phase with the optical frequency, the cavity round-trip length. As this parameter can be compensated by the mechanical positioning of the cavity mirrors, the eigen-CEO of the cavity can be independently accessed.

Nevertheless, this approach of pressure tuning cannot compensate for the residual higher order dispersion of the cavity mirrors, $\phi_{\text{cavity}}(\omega)$, shown in Fig. 2.16, left scale. The resulting spectral phase at the comb frequency ω_n leads to a change of the cavity FSR by

$$\Delta\omega_{\text{FSR}}(\omega_n) = \omega_{\text{rep}} \cdot \phi_{\text{cavity}}(\omega_n)/2\pi. \quad (2.113)$$

Assuming a cavity lock at the comb central wavelength of 800 nm, this frequency shift is also shown in Fig. 2.16, right scale. For the entire comb, this frequency shift can be estimated to be inferior to 100 kHz. The cavity used here has a linewidth of the same order of magnitude, so this effect will not significantly impact the over-all transmitted intensity at resonance.

Nevertheless, for any noise side-band of a comb line ω_n , the side-band frequency "seen" by the cavity will change to the apparent value Ω_{A} :

$$\Omega_{\text{A}}(\omega_n) = \Omega \pm \Delta\omega_{\text{FSR}}(\omega_n) \quad (2.114)$$

As discussed below, this change may have significant impact on the phase-to-amplitude noise conversion of phase noise sidebands.

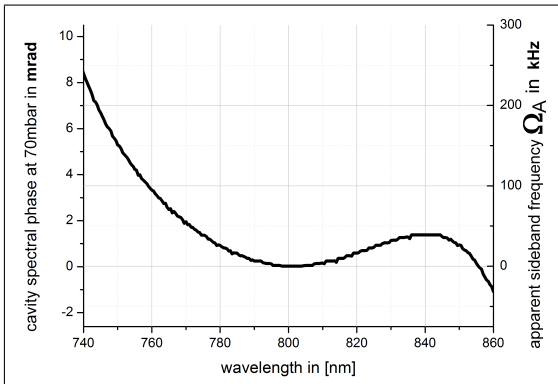


Figure 2.16: Realistic spectral phase and shift of the apparent side-band frequency. Shown is the estimated, minimal spectral phase (dispersion) of the passive cavity studied in the experimental part of this thesis (6 quarter-wave zero dispersion mirrors, 1.92 m laboratory air at 70 mbar). If the cavity is resonant at the comb central frequency, a spectral phase (*left scale*) is equivalent to a frequency shift (*right scale*) of the cavity-resonances compared to regular spaced optical signal.

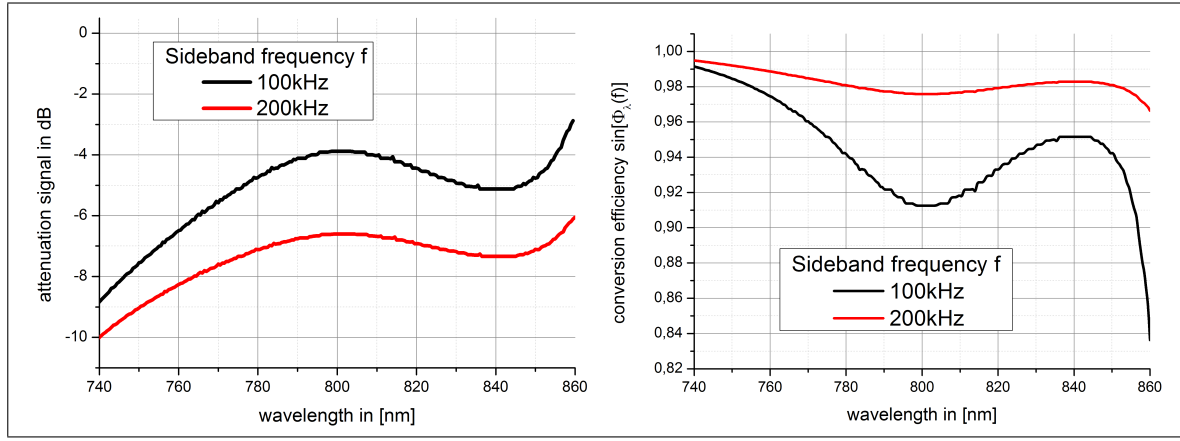


Figure 2.17: Impact of the cavity's spectral phase on the conversion of phase noise side-bands to amplitude noise. For two detection frequencies of 100 kHz and 200 kHz, the impact on *left*: the attenuation τ , *right*: the factor $\sin(\dots)$ in the conversion efficiency

The noise quadrature conversion Eq.(2.111) is a possible application of a passive cavity. It provides the analysis of phase noise in the seeding comb from a simple noise measurement on the transmitted intensity. Assuming negligible amplitude noise and for a transmitting cavity, the phase to amplitude noise quadrature conversion described in Eq.(2.110) is given by:

$$Q_{\text{out}}(\Omega) = -\tau(\Omega) \cdot \sin[\Phi_t(\Omega)] \cdot P_{\text{in}}(\Omega) \quad (2.115)$$

The conversion efficiency is consequently a function of the side-band frequency Ω .

By a subsequent analysis over the optical spectrum, even the spectral phase noise of the comb becomes accessible. In this case and with respect to Eq.(2.114), the conversion efficiency depends then on the apparent side-band frequency Ω_A that varies over the optical spectrum:

$$Q_{\text{out}}(\Omega) = -\tau(\Omega_A) \cdot \sin[\Phi_t(\Omega_A)] \cdot P_{\text{in}}(\Omega) \quad (2.116)$$

Figure 2.17 shows the dependence of the factors τ and $\sin(\dots)$ on the dispersion of the cavity for a noise side-band at the cavity 3 dB cutoff-frequency Ω_c . The residual cavity dispersion affects mostly the attenuation of the signal τ . The relative impact of the cavity dispersion on the conversion efficiency diminishes at higher detection frequencies $\Omega \gg \Omega_c$.

Although the analysis of intensity noise in the resonant transmitted signal seems initially to be promising, care has to be taken when a quantitative analysis is done. Precise information on the cavity dispersion is necessary to determine absolute values of spectral phase noise in the seeding comb without ambiguity.

Phase noise and amplitude-phase correlation measurements. The principal effects of a passive cavity on a seeding resonant beam are the filtering and the interconversion of the noise field quadratures, see Eq.(2.111). Nevertheless, in order to use and quantify such effects, it has to be considered that the measurable noise densities are the mean squares $S = \langle |.|^2 \rangle$ at any detection angular frequency Ω :

$$S_I(\Omega) = \langle |Q(\Omega)|^2 \rangle, \quad S_\phi(\Omega) = \langle |P(\Omega)|^2 \rangle \quad (2.117)$$

In a typical experiment like section 4.2, the intensity noise of the seed and the resonant transmitted beam are readily available. By the use of Eq.(2.111), they are related by:

$$Q_{\text{out}} = \tau \cos[\Phi] Q_{\text{in}} - \tau \sin[\Phi] P_{\text{in}} \quad (2.118)$$

Holding for all side-bands Ω , this relation can be written in terms of the measurable noise densities $S(\Omega)$. An amplitude-phase correlation term appears and one obtains:

$$S_{I,\text{out}} = \tau^2 \cos^2[\Phi] S_{I,\text{in}} + \tau^2 \sin^2[\Phi] S_{\phi,\text{in}} + \underbrace{2\tau^2 \cos[\Phi] \sin[\Phi] \langle P_{\text{in}} Q_{\text{in}} \rangle}_{c_{PQ}} \quad (2.119)$$

If the correlation term c_{PQ} is negligible, the phase noise of the seeding beam can be calculated. Only the intensity noise of the seed $S_{I,\text{in}}$ and the cavity output $S_{I,\text{out}}$ are required:

$$S_{\phi,\text{in}} = \frac{S_{I,\text{out}} - \tau^2 \cos^2[\Phi] S_{I,\text{in}}}{\tau^2 \sin^2[\Phi]} \quad (2.120)$$

For typical detection frequencies above the cutoff frequency and typical intensity noise levels recorded within this thesis this result can be simplified. The intensity noise of the seed is close to the SQL and negligible compared to the output: $S_{\text{SQL}} \simeq S_{I,\text{in}} \ll S_{I,\text{out}}$. The phase noise of the seed is readily calculated by

$$\boxed{S_{\phi,\text{in}} \approx \frac{S_{I,\text{out}}}{\tau^2 \sin^2[\Phi]}} \quad (2.121)$$

In order to underline the applicability of Eq.(2.121) and to provide a simple accessible conclusion, the coefficients of the intensity noises Eq.(2.120) are plotted in Fig. 2.18. They are ① for $S_{I,\text{in}}$ and ② for $S_{I,\text{out}}$. Above the cavity cutoff frequency at 100 kHz, it is the coefficient ② that contributes most significantly. The output intensity noise of a resonant transmitting cavity contains consequently major information about the phase noise of the cavity seeding beam.

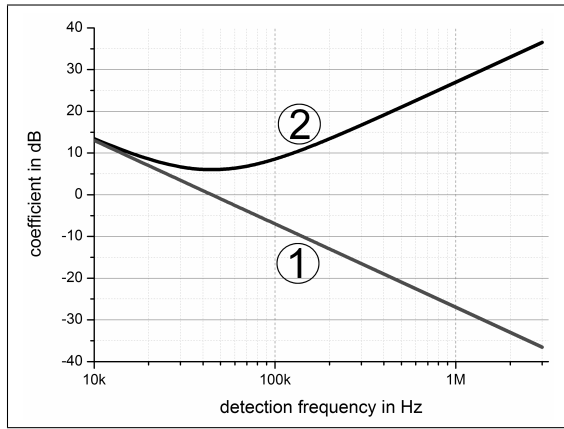


Figure 2.18: Phase noise measurements based on cavity intensity excess noise - the seed intensity noise as a possible error source. The phase noise $S_{\phi, \text{in}}$ of the seed of a transmitting cavity can be represented in terms of: the intensity noise of this seed $S_{I, \text{in}}$ with coefficient ① and the intensity noise at the cavity output $S_{I, \text{out}}$ with coefficient ②. This approach assumes vanishing amplitude-phase noise correlations for the seed of the cavity.

Assuming a signal-to-noise ratio $\text{SNR}=1$, the sensitivity of a phase noise measurement based on Eq.(2.121) is the inverse of the curve ② in Fig. 2.18. For typical detection frequencies above 100 kHz, the sensitivity to phase noise is 10 to 30 dB above the SQL. In consequence, the measurement of phase noise using noise quadrature conversion by a passive cavity is not of quantum-limited sensitivity.

Amplitude-Phase noise correlations. It is a special feature of optical frequency combs that the phase noise property common to all combs lines, the CEO-phase noise S_{CEO} , can be measured separately by e.g. an f - $2f$ beating. This permits to access the term P_{in} in Eq.(2.119) and consequently the *direct measurement of the amplitude-phase noise correlations of the seed*. In a simplified representation of the functional dependence $F[\dots]$ one obtains:

$$c_{PQ} = F[S_{i, \text{in}}, S_{i, \text{out}}, S_{\text{CEO}}] \quad (2.122)$$

The required data is readily accessible in an experiment. A corresponding measurement is presented in section 4.2.

Conclusions - transfer of noise field quadratures

Transmissive passive cavities are in conclusion a powerful tool to measure phase noise in optical frequency combs. Their interconversion of noise field quadratures makes phase noise in optical frequency combs readily measurable. Even the analysis of phase noise over the optical spectrum of the seeding comb might be possible - a measurement of highest complexity with other techniques. Nevertheless, care has to be taken if such a broadband resonance is exploited. Even smallest levels of intracavity dispersion may have a significant influence on the quadrature conversion, see the experiment in section 4.2. Transmissive passive cavities filter amplitude and phase noise of the seeding field. The resulting beam can be used as a "quiet" reference for phase noise measurements, as done in numerous experiments of chapter 4.

Chapter 3

Experimental Framework

Contents

3.1	Properties of the Ti:Sapph oscillator	60
3.1.1	Intensity noise	61
3.1.2	CEO-Phase noise	64
3.1.3	Repetition-rate phase noise	71
3.1.4	Estimation of the free running linewidth	74
3.1.5	Noise transfer functions	76
3.1.6	Summary of the noise properties of the Ti:Sapph oscillator . .	79
3.2	Design of a passive broadband cavity	80
3.2.1	Technical design of the cavity	80
3.2.2	Geometric properties	82
3.2.3	Conditions for broadband simultaneous resonance	83
3.2.4	Measured finesse and broadband transmission.	86
3.2.5	Properties of the PDH-Lock	87
3.2.6	The locked cavity - experimental characterization	90

This chapter prepares the main results of this thesis: a filtering scheme and new measurement principles for noise in optical frequency combs, close to the standard quantum limit (SQL). To this aim and in the first part, the noise of a Ti:Sapph oscillator is characterized extensively with standard methods. The second part of this chapter characterizes the principal new measurement tool of this thesis: a broadband resonant passive cavity.

3.1 Properties of the Ti:Sapph oscillator

The timing measurement depicted in Fig. 2.8, page 37, requires a broadband, femtosecond light source with low phase noise. A passively mode locked Ti:Sapph oscillator is such a source. Here, the properties of a commercial Femtolaser SYNERGY HP system pumped by a Coherent Verdi V10 are studied. The aim is to apply this oscillator to a proof-of-principle timing jitter measurement in the future. The oscillator provides pulses of shorter than 30 fs, with a bandwidth of 40 nm FWHM, centered at 800 nm and with a repetition rate of 156 MHz. Stable mode-locking is achieved between 750 mW and 1.6 W output power. As shown in section 2.5, the sensitivity of the homodyne timing measurement depends essentially on the phase noise of the used oscillator. Its intensity noise is nevertheless not neglected here: it is important for a better understanding of the underlying noise sources and processes.

Both amplitude and phase noise will be characterized relative to the SQL. This chapter does not develop new methods, but tries to use standard techniques at their highest sensitivities. The detailed characterization of the oscillator noise indicates its origin and provides conclusions on how to reduce it. This could finally increase the realistic sensitivity of the homodyne timing measurements.

For the following considerations, note that a passively mode-locked femtosecond laser generates a coherent pulse train with a coherence length of up to 10^6 m. It is consequently always also a CW laser. Intensity and phase noise properties are consequently well defined at side-band frequencies Ω well below the repetition rate ω_{rep} .

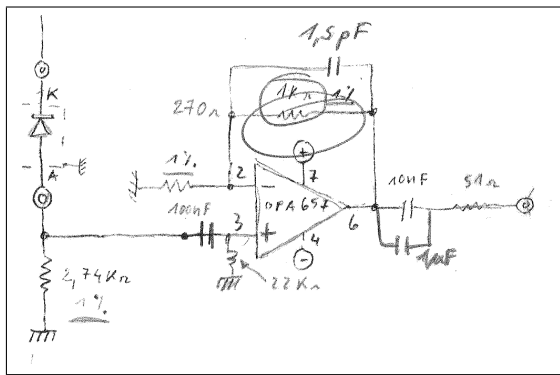


Figure 3.1: Sketch of the transimpedance amplification of the photodiode signal. The photodiode is polarized at -15V to increase the quantum efficiency of detection. The amplification is done separately for the DC part (low passed, not shown) and the AC signal (high passed). The cutoff frequency of the latter is chosen not lower than several kHz in order to prevent the OPA 657 from saturation by low frequency noise. The output gain is flat up to 10 MHz detection frequency.

3.1.1 Intensity noise

The circuit shown in Fig. 3.1 is used for shot noise resolving detection of optical signals. It provides high gain and avoids saturation by a separated amplification of the DC and the AC part of the signal. Standard Hamamatsu S5971 photodiodes are applied to characterize amplitude noise in a band from above 20 kHz to 10 MHz. The gain is restricted to this bandwidth as the Ti:Sapph oscillator considered here is expected to be at the shot noise level above 10 MHz detection frequency. Significant gain at the repetition rate 156 MHz would in addition saturate the amplifier. Intensity noise at low detection frequencies DC to MHz can also be analyzed using a complementary Thorlabs PDA36 detector. This off-the-shelf detector was measured to have signal dependent gain and is not suitable for shot noise resolving signal analysis. Nevertheless, the measurements with both detectors can be combined to the RF-broadband intensity noise analysis shown in Fig. 3.2, left. The shot noise level obtained by balanced detection Fig. 3.2, right, can be normalized to the carrier power P of the beam by Eq.(2.35): $S_{\text{SQL}} = 2h\nu/P$. Due to detector saturation, typical signals here detected are attenuated to below 10 mW average power. The entire detection of the available 1 W optical power would lead to a much lower SQL, but requires the development of highly evolved electronics [14, 15].

According to Fig. 3.2, left, the intensity noise of the Ti:Sapph oscillator and the Verdi V10 pump laser follow the same $1/f$ power law over 3 decades of detection frequency. They are therefore strongly correlated. The intensity noise of the Verdi pump laser is consequently the principal origin of the Ti:Sapph intensity noise. The broad noise peak at 500 Hz to 1 kHz lies in the same frequency region as the mechanical resonances of the typically used opto-mechanical assemblies. The optical table has been characterized to strongly attenuate mechanical vibrations above 1 kHz, see Fig. A.12. The $1/f$ intensity noise of the DPSS-laser Verdi V10 is supposed to arise from electronic noise processes in the pump diodes.

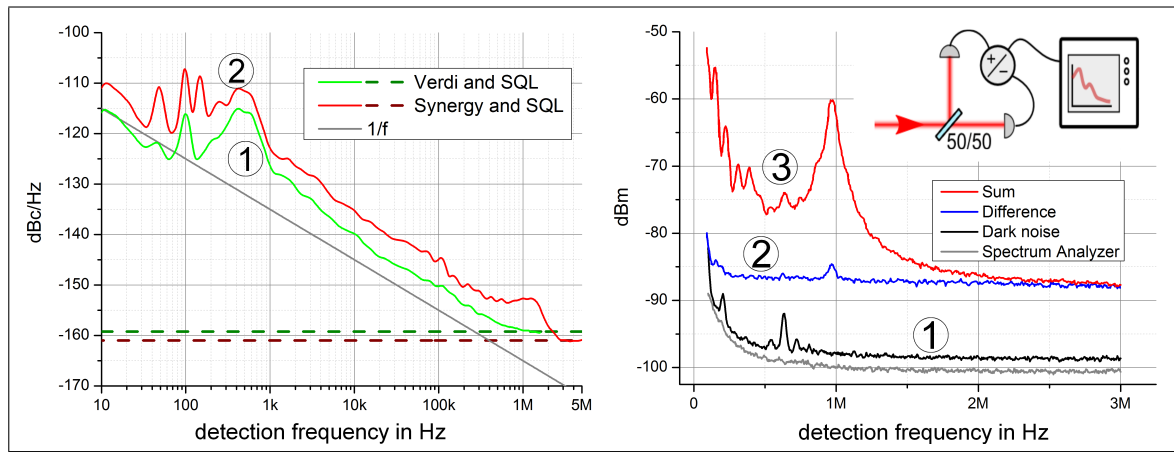


Figure 3.2: Intensity noise of the Ti:Sapph oscillator and its pump.

left: Broadband RF-analysis. Independently of mode-locked or CW-operation, the broadband $1/f$ RF-distribution of the Ti:Sapph intensity noise ② is originated by the pump laser ①. The data shown consist of two measurements in the RF domain: one with a spectrum analyzer close to the SQL using a linear frequency scale, a second covering 20 Hz to above 100 kHz with a network analyzer. Its log-scaling does not record the singular relaxation oscillation line of the Verdi at 100 kHz.

right: Close to the SQL. Typical intensity noise ③ close to the shot noise limit SQL ②, well above the measurement noise background ①. The significant RO-peak in the amplitude noise can be reduced by careful alignment of the laser. *Inset:* Balanced detection discriminates between shot noise (difference) and any classical amplitude noise (sum). At 1 mW detected optical power, the shot noise level is 10 dB above the electronic noise of the detector used here.

Figure 3.2, right, puts the focus on the shot noise limit. Independent of the alignment of the Ti:Sapph laser, the intensity noise reaches the shot noise level (SQL) at approximately 3 MHz for 5 mW of detected power. The relaxation-oscillation peak at 1 MHz is in contrast related to the strength of the Kerr-lens [92]. It can be reduced to below 2 dB above the continuous $1/f$ intensity noise distribution by optimizing the oscillator power and alignment.

The roll-off of intensity noise above the relaxation-oscillation (RO) frequency at 1 MHz can be explained by a simple rate equation model [39]. The competition of different longitudinal modes in the Coherent Verdi pump laser may also be an issue. Concerning all such effects, a detailed experimental and theoretical characterization has been done in [13] relative to the quantum limit. Their results are consistent with the data presented here. Note that the intensity noise properties have been observed to be independent to continuous wave or mode locked operation of the Ti:Sapph oscillator.

The pump laser intensity noise is close to the shot noise level at 1 MHz detection frequency. This region of detection frequencies and noise levels might appear to be of minor relevance in terms of quantum-limited intensity noise of the Ti:Sapph oscillator. However, the pump laser intensity noise is supposed to be a major driver of CEO-phase noise of the oscillator, see section 2.4.3. The only other "high frequency" noise source, spontaneous emission, adds only uncorrelated noise to the lines of the frequency comb.

In order to reduce intensity noise of the Verdi pump laser further down to the SQL, a passive filtering cavity can be suggested. This approach is studied in the appendix section A.1. It turns out to be not suitable. The Verdi laser is specified with a MHz linewidth. Filtering of amplitude noise with a passive cavity down to the SQL is not possible if significant phase noise is still present at the detection frequencies considered. Indeed, passive cavities convert phase noise to intensity noise.

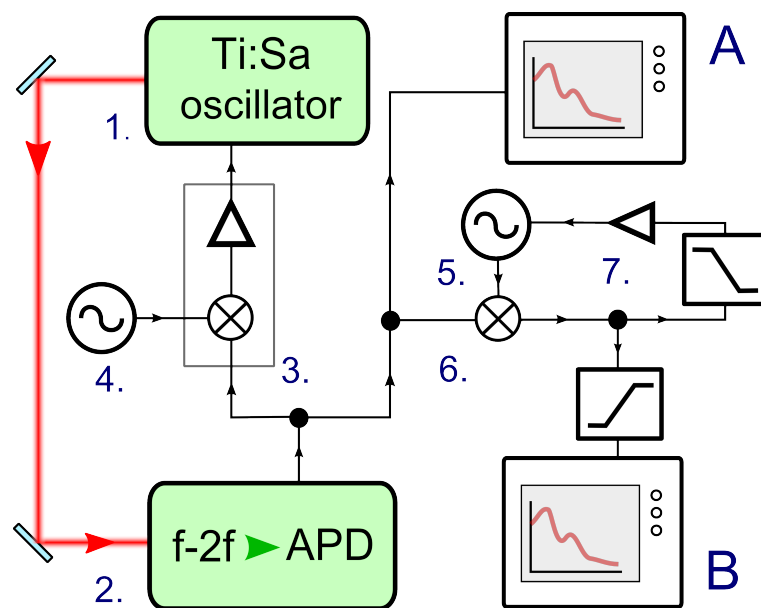


Figure 3.3: The measurement of CEO-phase noise. Principal lock and in-loop, out of lock bandwidth measurement.

Used components: 1. Ti:Sapph oscillator; 2. Menlo Systems f-2f interferometer, avalanche photodiode APD210; 3. Menlo Systems feedback loop - digital phase counter DXD 210/212, kHz bandwidth proportional-integrator-amplifier; 4. Agilent RF generator; 5. Rhode & Schwarz VCO/RF generator; 6. MiniCircuits analog phase detector (Mixer); 7. PI-amplifier of kHz bandwidth closing the phase-lock-loop PLL

Signal Analysis: **A** Spectrum analyzer: *Direct spectrum method* and *phase noise analysis tool MXA*, **B** Network/Spectrum analyzer: phase quadrature obtained from the PLL, signal 10 kHz high-passed.

3.1.2 CEO-Phase noise

It has been found in the theoretical considerations above, see Eq.(2.72), that the CEO-phase noise of a frequency comb is the limiting factor to a homodyne pulse-timing measurement. The sensitivity $\Delta u_{\min}(f)$ at a detection frequency f was obtained to be proportional to the CEO-phase SSB PSD $\Delta u_{\min}(f) \sim S_{\text{CEO}}(f)$. To evaluate this statement more precisely, the CEO-phase noise has to be quantified relative to its ultimate lower limit, the SQL.

This aim is different to the typical purpose of the literature: the characterization and reduction of the CEO-linewidth. Figure 3.3, gives a schematic of the entire experimental setup used here for phase noise characterization. In Fig. 3.4 the locked CEO-signal is detected and directly plotted. Although the carrier is of less than kHz bandwidth, noise side-bands are present up to 1 MHz detection frequency. These low levels do not contribute to the linewidth, but they turn out to be the limiting factor for the high sensitivity homodyne timing measurement.

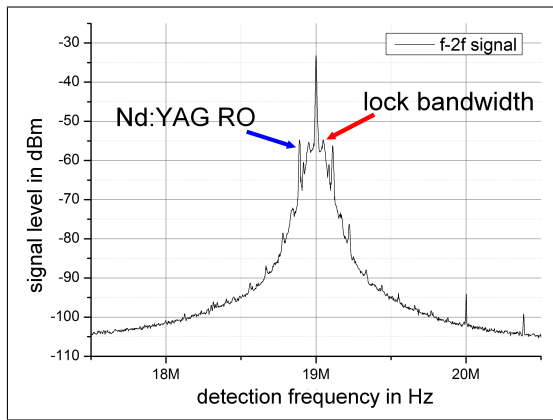


Figure 3.4: Typical data of the direct measurement of the CEO-frequency. Signal measured with 3 kHz resolution bandwidth (RBW). To provide comparison to other systems (data not shown): The signal to noise ratio is 60 dB at 100 kHz RBW, while seeding a polarization maintaining PCF with a pulse train of average power 500 mW and less than 30 fs pulse duration

Different phase noise measurement methods. Due to its complexity and required high sensitivity, the measurement of phase noise is an art itself. Several methods with different advantages and drawbacks are available. Three of them have been used to analyze the Ti:Sapph's CEO-phase noise and are described below.

Figure 3.3 shows the entire CEO-phase noise measurement setup containing all three approaches. All three are *in-loop* with the low-passed lock of the mean CEO frequency. The phase noise measurements themselves are nevertheless done far *out-of-bandwidth* of this feedback loop.

In order to lock the CEO carrier frequency, the signed signal of CEO-phase deviations is obtained from a $f-2f$ beating. A Menlo Systems digital phase comparator subsequently counts up to 12 bit phase difference, see Fig. 3.3 points 3. and 4. The proportional-integral-feedback-bandwidth is set to the lowest possible value of below 10 kHz. To this aim, the low-pass comparator output and an additional higher-order low pass filter are used. Corresponding to a π -phase shift in the low-pass PI-amplifier chain, the first oscillation of the CEO-lock occurs then at approximately 11 kHz. All CEO noise properties above this frequency will in consequence be considered to be such as of a *free-running* oscillator.

I. The direct measurement method \textcircled{A} . Being shown in the setup Fig. 3.3 \textcircled{A} it consists of: a *direct recording* of the electronic f_{CEO} signal and its noise side-bands. The assumption of negligible intensity noise allows then the interpretation of the signal as phase noise. It is reasonable considering the data Fig. 3.7 below. The data obtained has the advantage to be readily calibrated to the carrier power, so dBc-units. The phase noise SQL being available in units dBc with Eq.(2.35), the data can directly be related to the SQL. A typical measurement result is shown in Fig. 3.4. One distinguishes the 10 kHz CEO-lock bandwidth and a 100 kHz side-band arising from the relaxation-oscillations of the Verdi pump laser.

II. The Phase Lock Loop (PLL) method ② This method locks a second voltage controlled oscillator (VCO) to the phase quadrature of the already locked f_{CEO} . A MiniCircuits Phase Comparator ZRPD-1 and a loop of a below kHz bandwidth (Fig. 3.3, elements 5., 6., 7.) are used for this purpose. The high-passed signal of the calibrated mixer is subsequently analyzed with a spectrum- or network analyzer. This measurement provides the highest signal to noise ratio and an analysis of the CEO phase noise to up to 700 kHz side-band frequency. In order to simplify the measurement, it turned out that the phase-lock is even not necessary to detect sidebands at high detection frequency. The same noise distributions were obtained by just setting the oscillator element 5. in Fig. 3.3 to a frequency close to the CEO-carrier without any feedback. Within this method of highest sensitivity, the avalanche photodiode (APD) detecting the $f-2f$ -beating was observed to be subject to $1/f^2$ phase excess noise. It is nevertheless only present below -100 dBc and for detected power levels close to saturation at 1 mW. Being a function of the detected optical power, the measurement sensitivity for CEO phase noise is consequently limited by the phase distortion free dynamic range of the Menlo Systems APD210.

III. Spectrum analyzer built-in measurement ③ The phase-noise measurement tool available for spectrum analyzers Agilent MXA can be used for comparison. Having a rather high measurement noise floor, the practical use is to verify the calibrations for the CEO phase noise from the methods I. and II. above.

To summarize, a large number of measurement and calibration techniques are available to characterize phase noise of radio-frequency oscillators. In order to access lowest levels of phase noise, the main issue is typically a careful measurement calibration and a comparison of different measurements. This motivates the following measurement of a CEO-phase noise reference curve.

The CEO phase noise reference data. Figure 3.5 shows typical results of all three phase noise measurement types discussed above. Trace ① is of highest dynamic range and chosen to be the reference data for the further CEO-phase noise considerations in this thesis. It combines the direct-spectrum technique I with the PLL method II. The first calibrates the measurement and quantifies phase noise up to 100 kHz. The second is of highest sensitivity and is overlaid with the first in the region 50 kHz to 100 kHz. A direct calibration of II leads to values within the 3 dB overall error-bar.

The local maximum and the shape below 10 kHz is highly sensitive to changes of the CEO-lock parameters. The noise peak at 100 kHz arises from the relaxation oscillation (RO) of the Verdi pump laser (diode pumped Nd:YAG). The Kerr effect couples it to a modulation of the CEO frequency. The dashed shape of the trace ① below -120 dBc is due to phase excess noise from the APD.

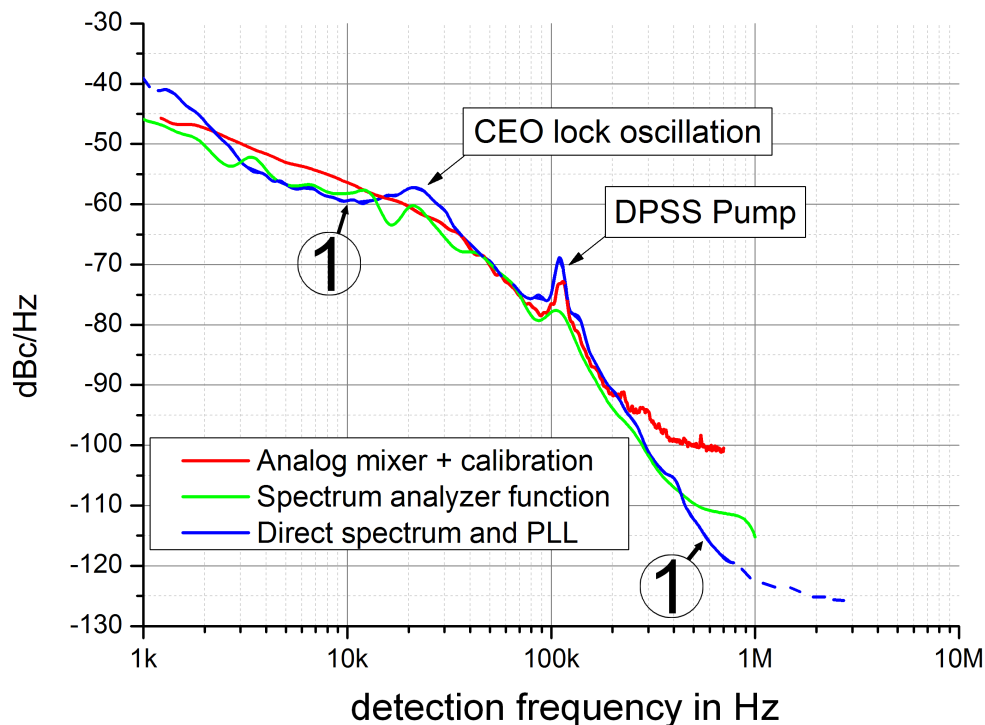


Figure 3.5: Principal reference curve of the CEO phase noise from independent measurements and with different methods. Trace ① is the principal reference data used in this thesis.

Ti:Sapph oscillator parameters: CEO carrier frequency 20 MHz, output power 1 W, optimized alignment to reduce relaxation oscillation amplitude noise peak at 1 MHz, photonic crystal fiber seed 500 mW. All signals smoothed using an FFT-filter. The estimated error bar is 3 dB for all traces.

Applied measurement methods:

green: Method III, measurement with spectrum analyzer software,

red: Method II, phase comparator measurement with 50Ω impedance, K_d approximately 50 mV/rad,

blue: using I, the direct recording of the CEO carrier and noise spectrum; in addition II, the phase comparator measurement with $1 M\Omega$ impedance, K_d approximately 20 V/rad,

To optimize the dynamic range, the signal on the APD has been attenuated until the intensity dependent $1/f^2$ phase modulation excess noise below -100 dBc vanished.

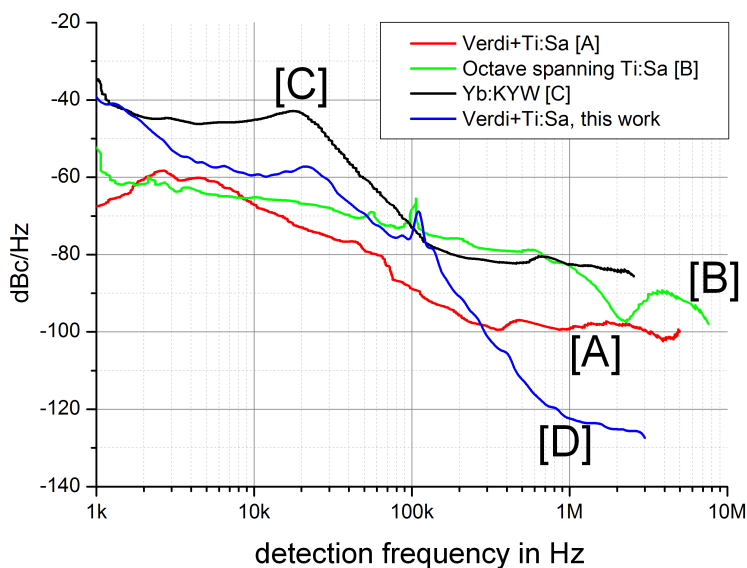


Figure 3.6: Comparison of the CEO noise reference data of this thesis (Fig.3.5) to non-fiber fs-oscillators. SSB CEO phase noise of a similar, Verdi pumped Ti:Sapph oscillator [A], an octave spanning Ti:Sapph oscillator [B], a direct diode pumped saturable absorber Yb:KYW system [C], the data of this thesis [D]

Comparison of the CEO-phase noise reference data to other fs-oscillators

Non-fiber oscillators. The CEO-noise reference trace Fig. 3.5 can be compared to other Ti:Sapph- and fs-oscillators, as shown in Fig. 3.6. The data obtained in this thesis [D] are compared to a similar Ti:Sapph oscillator pumped by a Verdi [A]¹, to an octave spanning Ti:Sapph oscillator pumped by a diode-pumped solid state laser source [B]² and to a fs-oscillator based on a saturable absorber Yb:KYW oscillator [C]³. All data were extracted from the cited publications and FFT-filtered for better visualization.

The data of this work has the lowest measurement noise floor and shows the most homogeneous shape over the covered RF-bandwidth. This confirms the quality of the measurement scheme used here.

In a first approximation, the CEO noise distributions of all oscillators show either a second or fourth-order decay. This is consistent with the theory of H.A.Haus, Eq.2.56. The slope predicted therein is essentially a function of the oscillator gain parameters. It arises from spontaneous emission in the gain medium and noise coupling processes. Fig.3.6 reveals that in comparison to the similar oscillators, it is the Synergy HP oscillator that shows the lowest level of CEO noise in the MHz region. The CEO can be expected to reach the SQL at lowest detection frequency. This oscillator is therefore one of the best on the market for experiments sensitive to CEO noise close to the SQL.

¹ Ti:Sapph, 20 fs, 105 MHz, 900 mW [27] ² Ti:Sapph, 570-1140 nm, 200 MHz, 270 mW [93]

³ Yb:KYW, centered at 1040 nm, 160 MHz, 260 mW [17]

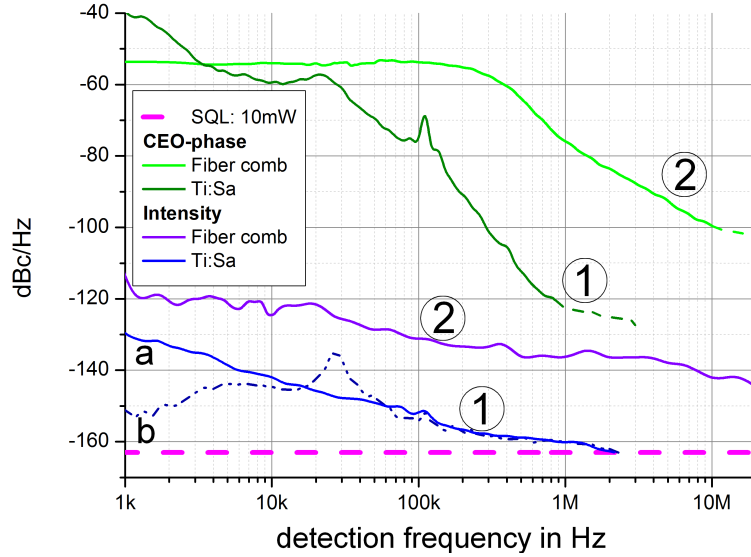


Figure 3.7: Comparison of the Ti:Sapph oscillator of this thesis ① to a Menlo Systems Fiber comb ②. Lower traces: intensity noise, above: phase noise. The fiber comb is of a linewidth of approximately 300 kHz. The intensity measurements for the Ti:Sapph were done with two different measurement configurations using a Network Analyzer and log-frequency scale: a first of the free running oscillator using DC-to MHz detector (a), a second of the CEO-locked oscillator using a 10 kHz high-pass detector (b). At 10 mW detected power, the noise of the fiber comb does not reach the SQL for any detection frequency.

For a larger comparison, the CEO noise of a chirped mirror Ti:Sapph oscillator has been compared to one using a prism pair in the literature [94]. Due to reduced beam steering effects, the results suggest an approximately 10 dB lower CEO noise when chirped mirrors are used.

Comparison to fibered oscillators. The Synergy Ti:Sapph oscillator can also be compared to a fiber oscillator, here the Menlo Systems fiber frequency comb. Fig. 3.7 shows intensity and phase noise relative to the SQL for 10 mW detected power. The mean-CEO frequency of the comb was locked using an f -2 f -interferometer. Nevertheless, a linewidth of approximately 300 kHz remained. This value is similar to a 200 kHz linewidth reported in the literature for an Er-fiber oscillator [95]. The CEO phase noise is defined only up to detection frequencies $f_{\text{rep}}/2 = 50$ MHz as it is sampled by the repetition rate. Although taking into account the second order decay out of the linewidth, the CEO phase noise never reaches the SQL until this limit. For all detection frequencies, the intensity noise of the fiber-comb is approximately 20 dB above the intensity noise of the Ti:Sapph oscillator.

In summary, the fiber based frequency comb studied here is not quantum-limited for any detection frequency. It is not suitable for quantum-limited measurements.

Conclusions on CEO-phase noise.

The CEO-phase noise of a commercial Ti:Sapph oscillator can be analyzed with readily available methods down to lowest levels of -120 dBc. The primary signal is obtained from an f - $2f$ beating after coherent broadening of the initial frequency comb (approx. 500 mW). The resulting beating signal is of less than 1 mW and has to be detected with an avalanche photodiode. It is finally the dynamic range of this detector that limits the measurement sensitivity.

Both intensity and phase noise of the Ti:Sapph oscillator reach the SQL purportedly below 10 MHz detection frequency. This is not the case for the fiber oscillator investigated here. The former is consequently not suitable for quantum-limited measurements. Section 4.4 shows that quantum limited fiber oscillators might nevertheless be technically feasible.

In order to overcome the limitations of the f - $2f$ detection scheme, a new measurement principle has been developed in this thesis. It is of quantum limited sensitivity to phase noise in optical frequency combs and presented in section 4.

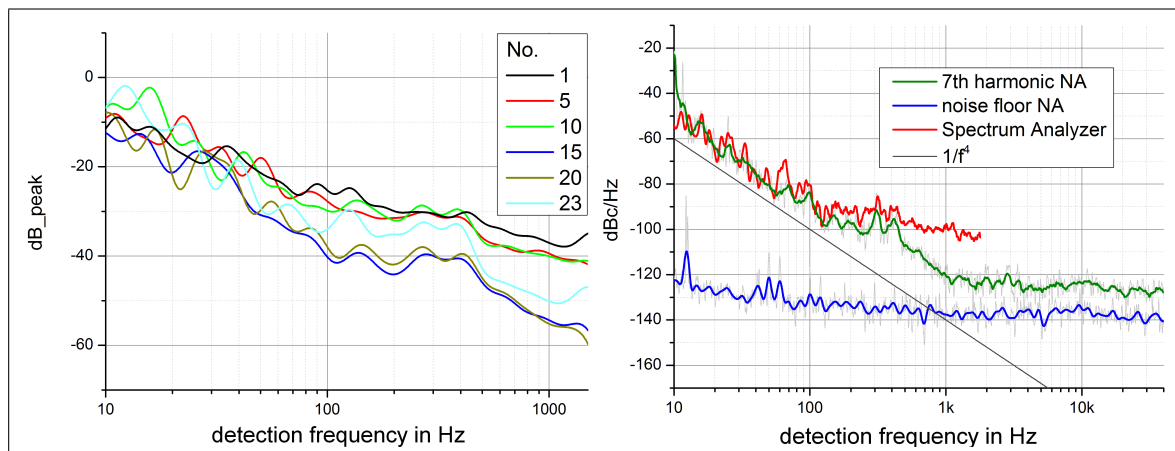


Figure 3.8: Repetition rate phase noise of the Ti:Sapph oscillator.

left: Side-band noise distribution for several harmonics of the repetition rate, obtained from a direct record of the photodiode signal with a spectrum analyzer, see [73]. In contrast to amplitude noise, phase noise side-bands should increase with the indicated harmonic number. Phase noise was not resolvable with this technique.

right: Phase noise of the 7th repetition-rate harmonic (1.090 GHz) obtained by homodyning the phase quadrature in a PLL configuration using a Rhode&Schwarz voltage-controlled oscillator.

3.1.3 Repetition-rate phase noise

Besides the CEO phase, a mode-locked fs-oscillator carries an additional phase/frequency property: the repetition rate. In the theory of H.A.Haus, Eq.(2.55), the fluctuations of the gain spectral response are the principal driving force for repetition rate fluctuations. They couple to the repetition rate by intracavity dispersion. Noise levels well below those of the CEO are expected for the repetition rate. Both originate from the phase fluctuations of the optical frequencies in the comb. Nevertheless, the former is directly associated to an optical carrier frequency, whereas the second is detected on the repetition rate (MHz) carrier.

A pulse train with a given repetition rate corresponds to an equally spaced Dirac-comb in the frequency domain. A detection of such a pulse train always also records the harmonics of the repetition rate. As it has been shown in Fig. 2.10, that phase noise side-bands of the repetition rate appear with higher amplitude at higher harmonics. Figure 3.8 shows the data of a measurement based on this approach. Nevertheless, in the case of the measurement presented here, the directly recorded side-bands do not systematically grow with the harmonic order. The method cannot be applied and the origin of the side-bands observed is cannot be repetition rate phase noise. Intensity noise of the Ti:Sapph oscillator or phase noise of the homodyning spectrum analyzer could be the origin of the signals shown.

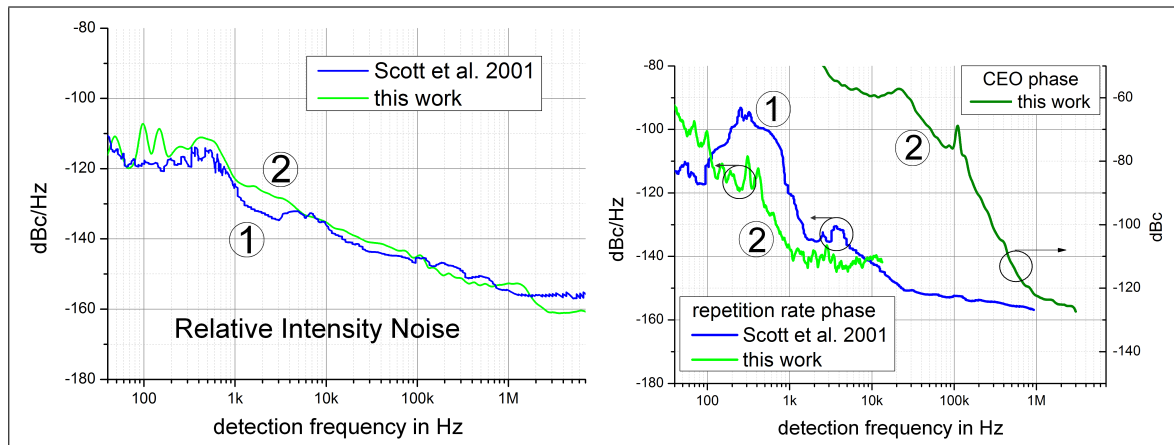


Figure 3.9: Comparison of the intensity- and repetition rate noise to a similar Ti:Sapph oscillator. Comparative data ① from [12]. The oscillator studied here ②. *left*: intensity noise, both oscillators pumped by laser diodes. *right*: repetition rate phase noise both scaled to 156 MHz, in addition *right scale* CEO phase noise recorded in this work; the dynamic range of the left *and* right scale is 100 dB, the right is 30 dB above the left

To eliminate intensity noise as a possible error source, the Ti:Sapph repetition rate signal phase noise has been characterized in a phase-lock-loop configuration. The recorded data are shown in Fig. 3.8, right. The 7th harmonic of the repetition rate has been chosen due to its best signal to noise ratio. The phase noise has been analyzed down to 10 Hz side-band frequency.

The repetition rate phase noise decays with fourth power of the detection frequency in the interval 10 Hz to 1 kHz. The deviations from this power law in the interval 500 Hz to 1 kHz can be attributed to mechanical resonances within the oscillator, see Fig. A.12. The noise level of detection is reached at -120 dBc. The theory of H.A.Haus, page 31, predicts a fourth order decay of the repetition-rate phase noise if spontaneous emission is the only noise driver. There is in consequence an indication for such a spontaneous emission limited repetition rate phase noise. A similar situation has been describe in the literature for a Ti:Sapph oscillator [42].

Comparison to the literature. It is in addition possible to relate the data observed here to the detailed analysis of Scott et al.[12]. For a Ti:Sapph oscillator similar to the one used here⁴, this reference compares different pump laser sources. It shows that the repetition rate noise above 10 kHz is strongly correlated to the intensity noise of the oscillator - and consequently the properties of the pump laser. In order to allow comparison, Fig. 3.9, left, shows that the oscillator studied here exhibits nearly the same intensity noise distribution as the one in [12].

⁴ KMLabs, average output power 750 mW, $f_{\text{rep}} = 80$ MHz

The oscillator considered in [12] is based on prism based dispersion compensation. Compared to the here used chirped mirror based oscillator a lower mechanical stability is consequently expected below 10 kHz. The comparison of the repetition rate phase noise of both oscillators is shown in Fig. 3.9, right. It confirms the argument of reduced stability for a prism based system below 1 kHz detection frequency. When approaching the measurement noise floor of -140 dBc both traces show similar values.

The intensity noise of both systems was measured to be comparable. It can consequently be assumed here that both systems show similar repetition rate noise at detection frequencies above 10 kHz. As such, the CEO-phase noise data of this thesis available above 10 kHz detection frequency can be compared to the repetition rate phase noise - using the data from [12].

Summary: Ti:Sapph repetition rate- and CEO-phase noise.

Figure 3.9, right, compares the repetition rate phase noise of both Ti:Sapph oscillators to the CEO phase noise reference data of this thesis. The latter is significantly above the repetition rate phase noise. The difference can be estimated to 70 dB at 100 kHz side-band frequency. Compared to the repetition rate, the CEO noise decreases with a much steeper slope.

Their respective impact on the phase noise of any individual line can be estimated by multiplying the repetition rate noise level with the longitudinal mode number $10^5 \dots 10^6$. Similar levels are obtained and it is not clear which comb property governs the phase noise of the individual lines of the comb. It will be a key result of this thesis to show that it is indeed the CEO-phase noise that is predominant, see section 4.5.1.

In addition, it is so far not clear how both will evolve close to the SQL. The theory of H.A.Haus describes the decay of both phase noises of a Ti:Sapph oscillator. It is predicted to be of the fourth power of the detection frequency, see Eq.(2.58) and Fig. 2.5. It is again section 4.5.1 that will present a new measurement method to analyze both phase noises close to the SQL.

3.1.4 Estimation of the free running linewidth

The considerations above concern the low level side-bands of the CEO-frequency and the repetition-rate. In order to provide rapid comparison to other oscillators and domains of laser metrology, it is always instructive to estimate the free running linewidth of the oscillator.

The average levels and slopes of the CEO and repetition rate phase noise can be compared using Fig. 3.9, right. In order to provide a comparison at a same carrier frequency, 50 to 60 dB have to be added to the repetition rate phase noise. Similar noise levels are reached. Anticipating the results of section 4.5.1, Fig. 4.37, right, it is finally the CEO-phase noise that dominates the phase noise of the entire frequency comb and all individual lines. It is consequently sufficient to consider this comb property when estimating the average optical linewidth.

First approach. The simplest measure of the linewidth of an electronically available signal is depicted in Fig. 3.10. It consists in an application of the *band-power* function of spectrum analyzers. Due to slow drifts of the absolute value of the CEO carrier frequency, this method is in practice not easy to apply to a free running Ti:Sapph oscillator. However, the linewidth can still be estimated with the following approach, considering the sensitivity of the CEO-frequency to oscillator power fluctuations.

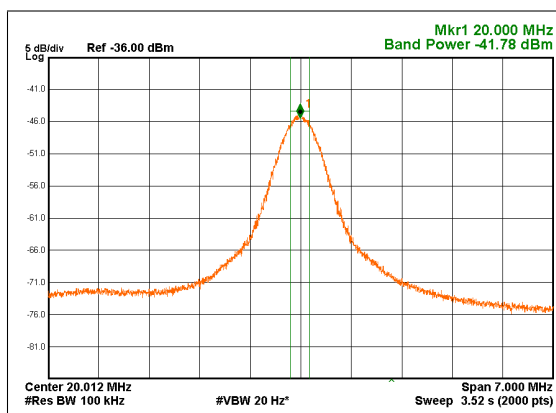


Figure 3.10: The simplest measurement of the linewidth of a free-running RF-oscillator. It uses the *band power* function of a spectrum analyzer. Here the CEO-frequency of a Menlo Systems Fiber comb is analyzed. After the measurement of the power in the entire signal, the measurement bandwidth is decreased until the 3dB decay of the band power. The resulting bandwidth is an estimate of the oscillator CEO-signal linewidth.

Second approach. Besides spontaneous emission, the principal noise driver of the Ti:Sapph oscillator are fluctuations of the pump/output-power. A slow, step-function modulation can be applied to the pump power while recording f_{CEO} and f_{rep} . Modulation timescales of approximately hundred milliseconds are sufficient to provide for thermal equilibrium under small pump power modulations. Using different modulation depths, one obtains at 0.3 Hz modulation frequency and 1 W output power P_{out} :

$$\frac{df_{\text{CEO}}}{dP_{\text{out}}} = 0.25 \text{ MHz/mW}, \quad \frac{df_{\text{rep}}}{dP_{\text{out}}} = 0.16 \text{ Hz/mW} \quad (3.1)$$

The low frequency deviations of the repetition-rate were recorded using the 10th harmonic of the signal. It was demodulated with a GHz carrier in order to measure the resulting kHz frequency shift with an oscilloscope. With regard to the measured values Eq.(3.1), the CEO-frequency is significantly more sensitive to pump power/gain fluctuations than the repetition-rate. The values obtained here will be of further use in the fix-point formalism, section 4.2.

At an output power of 1 W, 0.12% peak-peak and 0.014% r.m.s. output power fluctuations have been recorded for the Ti:Sapph oscillator. These values imply the following linewidths of in the limit of mHz detection frequencies.

$$\boxed{\Delta f_{\text{CEO}} \sim 33 \text{ kHz} \quad \Delta f_{\text{rep}} \sim 20 \text{ mHz}}. \quad (3.2)$$

The dependence of these coefficients on the modulation frequency is analyzed in the following section. Additional mechanical fluctuations will in practice lead to a larger Δf_{rep} . An active pump power stabilization system with only 20 kHz bandwidth can significantly reduce the linewidth of the CEO-frequency.

Summary. The phase noise of an average comb-line arises from both CEO-phase noise and repetition rate phase noise. The latter contributes times the mode-number n to the phase noise of the line $\omega_n = \omega_{\text{CEO}} + n\omega_{\text{rep}}$. The mode-number of the comb central frequency is approximately $2,5 \cdot 10^6$, leading to a linewidth estimation of 50 kHz. Independent to the comb property that governs the phase noise of the individual lines, their free-running linewidth can be estimated to 50 kHz for the Ti:Sapph oscillator considered here.

3.1.5 Noise transfer functions

The sections above studied the fluctuations of the free running Ti:Sapph oscillator: its *intensity*, the *CEO phase* and the *repetition rate phase*. Another way to characterize the oscillator noise is to study its noise transfer functions $H(f)$. They are the ratio of the change of oscillator output intensity and phases of CEO frequency and repetition rate, over the modulation amplitude of the pump power. Their knowledge permits an experimental evaluation of noise origins and possible ways to reduce them.

The measurement setup. The modulating driver is chosen to be the oscillator pump power: its fluctuations drive all oscillator noise properties. Small modulations can be easily addressed using an acousto-optical modulator, see Fig. 3.11. All properties of the stable free running oscillator change linearly with the perturbation. A sweep of the modulation frequency f leads to the transfer function $H^Y(f)$ for any oscillator property Y . Fig. 3.11 shows the measurement setup. The absolute value of the transfer functions is recorded with an Agilent E5061B network analyzer.

Intensity transfer function. The transfer properties of a Ti:Sapph oscillator in terms of intensity modulations have been extensively studied by [96]. The behavior measured here is similar to their results: According to Fig. 3.12, the Ti:Sapph oscillator is with less than 10 dB a weak amplifier for intensity modulations. This holds up to the relaxation-oscillation (RO) frequency at 1 MHz. Above, the transfer function drops rapidly. This effect is consistent with the rate equation based laser amplitude noise model of [97, 39, 13]. A tuning of the RO-frequency will turn out to be suitable tool to reduce oscillator noise close to the SQL.

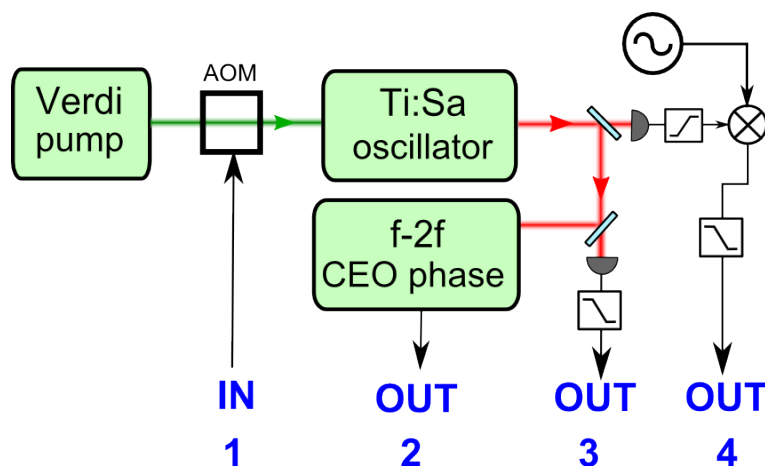


Figure 3.11: Measurement of the (noise) transfer functions of the Ti:Sapph oscillator. Characterized are the CEO-phase (1 \rightarrow 2), the output intensity (1 \rightarrow 3) and the repetition rate phase (1 \rightarrow 4). The numbers from this scheme are used again in Figure 3.12 that shows the measurement results.

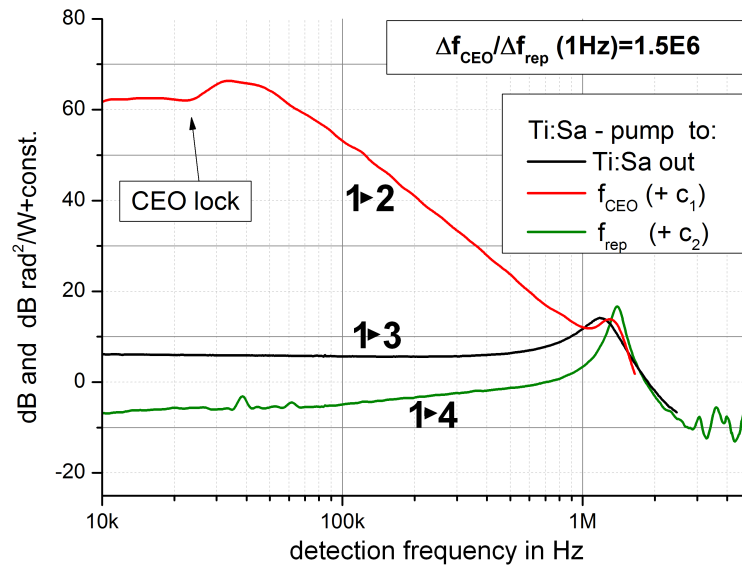


Figure 3.12: Measurement of the noise transfer functions. Intensity (1 → 3), CEO-phase (1 → 2) and the repetition rate phase (1 → 4). The intensity transfer function is the only calibrated curve of the three. The others are plotted with an arbitrary constant chosen for visualization. At a 1 Hz modulation of the pump power, the ratio of the CEO-frequency (20 MHz) modulation over the repetition-rate (156 MHz) modulation is approximately $1.5 \cdot 10^6$.

Note: The bandwidth of the transfer function measurements is limited by the 1 MHz bandwidth of the driving AOM. Its transfer function (not shown) drops to -100 dB/dec at 1.2 MHz and has been removed from all curves.

Repetition-rate phase: The transfer function *pump to repetition rate phase* (1 → 4), Fig. 3.12, increases slightly by approximately 0.5 dB/dec over two decades of RF frequency up to 1 MHz. This behavior is in contrast to those of the output intensity and the CEO-phase. Fluctuations of the repetition rate are equivalent to a less "rigid" lock of the relative phase of the comb lines. The observed slope is consistent with the findings of Paschotta et al.[19]. For detection frequencies above 100 kHz a decreasing strength of the relative phase lock between the individual frequencies is predicted.

CEO-Phase: The slope of the transfer function *pump to CEO phase* is determined by the properties of the active CEO-phase lock. It's action is visible up to 50 kHz. Above, the CEO-phase transfer function follows a fourth order decay up to the RO-frequency at 1.05 MHz. For higher detection frequencies it drops off even more rapidly.

The theory of Haus Eq.(2.56) predicts a second order decay if spontaneous emission (white intensity noise) is the major driving force. It predicts a fourth order decay if spontaneous emission driven spectral fluctuations of the center frequency drive the CEO-phase noise. The transfer functions are recorded using a white spectral density of modulation. As such, the observed effects are equivalent to those of spontaneous emission. In consequence, the coupling process and indirectly spontaneous emission are identified to be the mayor contributors CEO-phase noise.

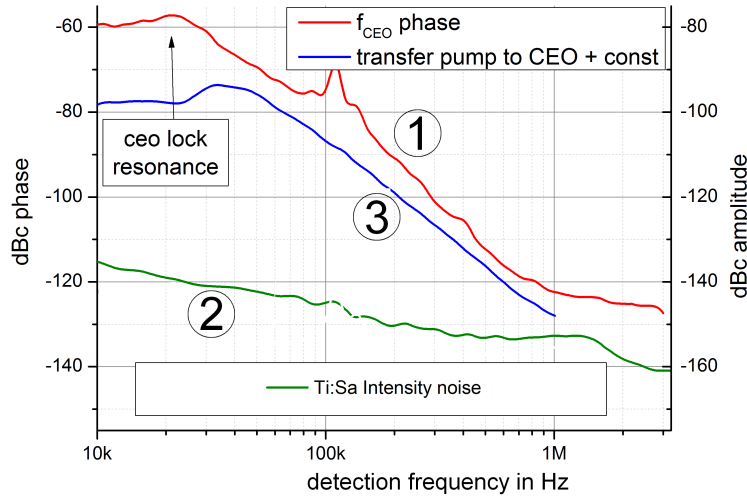


Figure 3.13: The free running CEO-phase noise ① and the intensity noise ② compared to the pump to CEO transfer function ③. The CEO-phase noise is similar to the transfer function, indicating that its driver is a white noise process. The additional CEO-phase noise arises most likely from intensity noise.

Comparison of free-running oscillator noise to transfer functions. Figure 3.13 compares the CEO-phase transfer function ① to the CEO-phase noise of the free running oscillator ③ and its output intensity noise ②. The free running CEO phase noise is nearly of the same slope as the transfer function. Above 100 kHz the ratio follows approximately the same distribution as the intensity noise of the Synergy. The measurement of a transfer function is equivalent to an excitation of the system with white noise. The CEO-phase noise of the free-running oscillator arises consequently mostly from couplings to other oscillator parameters that are themselves driven by spontaneous emission. The influence of the pump laser intensity noise is small compared to these couplings.

General slope of the transfer functions above 1 MHz. All transfer functions decrease significantly above the relaxation-oscillation (RO) frequency at approximately 1 MHz. In order to obtain quantum-limited properties at lowest possible RF-frequencies, one would have to set the RO-frequency of the concerned oscillator to the lowest possible values. The RO-frequency is given for resonator losses l , an intracavity power P_{int} , a round-trip time T_R and a saturation pulse energy⁵ E_{sat} by [98]:

$$f_{\text{ro}} \approx \frac{1}{2\pi} \sqrt{\frac{lP_{\text{int}}}{T_R E_{\text{sat}}}} \quad (3.3)$$

⁵ The saturation energy E_{sat} of a laser gain medium is the pulse energy of a short signal pulse which leads to a reduction in the gain to $1/e$ of its initial value. It is this parameter that contains the gain-properties in the formula for the RO-frequency.

An optimization of the oscillator properties in order to obtain a low f_{ro} is consequently possible. The simplest approach would be to reduce the oscillator repetition rate to obtain quantum-limited noise properties at lowest possible RF-frequencies.

3.1.6 Summary of the noise properties of the Ti:Sapph oscillator

The intensity noise of the Ti:Sapph oscillator is principally driven by the intensity noise of the pump laser. The same holds for the CEO-phase noise, but spontaneous emission and couplings from other noise sources contribute significantly. The repetition rate phase appears to be significantly less sensitive to pump power fluctuations than the CEO-phase. Nevertheless, if the point of view is the phase noise of the individual comb lines, this property can so far only be attributed to the significantly lower carrier frequency (radio frequency instead of an optical carrier).

The fluctuations of both repetition rate and CEO frequency contribute both to the width of the individual lines of the frequency comb. It is section 4.5.1 that analyzes the phase noise of individual comb lines and distinguishes the contribution of repetition-rate and CEO fluctuations.

The oscillator noise is expected to be quantum-limited below timescales of approximately 0.2 microseconds, both in intensity and phase. The frequency at which the oscillator is quantum-limited is principally set by the relaxation oscillation of the oscillator. All oscillator noise decreases rapidly above this frequency.

3.2 Design of a passive broadband cavity

The previous section studied noise properties of a femtosecond Ti:Sapph oscillator relative to the standard quantum limit SQL. Phase noise properties above the SQL limit the precision of the timing measurement scheme introduced in section 2.5. To filter such noise, a passive cavity has been studied theoretically in section 2.7. From this point of view, it turned out to be a valuable tool to filter and even to analyze noise in optical frequency combs.

The first suggestion to apply a passive cavity to optical combs is [99]. It mentions the possibility to analyze the spectral phase noise of a comb. A cavity assisted measurement of underlying low level, outer side-bands of phase noise has been studied for a CW laser by [100]. Therein a Pound-Drever-Hall setup was used reflection. White Shawlow-Townes limited frequency noise turned out to be detectable down to -100 dBc from only 100 μ W optical carrier signal.

This chapter describes practical issues of the experimental implementation of such a broadband cavity for a frequency comb. First of all, it has to be shown that a passive, high finesse cavity can be simultaneously resonant on a sufficiently large optical spectrum.

In order to lock such a cavity to a frequency comb, error signals for both f_{rep} and f_{CEO} can be obtained using spectral selective detection of a cavity reflection [101, 34, 81].

3.2.1 Technical design of the cavity

A schematic of the passive broadband cavity is shown in Fig.3.14. The cavity consists of two output couplers of reflectivity $R = 99.82\%$, two convex spherical high reflectivity (HR) mirrors of radius of curvature ROC -2000 mm and two plane HR mirrors, one of which is mounted on a piezo element. The pressure of the laboratory air environment of the cavity can be tuned down to 0.5 mbar.

The matching of the transverse mode of the seed beam is done by a telescope of 3 spherical mirrors (ROC -2000, -1000, +500 mm). Compared to the use of lenses, this approach does not add dispersion. Resulting chirp of the femtosecond pulses could hinder subsequent future experiments.

Locking the cavity to the seeding frequency comb. Locking is achieved using a Pound-Drever-Hall (PDH) scheme in reflection. Other schemes like Hänsch-Couillaud or Tilt-lock are more sensitive to low frequency fluctuations of the laboratory environment. Two approaches can be used to obtain a phase modulation on a beam injected into the cavity - without adding dispersion through an eventual EOM:

As one possibility, one of the mode-matching mirrors is placed on a piezo electrical element. Driven at a mechanical resonance above 500 kHz, this approach can provide a modulation depth sufficient for a lock of the cavity.

As a second possibility, a part of the seed beam is transmitted by an electro-optical modulator EOM and injected in counter-propagation into the cavity. The non-resonant EOM is used at a frequency of 1.6 MHz. The concerned beam part will be called the *reference beam*. The Ti:Sapph oscillator being of a coherence length of larger than 10^5 m, it would theoretically be possible to lock the cavity even with a reference beam undergoing a delay up to this value. This technique is advantageous as it does not perturb the signal transmitted by the cavity neither by a phase modulation nor by dispersion.

The performances of both approaches are compared in detail in Fig. 3.19.

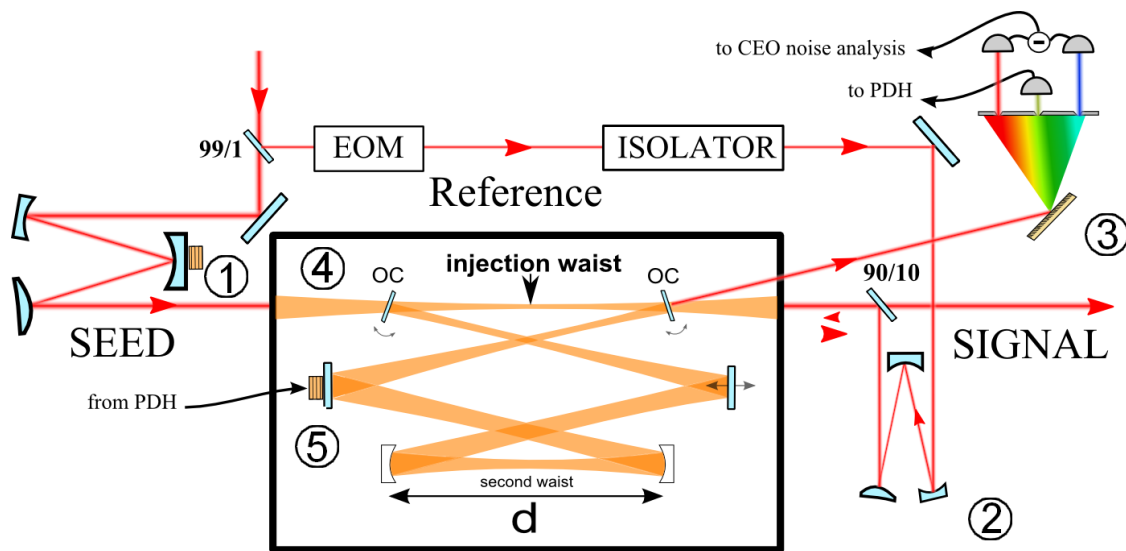


Figure 3.14: Implementation of the broadband cavity used in this thesis. The setup consists of: mode matching of the bright seed ① and the reference beam for PDH lock in reflection ②, the reflected reference is detected spectral resolved to obtain error signals for the PDH lock and CEO phase noise ③, the cavity itself in a vacuum chamber ④ consists of two output couplers, two spherical mirrors and two mirrors of variable position ⑤ - one on a micro-translation and one on a piezo element

3.2.2 Geometric properties

The optical path of the cavity Fig.3.14 can be simulated using a Gaussian beam propagation. For a given distance d of the spherical mirrors, the injection waist is determined by their radius of curvature (ROC). The general dependence is shown in Fig.3.15, left. For an experimentally convenient, symmetric setup as shown in Fig.3.14, the distance d is set to 300 mm. Within the interval of theoretically possible ROCs, spherical mirrors of ROC -2000 mm are readily available from suppliers. From the simulations Fig. 3.15, an injection waist of approximately 0,35 mm is expected. No singularity is observed for small deviations from these parameters. These two values are consequently chosen for the setup.

The stability of this choice against variations of the beam parameters can be verified using the round-trip propagation matrix M , see Eq.(2.97): With $\text{Tr}|M| < 2$ this criterion is satisfied, see Fig. 3.15, right. The astigmatism of the cavity due to the non vanishing angles of optical incidence (AOI) has also to be quantified. Any AOI θ leads to an apparent ROC $R' = R/\cos\theta$. For a realistic transverse beam distance of 20 mm at the spherical/piezo mounted mirror, the relative change of the horizontal waist relative to the vertical is neglectable ($<0.05\%$).

In addition, the following criterion has to be verified below: The Gouy-phase shift of a TEM_{nm} mode is a function of $k = n + m$, see Eq.(2.99) and [89]. From this fact, a cavity may be degenerate for several transverse modes if the difference in Gouy-phase mod 2π is very small. The cavity discussed here is non-degenerate.

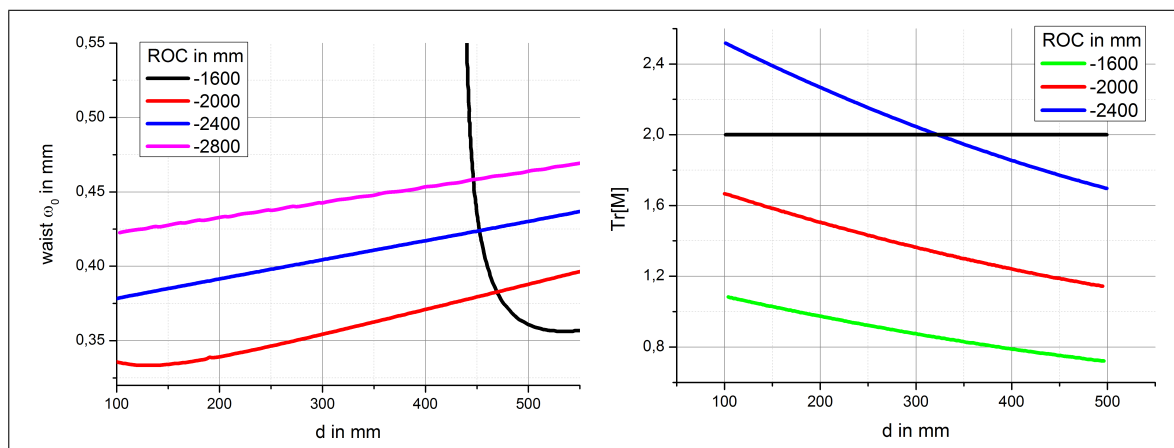


Figure 3.15: Numerical simulation of suitable cavity parameters.

left: Simulation of the injection beam waist as function of the distance d and the ROC of the spherical mirrors. The selected parameters are $d=300$ mm, $\text{ROC}=-2000$ mm. The only interest to plot the second waist would be to calculate peak intensities within the analysis of intensity related effects. The second waist is always larger than the injection one and no additional information would be obtained.

right: The cavity stability criterion is fulfilled for the chosen parameters and within possible deviations.

3.2.3 Conditions for broadband simultaneous resonance

It turns out that intracavity dispersion is the limiting factor when broadband simultaneous resonance of a high finesse cavity is desired. The following subsection studies this limitation in detail for the cavity presented here.

The optical path in a cavity is about the same for a single frequency beam or a frequency comb. However, the spectral transmission of a broadband cavity locked at a given wavelength is governed by the spectral phase $\phi(\omega)$, see Eq.(2.98). For a cavity of finesse F the spectral transmission $T(\omega)$ is approximately

$$T(\omega) \simeq 1 - F^2 \phi(\omega)^2 / \pi^2. \quad (3.4)$$

A linear phase $\phi(\omega)$ leads only to a change of the optical length of the cavity and can be compensated by piezo or fine-mechanic elements. The possible bandwidth of simultaneous resonance is limited by the higher order terms, the dispersion.

In Fig. 3.16, the main dispersion properties of two types of mirrors and laboratory air are shown. According to these characteristics, there are in principle two ways to achieve a cavity with zero dispersion over a largest possible bandwidth:

1. Chirped mirrors. One is to use standard broadband mirrors and at least one with negative dispersion. The residual negative dispersion of the cavity is subsequently compensated by tuning the pressure of a lab-air environment. The GVD of air is approximately $-21\text{fs}^2/\text{bar} \cdot \text{m}$, [102]. This technique has nevertheless the disadvantage that chirped mirrors always exhibit a residual dispersion modulation - or significant higher order dispersion. The amplitude depends on all parameters of the mirror design (materials, bandwidth, mean dispersion). It turns out that for the expected finesse of larger than 1200, this variation would limit the optical transmission bandwidth of the cavity to approximately 25 nm.

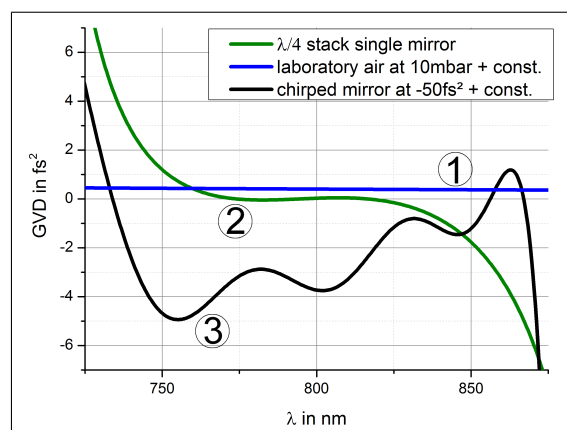


Figure 3.16: Dispersion of cavity elements. ① laboratory air, ② a $\lambda/4$ stack mirror and ③ a chirped mirror. It is the cavity dispersion that limits the simultaneously resonant optical bandwidth.

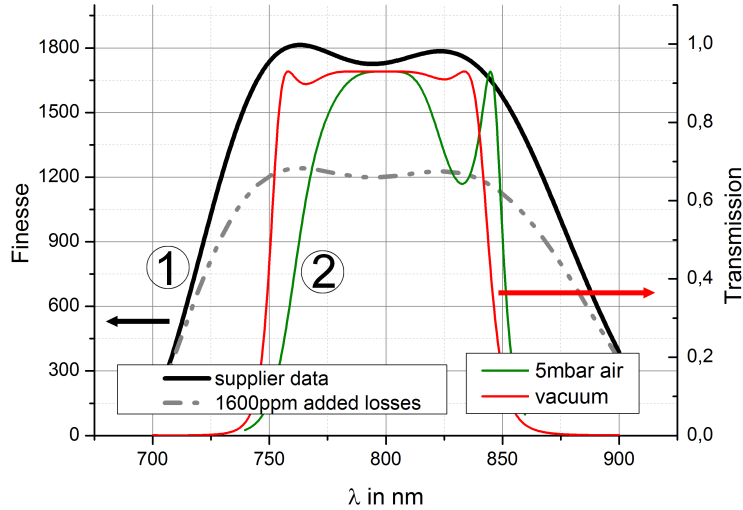


Figure 3.17: Influence of the mirror properties on the expected broadband cavity resonance.

The limited mirror bandwidth leads to a spectral variation of the finesse ①. The average finesse (measured in next section) is obtained by adding 1600 ppm losses per round-trip.

The calculated transmission of the cavity ②: From the calculated mirror dispersion properties, a transmission of 90 nm FWHM is obtained under vacuum below 1 mbar. Some mbar of lab-air environment reduce the bandwidth and modify the shape of transmission.

2. Zero dispersion mirrors and air pressure tuning. An alternative to fine-tune dispersion is the use of $\lambda/4$ -stack mirrors [103]. They consist of cost-efficient, alternating layers of high and low index of refraction dielectric material. Their reflectivity increases rapidly with the number of layers. For the fused silica ($n=1.45$) and niobium oxide ($n=1.9$) used here, 20 layer-pairs lead already to a reflectivity of $R=1-20$ ppm. Within a given bandwidth, such mirrors also provide lowest broadband dispersion. Using such mirrors the slight residual dispersion could be compensated by air pressure. This is the approach used here and Figure 3.17 shows the expected results. With calculated values of $|GVD| \leq 0.5 \text{ fs}^2$ up to over 90 nm bandwidth are expected.

Upper bounds for the GVD. The maximal dispersion providing still broadband resonance can be estimated using a Taylor approach for the spectral phase and Eq.2.98. For a given finesse F and a spectral bandwidth of $2\Delta\omega$, a 50% decay of the transmission in the wings of the spectrum sets the maximum mean GVD to

$$T(\omega_0 + \Delta\omega) \geq \frac{1}{2}T(\omega_0) \rightarrow \phi'' \leq \frac{2\pi}{F(\Delta\omega)^2} \quad (3.5)$$

For a finesse of 1400, a transmitted spectrum of 100 nm FWHM centered at 800 nm, one obtains a GVD below 0.2 fs^2 , for 40 nm FWHM a GVD below 1.2 fs^2 . For a more detailed analysis, a numerical integration of the GVD has to be done.

The configuration used here. The spectrum of the Ti:Sapph oscillator used here is centered at approximately 800 nm. Including even the spectral wings of lowest intensity below 1% peak intensity, its spectrum covers 100 nm. Nearly the entirety of this spectrum is covered by the low dispersion properties of the $\lambda/4$ -stack mirrors (centered at 800 nm). A simulation of the broadband resonance of a six $\lambda/4$ stack mirror cavity (geometry as shown in Fig. 3.14), assuming four mirrors of 30 ppm transmission and two output couplers of 1800 ppm transmission is shown in Fig. 3.17.

The variation of the cavity transmission due to varying reflection coefficients/finesse is neglectable over the covered bandwidth of 100 nm. The measured transmission values, which will be presented in detail in the next section, are only obtained by adding 1600 ppm of losses per round-trip. They may arise from e.g. impurities of the mirror surfaces or mirror roughness (scattering). These losses are at the order of magnitude of the output couplers, and a transmission of significantly more than 50% can consequently not be expected. The shown simulations of the spectral transmission do not take into account these losses. Nevertheless, they show that an up to 90 nm broad transmission is possible for a cavity set up under vacuum. A laboratory air environment of several mbar is supposed to slightly change the spectral shape of transmission.

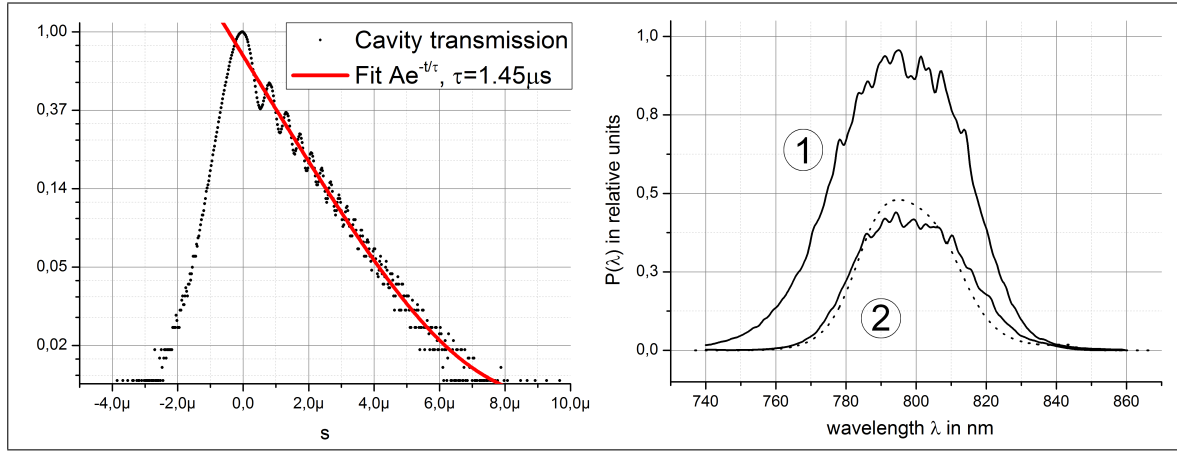


Figure 3.18: Unlocked/locked cavity transmission properties. *left:* unlocked cavity-ringdown permits the determination of the finesse. *right:* Broadband resonance at lock: seed spectrum ①, transmitted spectrum ② at $p=68$ mbar and calculated transmission at $p=30$ mbar (dotted).

3.2.4 Measured finesse and broadband transmission.

The finesse F of the cavity is another principal characterization parameter and has been introduced in Eq.(2.92). It can be determined from the cavity linewidth $\Delta\omega$ relative to the free spectral range (FSR) Ω_{FSR} : $F = \Omega_{\text{FSR}}/\Delta\omega$. Using this method a finesse of 1250 is measured for the setup presented here.

Another method to determine the finesse consists in measuring the ring-down time of the cavity after a sufficiently fast sweep over a resonance. With a round-trip reflectivity R and a round-trip time T_R one obtains for at a short time t after the resonance [104, 105]:

$$I_{\text{cav}}(t + n \cdot T_R) = I_{\text{cav}}(t) \cdot R^n = I_{\text{cav}}(t) \cdot \exp\left(-\frac{nT_R}{\tau}\right) \quad (3.6)$$

$$R = \exp\left(-\frac{T_R}{\tau}\right) = \exp\left(-\frac{2\pi}{F}\right) \quad (3.7)$$

The finesse is consequently measurable using the cavity decay time. A value of 1425 is obtained from the data. A typical trace is shown in Fig. 3.18, left. To avoid eventual effects of dispersion that would increase the apparent linewidth or decay time, a 1.5 nm FWHM interference filter was used for these two measurements. Although being different within a 15% error, the two measurements indicate a real finesse of the cavity below the theoretical values. Ring-down measurements are typically more reliable as they are independent to the linearity of sweep and include a high number of measurement points. With a finesse of 1425, the cutoff frequency of this cavity is 110 kHz.

The rapid oscillations of the signal shown in Fig. 3.18 are due to an interference effect of the light stored in the cavity and the seed. The former undergoes a Doppler-shift due to the speed of the piezo mounted mirror while sweeping the cavity. The resulting frequency difference leads to the observed beating [105, 106].

Broadband simultaneous resonance. A typical broadband resonance of the cavity is shown in Fig. 3.18. A transmission of 35 nm FWHM and more than 60 nm including the spectral wings is obtained. To underline the dependence on the applied air pressure, a the plotted simulation considers a slightly different one. This result demonstrates that the concept of a broadband passive, high finesse cavity is in principle applicable to a frequency comb.

3.2.5 Properties of the PDH-Lock

The cavity is locked to the Ti:Sapph oscillator with a Pound-Drever-Hall (PDH) scheme [78]. The experimental scheme is illustrated in Fig. 3.14. A counter-propagating reference beam is phase modulated at 1.6 MHz. When reflected by the cavity, an interference amplitude signal is obtained. The error signal is generated by subsequent demodulation. The PDH approach is applicable to a frequency comb: a phase modulation of the entire comb is equivalent to a phase modulation of each individual line. The detected error signal is consequently the sum of the detected beating signals from all individual lines. As the cavity may have spectrally inhomogeneous properties, the optical PDH-signal is detected spectrally resolved with nm bandwidth. The wavelength of detection will subsequently be called the lock-point and is typically set to 800 nm, the central wavelength of the comb.

Piezo versus EOM modulation. The phase modulation necessary for a PDH-scheme can be obtained by using a higher order mechanical resonance of a piezo element on which a mirror is mounted. A reflected light beam will be modulated in phase. Another method is to apply an EOM on a reference beam that counter-propagates through the cavity. Both methods do not to add significant amounts of dispersion on the seed beam. This is an important aspect. Best timing precision for the homodyne timing measurement scheme is only obtained for transform limited pulses and dispersion would temporally spread the seed pulses.

Both modulation techniques can be compared based on the properties of error signals of the same amplitude, see Fig. 3.19, left. Both signals were low pass filtered. The low modulation depth of the piezo-based signal requires nevertheless important amplification to obtain the same signal levels.

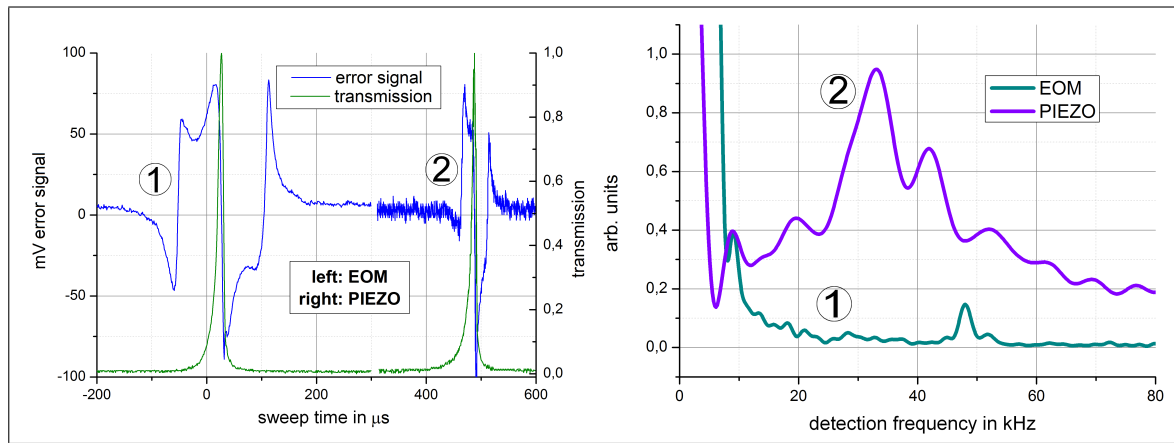


Figure 3.19: Comparison of two techniques for the generation of Pound-Drever-Hall phase modulation side-bands. The resonance of ① an electro optical modulator EOM and ② of a zero degree AOI piezo mounted mirror are used.

left: PDH error signals when sweeping the cavity. *right:* Cavity transmission intensity excess noise recorded with a 20 kHz low-pass filter. Curves obtained from the FFT of an oscilloscope record under lock conditions minimizing rms noise. Both traces are normalized to the peak at below 10 kHz that is the mechanical resonance of the intracavity piezo-mirror. This cavity property is independent to the electronic lock (typical bandwidth of below 5 kHz).

As shown in Fig. 3.19, left, at the same amount of error signal, the signal to noise ratio of the EOM based method is significantly better. When the cavity is locked using those signals, the transmitted intensity exhibits significant excess noise in the band kHz to 100 kHz, see Fig. 3.19, right. The EOM based modulation of a counter-propagating reference beam (see Fig. 3.14) is in conclusion the method of choice in order to obtain lowest possible kHz excess-noise in transmission.

The PDH-feedback bandwidth. The error signal of such a lock is shown in Fig. 3.20, left. The bandwidth of the error signal and PI-gain of approximately 10 kHz is larger than the bandwidth of the piezo mounted mirror below 4 kHz (first observed resonance). It leads to excess noise due to phase mismatch between error and feedback. The bandwidth of this feedback signal is principally limited by the mechanical resonance properties of the mirror-piezo-mount assembly. Methods to reduce these resonances have been discussed in the literature [107]. Their application is not necessary here, the implemented cavity shows low 0.5% r.m.s. intensity noise in transmission at a lock.

The remaining error signal at lock, Fig. 3.20, left, between 100 Hz and 10 kHz, can be attributed to mechanical fluctuations in the kHz range. They are not completely compensated by the feedback-loop. The gain has to be sufficiently low at the first resonances of the loop, situated in the kHz range. Outside the bandwidth of PDH-lock of the cavity, but within the bandwidth of error signal generation, the PDH error signal still provides information on the phase noise of the concerned beam [100]. Such

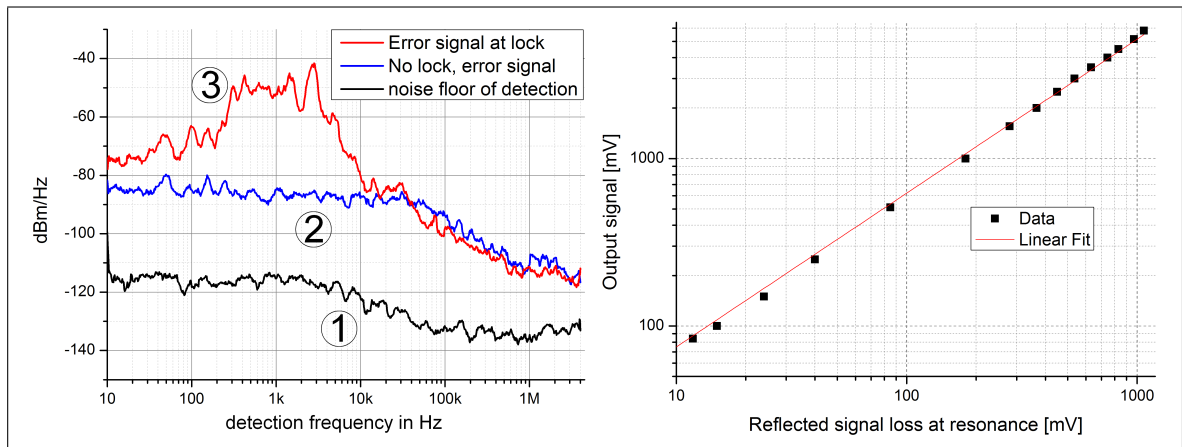


Figure 3.20: Principal properties of the locked cavity. *Left:* PDH error signal: electronic noise floor ①, cavity unlocked and out of resonance ②, at lock ③, *right:* Linearity of the cavity. The seed beam power is scaled from 4 mW to 400 mW

a signal will be compared to other measures of phase noise in chapter 4.

A number of broadband cavities have been reported in the literature for intracavity field enhancement [108, 109]. In these experiments, the intensity reaches the order of $10^{14}\text{W}/\text{cm}^2$. In the setup presented here, the peak intensity is about $10^{11}\text{W}/\text{cm}^2$. The linearity of the present cavity has been verified over two orders of magnitude of seed intensity as shown in Fig. 3.20, right. No significant nonlinearity has been observed. The vacuum chamber can be pressurized with laboratory air in the range 0.5 mbar to 1 bar. Simulations show that the impact of below 0.5 mbar air is negligible for the transmission of the cavity.

The cavity itself is shown in the photograph Fig. 3.21.

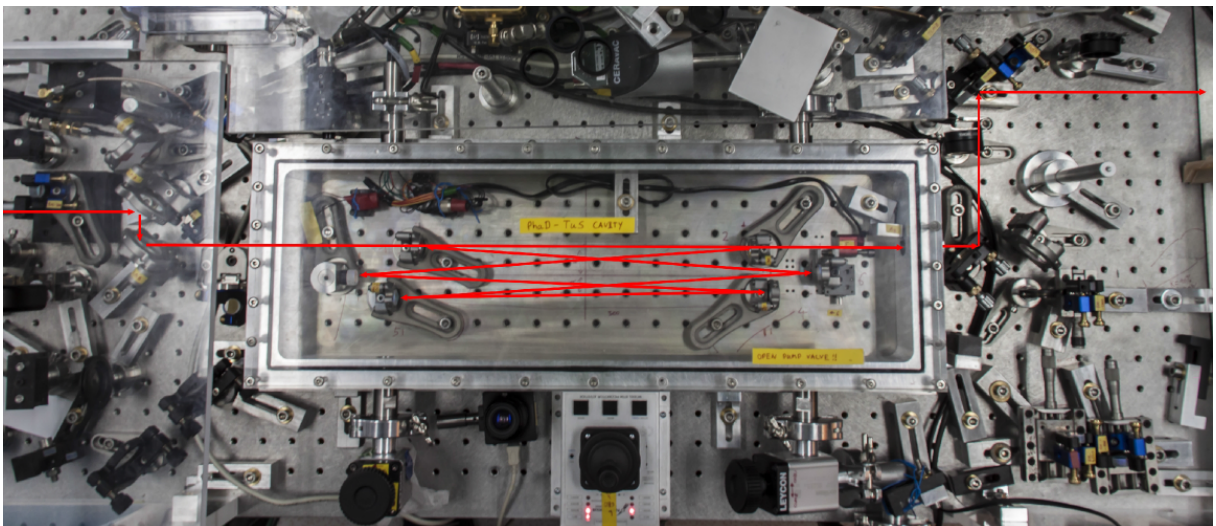


Figure 3.21: Photograph of the broadband cavity in the vacuum chamber. The principal optical elements are the mode matching of the seed (left) and of the reference via a 90/10 beamsplitter in counterpropagation (right). The setup is equivalent to the scheme Fig. 3.14

3.2.6 The locked cavity - experimental characterization

Several main parameters determine the spectral transmission properties of the present cavity:

- the air pressure/dispersion
- the seed CEO frequency
- the spectral lock-point, the electronic lock-point

Experimentally accessible characteristics of the locked cavity are the transmitted spectrum and its noise properties. The lock stability is a separate property. It is typically quantified by the r.m.s. of the error- or the transmitted signal. It contains both the in-loop noise of the locking scheme and the phase noise of the seeding beam.

The following experimental analysis addresses the measurement of the three cavity/comb parameters listed above. The aim is to provide optimal measurement conditions for cavity based filtering and detection of noise in optical frequency combs.

Dispersion analysis - different methods The dispersion of the cavity is the principal parameter limiting broadband simultaneous resonance - and therefore broadband transmission or the build-up of high peak powers within short fs-pulses. Due to the importance of this parameter, several methods have been reported in the literature in order to determine cavity dispersion precisely:

1st method. The simplest method consists of using Eq.(2.98) that determines the transmission $I(\omega)$ as a function of the spectral phase per round-trip $\Phi(\Omega)$. Its inverse can provide a first approximation of the cavity dispersion, but is typically of insufficient sensitivity.

2nd method. The second method consists of locking the cavity to a comb frequency ω_n and sweeping the repetition rate f_{rep} of the cavity [110]. The transmitted spectrum is recorded at the same time. Cavity dispersion leads then to a map of transmission peaks as a function of f_{rep} . A sensitivity of 1 fs^2 at 5 nm resolution bandwidth has been reported [110]. A similar method [111], [112] has been used to resolve magnetic dipole transitions in molecular oxygen in amplitude and phase and for spectroscopic fingerprinting of molecular iodine vapor.

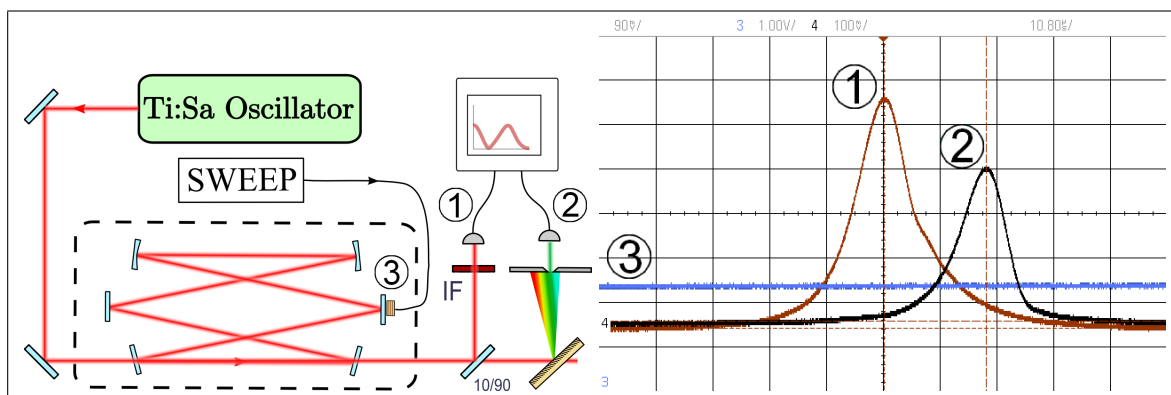


Figure 3.22: Cavity dispersion measurement based on continuous sweep. *Left:* Experimental measurement scheme. To avoid perturbations from slow cavity-length drifts, the resonance of the central wavelength triggers ① the measurement of the effective cavity length for each part of the comb ②. The cavity length is swept by a piezo-mounted mirror ③. *Right:* Typical oscilloscope output shows the mapping of cavity dispersion to μs timescales. Vertical scale: Voltage in arbitrary units, horizontal: time in μs

3rd method. Instead of sweeping the repetition rate, a further method consists of scanning the other degree of freedom of a comb, the CEO-frequency f_{CEO} , [113]. Using an automated setup, the resulting resonance map was used to determine the dispersion of a cavity with above 5 fs^2 sensitivity at 5 nm resolution bandwidth.

4th method. The remaining physical method is to interfere the incident and the transmitted beam of a cavity within spectral-interferometry [114]. This method has been used to characterize precisely the nonlinear dispersion of air with a sensitivity of 0.2 fs at 5 nm resolution bandwidth. Although simple to implement, the technique is difficult to calibrate as it requires the characterization of all optical elements in the cavity-beam path besides the cavity.

5th method. All the above methods require a continuous lock of the cavity. It is nevertheless also possible to adapt the method of [110, 115], that is a sweeping of the relative repetition rate of the cavity and the comb with an unlocked cavity. Being the most easy to implement, it has been chosen for the first characterizations of the cavity presented here. A schematic of the setup is shown in Fig. 3.22, left.

The cavity is swept over the entire resonance within μs . To avoid perturbations from slow mechanical drifts of the cavity, an oscilloscope is triggered to the resonance of the comb central wavelength. As shown in Fig. 3.22, right, the resonance of any other wavelength occurs then with a slight time shift due to dispersion.

It is worth mentioning that this method also has significant drawbacks. To avoid perturbation from drifts of the cavity length, the position sweep has to be done in μs timescales over the entire resonance. Nevertheless, the mirror position relative to the applied voltage depends also on small drifts of the cavity length. It may be

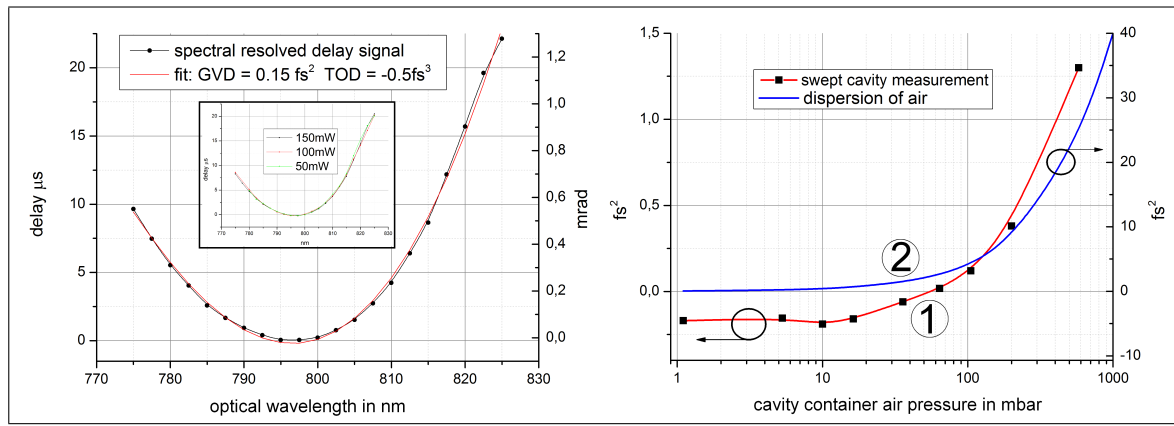


Figure 3.23: Measured dispersion of the cavity and comparison to expected values. Parameters $p = 105$ mbar, $f_{\text{CEO}} = 40$ MHz, 30 nm FWHM transmission. Best transmission bandwidth is obtained at 60 mbar. *left:* Typical measurement data for a swept-measurement. *Inset:* the same value of 0.15 fs^2 is obtained for seed powers 50 mW to 150 mW. *right:* Average cavity dispersion for the entire transmitted spectrum at different air pressures ① (left scale). For comparison: the dispersion of air ② (right scale).

corrected by a variable voltage offset and may vary during measurement time. This necessitates a precise calibration. Using the readily implemented scheme Fig.3.22, the average cavity dispersion has been quantified with an error of only 0.02 fs^2 .

A dispersion measurement. A calibrated measurement of the cavity dispersion is shown in Fig.3.23. Depending on the air pressure, the average dispersion of the cavity is close to zero and independent to a seed power variation of 300% (*left graph*). Nevertheless, under a variation of the air pressure (*right graph*), the measured average dispersion trace ① does not follow the expected curve for pressurized laboratory air trace ②. The latter should be the dominant contribution. Even anomalous dispersion is measured at pressures below 50 mbar. A change of sign is clearly observed at approximately 50 mbar. This is consistent with the measurement of broadest spectral transmission and highest transmitted intensity at this air pressure. Negative over-all dispersion is measured down to 1 mbar vacuum. It can consequently be supposed to be originated by the dielectric mirrors.

The possible emergence of nonlinearities. It has been observed in [114], that intensities of GW/cm^2 may cause negative dispersion in a cavity built of zero dispersion mirrors. In this reference, for a cavity consisting of six zero dispersion mirrors, -2 fs^2 have been observed under vacuum and at GW/cm^2 intensities. The same order of magnitude is measured in the present setup. The negative dispersion observed in [114] increases only slightly by a factor of ten when increasing the intracavity intensity by 10^5 . Higher intensities have been reported to lead to significant, non-linear two/multiple-photon absorption in the mirrors and even their damage [116].

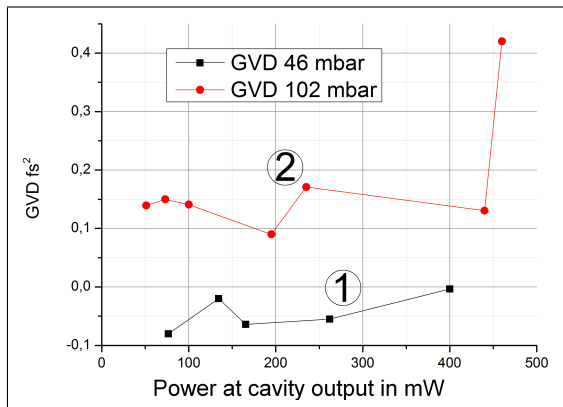


Figure 3.24: Possibly intensity dependent phase properties of the cavity. Dispersion of the cavity for different intensities, at 46 mbar ① and at 102 mbar ②.

Nevertheless, with regard to the linearity of the cavity observed here (Fig. 3.20, right), pure phase effects have so far not been studied in the literature. Going along with phase effects, the ionization of noble gasses has been reported for peak intensities of TW/cm^2 , [117]. These intensities are not reached here.

To provide an outlook for further investigations, Fig. 3.24 shows additional data from a preliminary measurement. The traces (GVD versus power) indicate that an intensity dependence of the dispersion might be present.

Conclusions on dispersion measurements. It turns out that the possible broadband resonance of a cavity is highly sensitive to dispersion. A light vacuum of 50 mbar laboratory air permits to set up a zero dispersion cavity with six purportedly zero-dispersion mirrors. It can not be excluded that intensity dependent dispersion contributes to this unexpected value.

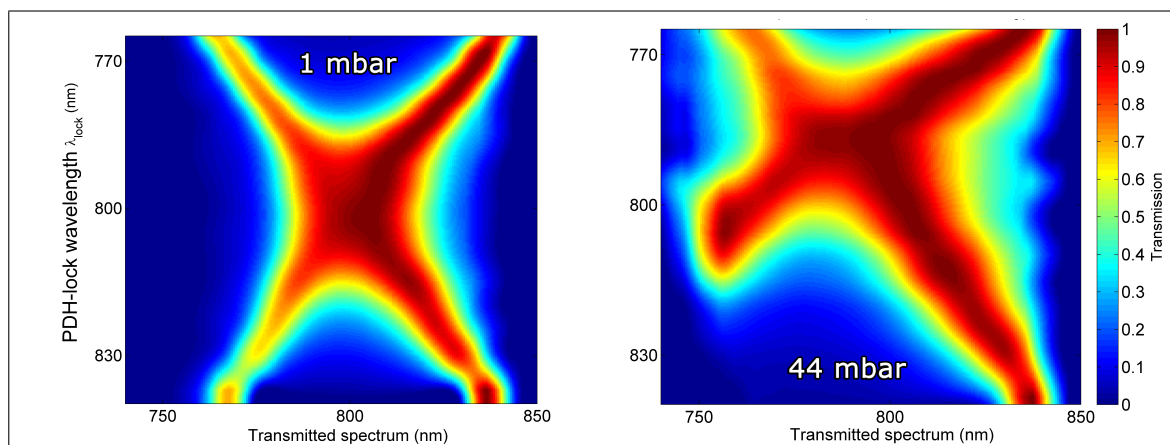


Figure 3.25: Transmission maps for different air pressures I. Vertical: wavelength locked with PDH-scheme, Horizontal: wavelength transmitted spectrum. *left: 1 mbar right: 44 mbar.*

Spectral effects at broadband transmission. An interesting representation of the experimental properties of a broadband resonant cavity are the so-called resonance plots. When the cavity is locked to the Ti:Sapph oscillator, two of the three parameters *lock-wavelength*, *CEO-frequency*, *air-pressure/dispersion* can be fixed, and one varied, see also [113] and [118]. The figures 3.25 and 3.26 show the spectrum transmitted by the cavity at $f_{\text{CEO}} = 35$ MHz. Broadest spectral transmission has been observed here for the largest pressure range. The air-pressure is set to the values of 1, 44, 92 and 127 mbar and the lock-wavelength is scanned.

The resulting graphs contain a large amount of information. Its entirety is not of use here. The plots are shown to underline the physical complexity of a broadband resonant cavity. They also demonstrate how to identify the cavity/comb parameters which maximize the transmitted bandwidth.

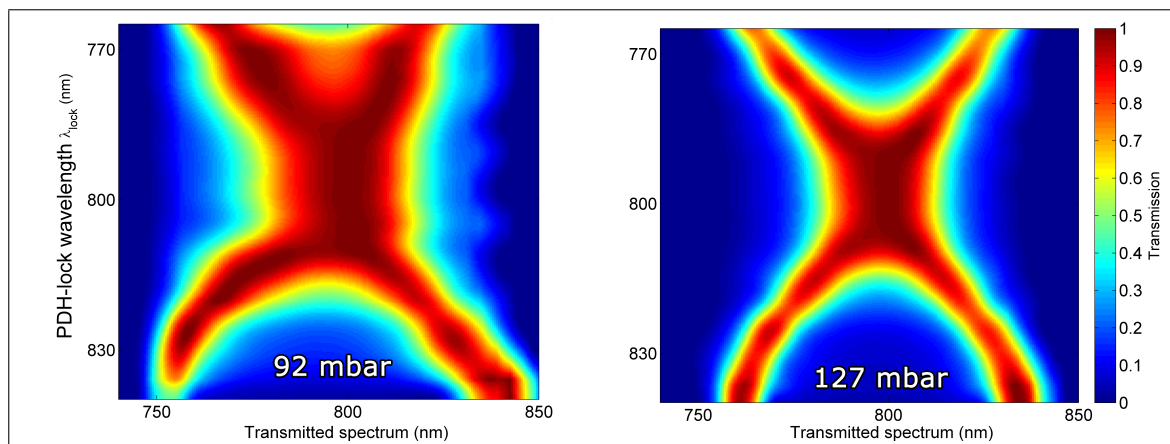


Figure 3.26: Transmission maps for different air pressures II. Vertical: wavelength locked with PDH-scheme, Horizontal: wavelength of the transmitted spectrum. *left: 92 mbar right: 127 mbar.*

The bandwidth of transmission is limited by intracavity dispersion, and the graphs show implicitly a non vanishing dispersion-structure of the cavity for all air-pressures. As expected from simulations, laboratory air can not perfectly compensate the residual mirror dispersion.

Broadest transmission with lowest dependence to the pressure and lock-wavelength is obtained at 50 to 60 mbar. At this range, the laboratory air compensates best a slight spectral asymmetry of the mirror dispersion. The air pressure determines the round-trip-phase acquired by the resonant beam and there is one CEO frequency for each air pressure corresponding to this phase. This is the configuration of broadest simultaneous resonance. For the observed optimal pressure of approximately 60 mbar, the value is $f_{\text{CEO}} \approx 50$ MHz.

Chapter 4

A passive cavity for comb phase noise metrology

Contents

4.1	Analysis and filtering of phase noise in an optical comb	98
4.2	Broadband spectrally resolved phase noise analysis	107
4.2.1	Additional considerations	118
4.3	The transfer function representation	122
4.4	Quantum-limited measurement of phase noise - ready to use	125
4.4.1	Comb phase noise from the cavity reflection	129
4.4.2	A ready to use schematic - applied to a Yb-fiber oscillator. . .	131
4.5	Spectral noise correlations in frequency combs.	134
4.5.1	Timing-jitter measurement close to the SQL	145

Structure of this chapter

This chapter contains the main results of this thesis. It is organized as follows:

In the *first section* 4.1, the noise in an optical frequency comb is characterized relative to the standard quantum limit in amplitude and phase. The methods developed to this aim use the broadband resonant, passive cavity to filter and to detect phase noise. High sensitivity to phase noise is obtained by shot noise resolving interference detection of the resulting signals. The results are applied to determine the realistic sensitivities of a homodyne measurement of pulse-timing jitter, predicted to have ultimate sensitivity.

The *second section* 4.2 uses the broadband passive cavity to detect phase noise of frequency combs close to the SQL spectrally resolved. The phase noise structure of a Ti:Sapph oscillator comb is compared to the one of a photonic crystal fiber PCF.

The *third section* 4.4 simplifies the methods developed in the first and second part significantly and applies them to a different Ti:Sapph- and a fiber-based oscillator.

The *fourth section* 4.5 introduces femtosecond pulse-shaping in order to reveal spectral correlations of amplitude and phase noise in an optical frequency comb. The resulting co-variance data contains the entire noise-information of the frequency comb. Correlated structures of noise define the *spectral modes* of classical noise in the comb. The underlying formalism is subsequently applied to compare CEO-phase and repetition-rate noise close to the SQL. Both noise properties appear to be special cases of noise modes.

In conclusion, it is shown that a broadband resonant cavity, together with shot noise resolving detection and pulse shaping, can reveal the entire correlation information of frequency comb noise. Amplitude and phase noise can be analyzed with these techniques down to the SQL. For such noise levels, it is shown that CEO-phase noise is the governing collective phase noise property of a Ti:Sapph oscillator.

4.1 Analysis and filtering of phase noise in an optical comb

Introduction. A highly sensitive homodyne timing measurement scheme using femtosecond (fs) lasers [5] has been shown in Eq.(2.72) to be limited by carrier-envelope-phase (CEO) noise close to the SQL. Although the noise of Ti:Sapph oscillators has been characterized extensively relative to the carrier, see Fig.3.5 and [16], no data are available relative to the quantum limit. By the use of a broadband passive cavity, the possibility of filtering and measuring phase noise at such low levels is demonstrated here. To this aim, shot noise resolving intensity noise detection is used. For completeness, also the amplitude fluctuations of the involved optical signals are determined relative to the common quantum limit. Improved realistic sensitivities are expected if the homodyne timing measurement scheme [5] would use cavity filtered signals. This outcome is discussed at the end of the section.

Theoretical concept. In order to provide a clear motivation and understanding of the experiments here done, it is useful to recall the principal theoretical context. The ultra sensitive pulse-timing measurements introduced in [5] rely on the homodyne detection of a pulse train. For the parameters of the 45 nm FWHM broad comb centered at 800 nm used here, the sensitivity $\Delta u_{\min}^2(f)$ at a detection frequency f simplifies to:

$$\Delta u_{\min}^2(f) \sim \frac{S_{\text{CEO}}(f)}{S_{\text{SQL}}} \quad (4.1)$$

This recalls the result Eq.(2.72), assuming the measurement time to be an arbitrary constant. Equation (4.1) points out that CEO-phase noise even close to the SQL limits the sensitivity. This is due to the fact that the CEO-phase noise is the phase noise common to all individual comb lines. Its characterization and filtering are the principal issues of the following measurements. Active locking schemes are typically of kHz-bandwidth. Side-bands above 100 kHz and levels close to the SQL are difficult to reach with active feedback [27]. A passive cavity can filter phase noise above 100 kHz down to the SQL. This is the approach studied here: The sensitivity Eq.(4.1) is also proportional to the inverse of the measurement time. Quantum limited phase noise at lowest detection frequency could provide space-time positioning with femtosecond oscillators at highest sensitivity.

As an aid to the reader, several aspects already discussed in the previous sections are recalled in the following.

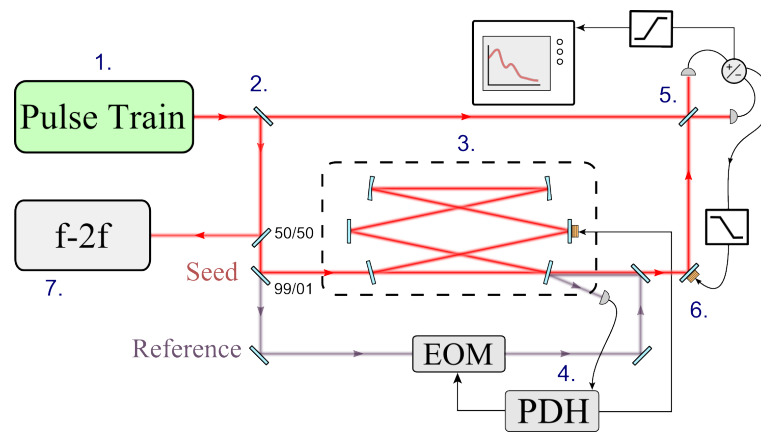


Figure 4.1: Experimental scheme. 1. Mode-locked Ti:Sapph oscillator, 2. selection of measurement type using a flip 50/50 beam splitter: amplitude noise measurement if released, interference measurement if set, 3. passive cavity in a mbar vacuum chamber, 4. PDH-locking scheme, 5. balanced (homodyne) detection, 6. lock of the relative phase of the interfering beams, 7. f-2f interferometer

Optical setup. The setup to access and manipulate the intensity and phase noise properties of an optical frequency comb is drafted in Fig.4.1. It consists of the commercial Ti:Sapph oscillator studied in section 3.1 and the passive cavity characterized in section 3.2. The latter is placed in one arm of a Mach Zehnder-like interferometer configuration. At resonance, the resulting interference with the seed-beam is detected in a shot noise resolving, balanced configuration. A Menlo Systems f-2f interferometer monitors in parallel the CEO frequency and its fluctuations after coherent spectral broadening. It allows to lock the mean Ti:Sapph CEO frequency with a separate feedback loop of less than 20 kHz bandwidth.

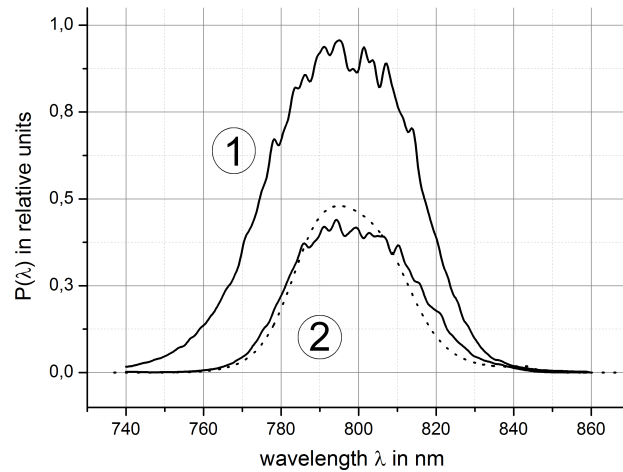


Figure 4.2: Cavity transmission spectrum showing broadband simultaneous resonance. Same graph as Fig. 3.18, right. ① A typical seed spectrum of the mode-locked Ti:Sapph oscillator. ② Transmitted spectrum at a container laboratory air pressure $p=68\text{mbar}$ and $f_{\text{CEO}} = 45\text{MHz}$, dotted simulation at $p=30\text{mbar}$. At optimized conditions, approximately 38% of the seed power are transmitted.

The filtering cavity. A transmissive optical cavity is a well known 2nd-order low-pass filter acting on both phase and amplitude noise of the input field [29]. The 3-dB cutoff frequency $f_c = c/(F \cdot L)$ is determined by the speed of light c , the cavity finesse F , and its length L . Residual dispersion is compensated by laboratory air. The constant pressure, set within $50 \pm 30\text{ mbar}$, is chosen to obtain best spectral shape of transmission. A Pound-Drever-Hall scheme is used to lock the cavity on resonance with the seed pulse train. To avoid the modulated reference to appear in the detected signal, a counter-propagating reference-beam is used to generate the error signal. When the cavity and the mean CEO-frequency are locked, the 45-nm FWHM spectrum generated by the Ti:Sapph oscillator is almost entirely (35 nm FWHM) transmitted through the cavity, see Fig.4.2. The simulations agree well with the spectra observed. A slightly different pressure is used for the simulation to illustrate the pressure dependence of the transmitted bandwidth. Concerning noise filtering, section 3.2 characterized an effective finesse of $F \approx 1200$. A measurement of the 3-dB cutoff frequency of this cavity confirmed $f_c \approx 130\text{ kHz}$.

Measurement of relative phase noise. To quantify the effect of phase noise filtering by the passive cavity, relative phase noise between a filtered and an unfiltered beam have to be measured down to the SQL. A shot-noise-resolving, balanced homodyne detection [119] can do so. Its implementation was shown in Fig. 4.1. It measures phase noise differences before and after the filtering cavity.

Two incident fields $E_i = A_i e^{i\phi_i}$, $i = 1, 2$ interfere. Locking on the phase quadrature $\langle \phi \rangle = \langle \phi_1 - \phi_2 \rangle = \pi/2$ leads to the beating signal $H = A_1 A_2 \sin(\delta\phi)$ where $\delta\phi$ are the zero mean fluctuations of the relative phase of the interfering fields. This signal efficiently converts this relative phase noise into amplitude fluctuations. A homodyne detection of the relative phase noise is used here. A bright *local oscillator* (LO) and an attenuated *signal* interfere. This configuration makes the scheme less sensitive to amplitude fluctuations. Using here an intensity ratio of 10 dB, higher order noise terms are negligible in the measured signal.

Assuming perfect quantum efficiency of the photodetectors and setting the elementary charge to one, the mean squared homodyne signal is obtained using the considerations in [38]:

$$S = \frac{\langle \delta H^2 \rangle}{(\hbar\omega_0)^2} \simeq \frac{A_{\text{LO}}^4}{10(\hbar\omega_0)^2} \langle \delta\phi^2 \rangle. \quad (4.2)$$

This signal detects relative phase fluctuations $\delta\phi$ of the interfering beams relative to the shot noise level $N \simeq A_{\text{LO}}^2/\hbar\omega_0$. The observed phase noise can be expressed relative to the carrier in units dBc/Hz=(1/2) · rad²/Hz [12]. For a signal to noise ratio SNR=S/N = 1 and a detected power P , the minimal resolvable relative phase noise is

$$\langle \delta\phi^2 \rangle_{\text{min}} = \frac{5\hbar\omega_0}{P} \simeq 2S_{\text{SQL}} \quad (4.3)$$

The measurement scheme Fig. 4.1 of relative phase noise is consequently of quantum-limited sensitivity. Indeed, the assumed SNR=S/N = 1 is caused by a phase noise level 3 dB above the SQL. For sufficiently high detection frequencies above the cavity-cutoff, the phase noise in the filtered arm becomes negligible. The detected signal is then proportional to the CEO-phase noise $\delta\phi \approx \delta\theta_{\text{CEO}}$. With $f_c \approx 130$ kHz used here, this holds at MHz detection frequencies. In conclusion, even absolute levels of CEO-phase noise become measurable down to the SQL [86].

Expected slope of the interference signal. The homodyne method presented above measures classical phase noise with quantum-limited sensitivity. The slope of a given CEO-phase noise distribution can be reconstructed as follows:

Both ϕ_1 and ϕ_2 originate from the same beam, they are - besides the filtering effect for the signal - perfectly correlated random variables. Assuming a phase noise transfer function of the cavity $H_\phi(f)$, the phases of the individual beams are for any detection frequency f :

$$\phi_1(f) = \delta\phi(f), \quad \phi_2(t) = H_\phi(f) \cdot \delta\phi(f) \quad (4.4)$$

The detected signal is now proportional to

$$\langle (\delta\phi)^2 \rangle_{\text{meas}} = \langle (\delta(\phi_1 - \phi_2))^2 \rangle \quad (4.5)$$

$$= \langle (\delta\phi)^2 \rangle + \langle (-H_\phi \cdot \delta\phi)^2 \rangle + \text{COV}(\delta\phi, -H_\phi \cdot \delta\phi) \quad (4.6)$$

$$= (1 - 2H_\phi + H_\phi^2) \langle (\delta\phi)^2 \rangle. \quad (4.7)$$

With the definition of the spectral variance $\sigma^2(f) = S(f) \cdot 1 \text{ Hz}$, see Eq.2.27, the above can be written in terms of spectral noise densities:

$$S_{\phi, \text{meas}}(f) = (1 - H_\phi(f))^2 \cdot S_\phi(f) \quad (4.8)$$

The homodyning signal being proportional to the *cavity filter efficiency* $1 - H_\phi(f)$, the measurement sensitivity increases with f . In the limit case above the cavity cutoff $f \gg f_c$, the signal $S_{\phi, \text{meas}}$ is identical to the seeding phase noise S_ϕ .

Above the cavity cutoff, the filter efficiency is linear in frequency: $(1 - H_\phi) \sim f$. It is important to remind that a passive cavity is a first-order filter for amplitude and phase noise. It only appears to intensity and measured mean squared phase noise as a second order filter. For a CEO-phase noise density $S_{\text{CEO}}(f)$ seeding the setup Fig. 4.1, the expected distribution of the homodyning signal $S_{\phi, \text{meas}}(f)$, $f > f_c$ is consequently [86]:

$$\boxed{S_{\phi, \text{meas}}(f) \approx f^2 \cdot S_{\text{CEO}}(f)} \quad (4.9)$$

For the observed $S_{\text{CEO}}(f) \sim f^{-4}$ a signal $S_{\text{meas}}(f) \sim f^{-2}$ is expected. This result is consistent with the observed signal slope shown in the following Fig. 4.4.

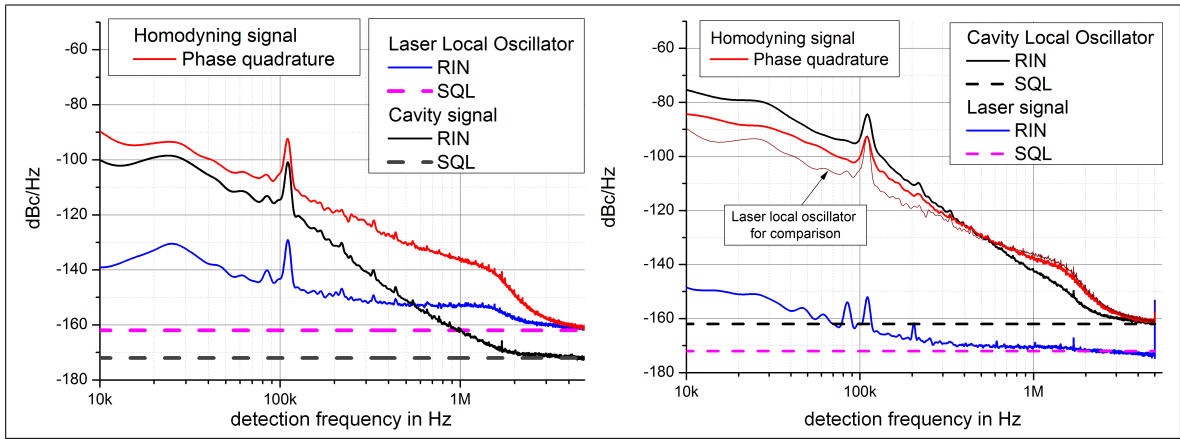


Figure 4.3: Homodyne detection of relative phase noise close to the quantum limit. The beating signal is independent to the detection configuration - the choice of the Local oscillator (LO). Signal levels dBc relative to the LO carrier. Local oscillator at 8 mW, signal 10 dB below.

left: Ti:Sapph local oscillator, *right:* Cavity local oscillator.

both left and right: Blue Ti:Sapph purple Ti:Sapph SQL, black Cavity output grey Cavity SQL, red Homodyning signal of the phase quadrature. *right,* dark red comparison of both configurations

Preliminary measurement data. The Mach-Zehnder interference measurement Fig. 4.1 can be done in two different configurations, depending on the choice of the local oscillator (LO) and the attenuated signal (S). *First:* the Ti:Sapph is the (LO) and the cavity beam the (S), *second:* the Ti:Sapph is the (S) and the cavity beam is the (LO).

These configurations have to be distinguished, as the beam transmitted by the cavity exhibits significant excess noise. Its origin is discussed in the next section. Figure 4.3, left, shows the intensity noise of cavity (S) and oscillator (LO) in the *first* configuration, together with the beating signal. Although the intensity noise of the (S) is significantly rising towards low detection frequencies, it does not perturb the significantly higher beating signal.

The situation is slightly different in the *second* configuration, shown in Fig. 4.3, right. Here, the cavity beam is the (LO) and the Ti:Sapph the signal (S). The cavity excess noise rises to levels equivalent to the beating signal and perturbs it. Nevertheless, for sufficiently high detection frequencies, the beating signal in this configuration is still equivalent to the one obtained with the first configuration.

This aspect confirms the validity of the measurement method. Being predicted to measure relative phase noise between the two arms of the interferometer, its output is insensitive to the relative intensities. In conclusion, it is the *first* configuration that will be used for all further measurements.

As far as perturbations from intensity noise are negligible, both configurations provide quantum-limited sensitivity to relative phase noise between the two arms, see Eq.4.3.

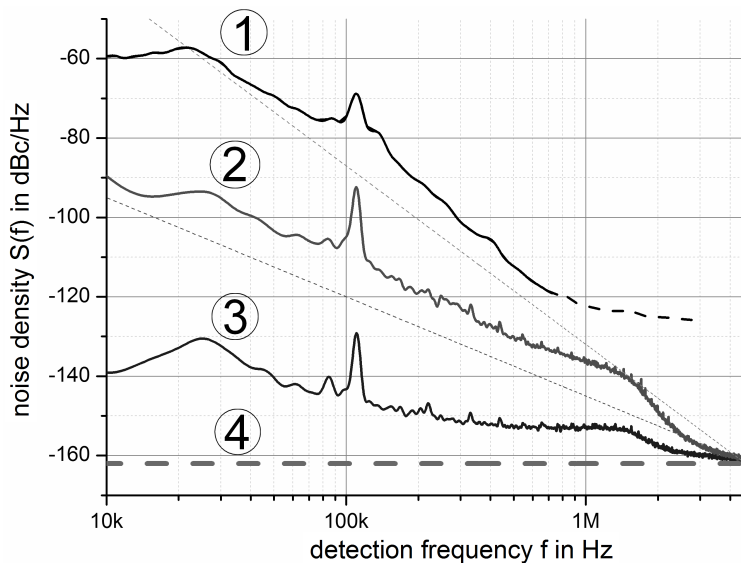


Figure 4.4: Relative phase noise after filtering with the cavity, detected with quantum limited sensitivity. ① SSB power spectral density of CEO phase noise from f - $2f$ measurement, dotted $f^{-4.5}$ power law, ② Phase quadrature of the homodyne beating signal between the oscillator (local oscillator) and the cavity-output (Signal), dotted $f^{-2.5}$ power law, ③ Ti:Sapph RIN, ④ SQL for 8 mW detected signal

Measurement Data. The Ti:Sapph oscillator used here has already been characterized in section 3.1. In order to provide a clear interpretation of the subsequent phase noise analysis, those measurements are partially recalled here. Figure 4.4 shows all measurement data necessary to characterize the Ti:Sapph oscillator phase noise down to the SQL: intensity noise (RIN) of the Ti:Sapph oscillator ③, f - $2f$ beating signal ① and the output of the interference measurement Fig. 4.1 ②.

The intensity noise reaches the SQL trace ④ above 3 MHz detection frequency. The only slightly distinguishable relaxation oscillation peak at 1.5 MHz depends on oscillator alignment and output power. It has been minimized for this measurement.

The signal ② itself arises from the phase noise of each individual comb line. For the entire comb, both repetition-rate and CEO-phase noise contribute to it. The locked f_{CEO} can be considered as free running above the lock-resonance at 30 kHz. Its power spectral density is shown by trace ①. It has already been discussed in section 3.1. As reported there, the levels observed are more than 60 dB above the repetition rate phase noise. The measured repetition rate noise levels have to be multiplied by the longitudinal mode number to estimate their contribution to the phase noise of an individual line. In addition, such an estimation has to take into account the distance to the noise fix-point frequencies discussed in the next section, Eq.4.12.

From this perspective, it is not possible to distinguish here if either repetition rate phase noise or CEO phase noise contribute mostly to phase noise of the individual lines and consequently to the measurement trace ②. Anticipating the results of section 4.5.1, Fig. 4.37, right, it has been shown for a similar Ti:Sapph oscillator that the CEO-phase noise is the governing collective phase noise property of the comb. As confirmed below, it is this collective comb phase property that is detected by the homodyne measurement Fig. 4.4, trace ②.

Principal result: Phase noise filtering and detection. The measured homodyning signal is given by trace ② in Fig. 4.4. It arises from the interference of the signal from the Ti:Sapph oscillator (LO) with the 10 dB less intense beam filtered from the cavity (S). The two beams have a spectral overlap of 94%. The signal from the cavity exhibits excess intensity noise arising from noise-quadrature interconversion by the cavity (see Fig. 4.3). Nevertheless, this does not change the RF-spectral distribution of the homodyning signal. Classical intensity noise of signal and local oscillator cancel in the balanced measurement configuration and only contribute to higher order terms of the signal S described in Eq.(4.2).

The homodyne signal of the phase quadrature follows an approximate $f^{-2.5}$ power law over nearly two decades of detection frequencies, see Fig. 4.4, trace ②. This is consistent with the considerations related to Eq.(4.9): The expected power law for the seeding CEO-phase noise is two orders steeper, $f^{-2.5-2}$. Indeed, the CEO-phase noise of the Ti:Sapph oscillator was observed to follow an $f^{-4.5}$ dependence, see Fig. 4.4, trace ①.

Two main outcomes of this measurement have to be distinguished: First, that shot noise resolving homodyne detection provides a measurement of relative phase noise down to the SQL. Second, that for the self-referenced setup used here even absolute levels of phase noise of an ultrafast oscillator become measurable down to the SQL. The latter insight opens the way to the main result of this thesis, the study of spectral correlations of phase noise, see section 4.5 below.

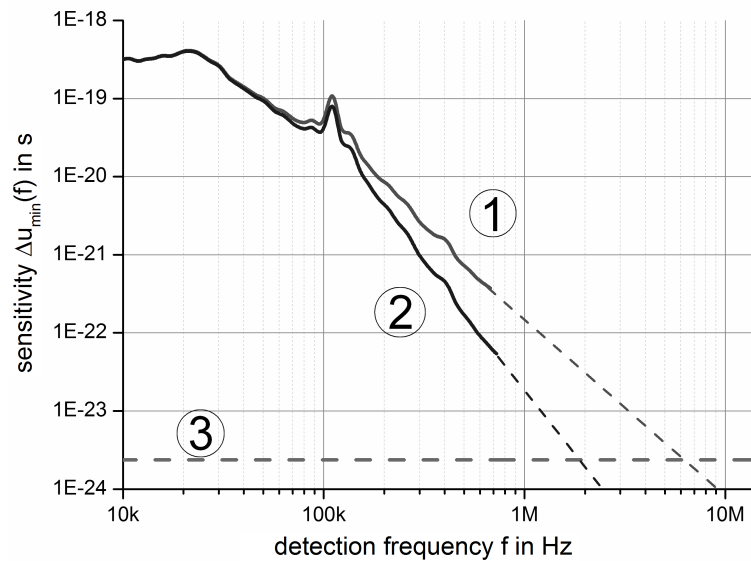


Figure 4.5: Predicted realistic sensitivity of the homodyne timing measurement using the Ti:Sapph oscillator studied here [5]. First using the oscillator itself ① and second after filtering with the passive cavity described here ②. *dashed lines* extrapolation of available data ③ Quantum limit for phase and intensity noise for 8 mW detected signal at 1 s integration time.

Improved homodyne-timing-measurement sensitivities. The consequences of the observed phase noise filtering for the timing measurement sensitivity discussed with Eq.(2.70) are shown in Fig. 4.5. Using the f - $2f$ CEO-phase noise data, the possible precision of the homodyne timing measurement [5] can be calculated for a filtered or an unfiltered beam. With Fig. 4.4 it follows in addition from the interference data that the slope of the CEO-phase noise does not significantly change at microsecond timescales. The achievable measurement precision shown in Fig. 4.5 can thus be calculated using the known filtering properties of the cavity, and be extrapolated down to the SQL. Using a passive cavity to filter phase noise, the expected sensitivity of the timing measurement could be improved by up to one order of magnitude.

Conclusions. A broadband resonant, passive cavity has been shown to be a tool for filtering and the detection of CEO-phase noise of a 45-nm FWHM frequency comb - close to the standard quantum limit. The approach extends the known filtering of noise in single optical frequencies [29] as frequency combs have a much more complex frequency and noise structure. Together with shot noise resolving homodyne detection, it is shown that a commercial Ti:Sapph oscillator is quantum-limited in amplitude and phase above 4 MHz detection frequency. Passive filtering of phase noise by the use of this cavity decreases this frequency by several MHz. It potentially improves the sensitivity of a homodyne pulse-timing measurement scheme by up to one order of magnitude.

4.2 Broadband spectrally resolved phase noise analysis

This section discusses assets and drawbacks of a broadband passive cavity used as a broadband detector for spectral phase noise in frequency combs.

Common comb noise properties. For optical metrology using frequency combs, absolute calibration of the comb frequencies is achieved by beating individual lines to external references. The inherent relative stability arises from the mode-locking process. The strength of this lock determines the possible relative phase deviations between individual lines. Such repetition rate fluctuations of Ti:Sapph lasers have been characterized down to lowest noise levels [7] and the same holds for fluctuations of the CEO-frequency [27]. Both are noise properties common to all individual frequencies of the comb. Their origins were at first studied by Haus et al. [10], see section 2.4.3. Assuming perfect mode-lock, this picture ignores any possible dependence of the noise on the considered optical frequency. It were Paschotta et al. [19] that pointed out that this ideal assumption has to be relaxed at RF-detection frequencies above 100 kHz. Increased levels of phase noise at microsecond timescales are the consequence.

Spectral phase noise. For a Ti:Sapph oscillator, the RF-distributions of phase noise have been analyzed theoretically over the optical spectrum by Wahlstrand et al. [20]. A slight dependence of the linewidth on the considered wavelength has been predicted but not yet verified experimentally. Another, indirect approach is the fix-point model of the comb [21]. It has been applied to a Ti:Sapph generated comb by Sutyryn et al. [16]. Therein, the spectral position of the line with minimum linewidth has been determined. Compared to Ti:Sapph oscillators, fiber based frequency combs are much noisier, and their spectral phase noise has been extensively studied by Newbury et al. [18]. Another experimental technique has been conceived for very broad spectra [120]. It consists of a dispersive Fourier-transform. Being suitable for very broad spectra, this scheme is nevertheless limited to 30 dB dynamic range. The method presented here solves these problems and provides a high dynamic range, direct measurement of CEO- and spectral phase noise at a glance.

This is achieved by exploiting the effect of phase (noise) to amplitude (noise) conversion by a transmissive passive cavity. The cavity has been shown to be broadband resonant. The spectral phase noise of the comb should consequently be readily accessible.

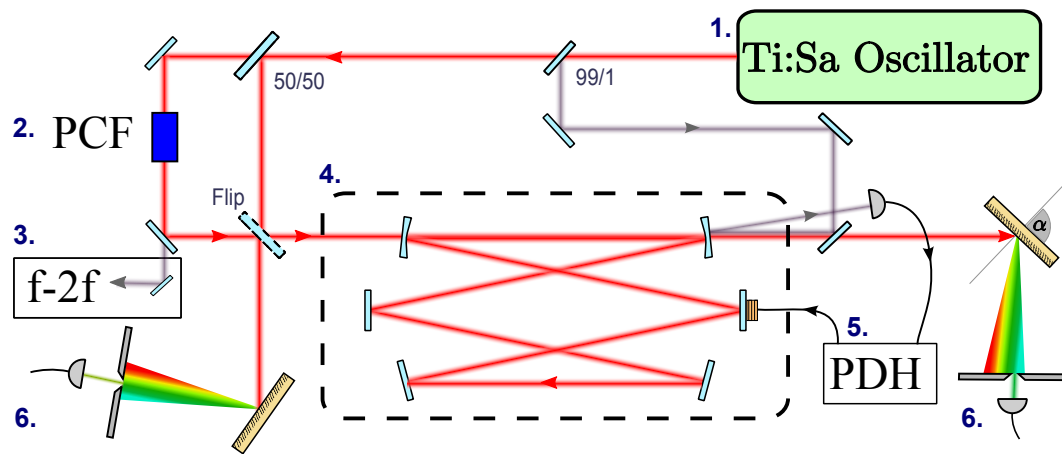


Figure 4.6: Experimental scheme to measure spectral phase noise through spectral resolved cavity excess noise. 1. Mode-locked Ti:Sapph oscillator at 156 MHz repetition rate; 2. Photonic Crystal Fiber PCF; 3. f - $2f$ interferometer for CEO lock and signal analysis; 4. passive cavity in a mbar vacuum chamber; 5. PDH-locking scheme in counterpropagation; 6. intensity noise detection either integrating the whole spectrum (in the text referred as **A**), or spectrally resolved (**B**)

Experimental setup. The experimental setup is shown in Fig. 4.6. It uses the Ti:Sapph oscillator characterized in section 3.1, the passive cavity of section 3.2 and the shot noise resolving photo detection mentioned therein.

Intensity noise is characterized with shot noise resolving sensitivity before and after the cavity. This can be done spectrally resolved or integrated over the whole spectrum. Spectral resolution is obtained using dispersion by optical gratings. To prevent the CEO-frequency from slow drifts that change the cavity transmission, the CEO-phase is locked with a bandwidth below 20 kHz. The f - $2f$ interferometer used for this purpose also monitors the phase noise of the free-running Ti:sapph oscillator, in-loop but out of the feedback-bandwidth.

Similar to the considerations done in section 3.2 above, Fig. 4.7 shows general properties of the passive cavity. Emphasis is put on the influence of the spectral lock-point on the transmitted spectrum, in the context of the expected cavity dispersion. As discussed in section 3.2, it is the cavity dispersion that limits the bandwidth of transmission. It leads in addition to a dependence of the transmitted spectrum on the optical lock-point. Three typical situations are shown. In addition to these effects, it turns out in this section that lowest levels of dispersion, see Fig. 4.7, trace ③, may also considerably affect the noise-conversion of the cavity.

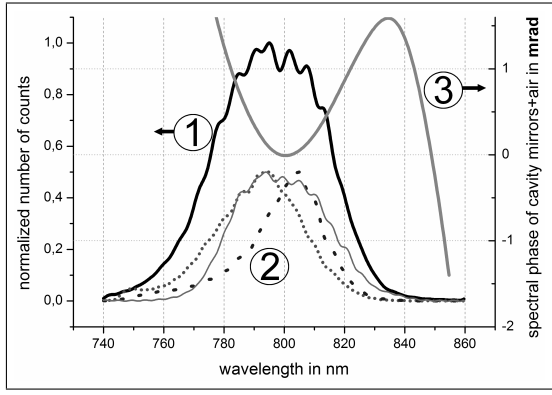


Figure 4.7: General properties of the broadband passive cavity - small values of dispersion.

① Spectrum of a 45 nm FWHM Ti:Sapph oscillator seeding the passive cavity, ② transmitted spectrum as a function of the optical lock point at 780 nm, 797 nm and 818 nm. The transmission is maximal at or close to the lock-point. ③ calculated dispersion of the cavity arising from mirror and air-pressure environment.

Noise quadrature interconversion. The transmission of the noise field quadratures P (phase) and Q (amplitude) by a passive cavity can be described using a unitary matrix A and an attenuation factor τ . They are both a function of the side-band angular frequency Ω , see section 2.7.2. Whereas the previous section put emphasis on filtering of phase noise, the interconversion of the seeding field quadratures is of interest here:

$$\mathbf{v}_{\text{out}}(\Omega) = \tau(\Omega)A(\Omega)\mathbf{v}_{\text{in}}(\Omega), \quad \mathbf{v}(\Omega) = [P(\Omega), Q(\Omega)]^T \quad (4.10)$$

In practice, this equation is inverted in order to calculate the seeding noise \mathbf{v}_{in} and especially P_{in} from \mathbf{v}_{out} and especially Q_{out} . In general, the transformation $A(\Omega)$ interconverts and mixes phase and amplitude noise. This holds especially for side-bands above the cavity cutoff at 130 kHz and applies to any line ω_n of the comb.

This approach has advantages and drawbacks: Measurable noise densities are proportional to the mean squares of the field quadratures and Eq.(4.10) is a simplified representation. Only under the assumption of negligible correlations between amplitude and phase noise, the seed phase noise spectral density $S_{\phi,\text{in}}$ can be calculated from the detected output intensity noise $S_{I,\text{out}}$, see Eq.(2.121):

$$\boxed{S_{\phi,\text{in}}(\Omega) \sim \Omega^2 \cdot S_{I,\text{out}}(\Omega)} \quad (4.11)$$

It is a special feature of optical frequency combs that one of the two global Ti:Sapph phase noise properties, the CEO-phase noise S_{CEO} , can be measured separately by e.g. an f-2f beating. It can be compared to the calculated $S_{\phi,\text{in}}$ in order to verify the assumption of negligible amplitude-phase correlations. In practice for a Ti:Sapph oscillator and if considered in the same units dBc, the intensity noise has been shown to be negligible compared to CEO phase noise and this consideration is even not necessary.

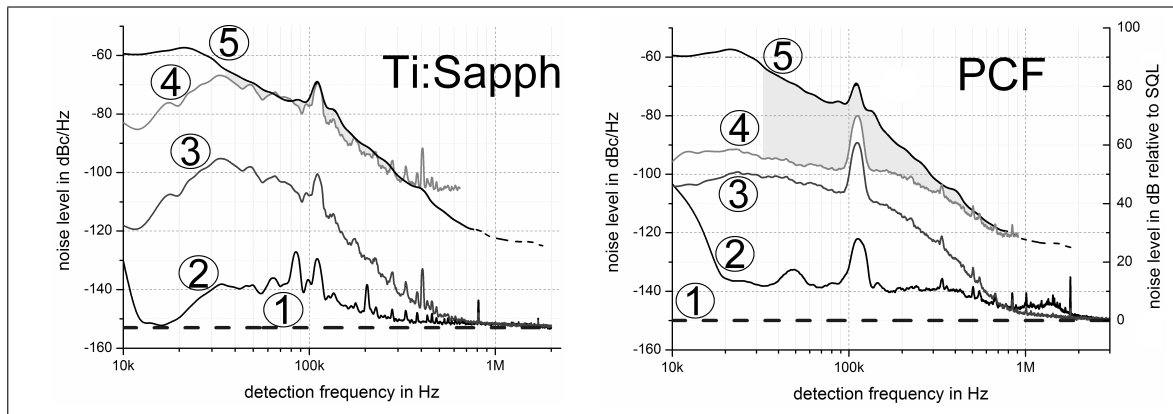


Figure 4.8: Noise quadrature conversion by the passive cavity for the Ti:Sapph oscillator (*left*) and after coherent spectral broadening in a PCF (*right*). For both graphs: ① standard quantum limit, ② intensity noise of the comb before the cavity and ③ after transmission through the cavity, ④ calculated phase noise distribution of the seed beam assuming negligible amplitude-phase noise correlations, shown with an arbitrary offset introduced for comparison with the CEO noise contribution, ⑤ CEO-phase noise of the seeding frequency comb measured with an f - $2f$ scheme, *for comparison:* the grey area shows the difference of the calculated and the separately measured phase noise, it corresponds to amplitude-phase noise correlations

Noise properties of frequency combs in the RF-domain. The experiment Fig. 4.6 is at first done without a spectrally resolved photodetection. As such, the intensity noise of the Ti:Sapph frequency comb and after coherent broadening in a photonic crystal fiber (PCF) are measured. The signals are transmitted through the broadband passive cavity and the intensity noise is measured before and after transmission. From these measurements, the phase noise distribution of the cavity seed is calculated using the exact form of Eq.(2.121). Nevertheless, this calculus assumes negligible amplitude-phase noise correlations. An arbitrary constant has been added to the calculated curves. It arises from the detection relative to shot noise levels of signals of different intensity. The result is compared to an f - $2f$ measurement. Both are shown in Fig. 4.8. Indeed, for the Ti:Sapph oscillator the assumption of negligible amplitude-phase noise correlations are verified:

For Ti:Sapph and PCF, the seed-intensity noise is significantly below the intensity noise at the cavity output and can be neglected. In the case of the Ti:Sapph oscillator, the calculated distribution of $S_{\phi,\text{in}}(\Omega)$ is identical to the distribution of $S_{\text{CEO}}(\Omega)$ from the f - $2f$ measurement. This confirms the assumption of negligible amplitude-phase noise correlations that lead to Eq.(4.11). The low-level intensity noise of the Ti:Sapph oscillator can be attributed to RIN properties of the pump laser, see section 3.1.

Spontaneous emission limited phase noise. If the phase noise of the Ti:Sapph oscillator is uncorrelated to its intensity noise, it can only be originated by spontaneous emission. This statement is equivalent to *spontaneous-emission limited phase noise*¹. This result is consistent with the theory of H.A.Haus [10]. By considering the coupling of different noise terms, and assuming that spontaneous emission is the only noise driver, this theory predicts a fourth order decay of the CEO-phase noise slope. This dependence is similar to the here observed one.

The situation is different for the PCF signal. Here, the phase noise calculated with the exact form of Eq.(4.11) only follows the slope of the f - $2f$ signal in the limit case of high detection frequencies Ω close to the noise limit of detection. The significant difference is explicitly shown in Fig. 4.8, *right*: the difference between the curves ④ and ⑤. This difference indicates that for a the signal of the PCF, amplitude and phase noise are - in contrast to the Ti:Sapph signal - significantly correlated. This effect may be due to the number of phase sensitive nonlinear processes present in the PCF.

Note that an arbitrary constant has been added to the calculated curve for comparison. No statement about the absolute amount of noise is possible here. This is first related to the different shot noise levels of the measured beams - to which the curves are intrinsically normalized. Second, the spectrum of the PCF signal is significantly larger than the cavity bandwidth. Detailed information about the cavity dispersion and the resulting apparent side-band frequency distributions would have to be integrated into the calculations. This is beyond the scope of this prove-of-principle experiment.

¹ Spontaneous emission limited noise properties refer to an oscillator still providing noise coupling terms. They lead to non-constant RF-distributions of phase noise. This behavior has to be distinguished from quantum-limited phase noise at the SQL that has a constant spectral density. See section 2.3

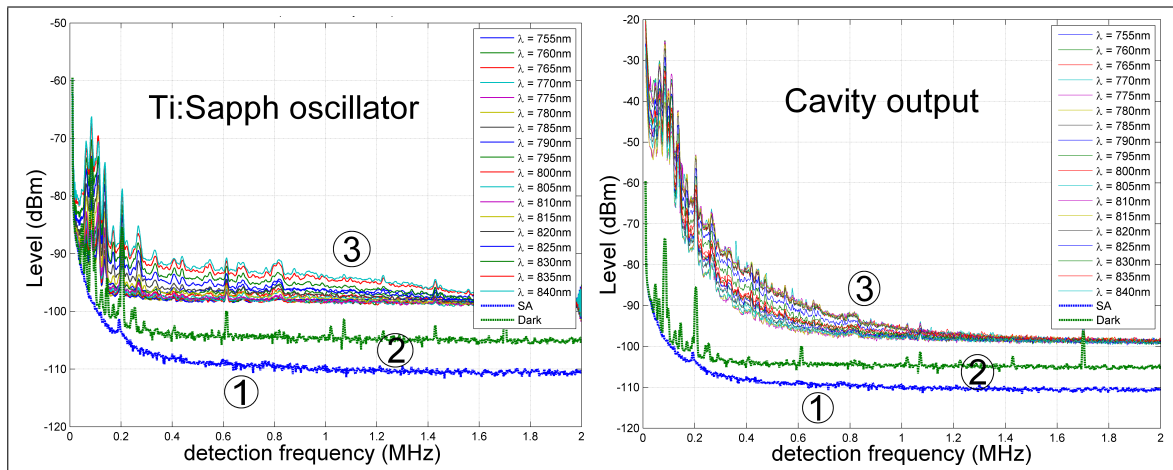


Figure 4.9: Typical measurement of the RF-distribution of spectral intensity noise for the cavity seed/the cavity output. The linear frequency scale has been shown for better visualization. ① Spectrum analyzer measurement noise floor, ② photodetector dark noise, ③: intensity noise measurement for *left*: Ti:Sapph oscillator SYNERGY, *right*: Cavity output when seeded with the Ti:Sapph oscillator left.

Phase noise analysis over the optical spectrum. The above analysis of RF-spectral densities $S(\Omega)$ concerns the entire optical spectrum of the frequency comb. The broadband simultaneous resonance of the passive cavity allows to do these measurements resolved over the optical spectrum, as shown in Fig. 4.6B.

Typical measurement data $S_\lambda(\Omega)$ for this configuration are shown in Fig. 4.9 for the Ti:Sapph oscillator. Intensity noise is measured for the oscillator itself (left) and after transmission through the passive cavity (right). A variation of the recorded noise level with the optical wavelength is evident from this data. In order to obtain further conclusions, the considerable amount of data can be reduced by setting a fixed analysis frequency Ω . It is chosen to 500 kHz: above the cavity-cutoff 130 kHz and below 1 MHz where noise levels are close to the SQL. The variation of the intensity noise slopes over the optical spectrum is negligible, see Fig. 4.9, left.

Two different ways to analyze the spectral phase noise $S_\lambda(500 \text{ kHz})$ are presented in the following. Both methods are subject to ongoing investigations.

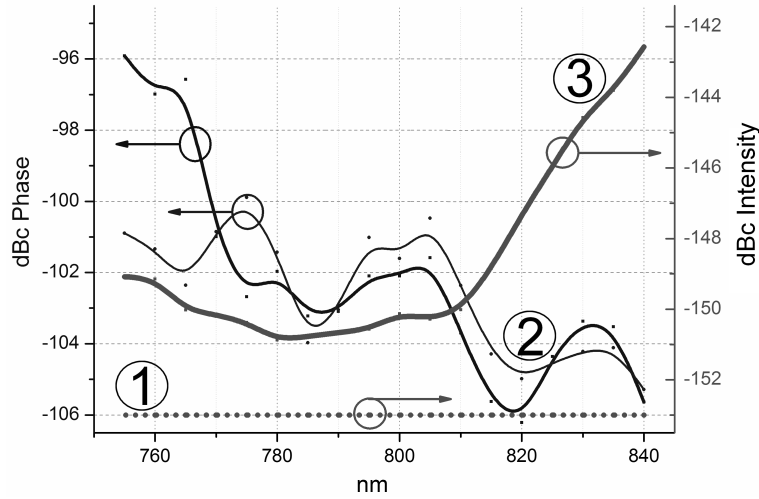


Figure 4.10: *First experimental analysis of spectral phase and intensity noise.* The Ti:Sapph oscillator at 500 kHz side-band frequency and 8 mW detected signal. **Right scale (intensity):** ① SQL and ③ intensity noise, **Left scale (phase):** ② spectral phase noise for two different strengths of the mode-locking Kerr-lens. For the beam waists in the Ti:Sapph crystal permitting stable mode-lock: *thick* mean value, *thin* largest value (weakest Kerr effect), spline interpolation of data for visualization

First approach: The noise properties of the entire optical spectrum are recorded using spectral windows of approximately 5 nm bandwidth, centered at ω_n . To provide identical measurement conditions, the detected intensity is set to the same value for each window. The following method is used to calibrate the measurements: From the f-2f technique, the CEO-phase noise $S_{\text{CEO}}(\Omega)$ is available for a broad range of detection frequencies. At a given Ω_0 the intensity excess noise of the entire spectrum of the cavity signal originates from this $S_{\text{CEO}}(\Omega_0)$. It is at the same time the integral of the excess noise over the cavity transmitted spectrum. This is a reasonable statement as the RF-spectra of cavity excess- and amplitude noise do not depend on the optical wavelength. For discrete spectral bands n of power P_n and a given Ω_0 , the measured signal levels $S(\omega_n)$ are calibrated by the condition: $S_{\text{CEO}} = \sum_n S(\omega_n)P(\omega_n)$.

Figure 4.10 shows the measurement results. A non constant distribution, asymmetric with respect to the central wavelength is measured for both intensity and phase noise. The structure of both curves is independent of the noise detection frequency Ω in an interval of 300 kHz. The spectral intensity noise shows a local minimum close to central frequency ω_0 and increases significantly towards the IR-wing of the spectrum. The phase noise shows in contrast a decay by approx 10 dB towards the IR-wing. For all wavelengths, the phase noise is by 40 to 50 dB larger than the intensity noise (comparing the left and right scales in Fig. 4.10). In addition, a modulation-like structure with a period of approximately 30 nm is present. By a variation of the stability range of the Ti:Sapph oscillator cavity, this structure was reproduced to be independent of the strength of the Kerr-effect.

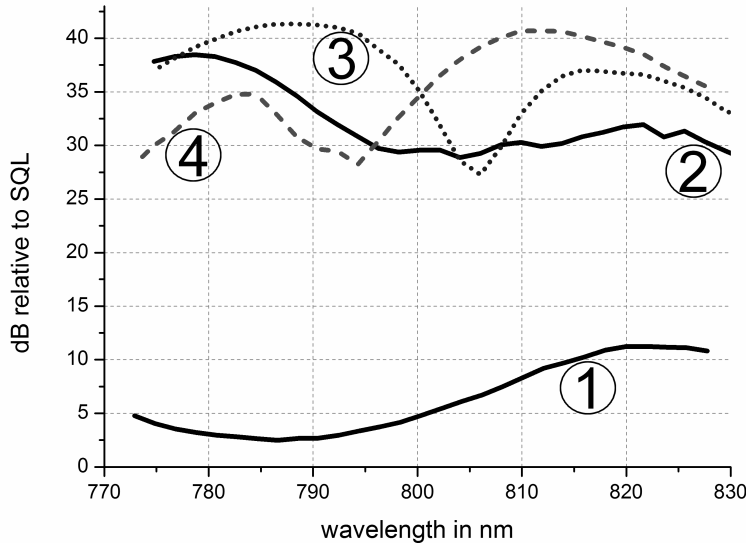


Figure 4.11: *Second experimental analysis of spectral phase and intensity noise.* The Ti:Sapph oscillator at a 500 kHz side-band frequency and 1 mW detected signal. Data relative to the SQL, ① intensity noise; phase noise for different optical lock wavelengths at 70 mbar, calculated from cavity excess intensity noise in transmission: ② 818 nm ③ 797 nm ④ 780 nm.

Second approach: In order to provide higher measurement precision and reproducibility, the measurement above was automated. To this aim, a photodiode was mounted on a translation stage to scan the dispersed optical spectrum of cavity-seed and -transmission. The advantages are a short measurement time and a large number of data-points, the disadvantage is the high dynamic range of detected intensities over the covered spectrum. Figure 4.11 shows the amplitude and phase noise of the Ti:Sapph oscillator. The latter has been calculated using Eq.4.11. In addition, the cavity has been locked at three different optical wavelengths.

The variation of the intensity noise of the comb, *first approach*, Fig.4.10, is confirmed. Nevertheless, the detected spectral phase noise is different: the observed noise levels ②, ③ and ④ in Fig.4.11 are a function of the optical lock-point. In two cases they show a significant variation with a local minimum close to the optical lock-point. This behavior may be explained with the considerations of section 2.7.2: The apparent detection frequency $\Omega(\omega)$ depends on the residual dispersion of the passive cavity $\phi_{\text{cavity}}(\omega)$, see Fig. 4.7. The phase to amplitude conversion factor $\tau(\Omega) \rightarrow \tau(\Omega[\phi_{\text{cavity}}(\omega)])$ in Eq.(4.11) is consequently a function of the optical wavelength. It is in addition a function of the optical and the electronic lock points in the Pound-Drever-Hall scheme. This context explains the characteristic detected noise minima close to the lock-wavelengths. The effect disappears for a lock at 818 nm, trace ②. The variation of the apparent Ω being purportedly smallest for this measure, it represents most-likely the phase noise distribution of the comb. The envelope is similar to the spectral phase noise observed with the first method, Fig. 4.10, trace ②.

In summary, both measurements show the same difference between the distributions of intensity and phase noise over the optical spectrum. At 500 kHz detection frequency, the phase noise is approximately 35 dB above the intensity noise. Both are measured to vary by up to 10 dB over the optical spectrum. For the oscillator investigated here, amplitude noise decays towards the VIS spectral wing and phase noise decays towards the IR wing. The observed modulation like structure of spectral phase noise requires further measurements to be confirmed.

Consistency with the rubber-band model. For a given frequency comb $\omega_n = n\omega_{\text{rep}} + \omega_{\text{CEO}}$, the distribution of phase noise over the optical frequencies of a comb can be described by the rubber-band model [21]. It has been discussed in section 2.4.4: For any perturbation of the oscillator generating the frequency comb, its lines will expand and contract around a given fix-point frequency. For the oscillator used here, fluctuations of the pump-intensity P were found to be a mayor driver of phase noise. The corresponding fix-point frequency has been found to be a function of the corresponding repetition-rate and CEO-frequency sensitivities, see Eq.(2.62):

$$\omega_{\text{fix}} \simeq \frac{d\omega_{\text{CEO}}}{dP} \left[\frac{d\omega_{\text{rep}}}{dP} \right]^{-1} \omega_{\text{rep}} \quad (4.12)$$

The phase noise spectral density S of a line ω_n , originated by pump intensity noise, is a function of the distance to the fix-point $S_{\omega_n} \sim (\omega_n - \omega_{\text{fix}})^2$. For the Ti:Sapph oscillator considered here, the pump-power fix-point is determined to be $\omega_{\text{fix}} = 2\pi \cdot 233$ THz (1284 nm) and is located on the IR-side of the gain-profile centered at 375 THz. The phase noise spectral density S_{ω_n} is in conclusion expected to rise from the IR-side of the optical spectrum. This is indeed the case for the slope of the data shown in Fig. 4.10 and Fig. 4.11.

Consistency with further literature. These results are consistent with the considerations of Wahlstrand et al.[20]. They simulate the linewidth of a frequency comb using several experimental measured noise coupling parameters (see page 32). Although this approach does not include a spectral variation of the oscillator dispersion, it predicts the position of the comb line of lowest linewidth. The latter is a function of the physical effect that dominates correlations between timing and CEO fluctuations. If this is timing jitter that couples through dispersion to phase, the comb frequency of lowest noise is predicted on the IR side of the covered spectrum. This is the case for the general slope of the spectral phase noise distributions reported here. It is therefore the cavity dispersion - and its variations - that governs the distribution of spectral phase noise.

Structured spectral phase noise. The possible modulation like structure of spectral phase noise visible in Fig.4.10 could be interpreted using the theory of H.A.Haus et al.[10]. Fluctuations of the shot noise driven central frequency drive fluctuations of the repetition rate. The origin of this effect is a non vanishing intracavity GVD. The latter is required for stable operation of soliton-fs lasers [92], and obtained by the use of chirped mirrors. Nevertheless, these mirrors are always subject to unavoidable higher order dispersion effects [92]. Their magnitude can be estimated as below 10% of the mirror GVD [121] and they could be the origin of the spectral modulation of phase noise. There is no other optical element in the oscillator cavity with such spectral dependent properties. The observed structure is in addition robust against a variation of main parameters of the Kerr-Lens mode locked laser used here. Nevertheless, the direct measurement of the residual dispersion of an oscillator cavity is rather involved and beyond the scope of this thesis.

In contrast to the arguments above, the term coupling central frequency fluctuations to the repetition rate is proportional to the square of the dispersion D of the cavity [10]. In this context, a 10% modulation of the GVD cannot be the origin of a 3 dB noise level change. The model of Haus et al. gives therefore only an indication for the origin of the observed structure, but is insufficient to model it.

In summary, a modulation like structure of spectral phase noise cannot be confirmed so far.

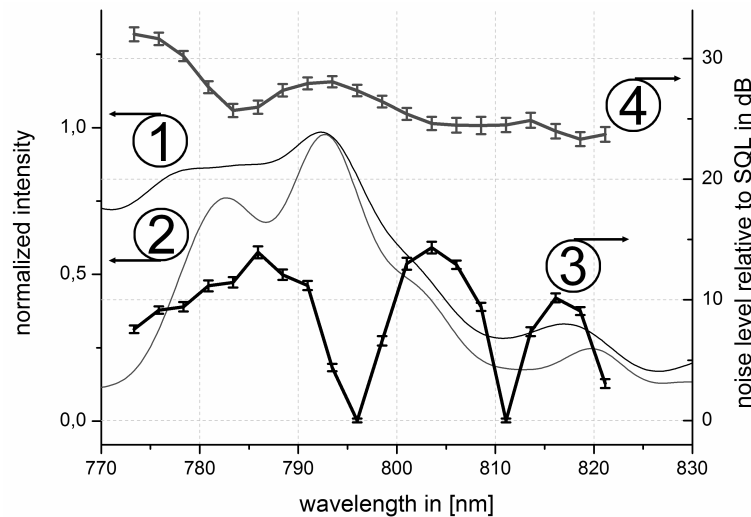


Figure 4.12: Spectral intensity and phase noise from a PCF seeded with the Ti:Sapph oscillator.

① spectrum of the generated supercontinuum seeding the passive cavity, ② spectrum transmitted by the cavity, ③ intensity noise of the PCF signal, ④ phase noise of the PCF signal obtained from the cavity excess intensity noise in transmission, eventual amplitude-phase-noise correlations are neglected

Noise analysis over the optical spectrum - a supercontinuum source. When seeded with the Ti:Sapph oscillator characterized above, a photonic crystal fiber (PCF) generates a coherent octave spanning frequency comb. The coherent part of the PCF signal can be transmitted through the broadband cavity, see Fig. 4.6. The measured intensity excess noise in transmission allows to analyze its spectral phase noise. The results are shown in Fig. 4.12. Data are obtained for a 50 nm broad spectral window of the supercontinuum that is resonantly transmitted by the cavity. The intensity noise trace ③ shows unstructured variations of 10 dB. In contrast, the phase noise trace ④ calculated with the exact form of Eq.(4.11) is nearly constant. In order to provide a first approximation, eventual amplitude-phase noise correlations have been neglected.

The slope is similar to the phase noise observed for the Ti:Sapph oscillator Fig. 4.10 and Fig. 4.11, and again orders of magnitude larger than the intensity noise.

The measurement scheme of phase noise suggested here is consequently applicable to any coherent frequency comb. Other techniques reported in the literature [122, 120] are typically of less dynamic range and sensitivity.

Conclusions. A broadband passive cavity is described as an efficient detector for CEO-phase noise and spectral phase fluctuations of optical frequency combs. Together with shot noise resolving intensity noise detection it provides high dynamic range and a sensitivity close to the SQL. It is intrinsically broadband concerning the optical spectrum and the noise analysis frequency. Revealing here a structured, within 10 dB non constant spectral phase noise for a Ti:Sapph oscillator, it can be applied to any coherent comb source.

4.2.1 Additional considerations

I. Properties of the Ti:Sapph oscillator cavity. One result of the section above is the precise measurement of non-constant spectral phase noise of a Ti:Sapph oscillator, Fig. 4.10. From the related literature, this phase noise structure could be attributed to spectral variations of dispersion in the oscillator cavity.

Intracavity dispersion of the oscillator used here is managed by chirped mirrors [92]. A schematic of the setup of this oscillator is shown in Fig. 4.13. The dispersion of such mirrors always exhibits a modulation in the order of several fs^2 [121]. The modulation depth is essentially a function of the optical bandwidth of the mirror. Considering all optical elements in a Ti:Sapph oscillator, the mirror dispersion is the only property that may vary significantly within the 100 nm bandwidth.

Two sets of chirped mirrors are used in the oscillator (see Fig. 4.13), one in the short- and one in the long arm. Their properties are directly measured by the use of *spectral interferometry* [123, 124]. The setup is shown in Fig. 4.15, left. A Coherent MIRA Ti:Sapph oscillator together with spectral broadening in a photonic crystal fiber has been used as broadband light source. The spectrum $I(\omega)$ propagates through a Michelson interferometer with exchangeable end-mirrors, see Fig. 4.14. A difference in dispersion in both interferometer arms leads to constructive and destructive spectral interference at the output port $\tilde{I}(\omega)$. Using a calibration of the interferometer with metallic mirrors, the GVD of a mirror can be obtained from the interference structure $\tilde{I}(\omega)$ recorded with a commercial spectrometer.

The measured values of spectral dependent GVD are shown in Fig. 4.15, left. It turns out that the obtained data is of poor quality due to additional interferences in the multimode fiber seeding the USB spectrometer. The obtained period of the GVD modulation structure depends strongly on the bandwidth of the FFT-filter necessarily applied to the measurement data. Nevertheless, the mean GVD value for the entire spectrum reproduces the expected value for a known mirror set and is robust to

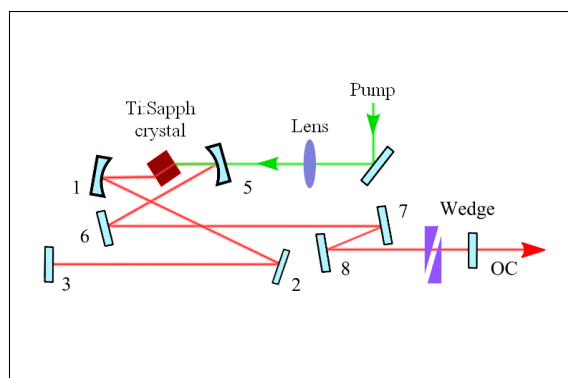


Figure 4.13: Scheme of the cavity of the Femto-lasers SYNERGY Ti:Sapph oscillator considered here. The cavity consists of two spherical mirrors M1 and M5, an output coupler OC and two arms containing chirped mirrors: a short (M2 +M3) and a long one (M6, M7, M8). A pair of thin intracavity edges provides static tuning of the CEO frequency. The Ti:Sapph crystal is the gain medium.

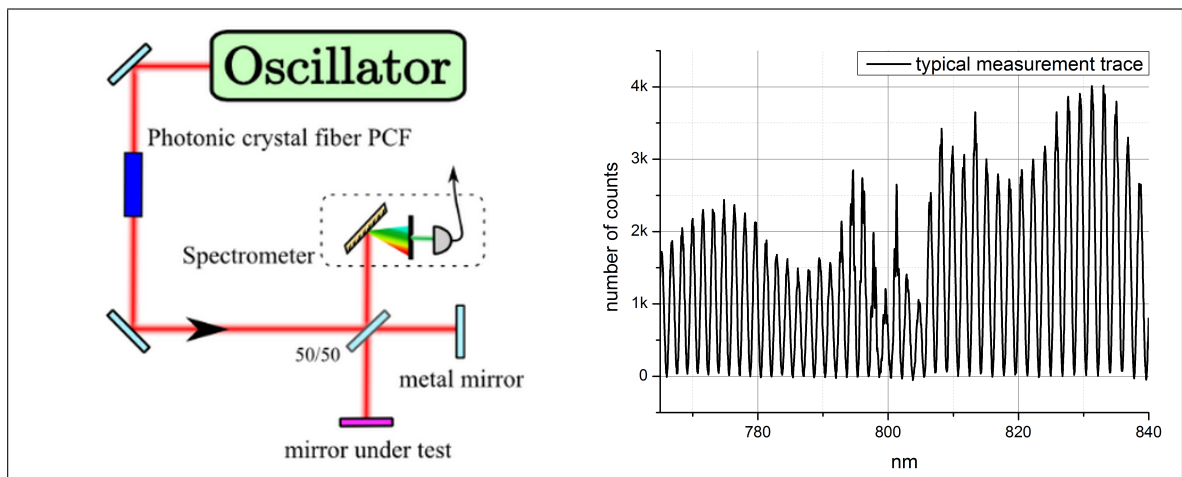


Figure 4.14: Measurement of the mirror dispersion by the use of spectral interferometry.

left: Michelson interferometer for spectral interferometry. A Ti:Sapph oscillator (120 fs, 5 nm FWHM) is used together with a photonic crystal fiber to generate a spectrum of 100 nm bandwidth. The test mirror replaces a metallic reference mirror that is used to measure the instrument function.

right: typical modulated spectrum recorded at the spectrometer

changes of the FFT-filter properties. The mean GVD values of the chirped intracavity mirrors are obtained.

This experiment is in conclusion not sufficiently sensitive to reveal the fine-structure of the intracavity dispersion of the SYNERGY oscillator. Nevertheless, a much simpler, indirect measurement can be used to obtain the GVD properties indirectly. This is the broadband measurement of the mirror transmission.

Figure 4.15, right, shows the normalized transmission of the SYNERGY cavity

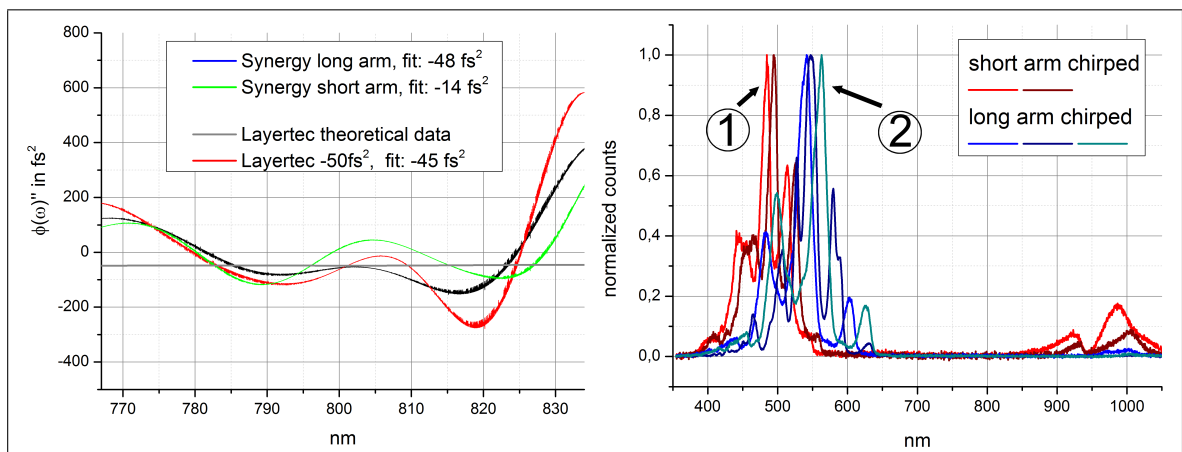


Figure 4.15: Detailed analysis of the dispersion properties of the SYNERGY Ti:Sapph oscillator.

left: Measurement of the dispersion properties by spectral interferometry reproduces expected mean values of the GVD. The quantification of the spectral modulation of the GVD is subject to significant uncertainties. *right:* Transmission of the chirped mirrors of the Ti:Sapph cavity. A spectral shift of otherwise identical mirror properties can compensate periodic dispersion variations of a mirror assembly. The mirrors of the oscillator exhibit group-wise (① and ②) the same reflectivity structure with a shift of approximately 10 nm for the two arms.

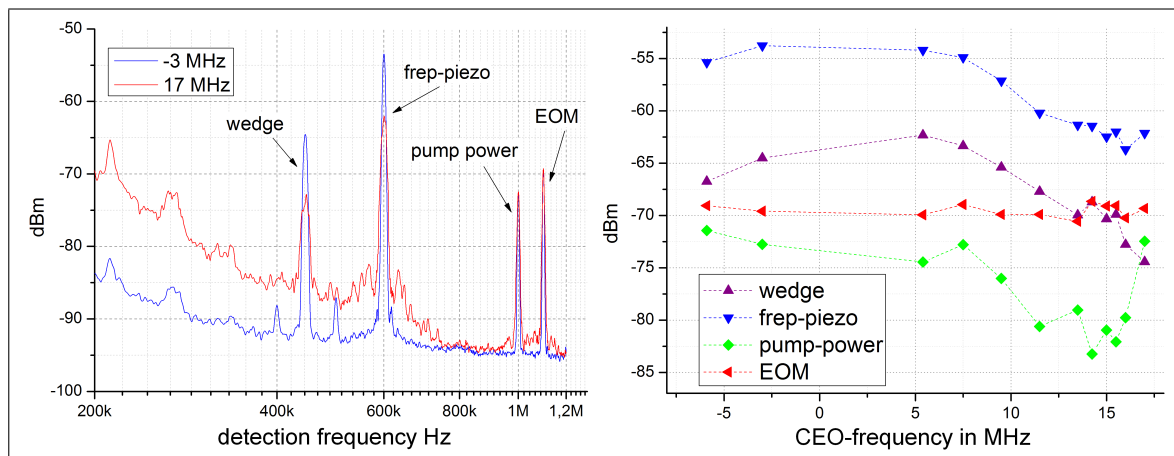


Figure 4.16: Phase to amplitude modulation transfer by the cavity. A comb can be phase modulated in different ways (see text). *left:* All types of phase modulation lead to an amplitude signal in transmission. Here for a cavity pressure of 106 mbar at 17 MHz and -3 MHz CEO-frequency.

right: Tuning the CEO-frequency of the comb, the conversion effect changes in different ways for the different modulation types. The wedge is mounted on a piezo-element that is driven at a resonance.

mirrors when measured with an incoherent white light source. Within the two mirror groups, the identical properties are shifted by approximately 10 nm. A designed shift of the spectral properties of a set of chirped mirrors, by half the underlying dispersion modulation period, is commonly used to reduce the dispersion variations for their assembly. Although the measurements above present several indications on a spectral variation of dispersion, they are insufficient to quantify this effect.

II. Transfer of different types of comb-phase modulation. The section above describes a broadband passive cavity as a detector of phase noise. Nevertheless, *phase noise* can have different meanings in an optical frequency comb. Repetition rate and CEO-phase noise are examples of this ambiguity. In terms of experiments, the following four types of phase modulation have been experimentally accessible for the Ti:Sapph oscillator used here:

1. a modulation of the position of an end-mirror of the oscillator cavity leading to a change of the repetition rate, the spacing of the frequency comb
2. a modulation of the pump-power of the oscillator, leading essentially to a change of the CEO-frequency, thus a frequency shift of the entire comb
3. a phase modulation by an EOM leading to a homogeneous phase side-band signal for any line of the comb spectrum
4. a rapidly moving wedge in the beam path leading to varying spatial and temporal chirp

Figure 4.16, left, shows that all the different phase properties of a frequency comb are detectable by the intensity signal transmitted by the cavity. The right plot shows that the transfer of these different phase modulations is in addition a function of the mean CEO-frequency of the comb. The spectrum transmitted by the passive cavity depends on the CEO-frequency. The modulation transfer is consequently a function of the transmitted spectrum if the underlying phase modulation is not constant over the optical spectrum. As expected, Fig. 4.16, right, shows that the modulation by the EOM is the same for all parts of the optical spectrum. This is not the case for the other types of phase modulation. It indicates in conclusion that their underlying spectral distribution of phase modulation is different from a constant.

4.3 The transfer function representation

The results of the sections 4.1 and 4.2 arise from the properties of a passive cavity to filter and to interconvert the noise field quadratures. In order to complete the characterization of the Ti:Sapph-cavity system, and to verify the consistency of the observed signals, the so-called transfer function approach can be applied [96, 125].

The complex transfer function $H(f)$ is defined as the ratio between the output signal $Y(f)$ to the input signal $X(f)$ of a linear, time-invariant system. Only the absolute value of $H(f)$ and small perturbations δ of the oscillator mean properties are considered here. In this context, $H(f)$ is called the *noise transfer function* of the system:

$$H(f) = \frac{\delta Y(f)}{\delta X(f)} \quad (4.13)$$

This approach is applied here to the entity of the electro-optical system of the preceding setups. It is shown in Fig. 4.17. The strength of the transfer function approach is that the measurement of $H(f)$ corresponds to an exposure of the system to white noise. The recorded slopes correspond thus to a characterization of the impact of spontaneous emission on the optical system.

The characterizations done here consist of a measurement of the transfer function of the cavity, the oscillator and different detection schemes for phase noise, see Fig. 4.17. The source of amplitude modulation is an acousto optical modulator (AOM) with a 3 dB cutoff at 1 MHz. Above, its transfer function decays by a slope of -100 dB/dec at 3 MHz. Due to this steep slope, noise transfer functions of all other elements can only be measured up to approximately 2 MHz.

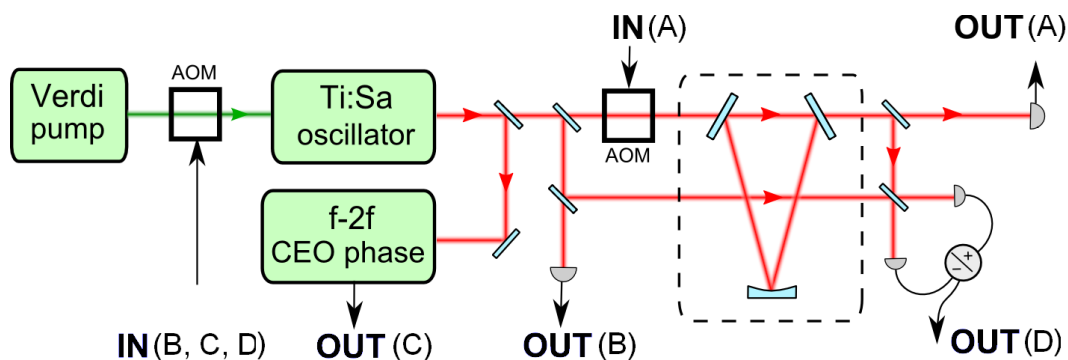


Figure 4.17: The properties of all noise conversion/filtering setups presented in this thesis are in principle accessible by transfer function analysis. Their measurement characterizes: **A**) the passive cavity; **B**) and **C**) the Ti:Sapph oscillator; **D**) the phase noise measurement: self-referenced homodyning of the cavity transmission. The intensity transfer function of the driving AOM has been characterized separately.

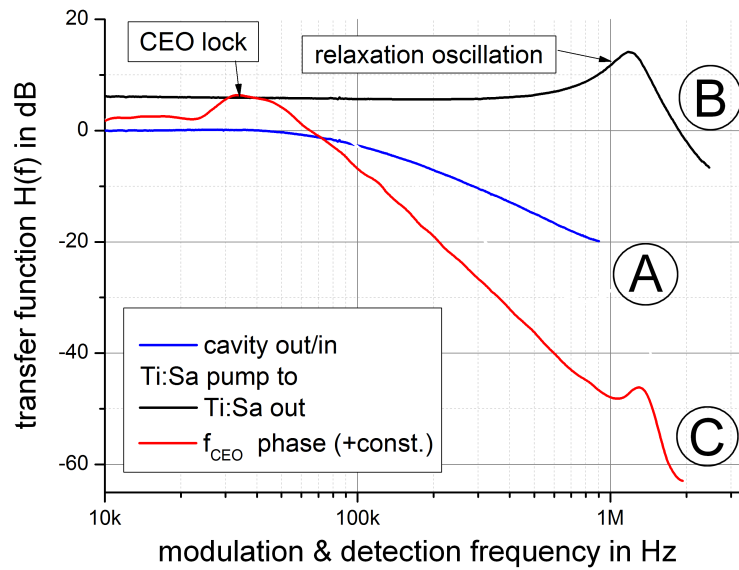


Figure 4.18: Characterization of the Ti:Sapph oscillator and the passive cavity. Noise transfer functions of the principal experimental objects of this thesis. Intensity transfer function of \textcircled{A} the passive cavity, \textcircled{B} the Ti:Sapph oscillator; \textcircled{C} the CEO-phase of the oscillator, in $\text{rad}^2/[\text{Hz} \cdot \text{W}]$

Characterization of the Ti:Sapph oscillator and the passive cavity. At first, the passive cavity itself is characterized. The setup Fig. 4.17, \textcircled{A} , is used to this aim. The data are shown in Fig. 4.18. They determine the cutoff-frequency of the cavity to approximately 130 kHz. This result is consistent with the ringdown measurement of section 3.2.4.

Second, the sensitivity of the Ti:Sapph oscillator output power and CEO-phase to pump power noise is characterized. To this aim the setups Fig. 4.17, \textcircled{B} and \textcircled{C} are used. The results are shown in Fig. 4.18: trace \textcircled{B} for the output power, trace \textcircled{C} for the CEO-phase. As shown by Scott et al.[96], the Ti:Sapph oscillator is a low gain white amplitude noise amplifier up to the peak at approximately 1 MHz. This is the relaxation oscillation (RO) of the oscillator. Above this frequency, the intensity noise transfer function drops rapidly. A rate equation model predicts -20 dB/dec [96]. The transfer of amplitude noise to CEO-phase noise drops by 40 dB/dec out of the bandwidth of the lock and below the RO-frequency. This behavior is consistent with the theory of H.A.Haus [10]. It strengthens the conclusion of page 111, stating that phase noise of the free running Ti:Sapph oscillator is spontaneous emission limited.

Indeed, the slope of the transfer function Fig. 4.18, trace \textcircled{C} is similar to the slope of the CEO-phase noise reference data Fig. 3.5. A transfer function measurement corresponds to a white noise excitation of the system. In consequence, the origin of the free running oscillator CEO-phase noise is purportedly spontaneous emission.

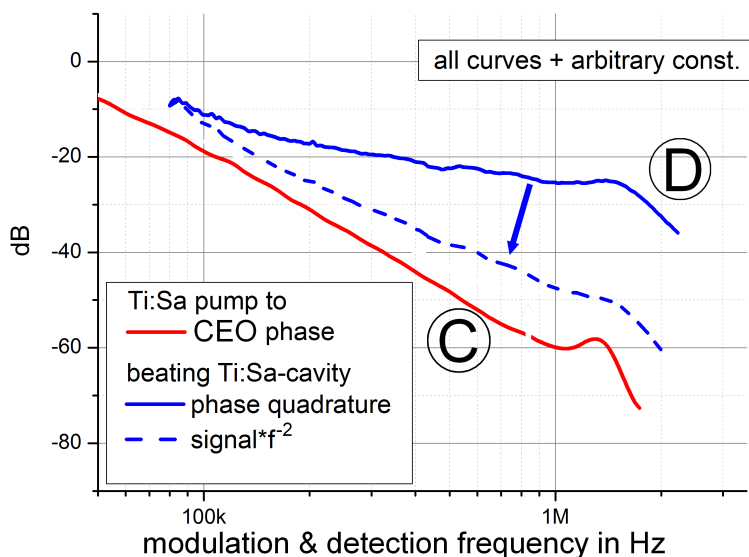


Figure 4.19: Characterization of different phase noise measurements. Noise transfer functions, oscillator pump modulation to f - $2f$ CEO \textcircled{C} and to the *cavity-homodyne-measurement* \textcircled{D} . The multiplication of the cavity-homodyne signal with the predicted second order decay shows that this beating measurement indirectly samples the CEO-phase (noise) distribution.

Characterization of the self-referenced cavity homodyne measurement.

Section 4.1 measured the phase noise of a Ti:Sapph oscillator down to the SQL using a setup of self-referenced interference. The transmission of the broadband passive cavity has been homodyned with the initial signal itself. Here, the transfer function approach is used to confirm the validity of this scheme from a different perspective.

The measurement results are shown in Fig. 4.19. The slope of the CEO-phase \textcircled{C} is reproduced if the detected signal \textcircled{D} is multiplied with the second order decay predicted from theory, Eq.(4.8).

The results above only discuss slopes of signal, an absolute calibration is neglected here. It is not necessary, the principal aim here is to underline the versatility of transfer-function measurements on complex electro-optical systems. They confirm here the outcomes of the previous sections.

4.4 Quantum-limited measurement of phase noise - ready to use

This section compares the methods to detect phase noise in frequency combs developed in the first and second section of this chapter. For sufficiently low intensity noise, these methods can be significantly simplified. The resulting, ready to use configuration is applied to compare phase noise of Ti:Sapph oscillators and a fiber-based oscillator relative to the SQL.

Introduction. One focus of this work is to study of the noise properties of a Ti:Sapph oscillator close to the SQL. The aim is to apply this oscillator to quantum-limited measurements. Its amplitude and phase noise has been extensively characterized close to the SQL in the previous sections. Both typically reach the SQL at microsecond timescales. Nevertheless, stable Ti:Sapph oscillators are cost expensive and not suitable for out-of-the-lab applications due to alignment issues.

Fiber-based oscillators are much more robust and can be low-cost. Although their noise properties have been characterized extensively [17, 126] no information is available relative to the SQL. A precise characterization relative to this limit will help to evaluate their applicability for high precision metrology experiments on short timescales [5] as also for quantum optical experiments with frequency combs [24]. This information becomes accessible here even if the comb is not suitable for coherent broadening/ f - $2f$ beating schemes.

The method presented here provides a readily applicable tool to characterize phase noise in any optical frequency comb close to the SQL. Similar to the previous section 4.2, these methods could also be applied to a spectral resolved analysis of phase noise.

This section is organized as follows: *First*, the different methods discussed so far are put into a common context. Subsequently they are compared to the simplest possible cavity-assisted phase noise detection. *Second*, the CEO-phase noise of a Ti:Sapph oscillator is characterized again using the simplified method based on the analysis of the reflection of a resonant passive cavity. For low noise levels at high sideband frequencies, the phase noise distribution obtained with an f - $2f$ measurement is reproduced. *Third*, this approach is applied to a fiber oscillator not suitable for coherent broadening within an f - $2f$ measurement. It turns out that even the strongly simplified experimental setup is sufficient to detect comb phase noise close to the standard quantum limit.

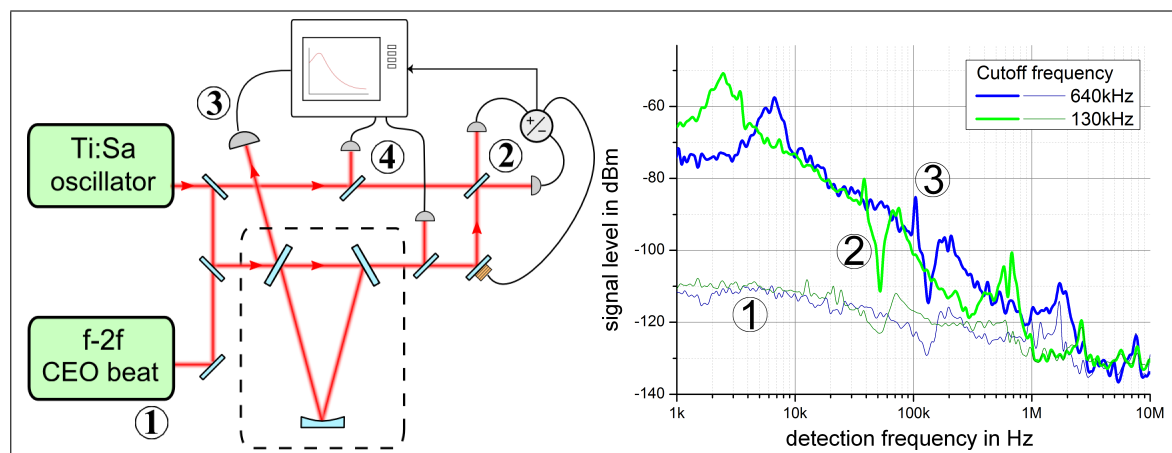


Figure 4.20: *Left:* Four methods to measure CEO-phase noise of a frequency comb. Repetition rate noise is assumed to be negligible. ① f-2f beat (after spectral brodening using a PCF if the oscillator is not octave-spanning); By the use of a passive cavity: ② homodyning the beam with a cavity-filtered part of it, ③ intensity noise in reflection, ④ intensity excess noise in transmission

Right: Typical Pound-Drever-Hall-error signal providing information about the seed phase noise. The signal depends on the cavity cutoff frequency: ① electronic noise level, ② 130 kHz, ③ 640 kHz

Comparison of different methods. Figure 4.20, left, shows possible methods for a cavity-assisted measurement of frequency comb phase noise. In parallel to an f-2f detection, the transmission of the cavity can be interfered with a part of the original signal (see section 4.1). This measurement is called here: *homodyne method*. Another approach is to evaluate the amplitude excess noise arising from incident phase noise, in transmission from the cavity (see section 4.2). It is called here: *transmission method*. The homodyne method is of highest sensitivity to phase noise and even quantum-limited. The transmission method is less sensitive: the cavity also filters amplitude excess noise that may arise from phase noise. It will turn out here that the cavity reflection can also be used to detect phase noise down to the SQL. It has been shown in the literature that this signal can be used to measure all the information about the noise in a state of light [30].

All these four techniques can be compared to a direct evaluation of the Pound-Drever-Hall error signal [100]: A typical data-trace for this method is shown in Fig. 4.20, right, for a MIRA Ti:Sapph oscillator. This method is in practice subject to amounts of electronic noise. It turns out to be not suitable for an evaluation of phase noise properties close to the SQL.

For this reason, the following measurements apply only the *transmission method* and the *homodyne method* to compare the phase noise of different oscillators close to the SQL.

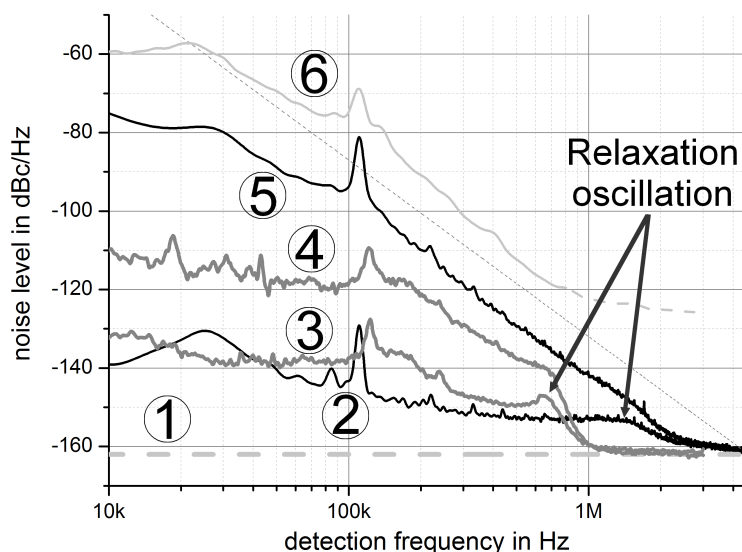


Figure 4.21: Transmission method to characterize low peak power Ti:Sapph oscillators. The intensity noise of a passive cavity in transmission exhibits excess noise arising from comb phase noise. Data relative to the SQL ①. **SYNERGY**: CEO phase noise from f - $2f$ beating ⑥, intensity noise of seed ②, cavity output ⑤. **MIRA**: intensity noise of seed ③, cavity output ④.

I. Transmission method - applied to a low peak power Ti:Sapph oscillator.

Fig. 4.21 compares the intensity and phase noise of different Ti:Sapph oscillators close to the SQL. They are: the Femtolasers SYNERGY² oscillator studied in the previous sections and the Coherent MIRA oscillator³ used in the next section. An f - $2f$ scheme with preliminary coherent broadening cannot be applied to this oscillator due to its lower peak power.

According to Fig. 4.21, the intensity noise of both oscillators (traces ② and ③) is close to the SQL for the detection frequencies here relevant. The most significant difference arises from the relaxation oscillation (RO) frequency. For the MIRA it is approximately 300 kHz below the one of the SYNERGY. As discussed in Eq.(3.3), page 78, intensity and phase noise of a laser strongly decrease above this frequency. Quantum limited properties of the MIRA at lower radio-frequencies than for the SYNERGY can consequently be predicted, see Fig. 4.21 and Fig. 4.22.

In order to characterize phase noise, the results of the *transmission method* are shown in Fig. 4.21, traces ④ and ⑤. Above the cavity cutoff⁴ and below the relaxation oscillation, the slope of the cavity excess intensity noise appears to be the same for both oscillators. With respect to their negligible intensity noise and close to the SQL, the phase noise properties of both oscillators are consequently very similar.

² 1 W, 30 fs, 156 MHz repetition rate ³ 1 W, 140 fs, 75 MHz repetition rate ⁴ approximately 200 kHz for the one applied to the MIRA

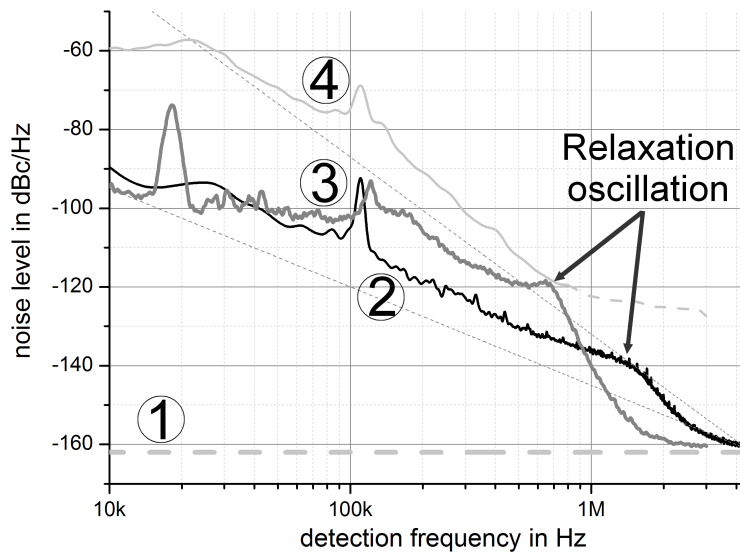


Figure 4.22: Homodyne method. Homodyne detection of the cavity output (signal) with the oscillator output itself (local oscillator), in phase quadrature. Data relative the SQL ①.

SYNERGY: ② homodyne signal, ④ $f-2f$ signal, **MIRA:** ③ homodyne signal. Dotted lines as a guide to the eye. Above the cavity bandwidth and below the relaxation oscillation-frequency the slopes of the signals are identical.

II. Homodyne method - applied to a low peak power Ti:Sapph oscillator.

Applied to both oscillators, the homodyne method phase noise measurement leads to the signals shown in Fig. 4.22. Trace ② for the SYNERGY, trace ③ for the MIRA. The method being of quantum-limited sensitivity to phase noise, the data shown are of higher signal to SQL ratio than those of the transmission method above. The conclusions from Fig. 4.21 are confirmed here: for a frequency interval above the cavity cutoff and below the relaxation oscillation, the phase noise of both oscillators follows the same slope. Nevertheless, due to different relaxation oscillation frequencies, the MIRA oscillator phase noise is quantum limited at a lower frequency than the SYNERGY oscillator.

Summary. It is in conclusion possible to characterize phase noise close to the SQL of an oscillator with insufficient bandwidth/peak-power for coherent broadening/ $f-2f$ beating. This is here the Coherent MIRA. By the use of two different, cavity assisted measurements, it is shown that: A careful choice of the relaxation oscillation frequency Eq.(3.3) could provide a Ti:Sapph oscillator, quantum-limited below 1 MHz detection frequency.

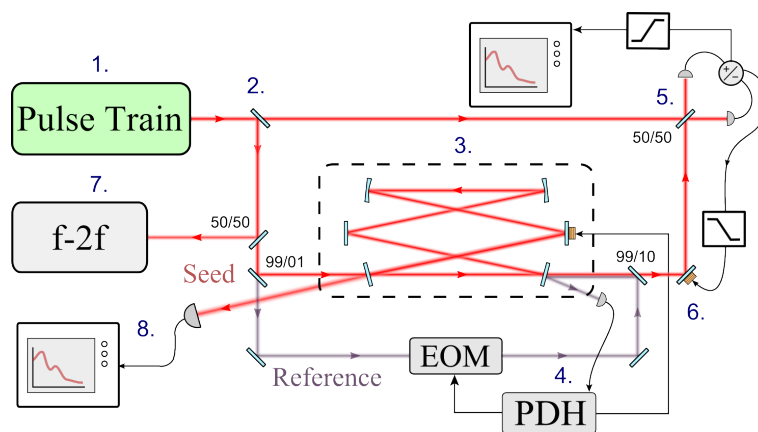


Figure 4.23: Experimental scheme used in this section together with the SYSNERGY oscillator. 1 Mode-locked Ti:Sapph oscillator at 156 MHz, output power 1 W, pulse duration below 30 fs, 2 selection of measurement type by a flip 50/50 beam splitter, *no splitter*: intensity noise measurement, *with splitter*: cavity-homodyne measurement, 3 passive cavity in a mbar vacuum chamber, 4 PDH-locking scheme, 5 balanced (homodyne) detection, 6 lock of the relative phase, 7 f-2f interferometer and signal analysis, 8 shot noise resolving analysis of the reflected signal

4.4.1 Comb phase noise from the cavity reflection

It has been discussed in the previous sections that the transmission of a broadband resonant cavity and shot noise resolving, interference detection can resolve phase noise of frequency combs with quantum-limited sensitivity. The scheme requires a lock of the mean relative phase of the two interfering beams, which adds experimental complexity. In order to provide a simplest possible and readily applicable measurement solution, it is shown here that for negligible intensity noise it is sufficient to consider the signal reflected from the locked cavity. This strongly simplifies the setup.

The experimental setup. Figure 4.23 shows the setup used to compare cavity-homodyne method to the direct analysis of the cavity-reflection. The interference method has been extensively discussed above. To recall the basic principle: Above its cutoff frequency the cavity filters the phase noise of the transmitted beam. This leads to a phase noise-difference compared to the original seed. The difference can be detected down to the SQL using a shot noise resolving, balanced interference detection. A seed phase noise distribution f^{-n} is detected within a f^{-n+2} slope.

Reflection of a passive cavity. An interference similar to the homodyne detection occurs in the reflection of the passive cavity. Even at resonance, a part of the seeding beam is reflected from the cavity. It interferes with a small signal leaking through the coupling mirror from the field stored inside the cavity. The relative phase between the directly reflected light and the one leaking from the resonant cavity is set by the electronic lock-point on the Pound-Drever-Hall error signal.

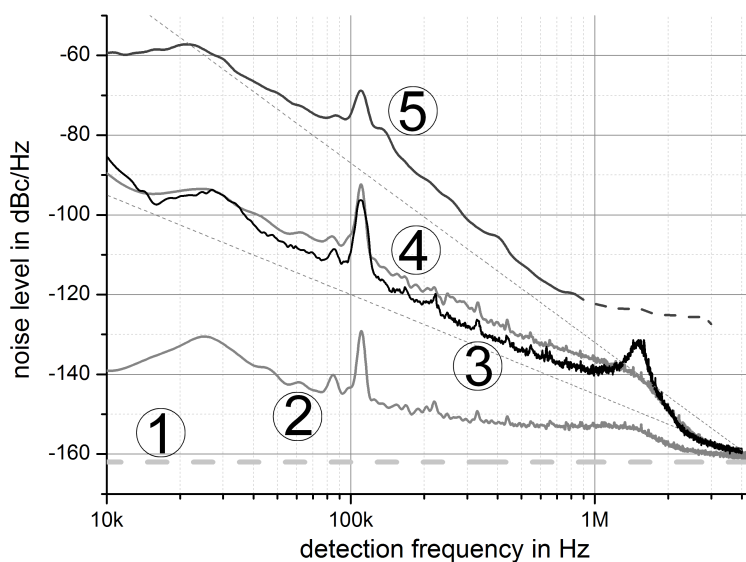


Figure 4.24: Equivalence of the cavity homodyne- and the cavity reflection-method for quantum-limited phase noise detection. ① SQL for 8 mW detected power, ② intensity noise of the Ti:Sapph oscillator, ③ cavity reflection at Pound-Drever-Hall lock point optimized for highest signal, ④ self-referenced cavity-homodyne signal, ⑤ CEO-phase noise recorded with an f - $2f$ interferometer. *Note:* The cavity reflection was recorded with a different setting of the oscillator stability range. This changes the relaxation oscillation peak at 1 MHz between traces ③ and ④.

To verify this concept, Fig. 4.24 compares the CEO noise obtained from an f - $2f$ beating, intensity noise, and the signals from *cavity-homodyning* and *cavity reflection*. The two latter signals show identical slopes. They are well distinguishable from amplitude noise. As expected, the slope of the CEO-phase noise times the squared detection frequency f^2 . This validates the approach.

Further remarks. First, the cavity-reflection measurement requires sufficiently low intensity noise of the seeding beam. In contrast to the cavity-homodyne measurement, the simplified approach in reflection is always sensitive to the intensity noise of the seeding beam. Second, the mean relative phase of both beams is set by the electronic lock point on the Pound-Drever-Hall error signal on which the cavity is locked. It is in practice difficult to measure this point with high precision. While tuning the electronic lock point, the maximum recorded intensity noise in reflection indicates the experimentally best possible mean relative phase between the two interfering beams.

Conclusions. The simplified approach using the cavity reflection is in consequence only suitable to detect the slopes of phase noise and for the verification of quantum-limited phase noise properties. Due to its sensitivity to intensity noise and the uncertainty contained in the electronic lock point, absolute phase noise quantification is subject to a number of uncertainties. This can nevertheless be solved by referring to a measured SQL.

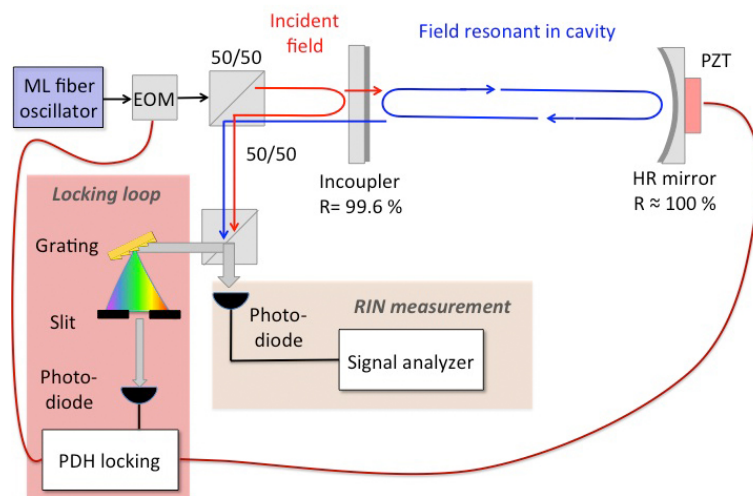


Figure 4.25: Schematic of the cavity-reflection method to measure oscillator phase noise in a simplified, ready to use configuration. It reduces the complexity of the homodyne scheme Fig. 4.23, and is applied here to a mode-locked fiber oscillator. The reflection of the passive cavity interferes with the leakage of the signal stored in the cavity.

4.4.2 A ready to use schematic - applied to a Yb-fiber oscillator.

The experimental setup. Figure 4.25 shows a schematic of the simplified experimental setup, applied to a fiber oscillator: The Yb-doped fiber oscillator to be characterized is of stretched-pulse type and is mode-locked by a saturable-absorber mirror. The center wavelength of the spectrum is about 1035 nm. The laser possesses a measured total GDD of 0.012 ps^2 . The repetition rate is 75 MHz. The stable operation of the fiber oscillator manifests in a low repetition rate fluctuation, which is -80 dBc at 100 Hz side-band frequency. The external resonator is locked to the laser by using the Pound-Drever-Hall (PDH) technique. The PDH error signal is obtained from the central frequency of the comb to avoid eventual bistabilities arising from cavity dispersion. An electro-optical resonator imprints a 5 MHz phase modulation on the laser's output. Only the central part of the spectrum is used for the derivation of the PDH error signal. By controlling the position of a piezo-actuated mirror, stable locking is achieved over a time span larger than 10 minutes. To keep the design of the external resonator as simple as possible, we chose a semi confocal resonator with a 300 MHz free-spectral-range. The cavity's linewidth is about 200 kHz. The seeding beam, reflected from the locked cavity is analyzed in terms of RIN relative to the SQL. Two cases are considered: First, the RIN measurement with the beam-path inside the cavity blocked, and second, a measurement with a locked cavity.

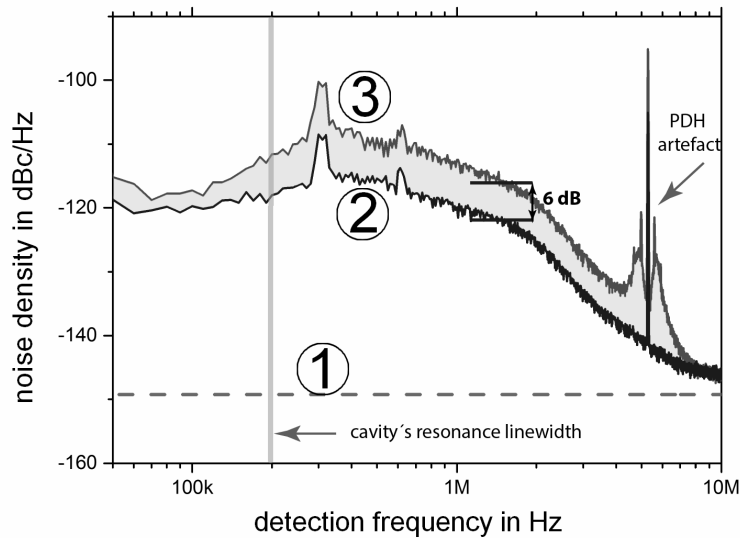


Figure 4.26: Recorded intensity noise with the ready-to use setup Fig.4.25. Quantum limit ① measured with a balanced detection. If the intracavity beam is blocked, the trace ② is observed. The case of a locked cavity is shown by trace ③. The additional noise is highlighted in grey. The grey vertical line indicates the passive cavity linewidth.

Phase noise of a fiber-comb. Figure 4.26 shows the effect of the cavity on the observed intensity noise. When the beam path inside the cavity is blocked, the incoupling mirror acts as a normal mirror and a conventional intensity noise measurement of the fiber oscillator is performed. The high levels, which are up to 30 dB above the SQL, are due to the intensity noise of the pump diodes. They are 10 to 20 dB above the levels observed for the Ti:Sapph oscillator. An independent balanced detector measurement allows the presentation of the data with respect to the SQL. If the cavity is locked, the laser's phase noise is partially converted to intensity fluctuations and manifest in an increase of intensity noise by a significant 6 dB. This effect decreases for frequencies below the cavity's linewidth of 200 kHz. Above 8 MHz detection frequency, the two measurements collapse and are by 3 dB close to the SQL. Consequently, both amplitude and phase noise reach levels close to SQL.

Assignment of the observed noise. The measurements Fig. 4.24 and Fig. 4.26 do not discriminate between repetition rate phase noise $S_{\text{rep}}(f)$ and CEO-phase noise $S_{\text{CEO}}(f)$. They are sensitive to the phase noise of any line of the comb and measure its average over the considered optical spectral band.

For the Ti:Sapph oscillator it will be shown in section 4.5.1 that its governing phase noise property is CEO-phase noise. An indication to this result was obtained earlier in section 3.1: At 1 kHz side-band frequency, the S_{rep} of the Ti:Sapph oscillator was measured at approximately -100 dB below S_{CEO} . The mode number of approximately 10^6 has to be taken into account to estimate its contribution to the phase noise of

individual lines. Nevertheless, the contribution from S_{rep} does not reach the levels of the S_{CEO} . As such, the phase noise observed in the measurements Fig. 4.24 has already been attributed to CEO-phase noise.

For the fiber-comb, the unambiguous measurement method section 4.5.1 is not available. The fiber oscillator pulse peak power is insufficient for coherent broadening to obtain an f - $2f$ beating. Argumentations similar to those for the Ti:Sapph oscillator can give a first indication on the relative contribution of S_{rep} and S_{CEO} to the phase noise in an individual line. The S_{rep} was recorded at -80 dBc at 100 Hz side-band frequency. For a similar fiber oscillator, S_{CEO} was measured significantly above this level [17]. In addition, noise simulations based theory of H.A.Haus [10] can be applied. Therein, the level and the expected slope of S_{CEO} can be calculated using Eq.(2.56), where the parameter τ_w is equivalent to $1/f_{\text{rep}}$. It is confirmed that contributions of S_{CEO} expected from theory are significantly above those of S_{rep} . In addition, the predicted second order decay of $S_{\text{CEO}} \sim f^{-2}$ is two orders lower than the predicted $S_{\text{rep}} \sim f^{-4}$. Together with the $\sim f^2$ sensitivity of the measurement itself (see Eq.4.9) the expected signal is constant. This is observed in Fig. 4.26: the 6 dB phase signal from phase noise is nearly constant over one decade of detection frequencies.

In conclusion, the phase noise measured with the cavity-reflection principle Fig. 4.26 characterizes most likely the CEO-phase noise of the fiber generated comb. The measured phase noise rises with a less steep slope than for the Ti:Sapph oscillator, and is supposed to follow a second order power law.

Conclusions of this section

Intensity and phase noise of the two different Ti:Sapph oscillators investigated here are quantum-limited above detection frequencies of several MHz. The intensity noise of these oscillators follows typically a first order decay. It is originated by the pump source. The phase noise follows typically by a fourth order decay, arising from spontaneous emission in the gain medium and subsequent coupling processes [10].

By simplifying the cavity based phase noise measurement method applied to the Ti:Sapph oscillators, a ready-to-use schematic has been developed. It has been applied to a low-cost Yb-fiber oscillator. For detection frequencies above 8 MHz, this fiber comb reached by 3 dB quantum-limited behavior in intensity and phase. Further improving the noise of its pump source could bring quantum-limited noise properties into reach. This would provide an affordable source for quantum optical experiments with frequency combs.

4.5 Spectral noise correlations in frequency combs.

This chapter presents the main results of this thesis. The cavity based, quantum-limited phase noise detection developed in section 4.1 is complemented by femtosecond pulse shaping. This permits the analysis of spectral noise correlations, and subsequently the development of a new perspective on classical noise in frequency combs.

Context of metrology and quantum optics. The noise properties of frequency combs have been studied in the frequency metrology literature for two different regimes: in terms of the mean-field or for individual frequencies. Examples for the first are e.g. the CEO-frequency [28] or the repetition rate [7]. The second compare the properties of individual lines of the frequency comb [18, 16] by beating them to single frequency reference lasers. The phase noise distribution over the entire comb is then approximated by e.g. the rubber-band model [21] and has been modeled theoretically [20] for lowest noise levels.

Nevertheless, no experimental information is until now available concerning the spectral correlations of noise and how they evolve at MHz detection frequencies close to the standard quantum limit (SQL). Such correlations, or *modes* are not accessible from mean-field properties. Their knowledge could be used to reduce noise in broadband optical measurements: by a careful selection of the measurement spectral properties. It has been shown by B.Lamine et al.[5] that spectral modes can be used for precision metrology experiments. The implicitly underlying concept of this work is that repetition-rate and CEO-phase correspond to spectral modes of correlated noise. Also the well known oscillator noise theory of H.A.Haus [10] relies on such modes. It turns out that mean-field noise properties of frequency combs are special cases in the framework of noise-modes.

A recently developed branch of noise analysis for frequency combs studies non-classical quantum states of light [22, 24, 23]. The pre-requirement for the underlying concepts are quantum-limited noise properties. Many lasers have such properties at sufficiently short timescales of microseconds. The interaction of a frequency comb with a nonlinear medium can under this assumption lead to non-classical correlations of amplitude and phase noise in the frequency comb [22, 24]. It turned out that so-called *spectral modes*, structures of correlated noise, are a suitable formalism to describe these correlations [25, 24]. It is not clear how far this quantum-optical mode-representation is applicable to classical noise of frequency combs. This section aims to clarify this question.

Structure of this section. Spectral correlations of frequency comb noise are studied here for levels close to the SQL. They are independent to fluctuations in the laser environment which occur at lower detection frequencies. Concerning phase noise, it has been shown in the sections 4.1 and 4.2, that such low levels are accessible by the use of broadband transmissive, passive cavities and shot noise resolving, homodyne detection [85, 69]. Adding here pulse-shaping to these methods, spectral correlations of phase noise become accessible. The spectral amplitude and phase noise co-variance matrices of a Ti:Sapph oscillator are subsequently measured. Their eigendecompositions reveal the modes of correlated noise. In the second part of this section, it is shown how repetition rate and CEO-phase noise of a frequency comb are canonically represented by such modes. Using the phase noise covariance matrix data, the levels of both can be calculated even close to the standard quantum limit.

Experimental setup and measurements. The setup to verify the concept of spectral modes of classical noise in a frequency comb is shown in Fig.4.27. It consists of fs-pulse-shaping, a passive optical cavity and shot noise resolving intensity noise detection. The electric signals are analyzed using a spectrum analyzer. The pulse-shaper acts as a binary switch on 10 individual parts of the spectrum. They are non-overlapping and all together cover the entire spectrum. They permit to measure either the noise levels in individual bands or noise correlations by pairwise combinations.

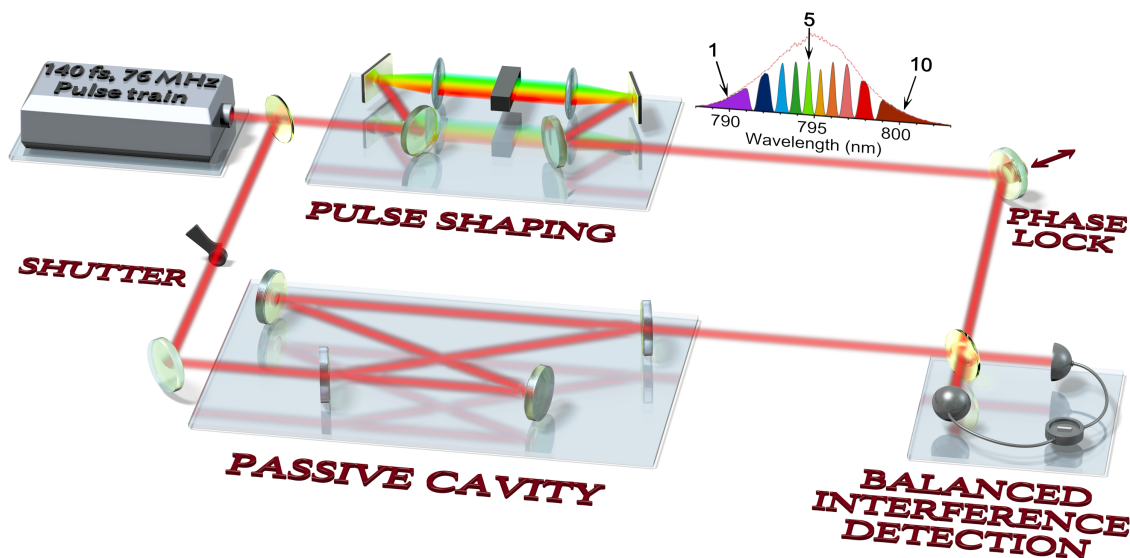


Figure 4.27: Experimental setup. A Ti:Sapph oscillator Coherent MIRA, repetition rate 78 MHz, average power 1.5 W, pulse duration 140 fs, bandwidth 6 nm FWHM, central wavelength 795 nm, is analyzed. A shutter selects one of two measurements: *closed* amplitude noise correlations, *open* phase noise correlations. The remaining components are a 4-f line with a spatial light modulator SLM, a passive cavity of Finesse 625, cutoff frequency at 125 kHz, a piezo-mounted mirror to lock the relative phase of the interfering beams, and a shot noise resolving, balanced interference detection. Only one detector is used if shutter is closed. The cavity is locked with a PDH-scheme in counterpropagation.

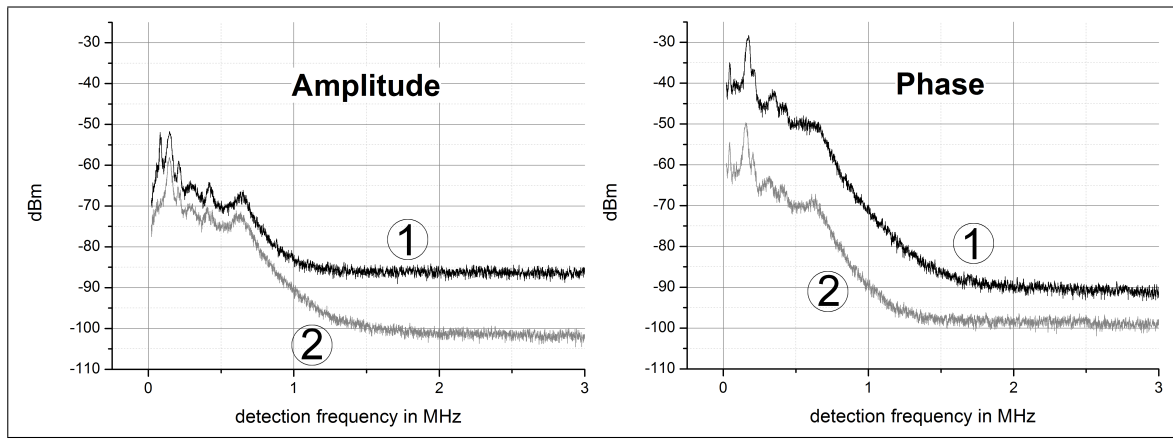


Figure 4.28: Typical measurement raw data: recorded intensity noise used to calculate the covariance matrices. *Left* for amplitude noise, *right* for phase noise. Shown are two example measurements of noise in the center ① and in the wing ② of the spectrum. The covariance matrices are subsequently calculated for a noise frequency Ω within a 30 kHz resolution bandwidth. The spurious noise peaks below 500 kHz arise from non-stationary fluctuations (jumps of the longitudinal mode) of the Ti:Sapph pump laser.

To analyze amplitude noise only the signal from the pulse-shaper is detected by a single photodiode. To analyze phase noise, both arms Fig.4.27 interfere with a mean relative phase of $\pi/2$. The signal is detected with the balanced, two detector configuration. The passive cavity filters comb phase noise in one arm of the interferometer leading to a difference in phase noise in both arms. As discussed in section 4.1, the resulting signal $S(\Omega)$ is proportional to the mean squared relative phase noise $\langle \delta\phi_{\text{rel}}^2(\Omega) \rangle$ and even proportional to the absolute phase noise of the Ti:Sapph oscillator, see Eq.(4.3):

$$S(\Omega) \sim \langle \delta\phi_{\text{rel}}^2(\Omega) \rangle \sim \Omega^2 \langle \delta\phi_{\text{Ti:Sapph}}^2(\Omega) \rangle \quad (4.14)$$

This measurement has been shown to be of quantum-limited sensitivity to phase noise, see Eq.(4.3). A homodyne configuration with one bright and one attenuated signal turns out to be not necessary here: The intensity noise in both interferometer arms was negligible compared to the phase noise signal. Typical measurement raw data are shown in Fig.4.28 for both quadratures. The classical noise at detection frequencies below 1 MHz is well distinguished from the white shot noise.

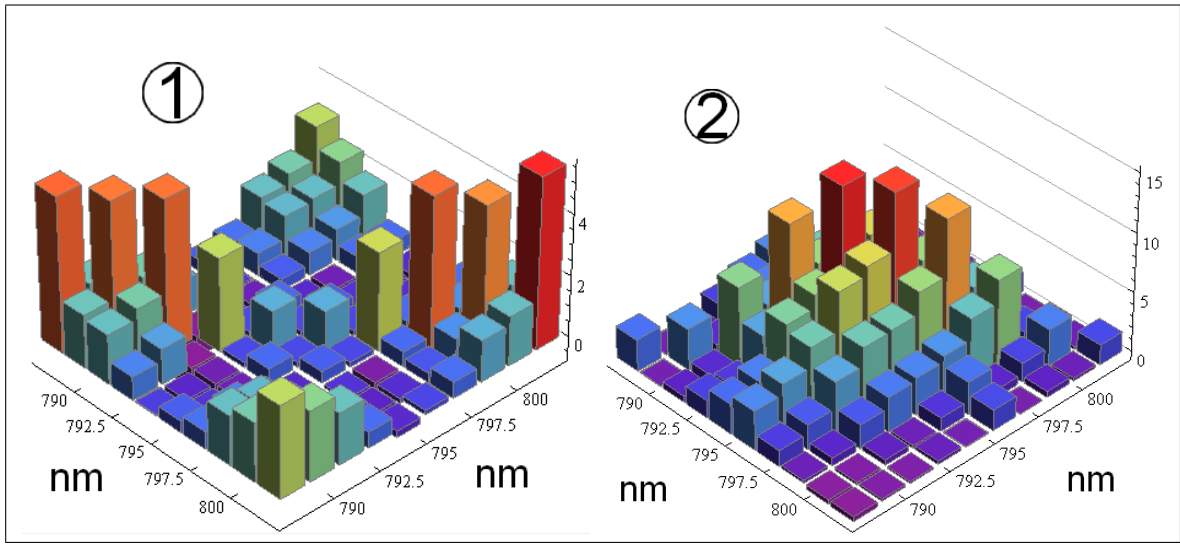


Figure 4.29: Covariance matrix for spectral amplitude ① and phase ② fluctuations at 1.2 MHz detection frequency. The amplitude noise ① has predominant weight and correlations in the wings of the spectrum. The spectral phase noise ② has an opposite structure. Its weight and correlations are predominant in the spectral center of the comb. Similar covariance matrices are found for all detection frequencies below 1.5 MHz where noise is sufficiently above the SQL.

Spectral Noise Correlations. Using the pulse-shaper, the analysis above can be resolved on the optical spectrum but also considering noise correlations. To this aim, either one or two spectral regions i and j are transmitted $i, j = 1..10$. For x being either amplitude or phase noise, the photo-detection records consequently the noise power $\langle (x_i + x_j)^2 \rangle$ at RF-frequencies $\Omega/2\pi$ from 200 kHz to 4 MHz. The detected optical P_i power is monitored in parallel. The individual elements of the covariance matrix $\langle x_i x_j \rangle$ at the detection frequency Ω are subsequently constructed by

$$\langle x_i x_j \rangle_{\Omega} = \left[\frac{1}{2} \langle (x_i + x_j)^2 \rangle_{\Omega} - \frac{P_i}{P_i + P_j} \langle x_i^2 \rangle_{\Omega} - \frac{P_j}{P_i + P_j} \langle x_j^2 \rangle_{\Omega} \right] \times \frac{P_i + P_j}{2\sqrt{P_i P_j}} \quad (4.15)$$

To build up the covariance matrix, the observed intensity noise $\langle x_{i, \text{Measure}}^2 \rangle$ is normalized relative to the shot noise level $\langle x_{i, \text{shot}}^2 \rangle$: $\langle x_i^2 \rangle = \langle x_{i, \text{Measure}}^2 \rangle / \langle x_{i, \text{shot}}^2 \rangle$. It can be shown that, under this condition, Eq.(4.15) is directly the covariance-matrix for the noise field quadratures amplitude and phase [127, 22, 25].

Typical properties of the covariance matrices obtained can be discussed using examples measured at 1.2 MHz (Fig.4.29), and at 3.5 MHz (Fig.4.30). At the latter detection frequency, both amplitude and phase noise covariance matrices are diagonal in any basis: all correlations vanish. The noise of both quadratures is at the SQL. Below 100 kHz, non-stationary classical noise is present in the Ti:Sapph pump laser. At 1.2 MHz, classical stationary Gaussian noise is present. The covariance matrices for amplitude and phase are significantly different and exhibit spectral noise correlations.

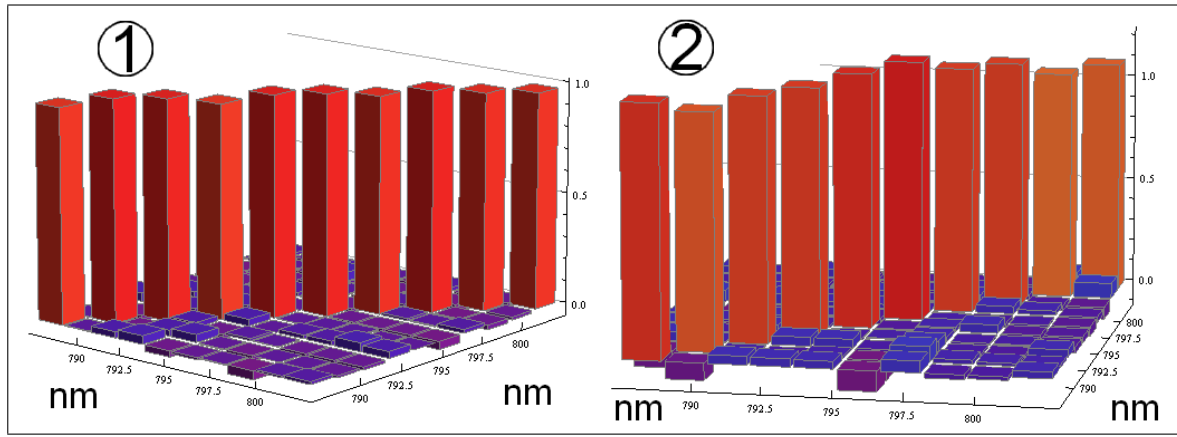


Figure 4.30: Covariance matrix for spectral amplitude- ① and phase-noise ② at 3.5 MHz detection frequency. Both amplitude and phase noise are here at the SQL. All spectral correlations represented by off-diagonal elements vanish. The diagonal elements are all of the same value as the underlying noise level is normalized to the photon number.

A further analysis of these covariance matrices has to distinguish the two principal parameters of the measured covariance matrices: the optical spectrum described by the indexes i and j and the detection frequency Ω . For a given detection frequency, the following considerations can be done:

The measured $\langle x_i x_j \rangle$ can be written in a generalized covariance matrix V . Writing q_i amplitude- and p_i phase-noise measurements, it is the matrix V that describes the entirety of noise correlations in the comb. It was partially probed here through the amplitude and phase covariance matrices V_{qq} and V_{pp} :

$$V = \begin{pmatrix} \Delta q_1 & \langle q_1 q_2 \rangle & \dots & \langle q_1 p_n \rangle \\ \langle q_2 q_1 \rangle & \Delta q_2 & \dots & \langle q_2 p_n \rangle \\ \vdots & \vdots & \ddots & \vdots \\ \langle q_n q_1 \rangle & \dots & \dots & \Delta p_n \end{pmatrix} = \begin{pmatrix} V_{qq} & 0 \\ 0 & V_{pp} \end{pmatrix} \quad (4.16)$$

All correlations between the two quadratures have been neglected here. This is reasonable with the results of section 4.1 and 4.4. Amplitude and phase noise of the Ti:Sapph oscillator close to the SQL are of different origins: The first arise from pump power fluctuations, the second from spontaneous emission.

In order to characterize the entire system, one typically seeks a diagonalization of V . The eigenvectors of V are the so-called *noise-modes*. With the assumption of uncorrelated amplitude and phase noise, it is consequently sufficient to consider both quadratures individually. The general case in quantum optics is called Williamson

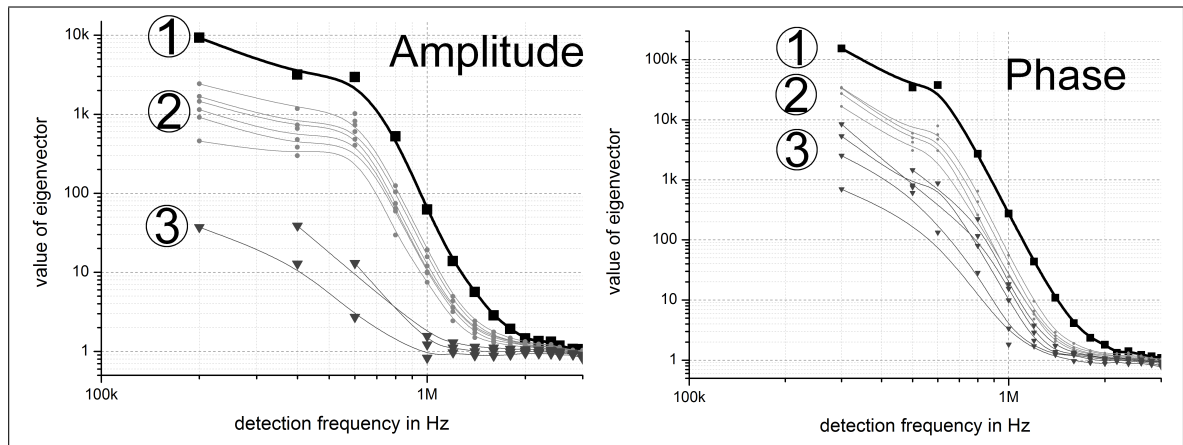


Figure 4.31: Evolution of the eigenvalues of the covariance matrices Fig.4.29 with the detection frequency. Spectral amplitude noise *left* and spectral phase noise *right*. Each eigenvalue quantifies the amount of noise in the corresponding eigenvector. All eigenvalues decay rapidly to the SQL above the relaxation-oscillation frequency at 700 kHz. The level of the first eigenvalue ① is well above the others for all detection frequencies below the SQL. Two other groups of eigenvalues, ② and ③, can be identified. The level of group ③ has been found to be significantly related to measurement instabilities and noise of the Ti:Sapph pump laser.

decomposition. A diagonalization is sought here using symplectic transforms that maintain the commutation relations between the operators \hat{p}_i and \hat{q}_i [128, 129, 130, 25].

In this representation, the eigenvalues of the covariance matrices are associated with the amount of noise contained in the corresponding eigenvector. In addition, any eigenvector or *noise mode* describes a distribution of perfectly correlated noise over the optical spectrum. This concept is applied here to classical noise. To this aim, the matrices V_{qq} and V_{pp} are diagonalized.

Broadband analysis of covariance matrix eigenvalues. Figure 4.31 shows the evolution of the eigenvalues of the noise covariance matrices for amplitude and phase with the detection frequency Ω , from the classical regime at 100 kHz to the SQL. For both quadratures, their value and thus the associated noise levels decay rapidly to the SQL, especially above the relaxation oscillation frequency at 700 kHz. Such an attenuation of classical noise for a Ti:Sapph oscillator has been discussed by [13] using a rate-equation based model, see section 4.4. The data of Fig.4.31 reveal three distinguishable groups of eigenvalues: A first one that carries approximately 75% of the noise, a second one that is a group of similar eigenvalues. They form a degenerate space of eigenvectors. The values of the third group are significantly smaller.

In order to study the relative evolution of the noise correlations with the detection frequency Ω , the representation chosen in Fig.4.32 provides a different perspective: All eigenvalues are normalized relative to the first one. At the SQL above 3 MHz detection frequency and within the measurement uncertainties, all eigenvalues are

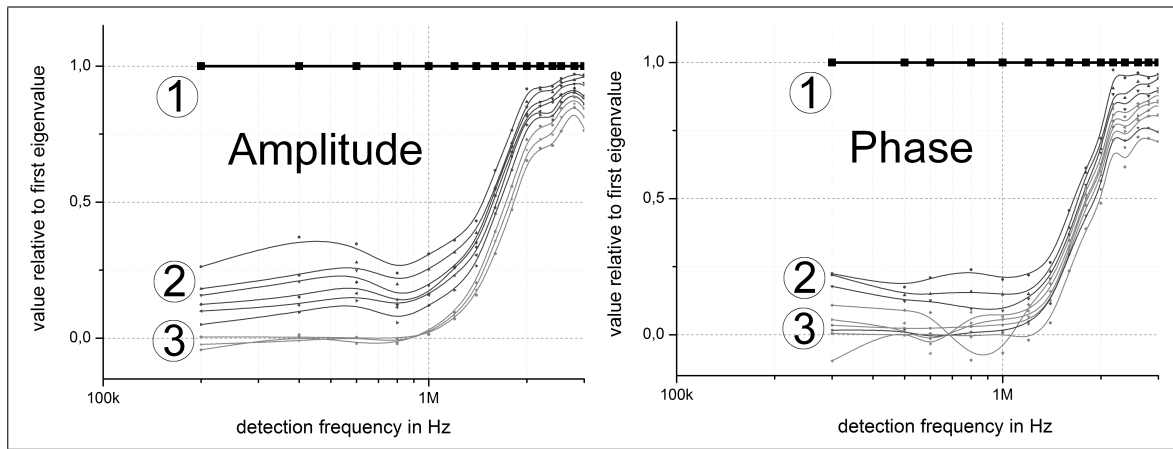


Figure 4.32: Evolution of the eigenvalues of the covariance matrices Fig.4.29 with the detection frequency. (same as Fig.4.31 - here the first eigenvalue is normalized to 1.) Above 1.5 MHz, all eigenvalues of both quadratures converge rapidly and in the same way to 1., this is equivalent to fully uncorrelated noise over the frequency comb.

equal to one. At microsecond timescales, all eigenvalues converge in the same way to this equal distribution. This indicates that the coherence time of the frequency comb is the same in any mode. The tripartite structure discussed in Fig. 4.31 is also visible Fig.4.32. In the linear scale of Fig. 4.32, also small, non-physical, negative eigenvalues appear. The corresponding noise levels are negligible compared to the over-all noise of the frequency comb. It has been observed in the experiment that these negative eigenvalues go along with the presence of non-stationary noise from a longitudinal mode instability of the pump-laser. In conclusion, they do not correspond to an intrinsic noise property of the free-running Ti:Sapph oscillator.

Eigenvectors of the covariance matrix. The eigenvalues of the noise covariance matrices contain the amount of noise in the frequency comb. The eigenvectors contain the spectral structure of noise correlations. It is their shape that will permit to interpret them in terms of global comb noise properties.

Before discussing general aspects of such correlations, Fig. 4.33 and Fig. 4.34 give an overview of the entire, experimentally observed noise structures. They show the eigenvectors of the noise-covariance matrices for amplitude (Fig. 4.33) and phase (Fig. 4.34) as a function of the detection frequency, from 200 kHz to the SQL. With respect to the amount of noise carried by these vectors (given by the eigenvalues Fig.4.31), only the first four eigenvectors are shown.

For both amplitude and phase, the first eigenvector ① exhibits the most pronounced structure. Its shape remains constant, independent to the detection frequency until vanishing in shot noise at the SQL. For all other eigenvectors, it is more difficult to attribute a unique structure. This might be due to degeneracy.

Amplitude noise eigenvectors

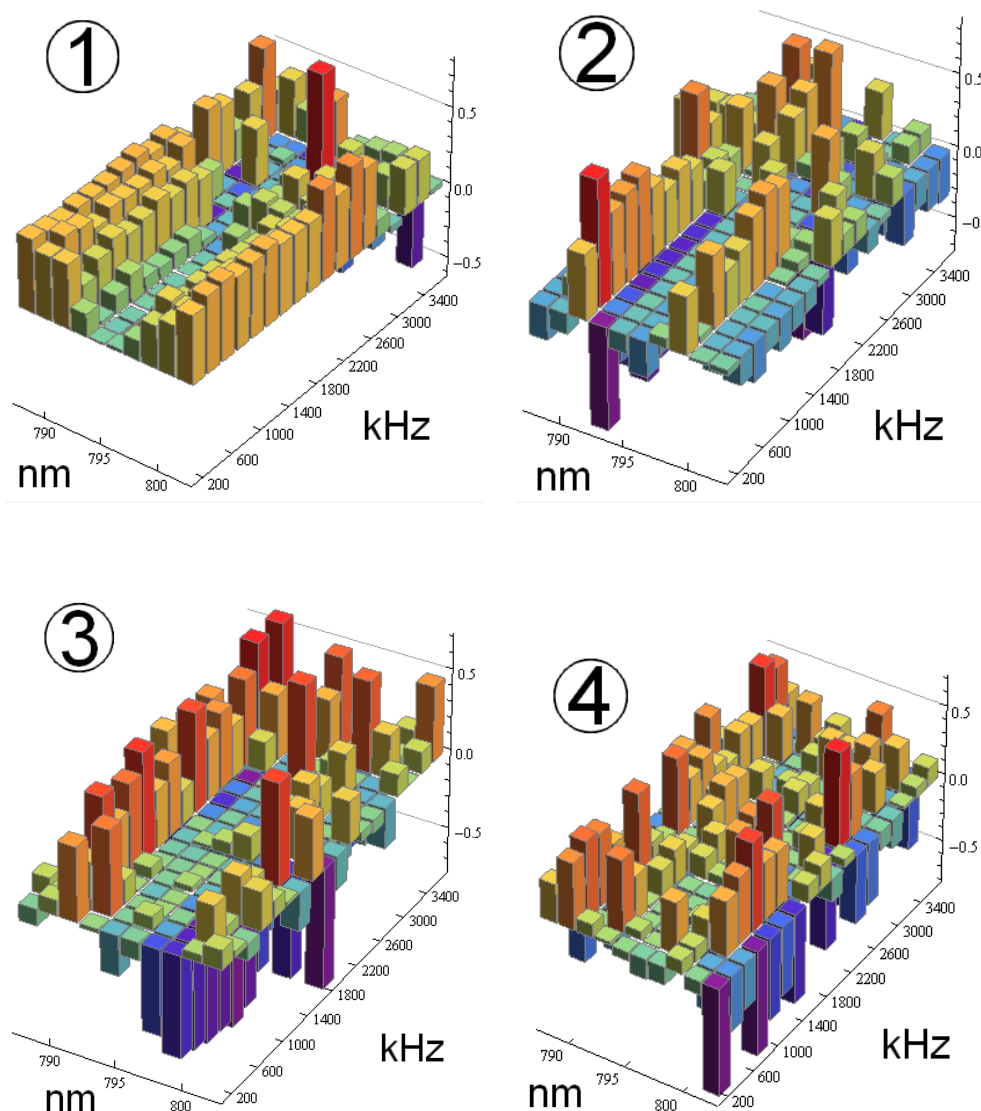


Figure 4.33: Amplitude noise. Eigenvectors of the spectral amplitude noise covariance matrix and their evolution with the frequency of detection. The plots ① to ④ show the eigenvectors corresponding to the eigenvalues (EV) plotted in Fig. 4.31. They are ordered by the magnitude of their EV. For the largest EV ①, a well defined structure is present below 2.2 MHz, independent of the detection frequency. It vanishes in shot-noise for higher detection frequencies but is otherwise always of the same shape. The same yields for ② and ③ where the structure is already less obvious. This may also be due to the nearly degeneracy of the corresponding EV. For the eigenvector No. ④ and higher, a unique structure is not visible.

Phase noise eigenvectors

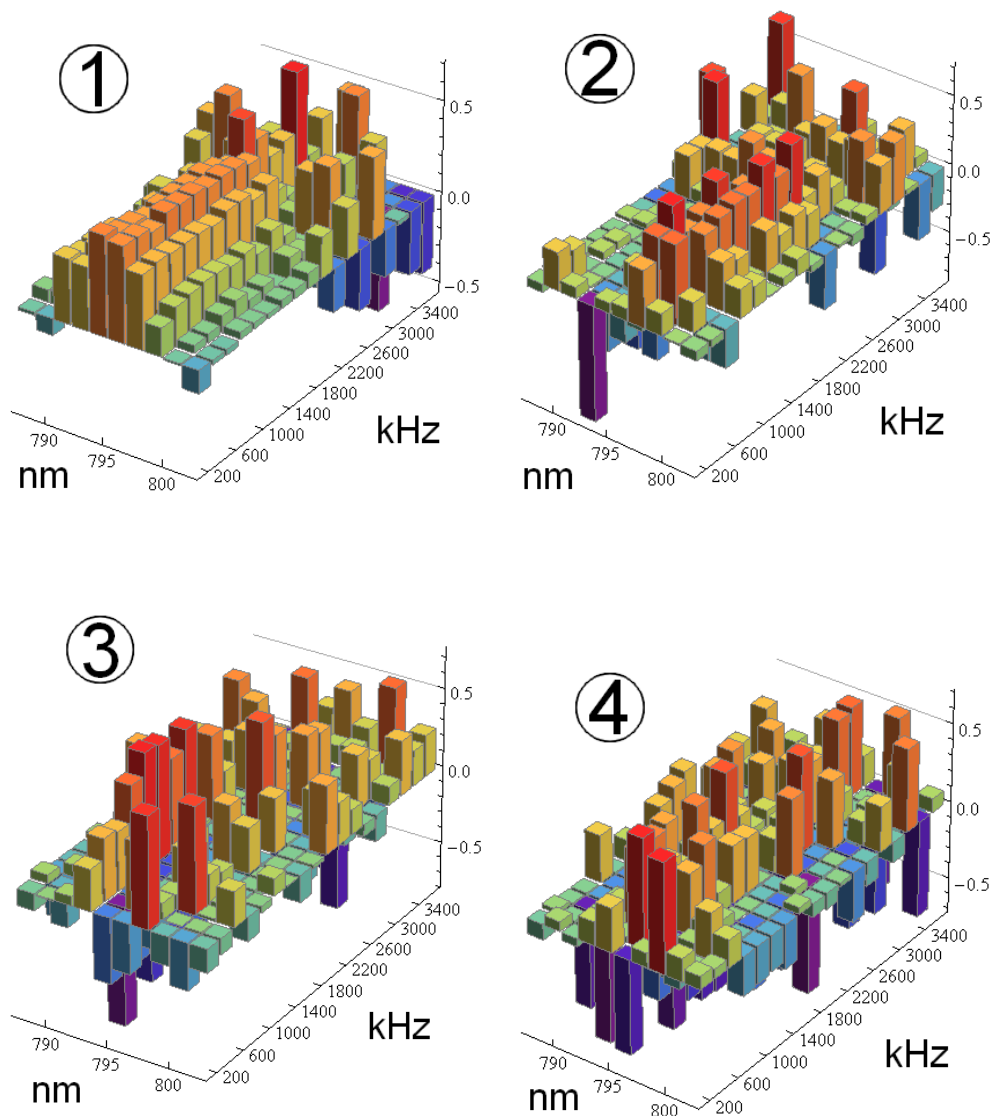


Figure 4.34: Phase noise in analogy to Fig.4.33. Eigenvectors of the spectral phase noise covariance matrix and their evolution with the frequency of detection. Similar to the observations for amplitude noise, it is again the first eigenvector that has a well defined structure. This shape is independent of the detection frequency and vanishes in shot noise at approximately 2.2 MHz. The structure of the nearly degenerated eigenvectors ②, ③ and ④ is, as for amplitude noise, less obvious.

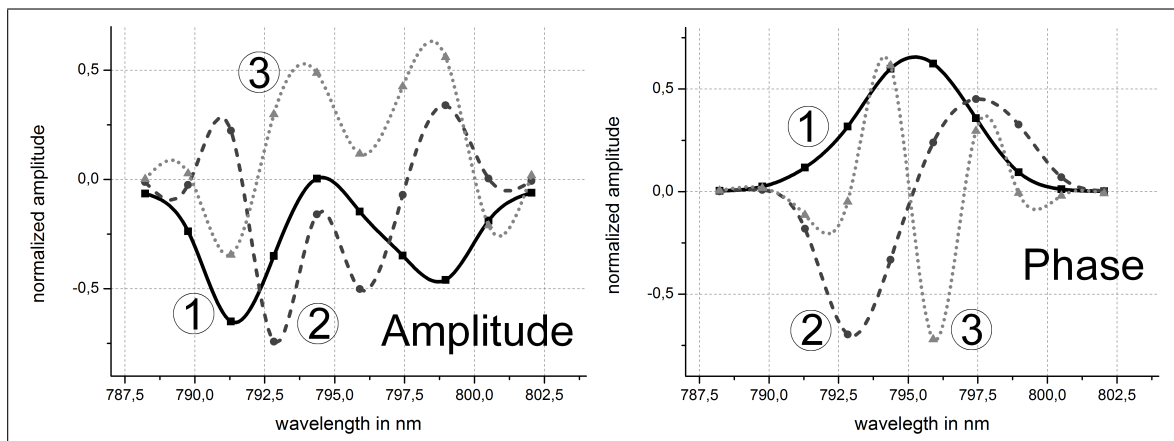


Figure 4.35: Spectral noise modes of the free running Ti:Sapph oscillator. The eigenvectors (Fig. 4.33) of the covariance matrices (Fig. 4.29) weighted with the Gaussian spectral amplitude of the field lead to the *spectral noise modes*. Spline interpolation of data points to improve visualization. *Left* amplitude noise and *right* phase noise. Only the first three modes ①-③ are shown. They are enumerated with and ordered by the magnitude of their contribution to the over-all comb noise. The modes for amplitude and phase noise are significantly different. Measurement at 1.2 MHz detection frequency.

Spectral modes from eigenvectors. The covariance matrices Eq.(4.15) are constructed from noise in a spectral band (diagonal elements) and noise correlations (off diagonals). Their eigenvectors are shown in Fig.4.33 and Fig.4.34. They characterize perfectly correlated noise structures over the entire frequency comb, in a decorrelated base. Multiplying the eigenvectors with the Gaussian spectral amplitude distribution of the comb field reconstructs the underlying field-distributions $v_j(\omega)$.

These vectors are subsequently called *spectral noise modes*. They describe the spectral distribution of perfectly correlated noise and are shown in Fig.4.35. The noise modes for amplitude and phase noise are significantly different. This indicates different physical origins. The data shown in Fig.4.35 have been recorded at 1.2 MHz detection frequency. The level of classical noise is here sufficiently above the SQL at 3 MHz and the laser is not perturbed by non-stationary fluctuations of the environment or the pump source as it occurs below 200 kHz. According to Fig. 4.33 and Fig. 4.34, the first eigenmode is independent to the detection frequency Ω . Due to degeneracy, this statement is not verified for the subsequent ones.

Within the context of noise models for ultrafast optical oscillators, the representation of noise by such spectral modes was first used implicitly by H.A.Haus et al.[10]. There, the modes are applied to describe the perturbations $\Delta E(\Omega)$ of a train of soliton-pulses with a spectrum $E(\omega)$. The independence of the spectral modes to the frequency of detection Ω permits to write the perturbations as:

$$\Delta E(\omega, \Omega) = \sum_i v_i(\omega) \cdot \Delta X_i(\Omega) \quad (4.17)$$

Examples for X_i are here the amplitude and phase of a considered pulse. The envelope functions v_i correspond to the noise-modes. The separability of femto- and microsecond timescales is verified at least for the first measured eigenvectors of amplitude and phase, see Fig. 4.34 and Fig. 4.33. They do not vary with the detection frequency.

The representation Eq.(4.17) is in addition similar to the one of B.Lamine et al.[5]. Considering generalized timing deviations in a coherent pulse train, this concept is discussed in the next subsection. Nevertheless, both approaches arise only from theoretical considerations. No explicit measurement of spectral modes of classical noise has yet been reported in the literature.

From Fig. 4.35 both amplitude and phase noise of the Ti:Sapph oscillator are associated with well distinguished noise modes. The noise of each of the two quadratures is in addition a superposition of several orthogonal modes. The correlations of amplitude and phase noise over the optical frequency comb are significantly different for spectral amplitude and phase noise. Finally, the amount of noise detected within an arbitrary measurement will depend on the spectral mode that can be attributed to the detection apparatus. This interpretation could permit to optimize measurements with frequency combs for best signal to noise ratios.

Conclusions: The measurement of spectral noise modes. It has been shown that pulse shaping together with a broadband transmissive, passive cavity and balanced interference detection can reveal the entire correlation structure (covariance matrix) of spectral amplitude and phase noise in a frequency comb. Noise correlations define spectral modes of correlated noise. The underlying concepts hitherto only used for nonclassical noise correlations in frequency combs [25, 24] can consequently be applied to classical noise. When approaching the standard quantum limit at detection frequencies of approximately 3 MHz, all classical noise modes disappear. As expected for the SQL, the remaining noise is uncorrelated. A comparison to the theoretically predicted spectral modes of a free-running Ti:Sapph is done in the next section.

4.5.1 Timing-jitter measurement close to the SQL

The measured spectral noise modes are compared here to the theoretical predictions. Using this concept and to demonstrate its versatility, timing jitter is obtained from noise covariance data even close to the SQL.

Introduction. For frequency combs, the levels of timing jitter (group-delay, time-of-flight) and CEO-phase noise of have been extensively characterized relative to the carrier power. Ultimate precision within homodyne detection timing measurements [5] requires nevertheless quantum-limited jitter and phase noise properties. To date, no measurements have been reported studying the transition of CEO-phase noise and timing jitter to this limit. It is shown here that both properties can be calculated from the covariance matrix of spectral phase noise. They correspond each to a specific *noise mode* into which the covariance matrix can be projected. The measurements presented here confirm that CEO-phase noise is the governing noise property of the Ti:Sapph oscillator studied here - even down to the quantum limit. It is consequently the limiting factor to homodyne timing measurements of highest sensitivity [5, 8].

The noise properties studied here are situated at detection frequencies above 100 kHz: Far above typical lock-bandwidths and impacts of the environment, the frequency comb can be considered as free-running. Nevertheless, its noise is not yet quantum-limited. The phase noise of ultrafast oscillators in this regime has been studied in theory and experiment by [7, 11, 10, 12], see also section 3.1. Here, repetition rate and CEO frequency are limited by spontaneous emission in the gain medium and noise coupling processes related to the mode-locking principle. The over-all expected decay of phase noise lies between f^{-2} (spontaneous emission) and f^{-4} (noise couplings). Consequently, all noise levels are supposed to reach the SQL at a given detection frequency.

For the repetition rate, the reach of the SQL has been studied by [14, 15]. The analysis of the CEO-phase noise in section 4.1 gave first indications that the SQL could be reached at microsecond timescales. Despite these considerations, it is not yet clear if either repetition rate or CEO phase noise is the governing noise property of frequency combs close to the SQL. The transition region close to the SQL is of particular interest: the low noise levels at the SQL are promising for metrology experiments [5, 8]. Nevertheless, low detection frequencies are required for numerous experiments but go along with increasing classical noise.

Multimode homodyne measurements. To measure timing jitter (group delay) and CEO phase noise at lowest levels, the homodyne detection concept [5], of section 2.5.1 can be used. It is convenient to recall here how the underlying theory applies the concept of modes of correlated noise: The mean field of the signal can be written in terms of a function $v(u)$, $u = r - ct$ containing both carrier and envelope $g(u)$ [35]:

$$\langle E_0^+(u) \rangle = \mathcal{E}g(u)e^{-i\omega_0 u} = \mathcal{E}v(u) \quad (4.18)$$

Assuming a space-time shift $u' = u - \Delta u$, the mode $v(u - \Delta u)$ can be written in form of a Taylor series [5]:

$$v(u - \Delta u) = v(u) + \Delta u \cdot \underbrace{[v_{\text{I}}(u) - v_{\text{II}}(u)]}_{w(u)} \quad (4.19)$$

The two emerging temporal modes are proportional to I: $iv(u)$ and II: $dv(u)/du$. It turns out that a homodyne detection of the space-time shifted signal with a local oscillator in mode I corresponds to a measurement of CEO-phase noise, see also section 4.1. A homodyne detection with mode II corresponds to the measurement of the group delay (time-of-flight, TOF) noise using only a single photodiode.

Equation (4.19) also permits to define the term *noise mode* more precisely. With Eq.(4.18), a *mode* $v(u)$ is nothing but a field distribution on u . In the context of Eq.(4.19), the mode $w(u)$ is associated with the noise amplitude Δu . Any noise Δu leads to perfectly correlated noise of shape $w(u)$. It is the so-called *noise mode*.

Timing jitter- and CEO phase noise-modes in the frequency domain. The covariance matrices Fig. 4.29 are available from measurements in the optical frequency domain. Writing $\tilde{v}(\omega)$ the Fourier transform of the Gaussian envelope $v(u)$ and neglecting normalization constants, the spectral modes corresponding to I and II are now given as follows, see Eq.(2.77):

$$\tilde{v}_{\text{I}}(\omega) \sim i\omega_0 \cdot \tilde{v}(\omega), \quad \tilde{v}_{\text{II}} \sim i(\omega - \omega_0) \cdot \tilde{v}(\omega) \quad (4.20)$$

The mode \tilde{v}_{I} is the spectral envelope of the initial field itself and corresponds to a measurement of the CEO-phase noise. The mode \tilde{v}_{II} corresponds to a measurement of the group-delay (time-of-flight) jitter. *Both CEO phase noise and timing jitter are spectral modes of phase noise.* This confirms the intuitive statement that any change of the spectral envelope of a frequency comb will never modify neither the pulse timing nor the CEO-phase.

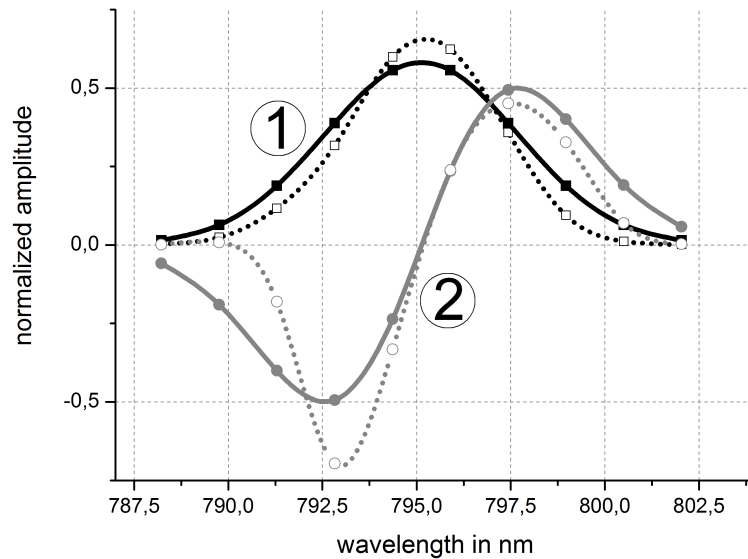


Figure 4.36: Main modes for frequency comb phase noise analysis. The continuous lines show the theoretical modes of CEO-phase noise ①, and timing-jitter/group delay ②. The dotted lines show the first two phase-noise modes obtained from the measured covariance data (see Fig. 4.35) at 1.2 MHz detection frequency.

Calculated and measured modes. Figure 4.36 shows the calculated and measured modes relevant for timing-jitter and CEO-phase noise analysis. From the spectrum of the frequency comb, \tilde{v}_I ① (CEO) and \tilde{v}_{II} ② (timing jitter) can be *calculated* using Eq.4.20 (continuous lines). Weighted with the spectrum of the frequency comb, the first two eigenvectors of the phase noise covariance matrix lead to the two dominant spectral modes of phase noise (dotted lines).

These modes can be compared to the ones obtained from the *measured* phase noise covariance matrix. The first mode that contains most noise shows an overlap of 0.94 with mode \tilde{v}_I representing the CEO phase noise. The measured mode of second highest noise level shows an overlap of 0.91 with \tilde{v}_{II} , representing the timing jitter/group delay. For detection frequency of 1.2 MHz here considered, the CEO-phase noise (I) in the comb is consequently larger than the timing-jitter (II).

In the following, this type of analysis is extended to all available detection frequencies.

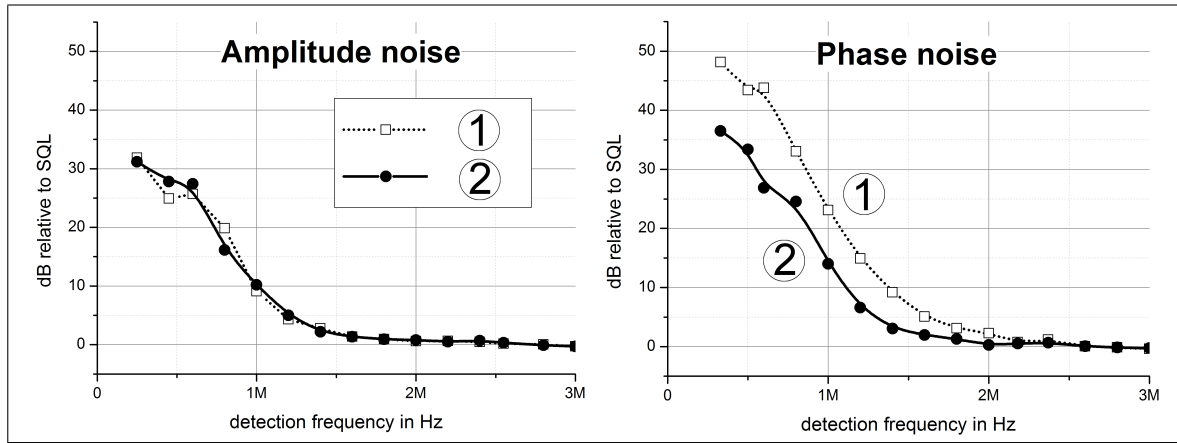


Figure 4.37: Projection of the measured noise covariances onto different modes. *Left:* amplitude noise, *right:* phase noise. For the comb spectrum $v(\omega)$ the modes are ①: $\omega_0 \tilde{v}(\omega)$ and ②: $(\omega - \omega_0) \tilde{v}(\omega)$. In the case of phase noise, ① corresponds to a CEO-phase and ② to a group-delay measurement. For amplitude noise, both modes are an examples of arbitrary, orthogonal modes. All noise levels relative to the SQL. With respect to the entire recorded optical power for covariance matrix measurements, the SQL is calculated at -175 dBc.

Indirect measurement of CEO- and TOF- noise down to the SQL. For a given noise mode $\tilde{v}(\omega)$, the noise level of the comb in this mode can be calculated by projecting $\tilde{v}(\omega)$ on any eigen-vector $\tilde{v}_i(\omega)$ of the covariance matrix. The calculation is done for any detection-frequency Ω where data are available. If the eigenvalues k of the covariance matrix are $e_{k,\Omega}$ and the eigenvectors are written as $\tilde{v}_{k,\Omega}(\omega)$, this projection is:

$$\sigma_{\tilde{v},\Omega}^2 = \sum_k e_{k,\Omega} \cdot \left| \int d\omega \tilde{v}(\omega) \cdot \tilde{v}_{k,\Omega}^*(\omega) + c.c. \right| \quad (4.21)$$

The eigenvectors \tilde{v} are real for the amplitude noise covariance matrix, imaginary $i\tilde{v}$ for the phase noise covariance. For the given comb spectrum $\tilde{v}(\omega)$, the method can be applied to the normalized modes ①: $\tilde{v}_I \sim i\omega_0 \tilde{v}(\omega)$ (CEO phase) and ②: $\tilde{v}_{II} \sim i(\omega - \omega_0) \tilde{v}(\omega)$ (timing jitter/TOF). The projection Eq.(4.21) corresponds then to a CEO phase and timing-jitter measurement respectively.

The results of projecting the amplitude and the phase noise covariance matrix on the absolute values of the modes ① and ② are shown in Fig. 4.37. For amplitude noise, both modes are just examples of arbitrary, orthogonal modes. The calculated noise level is similar for both modes. For phase noise, they correspond in contrast to the measurement of timing/CEO noise described above. The calculated phase noise is significantly different in the two modes. The level corresponding to CEO-phase noise ① is up to 20 dB above the level corresponding to a timing/group-delay jitter ②.

The CEO phase noise is consequently the governing noise property of the Ti:Sapph oscillator considered here. This holds not only in the low kHz regime, but also for any detection frequency up to the SQL. It is the key result of this section. At detection frequencies where the comb noise is close to the quantum limit SQL, the sensitivity of the homodyne timing measurement [5] is limited by the level of repetition-rate and CEO-phase noise relative to the SQL, see section 4.1. Consequently, the sensitivity is principally limited by the CEO-phase noise term. For a 6 nm FWHM frequency comb, the timing/group-delay noise can be neglected for any RF-frequency.

From a generalizing point of view, using Eq.(4.21), it is possible to characterize any noise property of a frequency comb by a spectral mode. The same holds for any measurement of a frequency comb. This leads to the following, important consequence: If the mode of detection can be modified with regard to the noise modes of the comb, it might be possible to improve the signal to noise ratio of measurements with frequency combs. An example is the measurement of a phase modulation. If suitable with the type of phase modulation, it would be advantageous to choose the mode of detection to the less noisier group-delay mode. This could increase the signal to noise ratio.

Summary: Indirect measurement of common comb noise properties. Noise covariance matrices have been shown in the literature to be a powerful tool for the characterization of frequency combs with non-classical noise correlations [22, 24, 23]. By the use of pulse shaping, a broadband transmissive passive cavity and shot noise resolving interference detection, the covariance matrices of spectral amplitude and phase noise of a 6 nm FWHM frequency comb have been measured here for the first time.

The obtained noise structure can be projected on any spectral noise mode. For example, expected timing jitter/group delay- and CEO phase-noise of the comb correspond to two orthogonal, spectral modes of phase noise. Projecting the phase noise covariance matrix onto these two modes, timing jitter/group delay- and CEO phase-noise have been calculated down to the SQL. Within this unprecedented sensitivity, it has been shown that CEO-phase noise is the governing phase-noise property of the investigated Ti:Sapph oscillator, even close to the SQL.

Chapter 5

Summary and Outlook

The main purpose of this thesis was to study the noise of Ti:Sapph oscillators close to the standard quantum limit (SQL). It was motivated by the theoretical work [5], suggesting that multi-spectral interferometry with optical frequency combs can lead to ultimate measurement sensitivity, provided that the comb noise is at the SQL.

Noise quantification. Due to the isotropy of vacuum, the SQL of amplitude and phase noise for an optical signal of average power P and central frequency ν are at the same level $S_{\text{SQL}} = 2h\nu/P$. A convenient measure to quantify the noise levels of both field quadratures are units relative to the carrier power dBc/Hz. For typical 1 mW of detected power, the SQL of a comb centered at 800 nm is at -153 dBc/Hz.

A frequency comb has two common phase properties, the phase of the repetition-rate and the carrier-envelope-offset (CEO). For the Ti:Sapph oscillators studied here above 100 kHz detection frequency, it was found that the CEO-phase governs the phase noise properties of the comb. It converges together with the repetition-rate phase noise to the SQL at approximately 3 MHz detection frequency. A newly developed measurement technique enabled this key result. In addition, the CEO-phase noise has been shown to exhibit typically levels far above those of the intensity fluctuations. Being at the origin of the mode-lock of the individual comb frequencies, the Kerr effect is also the source of the high sensitivity of the comb phase to even smallest intensity noise. Such intensity noise arises both from spontaneous emission and pump power fluctuations. The lowest CEO-phase noise measurable with optimized standard techniques was approximately -120 dBc/Hz for this work. This level is still approximately 30 dB larger than the expected SQL, hence these techniques did not provide quantum limited sensitivity to phase noise. In order to characterize and even to filter especially phase noise of the frequency comb close to the SQL, the following techniques have been developed.

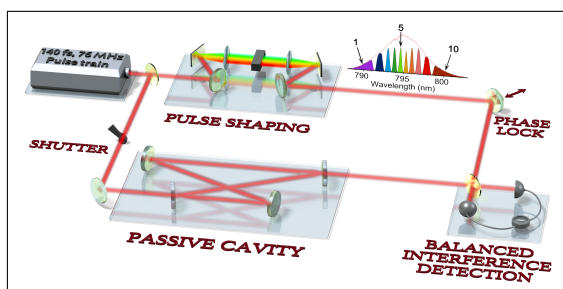


Figure 5.1: The principal experimental techniques developed in this thesis. As shown in section 4.5: A self-referenced interference of the transmission of a broadband passive cavity is detected in a shot noise resolving balanced detection. It measures phase noise in the seeding frequency comb with quantum limited sensitivity. Pulse-shaping of the reference provides access to the noise covariance of the frequency comb.

Noise filtering and broadband analysis. In order to reduce the CEO noise of the Ti:Sapph oscillator outside the kHz bandwidth of typical active feedback schemes, different approaches have been investigated. To start, a passive filtering cavity for the pump of the Ti:Sapph system was constructed, with the hope of reducing its intensity fluctuations. However, due to phase noise in the seeding pump beam, the filtering cavity exhibited significant intensity excess noise. Together with the Kerr-nonlinearity in the Ti:Sapph oscillator, this effect significantly increased the over-all level of CEO-phase noise of the oscillator. Thus, this approach was found to be a not suitable technique.

Another approach for reducing phase noise of an existing oscillator, even at levels close to the SQL, is passive filtering of the frequency comb itself. For this purpose, a broadband resonant optical cavity has been constructed. While filtering amplitude and phase noise, it was shown to transmit simultaneously an up to 100 nm broadband signal. Additionally, this cavity turned out to be a versatile tool for the analysis of phase noise in optical frequency combs:

At first, a passive cavity interconverts the noise quadratures efficiently and transforms CEO-phase noise to intensity noise which is readily detectable with shot noise resolving sensitivity. This effect provides access to the spectral phase noise properties of optical frequency combs, if the broadband transmitted signal is analyzed spectrally resolved. The alternative of measuring individual comb lines by comparing them to a number of optical reference signals would be an experiment of enormous complexity. For absolute levels close to the SQL, it was found that the spectral phase noise of a 45 nm FWHM Ti:Sapph comb varies by 10 dB over the covered spectrum.

Second, it was found that a passive cavity can provide phase noise detection with quantum-limited sensitivity. This is possible using a self referenced interference of the cavity-transmitted signal with a part of the original seeding beam and subsequent shot noise resolving, balanced interference detection. If the reference beam is in addition pulse-shaped, the covariance matrices of amplitude and phase noise become accessible. This is the key experimental result of this thesis. The corresponding setup

discussed in section 4.5 is drafted again in Fig. 5.1. The underlying physical principles are the filtering of phase noise by the passive cavity and the detection of relative phase noise by interference and shot noise resolving photodetection.

Both effects are also present in the reflection of a resonant passive cavity. For sufficiently low intensity noise, the self-referenced interference can be replaced by a noise analysis of the cavity reflection. This turns the concept into a ready-to-use experiment. It was applied to characterize a low-cost fiber based oscillator close to the SQL. In contrast to Ti:Sapph oscillators, the investigated system was not quantum-limited for any observed detection frequency. Nevertheless, with the new technique of characterization, this oscillator type can be systematically studied and improved. In the future, this could provide low-cost quantum limited optical frequency combs for quantum optical applications.

In some cases, the oscillator properties themselves can be modified. A reduction of the oscillator's relaxation-oscillation frequency might be a promising way to achieve quantum limited noise properties at low detection frequencies. All classical noise properties rapidly decay above this frequency. Compared to all other methods considered in this thesis, this approach seems to be the most simple and robust.

Measurement of noise modes. Using the setup Fig. 5.1, the covariance matrices of amplitude and phase noise have been determined over a broad range of detection frequencies. Based on these findings, the emergence of classical noise from the SQL and its correlations have been characterized precisely. In analogy to the considerations of non-classical noise in frequency combs [25, 24], spectral modes of perfectly correlated noise can be defined. Any measured noise covariances can be represented in a decorrelated, orthogonal basis of modes. Any mode corresponds to a global physical (noise) property. In this representation, the classical amplitude and phase noise of the investigated oscillator exhibit a structure that is clearly multimode. Considering spectral noise correlations, the commonly characterized repetition-rate and CEO-phase noise correspond to phase noise of well defined spectral modes. Both are consequently special cases of the modal representation of frequency comb noise.

For further analysis, the phase noise modes have been ordered by the amount of carried noise. The governing phase noise mode was found to have an overlap of $\sim 98\%$ with the theoretical mode representing CEO phase noise. The second experimental noise mode exhibited an overlap of $\sim 91\%$ with the theoretical mode representing repetition rate/group delay noise. This confirms that CEO-phase noise and repetition rate are the fundamental noise properties of the investigated frequency comb. Furthermore, the measurement of both quantities can be performed by

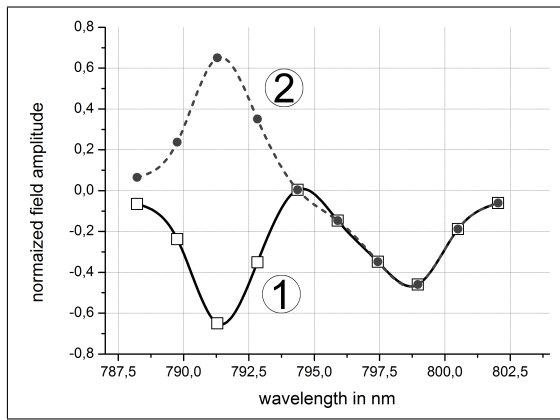


Figure 5.2: Visualization of the principal outlook of this thesis. The amplitude noise of the Mira Ti:Sapph oscillator was found to be contained by more than 60% in the mode ①. For an example experiment requiring the measurement of a broadband absorption with highest sensitivity, but at a detection frequency where the oscillator noise is not at the quantum limit: If the homodyne detection analyzes the absorption of mode ② the measurement will be insensitive to the intensity noise contained in mode ①. Both are orthogonal.

projecting the observed noise covariance matrices on the corresponding theoretical modes. This led to one of the principal findings of this thesis: It is the CEO-phase noise that governs the phase noise properties of the individual lines of the Ti:Sapph frequency comb considered. For any detection frequency and down to the SQL, the contribution of the CEO-phase is larger than the one of the repetition rate noise.

Outlook. The knowledge of the noise modes could improve the precision of homodyne metrology experiments with frequency combs. The underlying idea is depicted in Fig. 5.2 and can be understood by using the following example. The amplitude noise of the oscillator was found to be maximal in mode ①. If a given measurement with a frequency comb corresponds to the mode ②, the contribution of amplitude noise to this measurement will be minimized as both modes are orthogonal. The achievable signal to noise ratio and sensitivity will consequently increase. In a general case, the mode of detection could be slightly modified from the one associated with the aimed measurement: over-compensating the loss of measurement precision by a reduction of measured laser noise. Such a technique could increase the sensitivities of homodyne measurements with frequency combs, especially at timescales of milliseconds where significant classical noise is present.

Appendix A

Appendix

A.1 Filtering the oscillator's pump laser

Contents

A.1 Filtering the oscillator's pump laser	155
A.1.1 Reducing pump intensity noise to the SQL	155
A.1.2 A filtering cavity for the Ti:Sapph pump laser	157
A.1.3 Origins of low frequency cavity excess noise	163
A.1.4 Conclusions	169

A.1.1 Reducing pump intensity noise to the SQL

One of the aims of this thesis is to provide a frequency comb with quantum limited noise properties down to the lowest possible RF-frequency. Intensity noise of the Coherent Verdi pump laser has been shown to be the principal driver of intensity noise of a Ti:Sapph oscillator, see section 3.1, Fig. 3.2. In addition, the CEO-phase of this oscillator is highly sensitive to fluctuations of the pump intensity up to MHz detection frequencies, see section 3.1.4 and 3.1.5.

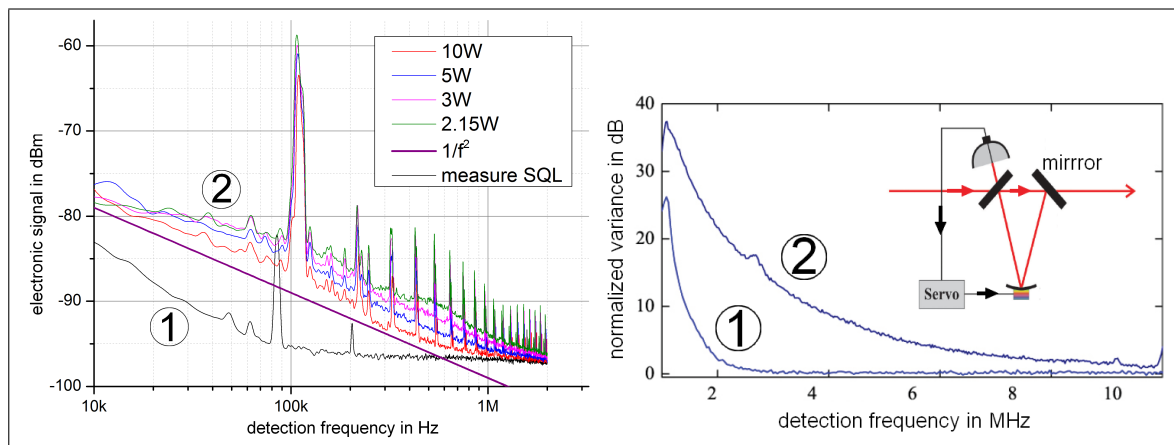


Figure A.1: Intensity noise of different lasers relative to the SQL. *Left:* The 10W single mode Verdi for different output powers ② relative to the measured SQL ①. The detected power is 8 mW for all traces. Detection bandwidth 60 kHz to 10 MHz. *Right:* a passive cavity (inset) efficiently filters intensity noise of a Nd:YAG source ② down to the SQL (cavity output) ②, figure from [131].

Being identified as an oscillator noise driver, the intensity noise of the Verdi pump laser is evaluated relative to SQL in Fig. A.1, left. It is not proportional to the output power. The lowest RIN is obtained at maximum output power. Driving the pump laser at maximum output power optimizes consequently the overall setup.

For the detection frequencies above 60 kHz, the intensity noise is close to the SQL but present up to 2 MHz. Active mechanisms are not suitable for a further reduction of such noise: they are either limited in bandwidth or may not reach the SQL¹. A possible solution has been suggested in [131] for a low power Nd:YAG laser of a specified linewidth of 1 kHz: the use of a passive filtering cavity. Figure A.1 shows the result obtained therein. The filtering cavity reduces intensity noise by up to 20 dB at microsecond timescales.

Nevertheless, it has been shown in section 2.7.2 that passive transmissive cavities also transfer phase noise to the amplitude quadrature. As such, it has to be verified if the specified Verdi linewidth does not prevent the applicability of a passive filtering cavity. Using an optical frequency comb as reference, the linewidth of a similar Verdi was measured in this thesis to above 300 kHz. The only available literature reference concerning a cavity filtering of a quasi identical laser system is [74]. It demonstrates intensity noise filtering but only considers detection frequencies above 4 MHz.

¹ A simple *noise eater* scheme of a detector, a PI-amplifier and an AOM only reaches the SQL in the limit of a entire detection of the beam.

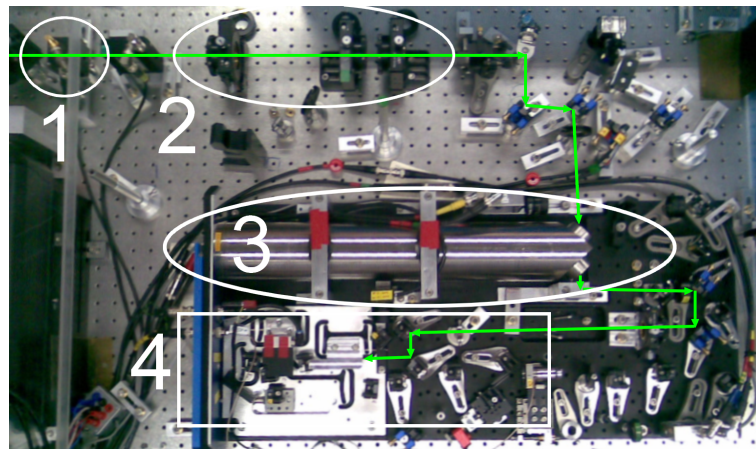


Figure A.2: Experimental implementation of the filtering cavity. The Verdi laser beam (green) is phase modulated with a resonant electro-optical modulator at 11 MHz ①, after mode-matching ② the beam is injected into the passive cavity ③. The reflection is recovered to generate a Pound-Drever-Hall (PDH) error signal. The transmitted signal is injected into the Ti:Sapph oscillator ④ after mode-matching.

A.1.2 A filtering cavity for the Ti:Sapph pump laser

A passive cavity is implemented into the pump beam of the Ti:Sapph oscillator as shown in Fig. A.2. This ring-cavity has an optical length of 1 m. It consists of three mirrors, one high-reflectivity mirror two output couplers. A finesse of 680 for S-polarization and 100 for P-polarization are measured. They correspond to cutoff-frequencies of 400 kHz and 3.3 MHz respectively. The high-finesse is used here. A transmission of up to 80% of the seed-power has been achieved. The Ti:Sapph requiring 4.5 W of pump power, non-linear effects occurred in the Pound-Drever-Hall EOM at intensities above 40 W/mm^2 . Fig. A.3 shows that the thermal lens of the KTP crystal and absorption are non-negligible. Nevertheless, a contrast of more than 95%

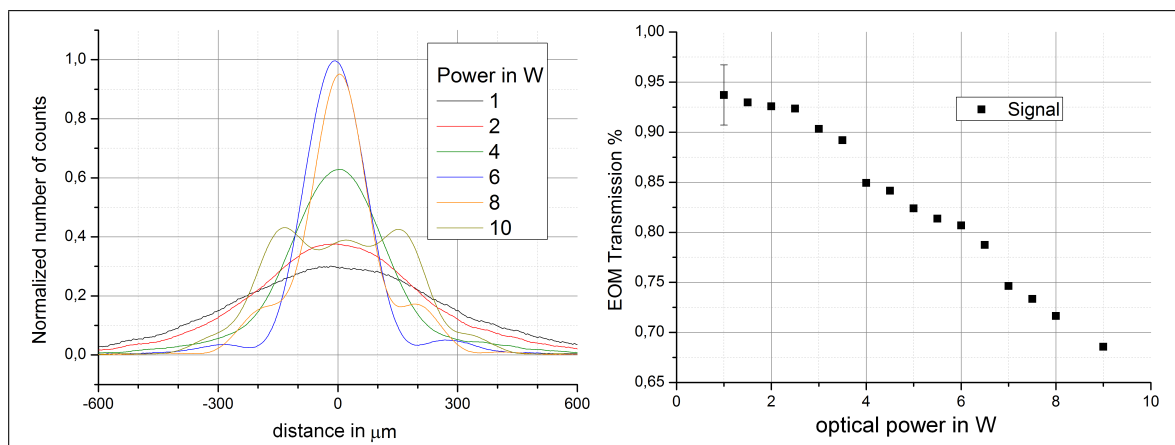


Figure A.3: Nonlinear properties of the used electro-optical modulator (EOM). *Left:* Transverse beam profile after the EOM (the thermal lens) strongly depends on the intensity. A Gaussian beam profile is obtained for sufficiently low optical power. *Right:* For a given intra-crystal beam diameter, the transmission/absorption is a function of the incident optical power.

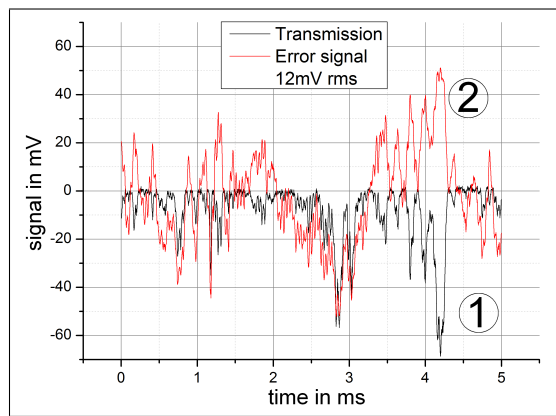


Figure A.4: Resonance properties of the filtering cavity in the kHz-band. The signal of the transmission photodiode ① shows measurable fluctuations in the order of larger than 0,5 to 5% r.m.s. Trace ② shows the PDH error signal. The intensity fluctuations are correlated with the error signal.

between the TEM00 and the next resonant mode has been achieved in the experiment.

Taking all losses into account, the setup Fig. A.2, provided up to 5 W of filtered pump light and thus a sufficient margin to drive a CEO-phase stabilization by pump power feedback. It was possible to lock the cavity to the laser on more than 10 min timescales using a standard Pound-Drever-Hall scheme [78] in reflection.

Results - Filtering pump intensity noise. The Verdi specifications indicate a relative intensity noise (RIN) below 0.02% r.m.s. Using all available resources for an improvement of the cavity-lock and alignment, the cavity filtered signal has never been better than 1% r.m.s.

From this value it is possible to estimate the resulting CEO-linewidth of the Ti:Sapph, see section 3.1.4. The sensitivity of the CEO-frequency to the Ti:Sapph output power has been measured to 0.25 MHz per mW output power. For a pump power fluctuation of 1% r.m.s., a CEO-linewidth of several MHz is expected. This result is in contrast to the aim to reduce also the phase noise of the Ti:Sapph oscillator, and to obtain quantum-limited noise properties below MHz detection frequencies. Note that the bandwidth of acusto-optical modulator based intensity noise stabilization is typically limited to several hundred kHz. Although the cavity filtering approach appears to be not suitable for the Verdi pump laser, it will be verified in the following if it can be further improved.

Excess noise characterization. The r.m.s. value of noise is a first indicator on intensity stability of a light beam. Up to 5% of r.m.s. RIN has been observed in transmission, see Fig. A.4. A typical signal transmitted by the cavity is shown in Fig. A.4. Within the lock-bandwidth of several kHz, significant variations of the transmitted intensity coincide with fluctuations of the PDH error signal. This indicates a non perfect lock of the cavity resonance to the central frequency of the Verdi.

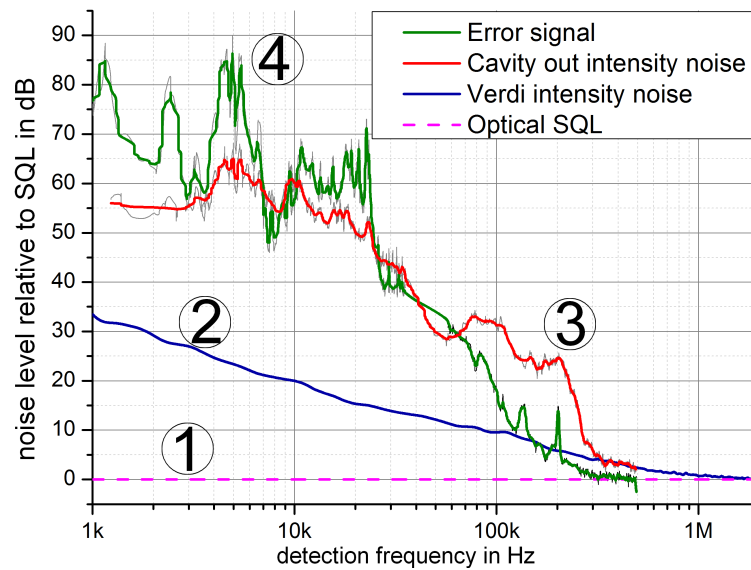


Figure A.5: Broadband analysis of the cavity resonance and excess noise in transmission. All traces relative to the SQL ①. Comparison of the intensity noise of the unfiltered ② and the filtered beam ③. Significant error signal ④ is recorded above the kHz-bandwidth of the cavity lock.

Broadband RF noise analysis. Figure A.5 shows the principal effects of the cavity on the distribution of intensity noise of the transmitted beam. Despite negligible filter effects above 500 kHz detection frequency, the transmitted beam contains a significant amount of *excess noise*: compare trace ③ (filtered) to trace ② (unfiltered). The data in Fig. A.5, is of poor quality as it fits together several independent measurements after the end of the experiment. It only gives a qualitative statement. It may serve for further, similar experiments as an example of a suitable characterization of a transmissive passive cavity. The plot covers at the same time the kHz-bandwidth of the lock-mechanism, the transition between intensity noise filtering and excess noise and the quantum-limited noise regime at MHz detection frequencies. Above the bandwidth of the cavity lock loop, the error signal itself contains information on the phase noise of the seeding laser [100].

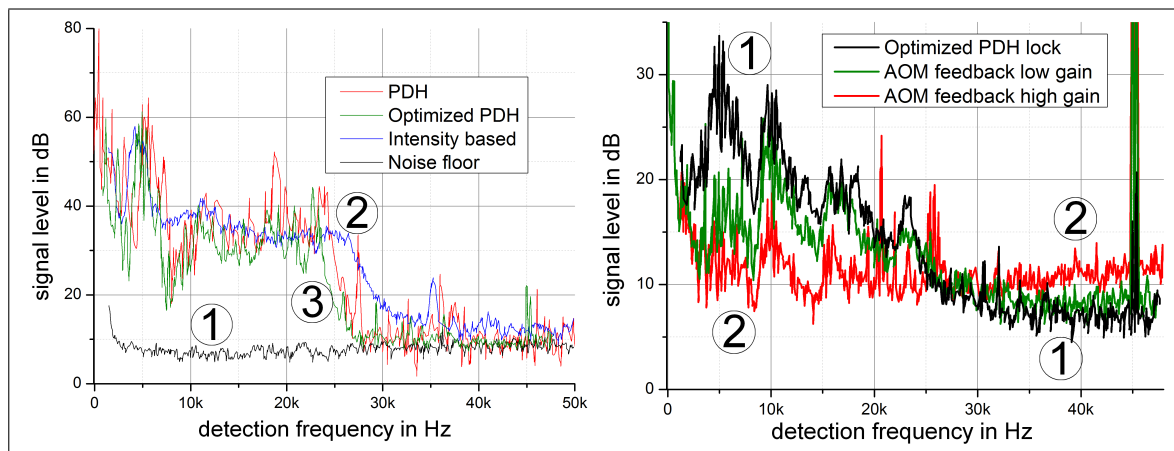


Figure A.6: Distributions of error signal and cavity excess noise in the RF-band below 50 kHz.

left: The error signal has a significant weight in a band below 30 kHz, independent to the generation principle: ② intensity based, ③ Pound-Drever-Hall with and without carefully signal optimization, ① error signal noise floor,

right: Reduction of intensity excess noise from the passive cavity with a subsequent AOM-based, active stabilization. Intensity noise of the transmitted beam for an optimized PDH-lock ①, AOM feedback with low broadband gain (intermediate trace) and AOM feedback with high broadband gain ②.

Improvement of excess noise in the 10 kHz band. Different ways to improve the lock mechanism are studied in Fig. A.6. The *left* graph shows that the distribution of the error signal generated with the PDH method is the same compared to a purely intensity based signal. The generation of the PDH error signal adds therefore no significant electronic noise terms and is not the origin of the excess noise discussed in Fig. A.5. The filtering cavity is locked by a back-action on the position of a piezo-mounted mirror. Note that typical here used HV-amplifiers for piezo-based feedbacks are kHz low-pass filters. The same holds for the piezo element itself: its intrinsic capacity limits the bandwidth of any driver. The resulting kHz bandwidth might be insufficient to compensate for phase noise of the Verdi in the 10 kHz band.

The *right* graph of Fig. A.6 shows the effect of an additional AOM based, active intensity stabilization (noise eater) after the passive cavity. Being a highly sensitive active feedback, it added a sensitivity to any kind of electronic noise. It turned out to be not beneficial to reduce the entire bandwidth of the cavity excess noise.

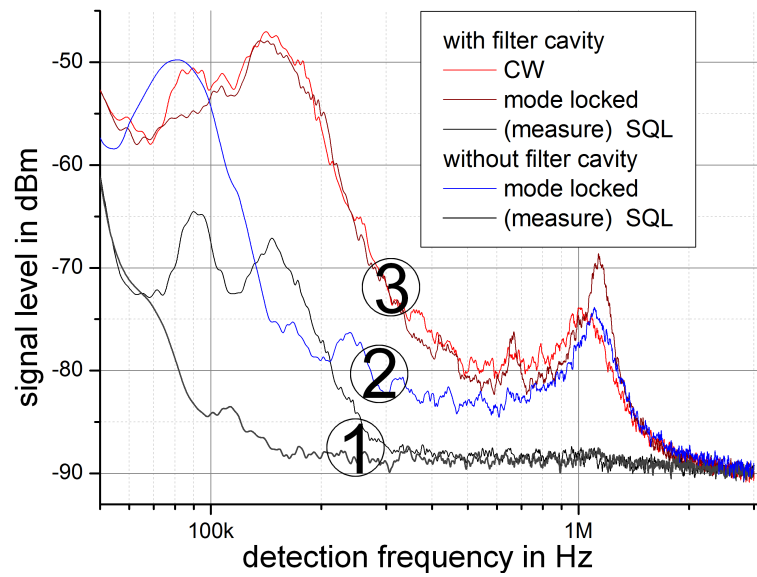


Figure A.7: Effects of the filtering cavity on the intensity noise of a mode-locked Ti:Sapph oscillator close to the shot noise level. ① The measured SQL. ② The oscillator directly seeded with the Verdi pump. ③ The oscillator seeded using the filtering cavity.

Results - Effects on the Ti:Sapph oscillator intensity and phase noise

The intensity noise properties of the cavity-pumped Ti:Sapph are shown in Fig. A.7. The use of the filtering cavity (400 kHz bandwidth) reduces and increases intensity noise depending on the frequency band considered: A less than 1 dB noise reduction is recorded above 1 MHz detection frequency whereas the excess noise reaches more than 20 dB at 100 kHz. A mode-lock has a negligible effect on the Ti:Sapph intensity noise. The excess noise depends on the quality of the lock of the filtering cavity.

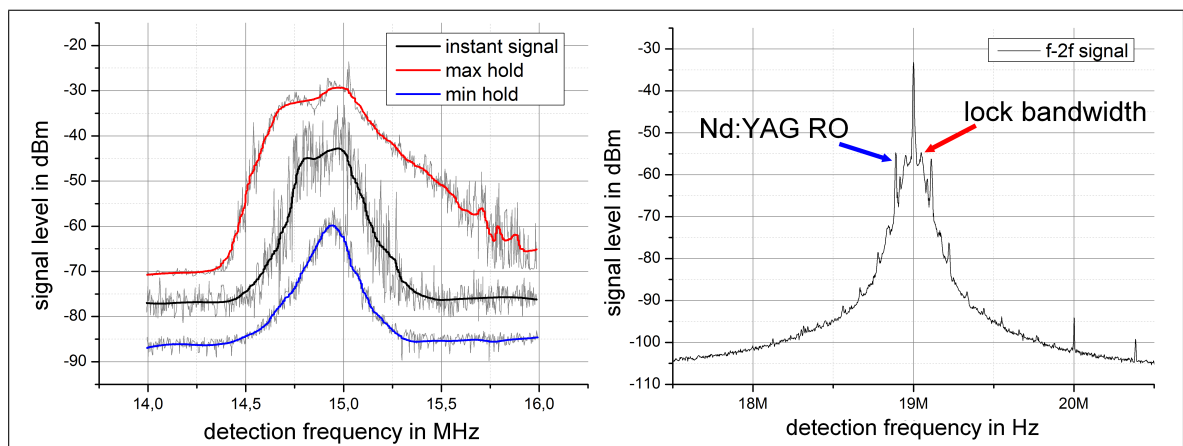


Figure A.8: Comparison of the CEO-phase noise of the Ti:Sapph oscillator seeded with the cavity-filtered and the unfiltered beam. The $f-2f$ electronic beating signal is directly recorded with a spectrum analyzer. *left:* Cavity filtered pump. At at video-bandwidth of 100 Hz, the instantaneous spectrum analyzer traces (*black*) vary between the maximum (*red*) and the minimum (*blue*). A $f-2f$ lock maintains the center of gravity of the CEO-signal. *right:* Unfiltered pump. The CEO-frequency is locked with kHz-bandwidth. Same picture as Fig. 3.4

Taking into account all the available data, the filtering cavity could reduce the intensity noise of a Ti:Sapph oscillator by 5 dB in the relaxation oscillation band at 1 MHz. Nevertheless, the intensity noise in this band can also be reduced to nearly vanishing values by careful alignment of the oscillator.

In contrast, the filter cavity intensity excess noise significantly perturbs the CEO-phase of the oscillator. The typical effect is shown in Fig. A.8, left. Using the filtering cavity and a subsequent CEO-lock of more than 100 kHz bandwidth, a mean CEO-frequency has been maintained for longer than one minute measurement time. The underlying CEO-linewidth was of 500 kHz scale. This is a factor approximately 10^5 compared to a lock under direct Verdi pumping, see Fig. A.8, right. In this situation, characterized in section 3.1, a linewidth of several Hz has been estimated.

Due to the phase to amplitude conversion discussed in section 2.7.2, it is in conclusion not suitable to filter intensity noise of laser sources with passive cavities of comparable line-widths.

A.1.3 Origins of low frequency cavity excess noise

Excess noise of a transmitting, passive cavity, has been considered theoretically in section 2.7.2. Phase noise is efficiently converted to amplitude noise above the cavity bandwidth. Excess noise above the bandwidth of the feedback loop can be considered to be a phase noise property of the seeding beam. The cavity-length is quasi-static at the corresponding timescales. At lower detection frequencies, within the bandwidth of the cavity, excess noise can arise from any electro-mechanical properties of the feedback loop. This section studies such effects.

As shown in Fig. A.5, the excess noise of the cavity aimed to filter the Verdi laser exhibits significant weight within the kHz bandwidth of the feedback loop. In order to analyze possible origins in detail, it turns out to be instructive to characterize also the loop properties themselves.

The transfer function of any feedback loop is always a combination of the complex transfer functions of the feedback-gain and error signal generation $G(\Omega)$ and the one of the servo $S(\Omega)$ [132, 133]. So-called proportional-integral-differentiate (PID) circuits are typically used to amplify the error signal. The function $G(\Omega)$ is of non-constant amplitude and phase. The same holds for any mechanical actuator. They can be modeled by a second order transfer function containing the resonance frequency Ω_0 and the quality factor ξ :

$$S(\Omega)_{\text{mechanical}} = \frac{\Omega_0^2}{\Omega_0^2 + i\frac{\Omega_0}{\xi}\Omega - \Omega^2} \quad (\text{A.1})$$

Any resonant behavior goes along with dephasing. If the overall feedback gain is not vanishing at the transfer function phase $\pi/2$, the entire feedback loop will oscillate. This is the so-called "ringing" typically observed when tuning cavity-lock parameters. Its properties can be used to optimize the gain properties of a PID feedback loop [134]. Nevertheless, an remaining oscillation will appear as a signal in the transmission of the resonant cavity. Resonances of a low quality factor will be recorded as broadband signals, so excess noise. This is the principal approach for the following analysis.

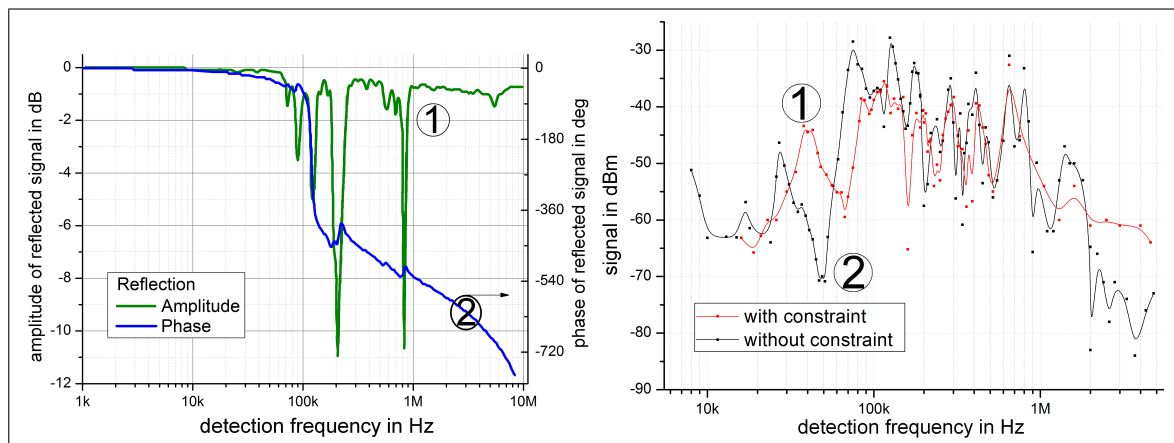


Figure A.9: Electrical and mechanical resonances of the standard piezo-actuator PI010.00H used in this thesis. *left:* Electronic resonances measured with a Network Analyzer in reflection. ① Amplitude, ② phase. *right:* Mechanical resonances of the same piezo mounted with a 1/2" mirror on a heavy counterweight. Measured in reflection with a quadrant detector geometry. ① with and ② without a mechanical counterforce.

Physical properties of a piezo-mounted mirror. A commonly used mechanical actuator for the lock of optical cavities are mirrors glued on a piezoelectric element. Including this actuator, a perfect feedback loop would have a linear behavior of the mirror position with the applied voltage. To describe a realistic situation, electronic and mechanical properties have to be analyzed.

Piezo-elements are DC isolators and have a specific capacity, typically above 10 nF. A piezo-element is consequently first of all an intrinsic low-pass and a phase retarder. Together with the gain and inductance of the electronic signal drivers, it will exhibit resonances.² Figure A.9, left, shows the electronic resonances of a standard piezo-element, measured in reflection. The first resonances appear above 80 kHz.

The mechanical resonances of a *piezo+mirror system* are shown in Fig. A.9, right. They arise from both electrical and mechanical properties. Occurring above 50 kHz, the first strong resonance of the mechanical system sets an upper frequency limit to any possible feedback loop. Its frequency can be increased by the application of a static counterforce [107]. Using this approach, Fig. A.9, right, shows the increase of the first resonance frequency from approximately 25 kHz to 45 kHz.

With and without counterforce, the *piezo+mirror system* exhibits many subordinate resonances at purportedly longitudinal vibrational overtones of the piezo-element. It turns out that they can be exploited for high-frequency phase modulation of optical beams. They may nevertheless give rise to excess noise within the realistic bandwidth of a typical feedback loop as used in this thesis.

² The output impedance of the high voltage amplifier used here is 10 k Ω , the gain bandwidth is below 10 kHz.

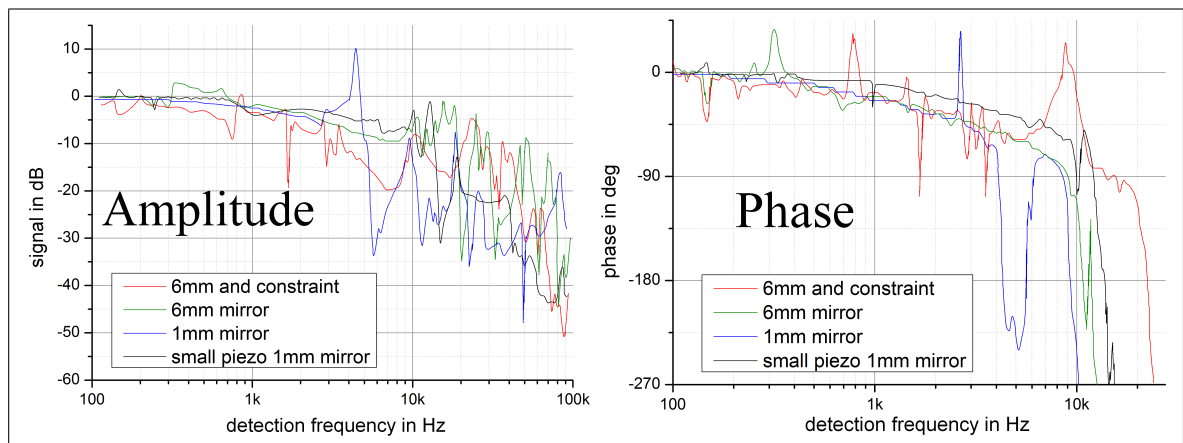


Figure A.10: Mechanical resonance properties of different piezo-mirror configurations.

Left: amplitude, right: phase. Measured in reflection with a quadrant detector geometry. The signal is proportional to the mirror displacement. Phase measurement relative to the signal driving the high-voltage amplifier. Mirrors of fused silica, 6 mm diameter. **Thick Piezo** PI010.00H: *red* 6 mm mirror with mechanical constraint, *green* 6 mm mirror, *blue* 1 mm mirror, **Thin Piezo** PL055.30: *dark* 1 mm mirror

Low kHz mechanical properties. The mechanical properties of a combined piezo-mirror element are studied in detail in in Fig. A.10. The left and right plot show how the slight resonances of these systems depend on a mechanical counterforce, the mirror weight and the used piezo-element. It turns out that all of the off-the-shelf combinations studied here exhibit a number of small resonances. The first significant ones are localized at low kHz frequencies, a large number is present above 10 kHz. They are located well below the fundamental electronic and mechanical resonances discussed above in Fig. A.9. For a transmitting cavity locked at resonance, they may lead to excess noise bands at kHz to above 10 kHz frequencies. In practice, it is typically one of these resonances that starts the "*ringing*" when the kHz proportional gain of a PDH feedback loop is too high. These resonances are less pronounced in the case of the thinnest, 1 mm thick mirror of lowest weight. In all cases, the mirror position is 180 deg out of phase to the electronic HV-amplifier input signal, for frequencies above 10 to 20 kHz.

In conclusion, typical "off the shelf" mirror-piezo systems can be used with feedback bandwidths below 10 kHz.³

³ The filtering cavity of section A.1 is locked using a 6 mm thick 1/2" mirror mounted on a PI010.00H piezo element.

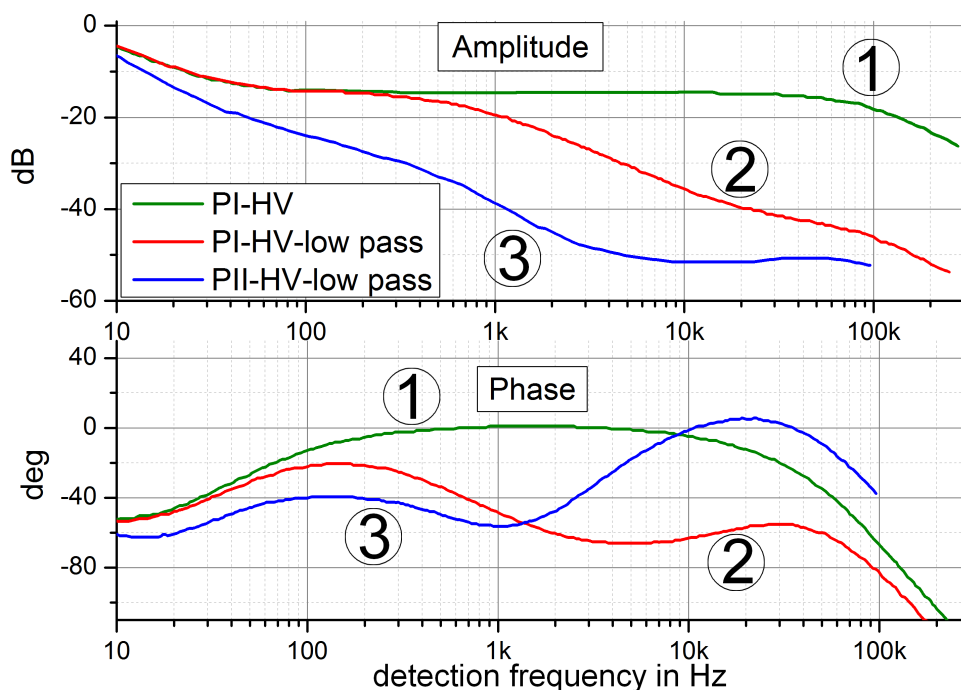


Figure A.11: Amplitude and phase transfer function of the entire electronic feedback-loop without the capacity of the piezo element itself. Transfer functions measured with a network analyzer. A typical optimization procedure strongly modifies also the phase lag of the loop: ① Typical configuration and parameters of PI-controller and High-Voltage amplifier. ② Additional 1 kHz low-pass filter between PI controller and HV-amplifier improving r.m.s. excess noise of cavity transmission. ③ Double integration stage and 1 kHz low-pass do not lead to further signal improvement.

Electronic properties of the piezo-drivers. The error signal amplification is an essential part of a feedback loop. A simple optimization of the gain parameters leads nevertheless to a complex modification of the feedback properties. Figure A.11 shows three typical configurations compared within section A.1.

The basic feedback loop consists typically of a proportional-integrate (PI) and a high voltage (HV) amplifier. To permit for higher low-frequency gain, a low-pass filter or a second integration stage can be added. The best results in terms of minimal r.m.s. fluctuations of the cavity transmission section A.1 have been achieved with the combination PI-HV-low pass, trace ② in Fig. A.11.

Up to the gain roll-off at kHz scales, the feedback loop driven piezo mounted mirror should compensate given phase perturbations of the cavity seeding beam. Considering Fig. A.5, this requirement is not achieved in practice. The low-frequency (integrator) gain might consequently be insufficient. Nevertheless, a potential increase of gain is limited by the ringing of the first small resonances of the mechanical actuator. It is at this point that the entire feedback loop of the filtering cavity is intrinsically limited.

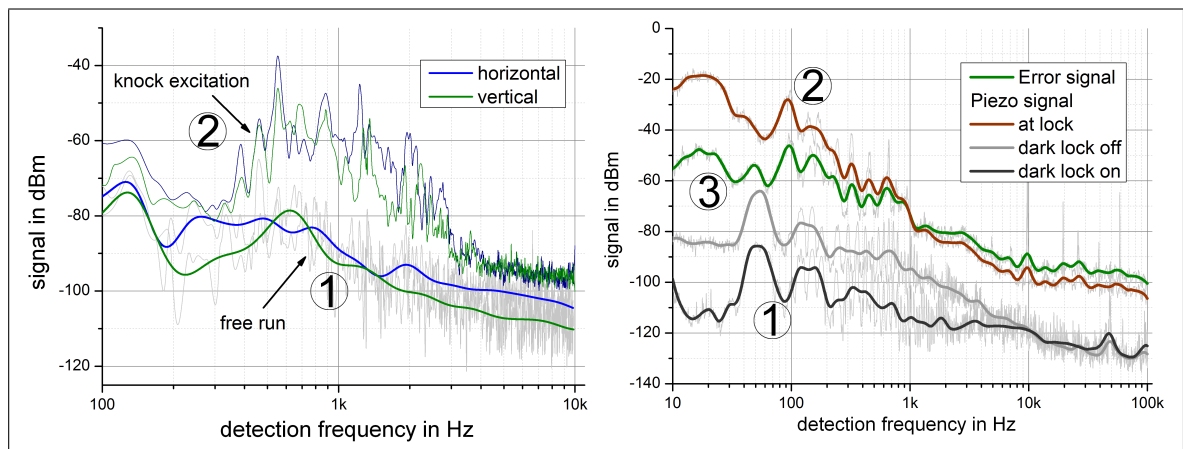


Figure A.12: Analysis of table vibrations and their impact on beam steering. The transversal coordinate left graph, longitudinal coordinate right graph. Plotted are the recorded signals.

left, transversal: Signal of a quadrant detector proportional to the beam deviation. ① "Free running" Verdi laser beam steering, ② mechanical resonances of the optomechanics excited by a "white noise like excitation"

right, longitudinal: Lock of the relative phase in a Mach-Zehnder interferometer of equal arms with a piezo mounted mirror. One arm-length is of approximately 1 m. Feedback loop signal on the piezo: ① electronic noise, ② in-loop signal applied to the piezo, ③ error signal in-loop

Beam pointing and vibrations. Excess noise in the cavity transmission may, under insufficient low frequency gain, also arise from vibrations of the setup. Such mechanical noise impacts both the steering (transversal) and the phase (longitudinal) of the seeding beam. The transverse fluctuations are qualitatively characterized in Fig. A.12, left. Pointing fluctuations arising purportedly from the resonances of the mechanical mirror mounts are present up to approximately 3 kHz. The data recorded were obtained under strong vibrational (δ -like) excitation of the optical table.

Longitudinal fluctuations are characterized using a Mach-Zehnder interferometer. The relative phase of both arms is locked using the output interference fringe pattern and a piezo based mirror in one arm. The error signal of the loop permits to analyze longitudinal beam steering fluctuations due to vibrational modes of the optical table and the mirror mounts. The measured distribution shown in Fig. A.12, right, indicates existing longitudinal perturbations at frequencies below 1 kHz.

One can conclude from Fig. A.12 that mechanical perturbations of the setup are situated within the kHz bandwidth of the piezo based feedback loop of section A.1 above. Being in addition of lowest amplitude, they unlikely the origin of the excess noise of the cavity. An absolute quantification is not necessary here. With the available resources, the setup of the filtering cavity could not be optimized further.

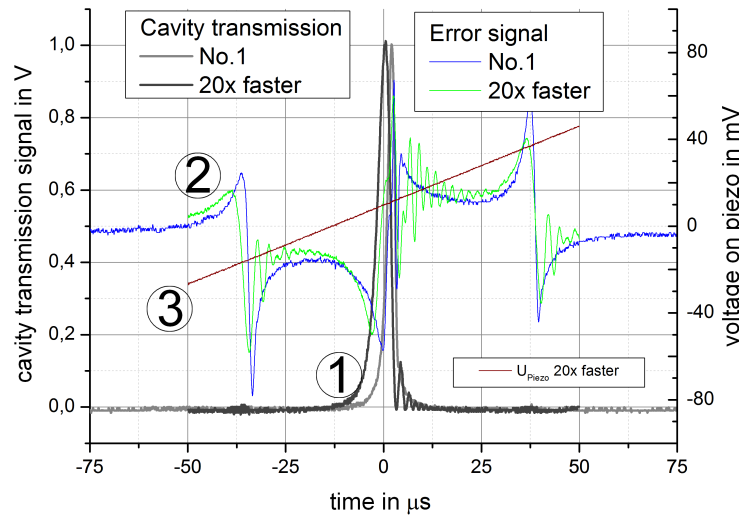


Figure A.13: Doppler-shift of the intracavity field induced by mirror movements. Such a frequency shift may lead to interference patterns with the cavity seed. The transmission peak ① and the Pound-Drever-Hall error signal ② show significant modulations for sufficiently high speed ③ of the piezo-mirror.

Doppler shift of the intracavity signal. A further origin of excess noise from the cavity can be the Doppler shift $\Delta\nu$ of the photons of frequency ν inside the cavity. It may arise due to the movement of the piezo-mirror with a speed v : $\Delta\nu \simeq (v/c) \cdot \nu$, see [105]. It can be estimated as follows: a piezo-element of $1 \mu\text{m}/1000 \text{V}$ can be driven with a commercial Thorlabs HV amplifier at $400 \text{V}/\mu\text{s}$. Assuming this speed of 0.4m/s , the intracavity field undergoes a shift of 10^5Hz . This value is comparable to the cavity-cutoff frequencies used here.

The lock of the cavity-resonance to a beam undergoing phase fluctuations leads to a continuous variation of the mirror position. Figure A.13, shows that such a movement could in principle significantly perturb the PDH-error signal. The measurements show nevertheless, that this perturbation becomes only measurable at mirror-speeds at least 100 times above those occurring at cavity lock. This is an indication that lock-induced Doppler-shift plays a negligible role concerning the emergence of excess noise from the filtering cavity.

PDH error signal generation. The generation of the PDH error signal requires two RF signal sources that are in phase and of the same frequency. They can be provided by a commercial two output signal generator. The jitter of the relative phases between the two ports is not of concern if the the signal of one generator is divided and different cable lengths provide for the necessary shift of the relative phases.

A.1.4 Conclusions

A single longitudinal mode Coherent Verdi laser beam of several Watt power can be resonantly transmitted through a passive cavity. Nevertheless, whether the amplitude noise of the beam can be efficiently filtered depends on the cutoff frequency of the cavity compared to the phase noise of the seeding beam. This is due to the noise-quadrature interconversion by the transmitting cavity, discussed in section 4.2.

It has been shown here that the application of a passive filtering cavity to a Coherent Verdi in order to pump a Ti:Sapph oscillator is not suitable. Its phase noise limits the properties of the transmitted beam. The supplier specification of the Verdi V10 linewidth is below 5 MHz. A beating measurement with a locked optical frequency comb during this thesis measured above 300 kHz. Both values are not compatible with significant filtering of amplitude noise at and below MHz frequency scales using a passive cavity of approximately 400 kHz.

Bibliography

- [1] T. Udem, R. Holzwarth, and T. W. Hänsch, "Optical frequency metrology," *Nature*, vol. 416, no. 6877, pp. 233–237, 2002.
- [2] B. Bernhardt, A. Ozawa, P. Jacquet, M. Jacquy, Y. Kobayashi, T. Udem, R. Holzwarth, G. Guelachvili, T. W. Hänsch, and N. Picqué, "Cavity-enhanced dual-comb spectroscopy," *Nature Photonics*, vol. 4, pp. 55–57, Nov. 2009.
- [3] T. Ideguchi, A. Poisson, G. Guelachvili, N. Picqué, and T. W. Hänsch, "Adaptive real-time dual-comb spectroscopy," *Nature Communications*, vol. 5, p. doi:10.1038/ncomms4375, 2014.
- [4] R. Le Targat, L. Lorini, Y. Le Coq, M. Zawada, J. Guéna, M. Abgrall, M. Gurov, P. Rosenbusch, D. Rovera, B. Nagórny, *et al.*, "Experimental realization of an optical second with strontium lattice clocks," *Nature communications*, vol. 4, 2013.
- [5] B. Lamine, C. Fabre, and N. Treps, "Quantum improvement of time transfer between remote clocks," *Physical review letters*, vol. 101, no. 12, p. 123601, 2008.
- [6] M. Cui, R. Schouten, N. Bhattacharya, and S. Berg, "Experimental demonstration of distance measurement with a femtosecond frequency comb laser," *Journal of the European Optical Society: Rapid Publications*, Jan. 2008.
- [7] A. J. Benedick, J. G. Fujimoto, and F. X. Kärtner, "Optical flywheels with attosecond jitter," *Nature Photonics*, vol. 6, no. 2, pp. 97–100, 2012.
- [8] P. Jian, O. Pinel, C. Fabre, B. Lamine, N. Treps, *et al.*, "Real time displacement measurement immune from atmospheric parameters using optical frequency combs," *Optics express*, vol. 20, no. 24, pp. 27133–27146, 2012.
- [9] L.-S. Ma, Z. Bi, A. Bartels, L. Robertsson, M. Zucco, R. S. Windeler, G. Wilpers, C. Oates, L. Hollberg, and S. A. Diddams, "Optical frequency synthesis and

- comparison with uncertainty at the 10-19 level," *Science*, vol. 303, no. 5665, pp. 1843–1845, 2004.
- [10] H. Haus and A. Mecozzi, "Noise of mode-locked lasers," *Quantum Electronics, IEEE Journal of*, vol. 29, no. 3, pp. 983–996, 1993.
- [11] D. Spence, J. Dudley, K. Lamb, W. Sleat, and W. Sibbett, "Nearly quantum-limited timing jitter in a self-mode-locked ti:sapphire laser," *Optics letters*, vol. 19, no. 7, pp. 481–483, 1994.
- [12] R. Scott, C. Langrock, and B. Kolner, "High-dynamic-range laser amplitude and phase noise measurement techniques," *Selected Topics in Quantum Electronics, IEEE Journal of*, vol. 7, no. 4, pp. 641–655, 2001.
- [13] H. Lu, J. Su, C. Xie, and K. Peng, "Experimental investigation about influences of longitudinal-mode structure of pumping source on a ti:sapphire laser," *Optics Express*, vol. 19, no. 2, pp. 1344–1353, 2011.
- [14] F. Quinlan, T. Fortier, H. Jiang, A. Hati, C. Nelson, Y. Fu, J. Campbell, and S. Diddams, "Exploiting shot noise correlations in the photodetection of ultrashort optical pulse trains," *Nature Photonics*, 2013.
- [15] F. Quinlan, T. M. Fortier, H. Jiang, and S. A. Diddams, "Analysis of shot noise in the detection of ultrashort optical pulse trains," *arXiv preprint arXiv:1302.6206*, 2013.
- [16] D. Sutyryn, N. Poli, N. Beverini, S. Chepurov, M. Prevedelli, M. Schioppo, F. Sorrentino, M. Tarallo, and G. Tino, "Frequency noise performances of a ti:sapphire optical frequency comb stabilized to an optical reference," *Optics Communications*, 2012.
- [17] S. Meyer, J. Squier, and S. Diddams, "Diode-pumped yb:kyw femtosecond laser frequency comb with stabilized carrier-envelope offset frequency," *The European Physical Journal D*, vol. 48, no. 1, pp. 19–26, 2008.
- [18] N. Newbury and W. Swann, "Low-noise fiber-laser frequency combs," *JOSA B*, vol. 24, no. 8, pp. 1756–1770, 2007.
- [19] R. Paschotta, A. Schlatter, S. Zeller, H. Telle, and U. Keller, "Optical phase noise and carrier-envelope offset noise of mode-locked lasers," *Applied Physics B*, vol. 82, no. 2, pp. 265–273, 2006.

- [20] J. Wahlstrand, J. Willits, C. Menyuk, and S. Cundiff, "The quantum-limited comb lineshape of a mode-locked laser: Fundamental limits on frequency uncertainty," *Optics Express*, vol. 16, p. 18624, 2008.
- [21] H. Telle, B. Lipphardt, and J. Stenger, "Kerr-lens, mode-locked lasers as transfer oscillators for optical frequency measurements," *Applied Physics B: Lasers and Optics*, vol. 74, no. 1, pp. 1–6, 2002.
- [22] T. Opatrny, N. Korolkova, and G. Leuchs, "Mode structure and photon number correlations in squeezed quantum pulses," *Physical Review A*, vol. 66, no. 5, p. 053813, 2002.
- [23] W. Wasilewski, A. Lvovsky, K. Banaszek, and C. Radzewicz, "Pulsed squeezed light: simultaneous squeezing of multiple modes," *Physical Review A*, vol. 73, no. 6, p. 063819, 2006.
- [24] J. Roslund, R. M. De Araujo, S. Jiang, C. Fabre, and N. Treps, "Wavelength-multiplexed quantum networks with ultrafast frequency combs," *Nature Photonics*, 2013.
- [25] O. Pinel, P. Jian, R. M. De Araujo, J. Feng, B. Chalopin, C. Fabre, and N. Treps, "Generation and characterization of multimode quantum frequency combs," *Physical review letters*, vol. 108, no. 8, p. 083601, 2012.
- [26] R. M. de Araújo, J. Roslund, Y. Cai, G. Ferrini, C. Fabre, and N. Treps, "Full characterization of a highly multimode entangled state embedded in an optical frequency comb using pulse shaping," *arXiv preprint arXiv:1401.4867*, 2014.
- [27] A. Vernaleken, B. Schmidt, M. Wolferstetter, T. W. Hänsch, R. Holzwarth, and P. Hommelhoff, "Carrier-envelope frequency stabilization of a ti: sapphire oscillator using different pump lasers," *Optics Express*, vol. 20, no. 16, pp. 18387–18396, 2012.
- [28] T. Udem, R. Holzwarth, and T. W. Hänsch, "Optical frequency metrology," *Nature*, vol. 416, no. 6877, pp. 233–237, 2002.
- [29] J. Hald and V. Ruseva, "Efficient suppression of diode-laser phase noise by optical filtering," *JOSA B*, vol. 22, pp. 2338–2344, 2005.
- [30] F. A. Barbosa, A. S. Coelho, K. N. Cassemiro, P. Nussenzveig, C. Fabre, A. S. Villar, and M. Martinelli, "Quantum state reconstruction of spectral field modes:

- homodyne and resonator detection schemes," *arXiv preprint arXiv:1310.2427*, 2013.
- [31] A. Weiner, "Femtosecond pulse shaping using spatial light modulators," *Review of scientific instruments*, vol. 71, no. 5, pp. 1929–1960, 2000.
- [32] A. Weiner, *Ultrafast optics*, vol. 72. Wiley, 2011.
- [33] S. Jiang, N. Treps, and C. Fabre, "A time/frequency quantum analysis of the light generated by synchronously pumped optical parametric oscillators," *New Journal of Physics*, vol. 14, no. 4, p. 043006, 2012.
- [34] O. Pinel, *Optique quantique multimode avec des peignes de fréquence*. PhD thesis, Université Pierre et Marie Curie-Paris VI, 2010.
- [35] N. Treps, V. Delaubert, A. Maître, J.-M. Courty, and C. Fabre, "Quantum noise in multipixel image processing," *Physical Review A*, vol. 71, no. 1, p. 013820, 2005.
- [36] G. Grynberg, A. Aspect, and C. Fabre, *Introduction to quantum optics: from the semi-classical approach to quantized light*. Cambridge university press, 2010.
- [37] W. Vogel and D.-G. Welsch, *Quantum optics*. John Wiley & Sons, 2006.
- [38] H. A. Haus, *Electromagnetic noise and quantum optical measurements*. Springer, 2000.
- [39] H.-A. Bachor and T. C. Ralph, *A guide to experiments in quantum optics*. Wiley-VCH, 2004.
- [40] M. C. Wang and G. E. Uhlenbeck, "On the theory of the brownian motion ii," *Reviews of Modern Physics*, vol. 17, no. 2-3, pp. 323–342, 1945.
- [41] A. Papoulis and S. U. Pillai, *Probability, random variables, and stochastic processes*. Tata McGraw-Hill Education, 2002.
- [42] D. Spence, J. Dudley, K. Lamb, W. Sleat, and W. Sibbett, "Nearly quantum-limited timing jitter in a self-mode-locked ti:sapphire laser," *Optics letters*, vol. 19, no. 7, pp. 481–483, 1994.
- [43] T. M. Fortier, D. J. Jones, J. Ye, S. T. Cundiff, and R. S. Windeler, "Long-term carrier-envelope phase coherence," *Optics letters*, vol. 27, no. 16, pp. 1436–1438, 2002.

- [44] T. M. Fortier, *Phase-stabilized modelocked lasers: From optical frequency metrology to waveform synthesis of ultrashort pulses*. 2003.
- [45] F. W. Helbing, G. Steinmeyer, and U. Keller, "Carrier-envelope offset phase-locking with attosecond timing jitter," *Selected Topics in Quantum Electronics, IEEE Journal of*, vol. 9, no. 4, pp. 1030–1040, 2003.
- [46] J. Rutman and F. Walls, "Characterization of frequency stability in precision frequency sources," *Proceedings of the IEEE*, vol. 79, no. 7, pp. 952–960, 1991.
- [47] J. Rutman, "Characterization of phase and frequency instabilities in precision frequency sources: Fifteen years of progress," *Proceedings of the IEEE*, vol. 66, no. 9, pp. 1048–1075, 1978.
- [48] Chronos and R. Besson, *La mesure de la fréquence des oscillateurs*. Masson, 1991.
- [49] K. Predehl, G. Grosche, S. Raupach, S. Droste, O. Terra, J. Alnis, T. Legero, T. Hänsch, T. Udem, R. Holzwarth, *et al.*, "A 920-kilometer optical fiber link for frequency metrology at the 19th decimal place," *Science*, vol. 336, no. 6080, pp. 441–444, 2012.
- [50] L. Cutler and C. Searle, "Some aspects of the theory and measurement of frequency fluctuations in frequency standards," *Proceedings of the IEEE*, vol. 54, no. 2, pp. 136–154, 1966.
- [51] R. Paschotta, *Encyclopedia of laser physics and technology*, vol. 1. Wiley-VCH Berlin, 2008.
- [52] A. L. Schawlow and C. H. Townes, "Infrared and optical masers," *Physical Review*, vol. 112, no. 6, p. 1940, 1958.
- [53] E. Rubiola, *Phase noise and frequency stability in oscillators*. Cambridge University Press, 2008.
- [54] R. Paschotta, "Noise of mode-locked lasers (part ii): timing jitter and other fluctuations," *Appl. Phys. B*, vol. 79, pp. 163–173, 2004.
- [55] N. Treps, "Time and frequency by a characteristic mode," *Unpublished considerations*, 2009.
- [56] F. Krausz, M. E. Fermann, T. Brabec, P. F. Curley, M. Hofer, M. H. Ober, C. Spielmann, E. Wintner, and A. Schmidt, "Femtosecond solid-state lasers," *Quantum Electronics, IEEE Journal of*, vol. 28, no. 10, pp. 2097–2122, 1992.

- [57] F. X. Kärtner, *Few-cycle laser pulse generation and its applications*, vol. 95. Springer, 2004.
- [58] T. Brabec and F. Krausz, "Intense few-cycle laser fields: Frontiers of nonlinear optics," *Reviews of Modern Physics*, vol. 72, no. 2, p. 545, 2000.
- [59] H. Y. Lai, "Quantum theory of self-induced transparency solitons: A linearization approach," *Phys. Rev. A*, vol. 42, no. 5, pp. 2925–2935, 1990.
- [60] S. T. Cundiff and J. Ye, *Femtosecond optical frequency comb: Principle, Operation and Applications*. Springer, 2005.
- [61] C. R. Menyuk, J. K. Wahlstrand, J. Willits, R. P. Smith, T. R. Schibli, and S. T. Cundiff, "Pulse dynamics in mode-locked lasers: relaxation oscillations and frequency pulling," *Opt. Express*, vol. 15, pp. 6677–6689, 2007.
- [62] J. Wahlstrand, J. Willits, T. Schibli, C. Menyuk, and S. Cundiff, "Quantitative measurement of timing and phase dynamics in a mode-locked laser," *Optics letters*, vol. 32, no. 23, pp. 3426–3428, 2007.
- [63] J.-M. Shieh, S.-C. Liu, and C.-L. Pan, "Characterization and reduction of phase noise in passively mode-locked titanium:sapphire lasers with intracavity saturable absorbers," *JOSA B*, vol. 15, no. 6, pp. 1802–1807, 1998.
- [64] P. Wai and C. Menyuk, "Polarization decorrelation in optical fibers with randomly varying birefringence," *Optics letters*, vol. 19, no. 19, pp. 1517–1519, 1994.
- [65] R. Holzwarth, *Measuring the frequency of light using femtosecond laser pulses*. PhD thesis, Ludwig Maximilians University Munich, 2001.
- [66] N. Newbury and W. Swann, "Low-noise fiber-laser frequency combs," *JOSA B*, vol. 24, no. 8, pp. 1756–1770, 2007.
- [67] V. Delaubert, N. Treps, M. Lassen, C. C. Harb, C. Fabre, P. K. Lam, and H. A. Bachor, "Tens of femtosecond homodyne detection as an optimal small-displacement and tilt-measurement scheme," *Physical Review A*, vol. 74, no. 5, p. 053823, 2006.
- [68] N. Treps, N. Grosse, W. P. Bowen, C. Fabre, H.-A. Bachor, and P. K. Lam, "A quantum laser pointer," *Science*, vol. 301, no. 5635, pp. 940–943, 2003.

- [69] R. Schmeissner, V. Thiel, C. Jacquard, C. Fabre, and N. Treps, "Analysis and filtering of phase noise in an optical frequency comb at the quantum limit, to improve timing measurements," *arXiv preprint arXiv:1401.3528*, 2014.
- [70] D. Allan, H. Hellwig, P. Kartaschoff, J. Vanier, J. Vig, G. M. Winkler, and N. Yannoni, "Standard terminology for fundamental frequency and time metrology," in *Frequency Control Symposium, 1988., Proceedings of the 42nd Annual*, pp. 419–425, IEEE, 1988.
- [71] D. B. Sullivan, D. W. Allan, D. A. Howe, and F. L. Walls, *Characterization of clocks and oscillators*. US Department of Commerce, National Institute of Standards and Technology, 1990.
- [72] Agilent, "Phase noise measurement solutions," tech. rep., Agilent, 2011.
- [73] D. von der Linde, "Characterization of the noise in continuously operating mode-locked lasers," *Appl. Phys. B*, vol. 39, pp. 201–217, 1986.
- [74] B. Willke, N. Uehara, E. Gustafson, R. Byer, P. King, S. Seel, R. Savage Jr, *et al.*, "Spatial and temporal filtering of a 10-w nd: Yag laser with a fabry-perot ring-cavity premode cleaner," *Optics letters*, vol. 23, no. 21, pp. 1704–1706, 1998.
- [75] A. S. Villar, "The conversion of phase to amplitude fluctuations of a light beam by an optical cavity," *American Journal of Physics*, vol. 76, p. 922, 2008.
- [76] J. Bienfang, R. Teehan, and C. Denman, "Phase noise transfer in resonant optical cavities," *Review of Scientific Instruments*, vol. 72, p. 3208, 2001.
- [77] T. Hansch and B. Couillaud, "Laser frequency stabilization by polarization spectroscopy of a reflecting reference cavity," *Optics communications*, vol. 35, no. 3, pp. 441–444, 1980.
- [78] E. D. Black, "An introduction to pound drever hall laser frequency stabilization," *American Journal of Physics*, vol. 69, p. 79, 2001.
- [79] R. Drever, J. L. Hall, F. Kowalski, J. Hough, G. Ford, A. Munley, and H. Ward, "Laser phase and frequency stabilization using an optical resonator," *Applied Physics B*, vol. 31, no. 2, pp. 97–105, 1983.
- [80] M. Houssin, M. Jardino, and M. Desaintfuscien, "Comparison of the calculated transient responses of a fabry-perot used in reflection and in transmission," *Review of scientific instruments*, vol. 61, no. 11, pp. 3348–3352, 1990.

- [81] M. J. Thorpe and J. Ye, "Cavity-enhanced direct frequency comb spectroscopy," *Applied Physics B*, vol. 91, no. 3-4, pp. 397–414, 2008.
- [82] R. Jones, T. Ido, T. Loftus, M. Boyd, A. Ludlow, K. Holman, M. Thorpe, K. Moll, and J. Ye, "Stabilized femtosecond lasers for precision frequency metrology and ultrafast science," *Laser Physics*, vol. 15, no. 7, p. 1010, 2005.
- [83] C. Gohle, T. Udem, M. Herrmann, J. Rauschenberger, R. Holzwarth, H. Schuessler, F. Krausz, and T. Hänsch, "A frequency comb in the extreme ultraviolet," *Nature*, vol. 436, no. 7048, pp. 234–237, 2005.
- [84] T. Steinmetz, T. Wilken, C. Araujo-Hauck, R. Holzwarth, T. Hänsch, and T. Udem, "Fabry–perot filter cavities for wide-spaced frequency combs with large spectral bandwidth," *Applied Physics B: Lasers and Optics*, vol. 96, no. 2, pp. 251–256, 2009.
- [85] R. Schmeissner, V. Thiel, C. Fabre, and N. Treps, "Broadband high sensitivity spectral phase noise analysis for frequency combs using a passive cavity," vol. to be submitted, 2014.
- [86] R. Schmeissner, J. Roslund, C. Fabre, and N. Treps, "Spectral noise correlations of an ultrafast frequency comb," *arXiv preprint arXiv:1410.4499*, 2014.
- [87] M. Born, E. Wolf, and A. Bhatia, "Principles of optics: electromagnetic theory of propagation, interference and diffraction of light, 7th (expanded) ed," *Cambridge U. Press, Cambridge, UK*, pp. 193–199, 1999.
- [88] H. Kogelnik and T. Li, "Laser beams and resonators," *Proceedings of the IEEE*, vol. 54, no. 10, pp. 1312–1329, 1966.
- [89] S. Gigan, *Amplification paramétrique d'images en cavité: Effets classiques et quantiques*. PhD thesis, Université Pierre et Marie Curie-Paris VI, 2004.
- [90] A. Yariv, *Optical electronics*. Saunders College Pub., 1991.
- [91] T. Udem, J. Reichert, R. Holzwarth, and T. Hänsch, "Absolute optical frequency measurement of the cesium d 1 line with a mode-locked laser," *Physical Review Letters*, vol. 82, no. 18, p. 3568, 1999.
- [92] C. Spielmann, P. F. Curley, T. Brabec, and F. Krausz, "Ultrabroadband femtosecond lasers," *Quantum Electronics, IEEE Journal of*, vol. 30, no. 4, pp. 1100–1114, 1994.

- [93] L. Matos, O. D. Mücke, J. Chen, and F. X. Kärtner, "Carrier-envelope phase dynamics and noise analysis in octave-spanning titanium:sapphire lasers," *Optics express*, vol. 14, no. 6, pp. 2497–2511, 2006.
- [94] F. Helbing, G. Steinmeyer, U. Keller, R. Windeler, J. Stenger, and H. Telle, "Carrier-envelope offset dynamics of mode-locked lasers," *Optics letters*, vol. 27, no. 3, pp. 194–196, 2002.
- [95] T. R. Schibli, K. Minoshima, F.-L. Hong, H. Inaba, A. Onae, H. Matsumoto, I. Hartl, and M. E. Fermann, "Frequency metrology with a turnkey all-fiber system," *Optics letters*, vol. 29, no. 21, pp. 2467–2469, 2004.
- [96] R. P. Scott, T. D. Mulder, K. A. Baker, and B. H. Kolner, "Amplitude and phase noise sensitivity of modelocked titanium:sapphire lasers in terms of a complex noise transfer function," *Optics express*, vol. 15, no. 14, pp. 9090–9095, 2007.
- [97] C. C. Harb, T. C. Ralph, E. H. Huntington, D. E. McClelland, H.-A. Bachor, and I. Freitag, "Intensity-noise dependence of neodymium: Yag lasers on their diode-laser pump source," *JOSA B*, vol. 14, no. 11, pp. 2936–2945, 1997.
- [98] A.E.Siegman, *Lasers*. University Science Books, 1986.
- [99] R. Jason Jones, J.-C. Diels, J. Jasapara, and W. Rudolph, "Stabilization of the frequency, phase, and repetition rate of an ultra-short pulse train to a fabry-perot reference cavity," *Optics communications*, vol. 175, no. 4, pp. 409–418, 2000.
- [100] Y. Cheng, P. Mussche, and A. Siegman, "Measurement of laser quantum frequency fluctuations using a pound-drever stabilization system," *Quantum Electronics, IEEE Journal of*, vol. 30, no. 6, pp. 1498–1504, 1994.
- [101] R. J. Jones, I. Thomann, and J. Ye, "Precision stabilization of femtosecond lasers to high-finesse optical cavities," *Physical Review A*, vol. 69, no. 5, p. 051803, 2004.
- [102] G. Bönsch and E. Potulski, "Measurement of the refractive index of air and comparison with modified edlén's formulae," *Metrologia*, vol. 35, no. 2, p. 133, 1998.
- [103] M.J.Thorpe, *Cavity-enhanced direct frequency comb spectroscopy*. PhD thesis, University of Colorado, 2009.
- [104] D. Z. Anderson, J. C. Frisch, and C. S. Masser, "Mirror reflectometer based on optical cavity decay time," *Applied Optics*, vol. 23, no. 8, pp. 1238–1245, 1984.

- [105] C. Gohle, *A Coherent Frequency Comb in the Extreme Ultraviolet*. PhD thesis, Ludwig Maximilians University, Munich, 2006.
- [106] J. Morville, D. Romanini, M. Chenevier, and A. Kachanov, "Effects of laser phase noise on the injection of a high-finesse cavity," *Applied optics*, vol. 41, no. 33, pp. 6980–6990, 2002.
- [107] A. Chadi, G. Méjean, R. Grilli, and D. Romanini, "Note: Simple and compact piezoelectric mirror actuator with 100 khz bandwidth, using standard components," *The Review of scientific instruments*, vol. 84, no. 5, pp. 056112–056112, 2013.
- [108] I. Pupeza, T. Eidam, J. Rauschenberger, B. Bernhardt, A. Ozawa, E. Fill, A. Apolonski, T. Udem, J. Limpert, Z. A. Alahmed, *et al.*, "Power scaling of a high-repetition-rate enhancement cavity," *Optics letters*, vol. 35, no. 12, pp. 2052–2054, 2010.
- [109] M. E. Fermann and K. F. Lee, "Xuv sources: 13-nm xuv pulses from a cavity," *Nature Photonics*, vol. 7, no. 8, pp. 587–589, 2013.
- [110] M. Thorpe, R. Jones, K. Moll, J. Ye, and R. Lalezari, "Precise measurements of optical cavity dispersion and mirror coating properties via femtosecond combs," *Opt. Express*, vol. 13, pp. 882–888, 2005.
- [111] C. Gohle, B. Stein, A. Schliesser, T. Udem, and T. Hänsch, "Frequency comb vernier spectroscopy for broadband, high-resolution, high-sensitivity absorption and dispersion spectra," *Physical review letters*, vol. 99, no. 26, p. 263902, 2007.
- [112] S. A. Diddams, L. Hollberg, and V. Mbele, "Molecular fingerprinting with the resolved modes of a femtosecond laser frequency comb," *Nature*, vol. 445, no. 7128, pp. 627–630, 2007.
- [113] A. Schliesser, C. Gohle, T. Udem, and T. Hänsch, "Complete characterization of a broadband high-finesse cavity using an optical frequency comb," *Optics Express*, vol. 14, no. 13, pp. 5975–5983, 2006.
- [114] I. Pupeza, X. Gu, E. Fill, T. Eidam, J. Limpert, A. Tünnermann, F. Krausz, and T. Udem, "Highly sensitive dispersion measurement of a high-power passive optical resonator using spatial-spectral interferometry," *Optics Express*, vol. 18, no. 25, pp. 26184–26195, 2010.

- [115] T. Hammond, A. Mills, and D. Jones, "Simple method to determine dispersion of high-finesse optical cavities," *Optics Express*, vol. 17, no. 11, pp. 8998–9005, 2009.
- [116] H. Carstens, S. Holzberger, J. Kaster, J. Weitenberg, V. Pervak, A. Apolonski, E. Fill, F. Krausz, and I. Pupeza, "Large-mode enhancement cavities," *Optics express*, vol. 21, no. 9, pp. 11606–11617, 2013.
- [117] I. Hartl, T. Schibli, A. Marcinkevicius, D. Yost, D. Hudson, M. Fermann, and J. Ye, "Cavity enhanced similariton yb fiber laser frequency comb," *Optics letters*, vol. 32, no. 19, pp. 2870–2872, 2007.
- [118] A. K. Mills, T. Hammond, M. H. Lam, and D. J. Jones, "Xuv frequency combs via femtosecond enhancement cavities," *Journal of Physics B: Atomic, Molecular and Optical Physics*, vol. 45, no. 14, p. 142001, 2012.
- [119] B. L. Schumaker, "Noise in homodyne detection," *Optics letters*, vol. 9, no. 5, pp. 189–191, 1984.
- [120] T. Godin, B. Wetzal, T. Sylvestre, L. Larger, A. Kudlinski, A. Mussot, A. B. Salem, M. Zghal, G. Genty, F. Dias, *et al.*, "Real time noise and wavelength correlations in octave-spanning supercontinuum generation," *arXiv preprint arXiv:1305.3714*, 2013.
- [121] A. Stingl, R. Szipöcs, M. Lenzner, C. Spielmann, and F. Krausz, "Sub-10-fs mirror-dispersion-controlled ti: sapphire laser," *Optics letters*, vol. 20, no. 6, pp. 602–604, 1995.
- [122] K. Corwin, N. R. Newbury, J. Dudley, S. Coen, S. Diddams, K. Weber, and R. Windeler, "Fundamental noise limitations to supercontinuum generation in microstructure fiber," *Physical review letters*, vol. 90, no. 11, p. 113904, 2003.
- [123] G. Labroille, *Imagerie tridimensionnelle multiphotonique des tissus biologiques à l'aide d'impulsions façonnées*. PhD thesis, Ecole Polytechnique X, 2011.
- [124] I. A. Walmsley and V. Wong, "Characterization of the electric field of ultrashort optical pulses," *JOSA B*, vol. 13, no. 11, pp. 2453–2463, 1996.
- [125] T. D. Mulder, R. P. Scott, and B. H. Kolner, "Amplitude and envelope phase noise of a modelocked laser predicted from its noise transfer function and the pump noise power spectrum," *Optics express*, vol. 16, no. 18, pp. 14186–14191, 2008.

- [126] A. Ruehl, A. Marcinkevicius, M. E. Fermann, and I. Hartl, "80 w, 120 fs yb-fiber frequency comb," *Optics letters*, vol. 35, no. 18, pp. 3015–3017, 2010.
- [127] R. M. De Araujo, *Génération et manipulation de peignes de fréquences quantiques multimodes*. PhD thesis, Université Pierre et Marie Curie-Paris VI, 2012.
- [128] R. Simon, S. Chaturvedi, and V. Srinivasan, "Congruences and canonical forms for a positive matrix: Application to the schweimler–wigner extremum principle," *Journal of Mathematical Physics*, vol. 40, no. 7, pp. 3632–3642, 1999.
- [129] R. S. Bennink and R. W. Boyd, "Improved measurement of multimode squeezed light via an eigenmode approach," *Physical Review A*, vol. 66, no. 5, p. 053815, 2002.
- [130] S. L. Braunstein, "Squeezing as an irreducible resource," *arXiv preprint quant-ph/9904002*, 1999.
- [131] G. Keller, *Génération et caractérisation d'états intriqués en variables continues*. PhD thesis, Université Pierre et Marie Curie-Paris VI, 2008.
- [132] J. Bechhoefer, "Feedback for physicists a tutorial essay on control," *Reviews of Modern Physics*, vol. 77, no. 3, p. 783, 2005.
- [133] G. F. Franklin, J. D. Powell, and A. Emami-Naeini, "Feedback control of dynamics systems," *Pretince Hall Inc*, 1986.
- [134] J. Ziegler and N. Nichols, "Optimum settings for automatic controllers," *trans. ASME*, vol. 64, no. 11, 1942.

Scientific publications

Peer Reviewed Journal Papers

- Roman Schmeissner, Jonathan Roslund, Claude Fabre, and Nicolas Treps, "Spectral Noise Correlations of an Ultrafast Frequency Comb", arXiv preprint arXiv:1410.4499 (2014), *published in Physical Review Letters*
- Roman Schmeissner, Valerian Thiel, Clement Jacquard, Claude Fabre, and Nicolas Treps, "Analysis and filtering of phase noise in an optical frequency comb at the quantum limit to improve timing measurements", arXiv preprint arXiv:1401.3528 (2014), *published in Optics Letters*
- Roman Schmeissner, Valerian Thiel, Claude Fabre, and Nicolas Treps, "Broadband high sensitivity spectral phase noise analysis for frequency combs using a passive cavity", *to be submitted*
- Roman Schmeissner, Damian N. Schimpf and co-authors, "Simplified quantum limited noise analysis comparing Ti:Sapphire and a fiber-based frequency comb", *writing in progress*

Conference Papers

- Roman Schmeissner, Valerian Thiel, Claude Fabre, and Nicolas Treps, "Direct measurement of correlations of amplitude and phase noise in optical frequency combs", European Frequency and Time Forum 2014, accepted as ID 7245
- Roman Schmeissner, Jonathan Roslund, Claude Fabre, and Nicolas Treps, "Generalized representation of noise in optical frequency combs by spectral correlation analysis", European Frequency and Time Forum 2014, accepted as ID 7309
- Roman Schmeissner, Jonathan Roslund, Claude Fabre, and Nicolas Treps, "Revealing spectral amplitude and phase correlations of an optical frequency comb with ultrafast pulse-shaping", accepted for conference CLEO 2014, talk SF1I.5
- Damian N. Schimpf, Roman Schmeissner, Jan Schulte, W.Liu, N.Treps, and Franz X.Kärtner, "Revealing phase fluctuations of fiber oscillators via passive optical cavities", accepted for Ultrafast Phenomena 2014, talk ID 1965365

- Roman Schmeissner, Jonathan Roslund, Claude Fabre, and Nicolas Treps, "Spectral amplitude and phase noise of an optical frequency comb revealed with ultrafast pulse shaping", Annual meeting of the German Physical Society, 2014, talk Q46.1
- Valerian Thiel, Roman Schmeissner, Claude Fabre and Nicolas Treps, "Filtrage et analyse passive de peignes de fréquence pour la métrologie projective à la limite quantique", Conférence COLOQ 2013, no.306
- Roman Schmeissner, Valerian Thiel, Claude Fabre, and Nicolas Treps, "Broadband cavities for noise analysis and filtering in optical frequency combs relative to the quantum limit." International Frequency Control Forum - European Time and Frequency Forum 2013, talk 1090
- Roman Schmeissner, Valerian Thiel, Jonathan Roslund, Claude Fabre, and Nicolas Treps, "Broadband femtosecond filtering cavities for quantum limited projective metrology", Annual meeting of the German Physical Society, 2013, talk Q10.6
- Roman Schmeissner, Valerian Thiel, Claude Fabre, and Nicolas Treps, "Towards optical frequency combs - quantum limited in the 500 kHz range.", International Conference on Space Optics, 2012, no. 0177
- Roman Schmeissner, Claude Fabre and Nicolas Treps, "Peigne de Fréquence Optique à la Limite Quantique pour la Métrologie Quantique", Conférence COLOQ 2012

Acknowledgments

I gratefully acknowledge the support of many people during the course of this thesis: First of all Nicolas Treppe and Claude Fabre for providing me the opportunity to join their group. All your assistance, support of ideas and the provided scientific latitude were more than exemplary. I hope that the insights presented here justify at least partially your confidence.

My sincere gratitude to Jonathan Roslund for his commitment.

I would like to say a special thanks to my direct collaborators Alessandra Croce, Clément Jacquard, Pu Jian, Damian Schimpf and Valerian Thiel.

Thank you all past and present colleagues at the institute, in particular Giulia Ferrini, Guillaume Labroille, Jean-Francois Morizur, Yin Cai, Olivier Morin, Olivier Pinel, Renné Medeiros de Araujo, Shifeng Jiang, Vanessa Chille, Valentin Averchenko and Zhang Zheng. It has been a great time.

The strong support from the mechanics and electronics department was a major pillar of this thesis. Many thanks to Arnaud Leclercq, Brigitte Delamour, Gael Coupin, Jean-Michel Isac, Jean-Pierre Okpiz and Pascal Travers.

Finally I would like to thank my family and friends, especially Anna, Leo and Annett Grobe.

